universität wien

DISSERTATION / DOCTORAL THESIS

Titel der Dissertation /Title of the Doctoral Thesis

„Comprehensive Study of Satellite Precipitation Products“

verfasst von / submitted by

Ehsan Sharifi

angestrebter akademischer Grad / in partial fulfilment of the requirements for the degree of

Doktor der Naturwissenschaften (Dr. rer. nat.)

Wien, 2019 / Vienna 2019

Studienkennzahl lt. Studienblatt / degree programme code as it appears on the student record sheet:	A 796 605 415
Dissertationsgebiet lt. Studienblatt / field of study as it appears on the student record sheet:	Meteorologie
Betreut von / Supervisors:	emer. o. Univ.-Prof. Dr. Reinhold Steinacker Univ.-Prof. Dr. Bahram Saghafian

University of Vienna

Abstract

Faculty of Earth Sciences, Geography and Astronomy

Department of Meteorology and Geophysics (IMGW)

Doctor of Philosophy

Comprehensive Study of Satellite Precipitation Products

By Ehsan Sharifi

Knowing the locations and extents of rain and snowfall is vital to understanding how weather and climate impact our environment and Earth's water and energy cycles, including effects on agriculture, fresh water availability, and response to natural disasters. In areas where a sufficiently dense gauge network and radar system is not available, the currently available satellite-based precipitation estimate (SPE) products can potentially provide the precipitation estimation needed for meteorological and hydrological applications. However, SPEs, like all datasets are subject to errors and uncertainties. Due to inherent biases embedded in satellite precipitation estimates, the accuracy of the new SPE products should be assessed before it can be employed in decision-making activities. These results will better guide those users who are taking advantage of these data to accommodate their various research and operational applications.

This thesis presents four main topics. At first an evaluation of the two recent post real time satellite datasets, final-run of the Integrated Multi-satellitE Retrievals for GPM (IMERG-V03) product, the post real-time of the Tropical Rainfall Measuring Mission (TRMM) and Multi-satellite Precipitation Analysis (TMPA-3B42). Furthermore, a common precipitation forecast model based reanalysis dataset, Era-Interim product from the European Centre for Medium Range Weather Forecasts (ECMWF), in daily, monthly and seasonal resolution is compared against synoptic rain-gauges for four different topography and climate conditions in Iran. Assessment is implemented for a one-year period from March 2014 to February

2015. In daily resolution the results reveal that all three products lead to an underestimation but IMERG performs better than the other products and underestimates precipitation slightly in all four regions. On the basis of daily timescale of bias and correlation coefficient in comparison with the ground data, the IMERG product far outperforms ERA-Interim and 3B42 products. Based on monthly and seasonal resolution, in Guilan all products, in Bushehr and Kermanshah ERA-Interim and in Tehran IMERG and ERA-Interim tend to underestimate. Moreover, based on monthly and seasonal scale, in Guilan, all products tend to underestimate while in Bushehr and Kermanshah, IMERG and 3B42, and in Tehran, 3B42 indicated an overestimation. In particular, for heavy precipitation ($P > 15$ mm/day), IMERG is superior to the other products in all study areas and could be used in future for hydro-meteorological models and applications.

Then, the focus moves to assess the IMERG products, IMERG-final run (FR) and real-time late-run (RT) V03 against a dense station network (62 stations) on a daily and sub-daily time-scale basis in northeast Austria from mid-March 2015 to the end of January 2016. Both products are examined against station data in capturing the occurrence and statistical characteristics of precipitation intensity. With regard to Probability Density Function (PDFs), the SPE products have detected more heavy and extreme precipitation events than the ground measurements. Both precipitation products at all time-scales, except for IMERG-RT 12- hourly and daily precipitation, capture less occurrence of precipitation than the station dataset for light precipitation. This partially explains the under-detection of precipitation events. For all time-scales, both IMERG products' Cumulative Distribution Functions (CDFs) are well above that of the stations' precipitation. Furthermore, for the entire spectrum of precipitation rates ($P \geq 0.1$ mm), 1, 3, 6-hourly, IMERG-FR did not show a clear improvement of the Bias over IMERG-RT, while for 12-hourly and daily precipitation estimates, the bias in IMERG-FR has improved compared to IMERG-RT. In addition, IMERG-FR shows a considerable improvement in RMSE as compared to IMERG-RT. Despite the general low probability of detection (POD) and threat score (TS) and the high false alarm ratio (FAR) within specified precipitation thresholds, the contingency table shows rather acceptable values of the POD, TS and FAR for precipitation without classification.

Furthermore, this thesis investigates a copula-based error-adjustment approach based on the statistical differences between SPE products (IMERG-FR V04) and in-situ observations (observed errors) employing two widely-used error models, namely additive and multiplicative error models, in an attempt to assess their suitability for the error correction of satellite-based daily precipitation estimates over northeast Austria. Then, the error-adjusted realizations based on the concept of the copula are simulated and applied to correct the supplied precipitation fields. Afterwards, an uncertainty analysis associated with original satellite precipitation estimate (OSPE) and error adjustment satellite precipitation estimate (EASPE) linked with additive and multiplicative error models were quantified. It was found that IMERG precipitation estimates improved after an error adjustment when compared to OSPE. The additive error model resulted in a better improvement by fitting the entire range of data when compared with the multiplicative error model. However, the overall spatial dependence of the observed errors is reasonably preserved as that of the generated errors by copula. In addition, the validation results implied that the simulated realizations error-adjusted band, encompassed the observed data reasonably. Moreover, the copula-based simulations associated with the additive error model performed much better in comparison to the multiplicative error model. Overall, by using the t-copula model with an emphasis on the additive error model and imposing the simulated error fields on the OSPE, one may generate multiple realizations of precipitation fields.

Since precipitation within a region may occur at finer scales compared with the pixel size of satellites, satellite data should be sufficiently accurate before used as inputs to the hydro-meteorological and water management models. Therefore, as the last part of this thesis, various downscaling techniques namely multiple linear regression (MLR), artificial neural networks (ANN) and spline interpolation are adopted for downscaling of IMERG-FR V05B precipitation data. In this respect, the relationship among IMERG data and different cloud variables, such as cloud effective radius (CER), cloud optical thickness (COT), and cloud water path (CWP) were evaluated. Downscaled IMERG data, were subsequently validated using 54 independent precipitation datasets from a rain-gauge network on a daily time-scale. According to the results, all downscaled products were more accurate than the original IMERG data. Furthermore, all downscaling techniques captured the spatial patterns of precipitation reasonably well with more detailed information when compared with the original IMERG. Moreover, the proposed methods, which consistently showed increased correlation and reduced mean absolute error and root mean square error for average of all selected events, can more accurately produce downscaled precipitation data.

The results of this thesis suggest that using the new multi-satellite precipitation estimate products, the bias-corrected and downscaled precipitation products may be applied for fulfilling the needs of applications in natural hazard, hydro-meteorology, agricultural, climate change studies etc. where the need for high quality and fine scale precipitation data is of paramount importance.

Universität Wien

Zusammenfassung

Fakultät für Geowissenschaften, Geographie und Astronomie

Institut für Meteorologie und Geophysik

Doktor der Naturwissenschaften

Umfassende Untersuchung von Satelliten-Niederschlagsprodukten

von Ehsan Sharifi

Das Wissen über die geographische Lage und Ausdehnung von Niederschlags ist für das Verständnis des Einflusses von Wetter und Klima auf unsere Umwelt, sowie die Wasser- und Energiezyklen der Erde, inklusive Effekte für die Landwirtschaft, Süßwasserverfügbarkeit und Reaktion auf Naturkatastrophen unverzichtbar. In Gebieten in welchen kein ausreichend dichtes Netzwerk an Niederschlagsmessern oder Radarsystemen vorhanden ist, können die aktuell verfügbaren „satellite-based precipitation estimate" (SPE) Produkte potenziell eine Abschätzung des Niederschlags ermöglichen, wie sie für meteorologische und hydrologische Anwendungen benötigt wird. Allerdings unterliegen SPEs, wie alle Datensätze, Fehlern und Unsicherheiten. Aufgrund von inhärenten systematischen Messabweichungen in den satellitengestützten Niederschlagsabschätzungen, sollte die Genauigkeit der SPE Produkte evaluiert werden bevor diese in Entscheidungsprozessen herangezogen werden. Diese Resultate werden den Benutzern, welche Nutzen aus den Daten ziehen und sie in Forschung und verschiedensten Anwendungsbereichen einsetzen, bessere Dienste leisten.

Diese Arbeit präsentiert vier Hauptthemen. Zuerst eine Beurteilung der zwei aktuellen „post real time satellite" Datensätze, dem „final run" des „integrated Multi-satellite Retrievals for GPM" (IMERG-V03) Produkts, dem „post real-time" der „Tropical Rainfall Measuring Mission" (TRMM) und der „Multi-satellite Analysis" (TMPA-3B42), sowie einem gängigen, mit Hilfe eines Vorhersagemodells erstellten Reanalyse-Datensatzes des

Niederschlags, „Era-Interim“ Produkts des European Centre for Medium Range Weather Forecasts (ECMWF), auf täglicher, monatlicher und jählicher Skala im Vergleich mit synoptischen Niederschlagsmessern aus vier verschiedenen topographischen und klimatischen Bedingungen im Iran. Die Einschätzung wird für eine einjährige Periode von März 2014 bis Februar 2015 implementiert. Auf einer täglichen Skala zeigen die Ergebnisse, dass alle drei Produkte zu einer Unterschätzung führen, IMERG schneidet von den Produkten am besten ab und unterschätzt den Niederschlag in allen vier Regionen nur leicht. Auf Basis einer täglichen Zeitskala des Bias und der Korrelation im Vergleich mit den Bodendaten, übertrifft das IMERG Produkt die ERA-Interim und 3B42 Produkte. Basierend auf monatlichen und saisonalen Zeitskalen tendieren in Guilan alle Produkte, in Bushehr und Kermanshah das ERA-Interim und in Tehran das IMERG und das ERA-Interim zur Unterschätzung. Weiters tendieren auf Basis von monatlichen und saisonalen Skalen in Guilan alle Produkte zur Unterschätzung, während in Bushehr und Kermanshah IMERG und 3B42 und in Tehran 3B42 eine Überschätzung erkennen lassen. Besonders für starke Niederschläge ($P > 15$mm/day), ist IMERG den anderen Produkten in allen Gebieten dieser Studie überlegen und könnte in Zukunft für hydrometeorologische Modelle und andere Anwendungen verwendet werden.

Danach wird der Fokus auf die Beurteilung der IMERG Produkte, des „IMERG-final run“ (FR) sowie des „real-time late-run“ (RT) V03 im Vergleich zu einem dichten Stationsnetzwerk (62 Stationen) auf Basis von Zeitskalen im Umfang eines Tages oder geringer in Nordostösterreich von Mitte März 2015 bis Ende Jänner 2016 gelegt. Beide Produkte werden mit einem Vergleich zu Stationsdaten auf ihre Fähigkeit der Aufzeichnung des Auftretens und der statistischen Charakteristika von Niederschlagsintensität überprüft. In Hinsicht auf die Wahrscheinlichkeitsdichtefunktion (PDF), haben die SPE Produkte mehr schwere und extreme Niederschlagsereignisse detektiert als Bodenmessungen. Beide Niederschlagsprodukte aller Zeitskalen, außer den 12 stündigen und täglichen „IMERG-RT“ Niederschlagsprodukten, zeichnen weniger Niederschlagsereignisse auf als der Stationsdatensatz für leichten Niederschlag. Dies erklärt teilweise die Unterschätzung der Niederschlagsereignisse. Die kumulativen Verteilungsfunktionen beider IMERG Produkte liegen auf allen Zeitskalen weit über jenen des Niederschlags an den Stationen. Weiters zeigte das IMERG-FR für das ganze Spektrum an Niederschlagsklassen ($P \geq 0.1$ mm), 1, 3, 6-stündig keine Verbesserung des Bias gegenüber dem IMERG-RT, während sich der BIAS des IMERG-FR für 12-stündige und ganztägige Niederschlagsabschätzungen gegenüber dem des IMERG-RT verbessert hat. Zusätzlich zeigt das IMERG-FR eine nennenswerte Verbesserung in RMSE verglichen mit dem IMERG-RT. Trotz insgesamt geringer Entdeckungswahrscheinlichkeit (POD) und threat scores (TS) und einem hohen blinden Alarm Anteils (FAR) innerhalb festgelegter Niederschlagsschranken, zeigt die Kontingenztabelle für Niederschlag ohne Klassifikation akzeptable Werte für die POD, den TS und die FAR.

Weiters untersucht diese Arbeit einen Copula-basierten Fehleranpassungsansatz basierend auf den statistischen Unterschieden zwischen SPE Produkten (IMERG-FR V04) und in-situ Beobachtungen (beaobachtete Fehler) unter Einsatz zweier verbreiteter Fehlermodelle, einem additiven und einem multiplikativen, um zu versuchen deren Verwendbarkeit für die Fehlerkorrektur von satellitenbasierten täglichen Niederschlagsabschätzungen über Nordostösterreich festzustellen. Im Anschluss werden die im Fehler angepassten Realisierungen, basierend auf dem Konzept der Copula, simuliert und angewandt, um die gegebenen Niederschlagsfelder zu korrigieren. Im Anschluß wird eine Unsicherheitsanalyse im Zusammenhang mit den "original satellite precipitation estimate" (OSPE) sowie "error adjustment satellite precipitation estimate" (EASPE) verbunden mit additiven und multiplikativen Fehlermodellen quantifiziert. Es zeigt sich, dass sich die Niederschlagsabschätzung der IMERG nach der Fehleranpassung im Vergleich zur OSPE verbessert hat. Das additive Fehlermodell führt, im Vergleich zum multiplikativen Fehlermodell, bei Anpassung des gesamten Datenbereichs zu einer größeren Verbesserung. Allerdings bleibt die gesamte räumliche Abhängigkeit des beobachteten Fehlers erhalten, wie auch jene der erstellten Fehler nach Copula. Zusätzlich implizierten die Validierungsergebnisse, daß das simulierte fehler-adjustierte Band der Realisierungen die beobachteten Daten akzeptabel wiedergibt. Die Copula-basierten Simulationen, welche mit dem additiven Fehlermodell in Verbindung stehen, konnten im Vergleich wesentlich bessere Ergebnisse erzielen, als jene des multiplikativen Fehlermodells. Insgesamt können unter Verwendung des T-Copula Models mit einem Schwerpunkt auf das additive Fehlermodell und Anwenden des simulierten Fehlerfeldes auf das OSPE mehrere Realisierungen des Niederschlags generiert werden.

Da Niederschlag in einer Region auf feineren Skalen als die Pixelgröße eines Satellits vorkommen kann, sollten Satellitendaten hinreichend genau sein, bevor sie als Input in hydrometeorologischen und wasserwirtschaftlichen Modellen verwendet werden.

Deswegen wurden für den letzten Teil dieser Arbeit verschiedene Verfahren zum Downscaling von IMERG-FR V05B Niederschlagsdaten verwendet, “multiple linear regression” (MLR), “artificial neural networks” (ANN) und “spline interpolation”. Zu diesem Zwecke wurde die Verbindung zwischen IMERG Daten und verschiedenen die Wolken betreffenden Variablen, wie beispielsweise “cloud effective radius” (CER), “cloud optical thickness” (COT) und “cloud water path” (CWP), beurteilt. Downscaled IMERG Daten wurden daraufhin unter Verwendung von 54 unabhängigen Datensätzen des Niederschlags eines Netzwerks von Niederschlagsmessern auf einer täglichen Zeitskala validiert. Gemäß der Ergebnisse waren alle diesem Downscaling-Prozess unterzogenen Produkte besser als die originalen IMERG Daten. Weiters konnten die Downscaling Techniken die räumlichen Muster des Niederschlags hinreichend gut aufzeichnen, detaillierter als mit dem originalen IMERG. Zudem können die vorgeschlagenen Methoden, welche konstant eine erhöhte Korrelation sowie reduzierte mittlere absolute und quadratische Fehler für einen Durchschnitt aus allen ausgewählten Ereignissen zeigten, downscaled Niederschlagsdaten mit erhöhter Genauigkeit generieren.

Die Ergebnisse dieser Arbeit legen den Schluss nahe, dass, unter Verwendung der neuen “multi-satellite precipitation estimate” Produkte, die Bias-korrigierten und downscaled Niederschlagsprodukte verwendet werden können, um den Bedarf von Anwendungen in den Bereichen Naturgefahren, Hydrometeorologie, Landwirtschaft, Klimawandelsstudien etc. , wo hochqualitative und feinskalige Niederschlagsdaten höchste Priorität haben, zu erfüllen.

Dedicatory

To my beloved parents

For their endless love, support and encouragement

To my dear wife and best friend, Suzza

For her practical and emotional support

To my siblings

For their affection, support and example during all my life.

Without your unconditional support in this trip that we tackled together, I doubt that my doctoral studies have been completed

Acknowledgements

Completing this dissertation has definitely been a challenge and could not have been accomplished without the assistance and support of many individuals and institutions.

I would like to sincerely thank my supervisor, Prof. Dr. **Reinhold Steinacker**, for his guidance and support throughout this study. His comments and questions were very beneficial in my completion of this thesis. I appreciate all his contributions of time and ideas to make my PhD experience productive and stimulating.

My deepest gratitude goes to my supervisor, Prof. Dr. **Bahram Saghafian** for his detailed criticism and unyielding support. His profound knowledge and expertise in this area of research has always led me throughout my work. I am also thankful for the knowledge I gained while attending his conducting research with him and for allowing me to grow as an independent research scientist.

I wish to express my heartfelt gratitude to Dr. **Manfred Dorninger** for his kind supports in countless aspects to made possible the accomplishment of this PhD thesis. I would also like to thank Prof. Dr. **Leopold Haimberger** who has been supportive and has encouraged me to pursue my dissertation without objection.

I would like to thank my dissertation chairman and the rest of committee members for their time, efforts and excellent feedback that helped me broaden my research perspectives.

I would also like to express my most sincere gratitude to other people that significantly contributed to my education, particularly to Dr. **Saber Moazzami** and Prof. Dr. **Vlado Spiridonov** for sharing their experience and information, which have provided me an opportunity to establish successful collaborative research work.

Data availability is the basic premise for research. With this respect, I acknowledge the Austrian Central Institute for Meteorology and Geodynamics (ZAMG) and Iran Meteorological Organization (IRIMO) for providing the observational data used in this study. I am also grateful to NASA/Goddard Space Flight Center's and PPS, which develop and compute the 3B42 and IMERG as a contribution to TMPA and GPM constellation satellites, and archived at the NASA GES DISC. We also acknowledge the ECMWF-ERA-Interim datasets from the Meteorological Archiving System (MARS) of the European Centre for Medium Range Weather Forecasts (ECMWF).

I also thank the various anonymous reviewers that provided insightful comments to early versions of the published papers that conform the main body of this PhD Thesis, listed in Chapters 2, 3, 4 and 5.

Further, I would like to thank **Michael John Flynn**, **Paul Nogid**, **Kevin Fleming**, **Tony Willis**, and **Kyle Baugher** for proofreading the published/accepted manuscripts.

I also gratefully thank my colleagues in the Meteorology group, whose support made this thesis an enjoyable experience for me.

Last, but not least, I would like to express appreciation to my beloved wife and best friend, **Suzza**, who was beside me and was always my support at every moment. Her quiet patience and unwavering love, support, and encouragement made this dissertation possible. Words cannot express how grateful I am.

Table of Contents

List of Figures

List of Tables

Acronyms

AMSU	Advanced Microwave Sounding Unit
ANN	artificial neural networks
CC	correlation coefficient
CDF	Cumulative Distribution Function
CER	cloud effective radius
CMORPH	climate prediction center morphing technique
COT	cloud optical thickness
CPC	climate prediction center
CSI	Critical success index
CWP	cloud water path
DPR	dual-frequency precipitation radar
EASPE	error-adjustment satellite precipitation estimate
ECMWF	European Centre for Medium Range Weather Forecasts
ETS	Equitable threat score
EUMETSAT	European Organisation for the Exploitation of Meteorological Satellites
FAR	False alarm ratio
Fbias	Frequency bias
FR	Final-Run
GCI	GPM Combined Instrument
GEO	Geostationary Earth Orbiting
GHz	Gigahertz
GMI	GPM Microwave Imager
GOES	Geostationary Operational Environmental Satellite
GPCC	Global Precipitation Climatology Centre
GPCP	Global Precipitation Climatology Project

GPM	Global Precipitation Measurements
GSFC DISC	Goddard Earth Sciences Data and Information Services Center
HK	Hanssen and Kuiper discriminant
IA	Index Agreement
IMERG	Integrated Multi-satellite Retrievals for GPM
IR	Infrared
IRIMO	Iran Meteorological Organization
JAXA	Japanese Space Agency
Ka	Kurz-above
Ku	Kurz-unten
LEO	Low Earth Orbiting
MAE	Mean Absolut Error
Mbias	multiplicative bias
MHS	Microwave Humidity Sounder
MLR	multiple linear regression
MODIS	Moderate Resolution Imaging Spectroradiometer
MPE	Multi-sensor Precipitation Estimates
MSE	Mean Square Error
MTSAT	Japanese Multi-functional Satellite Augmentation System
MW	microwave
NASA	National Aeronautics and Space Administration
NDVI	Normalized Difference Vegetation Index
NOAA	National Oceanic and Atmospheric Administration
NRL	near real-time
NUBF	non-uniform beam filling
NWP	numerical weather prediction
NWS	National Weather Service
OR	Odds ratio
OSPE	original satellite precipitation estimate
PDF	probability density function

PERSIANN	Precipitation Estimation from Remotely Sensed Information using Artificial Neural Networks
PMW	Passive Microwave
POD	Probability of detection
POFD	Probability of false detection
PPS	Precipitation Processing System
PPU	percentage prediction uncertainty
RBias	relative bias
RMSE	root mean square error
RT	Real-Time
SPE	Satellite Precipitation Estimates
SR	Success ratio
SSMIS	Special Sensor Microwave Imager Sounder
TCI	TRMM Combined Instrument
TMI	TRMM Microwave Imager
TMPA	TRMM Multi-satellite Precipitation Analysis
TRMM	Tropical Rainfall Measuring Mission
TS	threat score
TSS	true skill statistic
USA	United States of America
VERA	Vienna Enhanced Resolution Analysis
VIS	Visible
ZAMG	Zentralanstalt für Meteorologie und Geodynamik

Chapter 1

1 Introduction

1.1 Background

Rainfall measurements are traditionally performed using rain gauges. Not only do these gauges need a manual activity for the data collection, they only measure the precipitation within a certain radius around the gauge point. Where the precipitation variation in the landscape is significant, such as mountainous area, the density of the gauge network is sparse. Orographic lifting effects and other complex feedback mechanisms, which take place in areas with high elevation differences and wet surfaces that enhances moisture exchanges between land and atmosphere (Chen et al., 2001), may cause a significant spatial and temporal variability of precipitation. The precipitation collected from point measurements is used, not only in hydrological models for flood, and drought forecasting and water resource management, but also in meteorological models for numerical weather prediction (NWP) and climate changes. While weather radars and rain-gauges are the primary sources of precipitation information, they are typically restricted to populated areas over land and can only extend out a short distance over oceans. These locations are, however, the most interesting spots for precipitation measurements, because both, the amount of precipitation and its spatial variation, are significant. Precipitation input data obviously needs to be accurate in order to satisfy model performance. With a network of rain-gauges, the precipitation of a total area of interest can be calculated using different geospatial interpolation techniques. As a point measurement only tells us something about the precipitation within a certain radius around the measurement location, interpolation using a limited amount of rain-gauges for a large area may not reflect the actual precipitation pattern. Therefore, interpolated maps often are not correct and do not provide the actual spatial variation of precipitation. The accuracy of hydro-meteorological models significantly increases by knowing the spatial variation of precipitation (Liang et al., 2004).

Recent technological advances in the field of remote sensing have led to an increase in available precipitation data on a regional and global scale. Satellites, therefore, provide crucial information to fill in these huge data voids, especially over ungauged regions and oceans. However, where point measurements do not record the precipitation spatial variation, satellite imagery can be used to do that. Ground-based radar systems are also very valuable, but they are mainly restricted to developed countries because of the high investment and difficulty of maintenance.

Satellite-based Precipitation Estimates (SPEs) are therefore a very attractive source of geospatial data, that needs more exploration, especially for areas with sparse/absence of rain-gauges. The biggest advantages and benefits of using satellite data are due to their coverage of large portions of the earth more or less continuously and that the areal total precipitation can be determined in a more accurate manner compared to point measurements. Meteorological Satellites measure different atmospheric parameters such as: cloud cover and temperature, atmospheric moisture, precipitation etc. However, the advantages of using satellite data are limited by complications related to the indirect nature of remotely sensed estimates. In addition, it causes to spread uncertainties into hydro-meteorological models. Therefore, efforts are required to determine the accuracy of data and their associated uncertainties before using them operationally. Using SPE has increased rapidly in the recent years, however, to our knowledge, there are only a few studies on this regard over Austria and Iran, but there has not been done yet any comprehensive study to assess different SPE products over these countries. Hence, in this study, the author has evaluated the accuracy of some well-known SPE products such as IMERG-FR V03, IMER-RT V03, IMERG-FR V04, IMERG-FR V05 B, TMPA-3B42 V07, and ERA-Interim in the diverse climate conditions over different regions in Austria and Iran.

The author has also improved a model to error-adjustment and uncertainty analysis of the new generation of SPEs, IMERG, over northeast of Austria. The proposed model is based on the t-copula in order to describe the spatial dependence structure of error from SPEs and also to simulate multivariate precipitation error fields. This is different to the traditional statistical correlation approaches. The strategy of this method is the identification and description of the underlying dependence structures between observed and SPE variables and its application for bias correction. It is known that the traditional measures of dependence (e.g., Pearson's correlation coefficient) can only capture the strength of the linear dependence as a single global parameter. Alternatively, Copulas are able to describe the complex nonlinear dependence structure between variables (Bárdossy and Pegram, 2009). Based on the identified dependence structure between observed and SPE and the identified respective marginal distributions, a set of realizations is obtained (Mao et al., 2015).

Furthermore, meteorological fields over complex terrain are highly influenced by the earth's surface in various ways depending on the properties of the surface and on the scale of interest. As already mentioned an interpolation of irregularly spaced station data to a regular grid becomes challenging particularly if topography is complex and the fields have to be representative for the upper meso-Gamma scale (2-20 km). However, SPEs spatial resolution, particularly IMERG as a highest spatio-temporal precipitation product (0.1° × 0.1°) is still too coarse for hydro-meteorological models when applied to local basins and regions. Recent investigations on this matter showed that the spatial variation of precipitation has profound effects on behaviors of related models (Xu et al., 2015). Since spatial resolution can greatly influence model/forecast outcomes, finer resolution precipitation data are crucial for improving our understanding of local-scale hydrometeorology. During the last several years, many attempts have been made to downscale SPE data and different techniques by incorporating auxiliary data (e.g. vegetation index, elevation and cloud top temperature). There are two types of downscaling: statistical and dynamical methods that combine a coarse resolution with small resolution models.

As above mentioned, in the downscaling method a low-resolution image is enhanced to a finer resolution using another higher resolution data via a certain regression procedure. Time scale is an important point for downscaling to select the auxiliary data type. When using an index for the greenness of the earth's surface, which represents for instance the amount of vegetation in a certain area, the response of this index to a precipitation event lies in the order of one to three weeks (Cheema et al., 2011). Normalized Difference Vegetation Index (NDVI) is an index for the greenness of a surface, and one can imagine that the greener the surface the more water should be available at that location. When lack of groundwater or a nearby water body is recognized, this greenness can be contributed to precipitation; hence a relationship between NDVI and precipitation exists. But the weakness point of using this index for downscaling appears in regions with high annual precipitation, because these regions reach the saturation point and more precipitation does not mean a higher NDVI. As another example, the time scale between precipitation and cloud cover is much smaller and is typically hourly to daily. Determining the ideal data product for downscaling also depends on the existence of a relationship with sufficient coherence between two variables. Also, a higher precipitation can occur because of changes in air pressure, air temperature, relative humidity and the resulting circulation of moist air. Precipitation can increase along mountain edges as well. The size and effect of this mechanism are dependent on the orientation of a mountain range and its ability to slow down the movement rate of a storm and causing an uplift of the air mass (Daly et al., 1994). In addition, the slope of the elevation has an effect on the increase of precipitation with an increase of elevation, barriers close to the coast can show a higher precipitation increase. Researches have shown that higher elevation areas mostly receive a higher precipitation amount in comparison to lower lying areas (Garcia-Martino et al., 1996).

Most studies for downscaling of low-resolution precipitation products have used topography and an NDVI index as high-resolution auxiliary variables (Chen et al., 2014; Immerzeel et al., 2009; Jia et al., 2011). These environmental variables that are easily derived from high-resolution satellite data, however, are closely related to precipitation only in arid areas. Significant relationships between precipitation and these variables may not be observed in high precipitation and monsoon areas. In addition, most downscaling studies have been done for monthly or yearly precipitation time-scale, while precipitation at a certain time or for a short-term extreme precipitation event, which is highly important for monitoring and forecasting of local heavy precipitation, have not been fully considered for downscaling. This instantaneous precipitation is much more related to local weather conditions (i.e. lifting mechanisms) than to topography and vegetation.

1.2 Meteorological Satellites

Meteorological satellite observation systems have transformed many aspects of natural hazard monitoring since they were first introduced in the 1960s. Satellites are designed to observe the land surface, biosphere, atmosphere, and oceans of the Earth. A meteorological satellite is a type of satellite that is primarily used to monitor the weather and climate of the Earth. These type of satellites, however, observe more than clouds and cloud systems such as: temperature profile, temperature at the cloud top and at the surface of the sea and land, humidity profile, wind at cloud level and at the ocean surface, liquid and total water and precipitation rate, net radiation and albedo, cloud type and height of cloud top, total ozone, the coverage and the edge of ice and snow.

They are also useful in many applications such as weather forecast, flash flood applications etc. The images provided by satellites are typically used to help forecasters track the progression of frontal systems, tropical cyclones, and other major features. However, satellite observations play an important role in data assimilation for NWP models and in producing multi-sensor precipitation products.

A number of different methods are used to retrieve precipitation from satellites. In general methods can be categorized into Low Earth Orbiting (LEO) and Geostationary Earth Orbiting (GEO) as well as by their observing spectral ranges (visible, IR, passive and active microwave) or multispectral (i.e., use of one or more of these individual spectrums). Some brief background on the various retrieval techniques is described below (Qu et al., 2013).

1.2.1 GEO and LEO satellites

GEO satellites are placed into an orbit chosen to maintain a fixed position relative to a point on the ground, with an orbital height of about 36,000 km. At this altitude, a satellite needs exactly 24 hours to orbit around the earth, the same time the earth takes to perform a complete revolution around its axis. The satellites seem to be stationary in the sky when seen from the earth which enable observations with a high temporal resolution of 15 or 30 min. Hence, the satellites always observe the same section of the earth surface and atmosphere. Currently, the main meteorological GEO satellites are those within the NOAA GOES, European Meteosat and Japanese MTSAT programs, together with those operated by India, China and the Russian Federation (Sene, 2013).

LEO or polar satellites, by contrast, are operative at much lower altitudes and thus ordinarily provide observations with higher resolution, but relocated relative to a certain location on the ground and observing different sections of the earth in narrow bands. For example, this type of satellites typically has an altitude of 200-1000 km with an orbital time of about 90-100 min. Global coverage is then provided over a number of orbits. However, most meteorological satellites are placed into sun-synchronous polar orbits so that the satellite passes several times over a given location on the equator at approximately the same time each day. The term sun-synchronous means that the section monitored by the satellites is always radiated by the sun in the same way and the satellites always fly over a particular section always at a specific local time. Recording conditions stay constant and scenes from different time periods can be easily compared (Löffler et al. 2005). As the name suggests, polar orbits pass over the Earth's polar regions. The orbital track of the satellite does not have to cross the poles exactly for an orbit to be called polar, an orbit which passes within 20 to 30 degrees of the poles is still classed as a polar orbit. A low Earth orbit is normally at an altitude of less than 1000 km and could be as low as about 200 km above the Earth. The mean orbital velocity in this circular orbit is around 7.8 km/s. Sun-synchronous orbits are polar orbits which are synchronous with the Sun. A satellite in a sun-synchronous orbit would usually be at an altitude of between 600 to 800 km. Generally, with this orbits, the ground observation is improved since the surface is always illuminated by the Sun at the same angle when viewed from the satellite.

1.2.2 Visible and Infrared Methods

Visible (VIS) and Infrared (IR) techniques were the first satellite methods to be developed and are rather simple to apply. However, as already mentioned these techniques typically show a relatively low degree of accuracy. On the other hand, GEO weather satellite VIS and IR imagers uniquely provide the rapid temporal update cycle needed to capture the growth and decay of precipitating clouds. Precipitation can be indirectly estimated from IR or VIS sensors on board GEO satellites using an empirical relationship between precipitation and the cloud top temperature (PETTY and Krajewski, 1997).

One disadvantage of VIS/IR techniques for estimating precipitation rates is that are necessarily inferential (precipitation is inferred from cloud observations). The accuracy of such techniques is not adequately specified and the techniques are not readily transferable from location to location. In contrast, microwave (MW) remote sensing techniques can give direct information on precipitation. Passive MW radiometry from satellite platforms has also the potential to estimate rainfall rates because the microwave radiation contains direct signals of the cloud and precipitation microphysics.

1.2.3 Passive Microwave Methods

Unlike VIS and IR signals, MW energy can penetrate clouds, in particular, cirrus clouds, and its signal has a strong interaction with the size drops of precipitation and ice particles. This direct impact on the MW measurements by hydrometeors allows for the quantitative detection of precipitation properties in the atmosphere as well as on the surface. It is valuable to mention that passive MW (PMW) detect natural energy (radiation) that is emitted or reflected by the object or scene being observed (earth's surface and atmosphere) that interacts with clouds and precipitation and is measured by a radiometer on board a satellite. Reflected sunlight is the most common source of radiation measured by passive sensors (Figure 1.1). MW sensors receive microwaves, which is longer wavelength than visible light and infrared rays, and observation is not affected by day, night or weather. Most PMW radiometers launched to date operate in frequencies ranging from 6 to 190 GHz. At different frequencies, MW radiometers observe different parts of the rain profile. Below 20 GHz, emission by precipitation-size drops dominates, and ice particles above the rain layer are nearly transparent. Above 60 GHz, ice scattering dominates, and the radiometers cannot sense the raindrops below the freezing layer. Both emission and scattering effects are important for frequencies between 20 and 60 GHz. In general, emission by liquid drops raises brightness temperature, while scattering by ice particles has the opposite effect (Qu et al., 2013). Microwave instruments are often carried on polar-orbiting satellites and sensors carried vary between systems but some examples include the Special Sensor Microwave Imager Sounder (SSMIS), Advanced Microwave Sounding Unit (AMSU), Microwave Humidity Sounder (MHS) and GPM Microwave Imager (GMI) etc.

Microwave radiometers measure emitted microwave radiation, expressed in terms of brightness temperature (T_B), for vertical or horizontal polarization. The emission of microwave energy is commonly referred to as the microwave brightness temperature. The T_B is the fundamental parameter measured by passive microwave radiometers (Liang et al., 2012). There are also two major categories in rainfall estimation using PMW radiometry: emission-based method and scattering-based method.

Emission-based rainfall algorithms are mostly applicable over ocean because water surfaces are relatively homogeneous and provide a cold background due to low emissivity. The presence of the raindrops allows for absorption and emission over the water surfaces and results in a dramatic warming of the satellite measurements. Due to the high and more varying emissivity of the land surface, the only reliable means of detecting rainfall over land is by isolating depressed T_B as a result of scattering by millimeter-sized ice particles that exist in most rain clouds. Since the signal being captured is a result of ice particle instead of raindrops, the scattering-based rainfall estimation is an indirect measure of rainfall, as it relates the magnitude of the scattering near the freezing layer to surface rainfall.

The combination of VIS/IR and PMW observations was therefore seen as an opportunity to combine the good sampling (VIS/IR) with better retrievals (PMW) to provide not only better estimates overall, but estimates with improved temporal and spatial resolution (Tapiador et al., 2012).

1.2.4 Active Microwave Methods

Active sensors, in contrast to PMW radiometers, provide their own source of energy to illuminate the objects they observe. An active sensor emits radiation in the direction of the target to be investigated. The sensor then detects and measures the radiation that is reflected or backscattered from the target. However, they are able to determine fine-scale and vertical distribution of rainfall. In orbit since 1997, the Precipitation Radar (PR) on the Tropical Rainfall Measuring Mission (TRMM) satellite is the first instrument designed to measure rain from space. The many approaches proposed in the last decade to build upon the success of the TRMM era have crystallized into the Global Precipitation Measurement (GPM) mission. It was launched in February 2014 by the National Aeronautics and Space Administration (NASA, USA) and the Japanese Space Agency (JAXA, Japan). The GPM mission consists of a core satellite (Figure 1.2) in non-sun-synchronous orbit (65° inclination on a 407 km-high circular orbit) with a dual-frequency precipitation radar (DPR) and a microwave radiometer (GPM Microwave Imager, GMI).

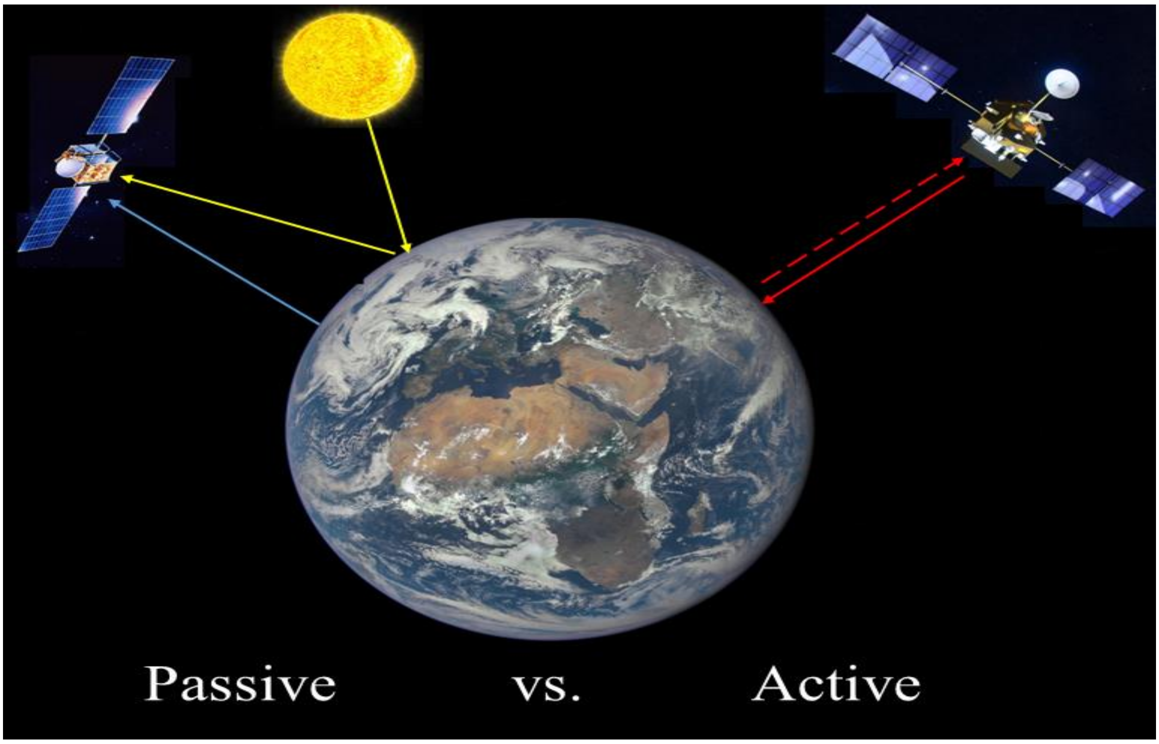

Figure 1.1. Scheme of active and passive sensors

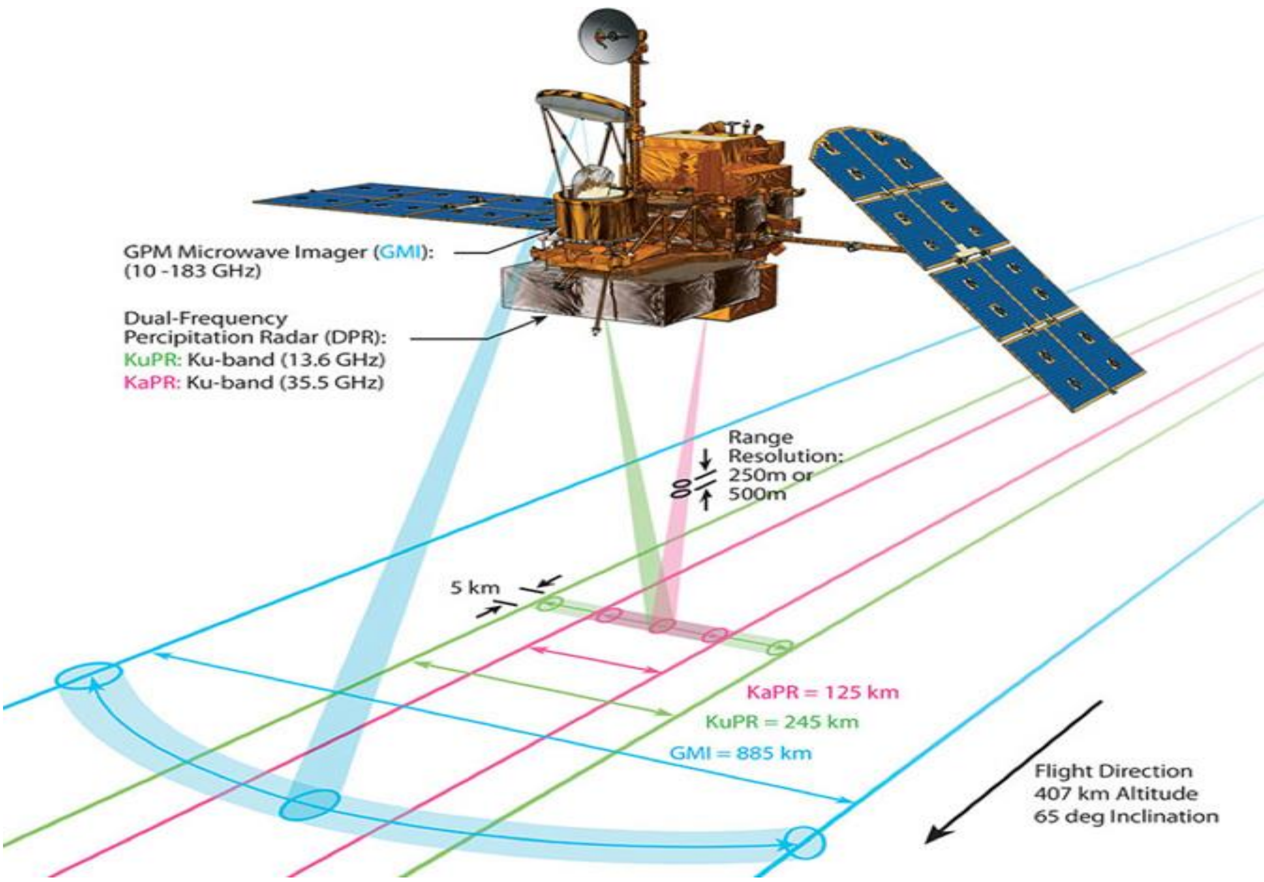

Figure 1.2. Diagram of swath coverage by GPM core satellite sensors. Image credits: NASA

Although an excellent source of rainfall information directly, its primary purpose is to be used in conjunction with the more widely available satellites that contain only PMW sensors. The combination of radar and radiometric methods has already proved useful with TRMM TMI and PR instruments. The DPR improves the single frequency radar capabilities of the TRMM era, providing estimates of the shape and size of hydrometeors and the water phase. In addition to the dual frequency (Ku/Ka-band) radar capability, the DPR can also scan in an interlaced mode with higher sensitivity at Ka-band for detection of light rain and snow.

1.2.5 High Resolution Precipitation Product

The sensors discussed so far each has their limitations which makes them unsuitable for use in certain situations. For instance, PMW estimates over the ocean might be more accurate than GEO-IR estimates, but the latter are better suited for studies of the diurnal cycle due to the superior sampling obtained from a GEO satellite. On the other hand, most GEO-IR sensors only cover a limited geographic domain, whereas the LEO essentially covers the entire globe. However, as mentioned above, techniques using visible channels rely essentially on the presence/absence of cloud, while the infrared techniques rely primarily upon the temperature of the cloud tops. Although techniques based upon PMW sensors provide more direct observations of the hydrometeors (Tapiador et al., 2012). Therefore, a logical next step is optimizing the strength and weakness of each data source and combining them with surface measurements where they are deemed to be the most reliable and create a single estimate. In weather radar research, products of this type are often called Multi-sensor Precipitation Estimates (MPE) whilst the term High Resolution Precipitation Product (HRPP) is also used in satellite-based applications.

The generation of this type of products has been a topic for research for many years with many operational applications appearing in the past several years. Over the past decade, recent increased availability of PMW data have led to the emergence utility for near-global, high-resolution products which have been showing utility for near-real time use. Although not truly global, these products have found a wealth of users in the weather forecasting, climate monitoring, and hydrological communities. Typically, they cover the geographic domain 60°S to 60°N, have 3-hour temporal sampling, and are at 0.25° spatial resolution. This is except the GPM-IMERG products whose spatial and temporal resolution are 0.1° and 30 minutes respectively (Figure 1.3). In the next section the related information about this product is described. Commonly, referred to as HRPPs, they use the high spatial and temporal resolution of IR data to resolve deficiencies in resolution of the higher quality PMW data, although there are substantial differences between the exact methodologies employed.

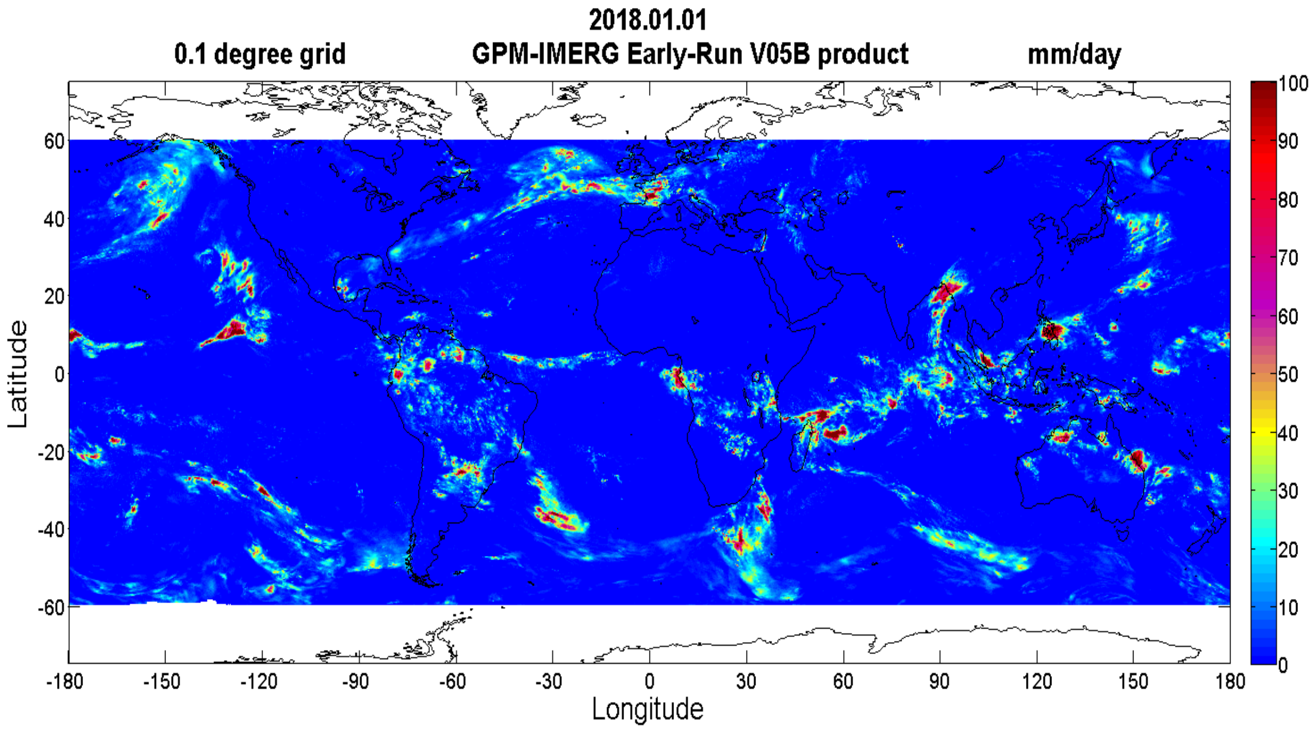

Figure 1.3. Version V05B IMERG early-run daily precipitation fields for 01.01.2018

1.2.6 GPM Constellation Satellites

The GPM core satellite caries a dual-frequency precipitation radar that measure a broader spectrum of precipitation types than its predecessor on TRMM. Three critical improvements in GPM are that 1) the orbital inclination has been increased from 35° to 65°, affording coverage of important additional climate zones; 2) the radar has been upgraded to two frequencies, adding sensitivity to light precipitation; and 3) "high-frequency" channels (165.5 and 183.3 GHz) have been added to the PMW imager, which are expected to facilitate sensing of light and solid precipitation. The observation systems of GPM constellation consists of 1) core satellite, 2) MW constellation, 3) IR constellation, 4) additional satellites (even assuming that high-frequency channels of MW sensors of the constellation can provide high-quality precipitation estimates at high latitudes, the Global Precipitation Climatology Project (GPCP), so-called sounding-based estimates, is needed to fill gaps in the collection of high-latitude estimates.), and 5) precipitation gauges. Figure 1.4 illustrate the multiple precipitation measurement satellites which comprise the GPM constellation.

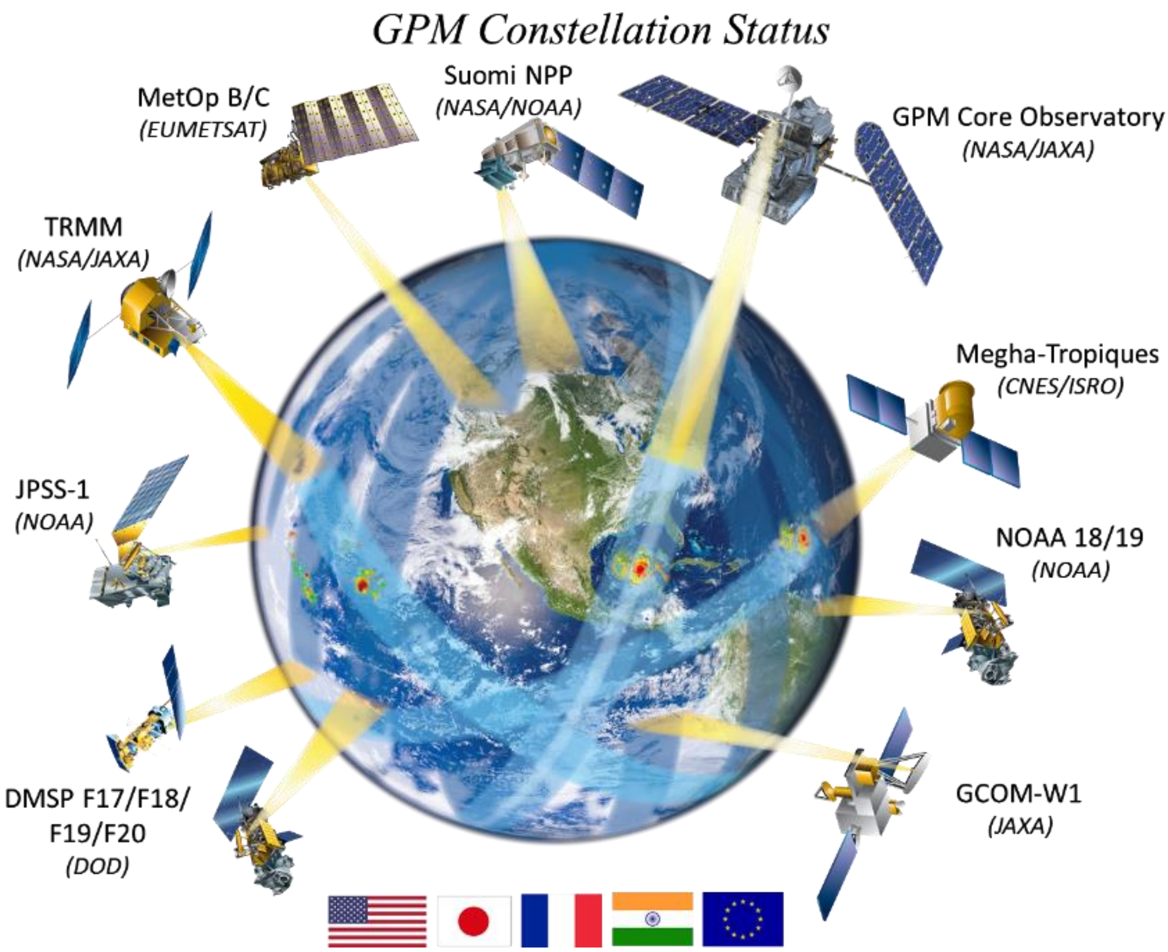

Figure 1.4. GPM constellation satellites (updated 1/13/14)

The GPM-IMERG algorithm is intended to inter-calibrate, merge, and interpolate all satellite MW precipitation estimates, together with MW-calibrated-IR satellite estimates, precipitation gauge analyses, and potentially other precipitation estimators at fine time and space scales for the GPM eras over the entire globe.

IMERG is designed to compensate for the limited sampling available from single leo-satellites by using as many leo-satellites as possible, and then filling in gaps with geostationary IR estimates. This happens in two ways. First, the leo-PMW data are morphed (linear interpolation following the geo-IR-based feature motion). Second, geo-IR precipitation estimates are included using a Kalman filter when the leo-PMW are too sparse. Additionally, at high latitudes the usual PMW imager channels have significant shortcomings, but satellite-sounding-based and experimental sounding-channel based algorithms have shown utility and numerical-model-based estimates have the potential to add value. Finally, precipitation gauge analyses are used to provide crucial regionalization and bias correction to the satellite estimates. Therefore, IMERG uses as many satellites of opportunity as possible in a very flexible framework. Table 1.1 gives a listing of the current and planned data sources, the date spans of useful operation, and the responsible institution. Note that a continuous record from the beginning of TRMM is planed according with GPM-IMERG product (Huffman et al., 2015).

Table 1.1: List of current and planned contributing data sets for IMERG, broken out by sensor type. Data sets with start dates of Jan 98 extend before that time, but these data are not relevant to IMERG. Square brackets ([ ]) indicate an estimated date

Merged Radar – Passive Microwave Imager Products	
Product	*Period of Record*
GPM DPR-GMI	Mar 14 - [Feb 19]
TRMM PR-TMI	Jan 98 - Sep 14

Conically-Scanning Passive Microwave Imagers and Imager/Sounders	
Sensor	*Period of Record*
Aqua AMSR-E	Jun 02 - Oct 11
DMSP F13 SSMI	Jan 98 - Jul 09
DMSP F14 SSMI	Jan 98 - Aug 08
DMSP F15 SSMI	Feb 00 - Aug 06
DMSP F16 SSMIS	Nov 05 - [Nov 15]
DMSP F17 SSMIS	Mar 08 - [Nov 18]
DMSP F18 SSMIS	Mar 10 - [Mar 20]
DMSP F19 SSMIS	Dec 14 - [Jan 24]
GCOMW1 AMSR2	May 12 - [May 22]
GCOMW2 AMSR2	[Feb 16] - [Jan 26]

Cross-Track-Scanning Passive Microwave Sounders	
Sensor	*Period of Record*
GPM GMI	Mar 14 - [Feb 19]
TRMM TMI	Jan 98 – Apr 15
JPSS-1 ATMS	[Jun 16] - [Jun 21]
METOP-2/A MHS	Dec 06 - [Dec 16]
METOP-1/B MHS	Aug 13 - [Aug 23]
METOP-3/C MHS	[Apr 16] - [Apr 26]
M-T SAPHIR *	[Oct 11] - [Jan 15]
NOAA-15 AMSU	Jan 00 - Sep 10
NOAA-16 AMSU	Oct 00 - Apr 10
NOAA-17 AMSU	Jun 02 - Dec 09
NOAA-18 MHS	May 05 - [Jun 15]
NOAA-19 MHS	Feb 09 - [Apr 19]
NPP ATMS	Nov 11 - [Nov 21]

Geosynchronous Infrared Imagers		
Satellite	*Sub-sat. Lon.*	*Agency*
GMS, MTSat, Himawari series	140E	JMA
GOES-E series	75W	NESDIS
GOES-W series	135W	NESDIS
Meteosat prime series	0E	EUMETSAT
Meteosat repositioned series	63E, from Jul 98	EUMETSAT

IR/Passive Microwave Sounders		
Sensor	*Period of Record*	*Institution*
Aqua AIRS	Sep 02 - [Sep 18]	NASA/GSFC DISC
NOAA-14 TOVS	Jan 98 - April 05	Colo. State Univ.; NOAA/NCDC
NPP CrIS	Nov 11 - [Nov 21]	NASA/GSFC DISC

Precipitation Gauge Analyses	
Period of Record	*Institution*
Jan 98 - ongoing	DWD/GPCC

1.3 Objectives

The quantification of precipitation and its spatio-temporal variability is very important for reliable hydro-meteorological modeling since uncertainties in the precipitation values used as key input data will propagate throughout the employed hydro-meteorological models. Therefore, this study tries to evaluate the accuracy of the multi-satellite precipitation products, adjust the bias and break the spatial resolution down to a local perspective and bridges the gap between satellite- and ground-based precipitation studies. This thesis aims therefore to contribute to evaluate the accuracy of the new generation satellite precipitation products' discussion and the results provides further context and a better understanding of the features associated with currently available IMERG precipitation estimates and a broader perspective to users.

Moreover, this study focuses on questions regarding the use of satellite-based precipitation estimates in different climate conditions. In addition, the local precipitation variability and complexity cannot be interpreted from coarse scale, particularly for daily and sub-daily time-scale, and different downscaling techniques are presented to provide a better understanding of the actual precipitation. The research is conducted in northeast Austria and different parts of Iran.

In general, the objectives of this thesis are listed as follow:

- assess the accuracy of the new generation of SPE products against the in-situ observation at different climate conditions.
- assess the accuracy of the SPE products at daily and hourly time-scale over a dense network at varied precipitation thresholds which are referred to as light, medium, heavy, very heavy and extreme precipitation in northeast Austria.
- error-adjustment of the SPEs through a copula-based model linked with additive and multiplicative error models.
- to develop the two integrated downscaling methodologies and incorporation of freely-distributed satellite MODIS data in the downscaling process to a spatial resolution meaningful for applications in hydro-meteorology and water resource studies.

1.4 Research questions

The major research questions that frame the work:

- Do satellite-based precipitation estimates have the capability as an alternative data supplement for in-situ precipitation observations?
- How does the developed error-adjusted model improve the accuracy of the SPEs?
- Could we consider the new downscaled products as input data for hydro-meteorological applications due to their high spatial resolution?

1.5 Outline of thesis

The dissertation consists of four major themes. At introduction part the topic is introduced and giving an overall stating the problem. Moreover, the introduction includes an explanation of the conceptual foundations and detailed information of satellite observation techniques, research question, objectives etc.

Each theme introduces each paper with synopsis of the paper, presenting its bibliographical information. The papers are reformatted to preserve consistency in their presentation, with font styles and sizes aligned. Figures and tables might be relocated within the text and are numbered based on chapter numbers throughout all publications to find the related tables and figures easily by readers. Moreover, a uniform citation style is applied and all references are consolidated at the end of the thesis. Analogous to the references, all abbreviations, figures, and tables are separately listed at the beginning of this dissertation. At the end a conclusion that provides a positioning of the dissertation and give insights regarding limitations as well as future research.

The introduction (chapter 1) is followed by the related publications. They comprise four major themes and summarized as follow:

Theme 1:

In this theme (chapter 2) for the first time we evaluated daily, monthly and seasonal precipitation estimates (derived from half-hourly precipitation estimates of IMERG and 3-hourly precipitation estimates of TMPA 3B42) and ERA-Interim precipitation fields with the corresponding rain-gauge observations according to four different topographic and climatic conditions over parts of Iran.

This section has been published as: Sharifi, E., Steinacker, R., Saghafian, B., 2016. Assessment of GPM-IMERG and Other Precipitation Products against Gauge Data under Different Topographic and Climatic Conditions in Iran: Preliminary Results. *Remote Sensing* 8 (2), 135.

Theme 2:

A comprehensive assessment has been performed to examine the performance of the Day-1 IMERG-FR and IMERG-RT late-run version V03 against 62 meteorological synoptic station data on a multi timescale such as daily and sub-daily time resolution over northeast Austria from mid-March 2015 till end of January 2016 (chapter 3).

This section has been published as: Sharifi, E., Steinacker, R., Saghafian, B., 2018. Multi time-scale evaluation of high-resolution satellite-based precipitation products over northeast of Austria. *Atmospheric Research* 206, 46-63.

Theme 3:

In this part, a copula-based model that preserves the spatial dependency among pixels independent of their marginal and then the simulation of multivariate random precipitation fields has been done to error adjustment of the satellite product. However, the uncertainties associated with high resolution SPE product (IMERG-FR V04) were quantified through above mentioned model associated with additive and multiplicative error models (chapter 4).

This section has been submitted as: Sharifi, E., Saghafian, B., Steinacker, R., 2018. Copula-based Stochastic Uncertainty Analysis of Satellite Precipitation Products. *Journal of Hydrology*, under-review.

Theme 4:

In chapter 5, we developed an operational method to downscale IMERG satellite data to a resolution being meaningful for applications in hydrology and water management. In this chapter, we have presented two downscaling algorithms on the basis of the relationships between SPEs and cloud optical and microphysical properties alongside with spline interpolation in northeast Austria.

This section has been submitted as: Sharifi, E., Saghafian, B., Steinacker, R., 2018. Downscaling Satellite Precipitation Estimates with Multiple Linear Regression, Artificial Neural Networks and Spline Interpolation. *Journal of Geophysical Research: Atmosphere*, under-review.

1.6 software

Apart from the small part of the analysis which was done with Excel; the Geo-spatial data management and analysis, raster processing, (geo-) statistics, modeling, visualization and mapping were conducted with MATLAB and ArcGIS.

Chapter 2

2 Accuracy Assessment of Satellite Products over Iran

This chapter has been published as: Sharifi, E., Steinacker, R., Saghafian, B., 2016. Assessment of GPM-IMERG and Other Precipitation Products against Gauge Data under Different Topographic and Climatic Conditions in Iran: Preliminary Results. *Remote Sensing* 8 (2), 135, https://doi.org/10.3390/rs8020135.

2.1 Abstract

The new generation of weather observatory satellites, namely Global Precipitation Measurement (GPM) constellation satellites, is the lead observatory of the 10 highly advanced earth orbiting weather research satellites. Indeed, GPM is the first satellite that has been designed to measure light rain and snowfall, in addition to heavy tropical rainfall. This work compares the final run of the Integrated Multi-satellitE Retrievals for GPM (IMERG) product, the post real time of TRMM and Multi-satellite Precipitation Analysis (TMPA-3B42) and the Era-Interim product from the European Centre for Medium Range Weather Forecasts (ECMWF) against the Iran Meteorological Organization (IRIMO) daily precipitation measured by the synoptic rain-gauges over four regions with different topography and climate conditions in Iran. Assessment is implemented for a one-year period from March 2014 to February 2015. Overall, in daily scale the results reveal that all three products lead to underestimation but IMERG performs better than other products and underestimates precipitation slightly in all four regions. Based on monthly and seasonal scale, in Guilan all products, in Bushehr and Kermanshah ERA-Interim and in Tehran IMERG and ERA-Interim tend to underestimate. The correlation coefficient between IMERG and the rain-gauge data in daily scale is far superior to that of Era-Interim and TMPA-3B42. On the basis of daily timescale of bias in comparison with the ground data, the IMERG product far outperforms ERA-Interim and 3B42 products. According to the categorical verification technique in this study, IMERG yields better results for detection

of precipitation events on the basis of Probability of Detection (POD), Critical Success Index (CSI) and False Alarm Ratio (FAR) in those areas with stratiform and orographic precipitation, such as Tehran and Kermanshah, compared with other satellite/model data sets. In particular, for heavy precipitation (P >15 mm/day), IMERG is superior to the other products in all study areas and could be used in future for meteorological and hydrological models, *etc*.

2.2 Introduction

Water is fundamental to life on Earth. Knowing the locations and extents of rain and snowfall is vital to understanding how weather and climate impact our environment and Earth's water and energy cycles, including effects on agriculture, fresh water availability, and response to natural disasters. Since rainfall and snowfall vary greatly on a small scale and over time, satellites can provide a better picture of rain and snow distribution around the globe than the ground instruments, particularly in areas where surface measurements are lacking. Nonetheless, evaluation of satellite precipitation estimates is essential prior to operational use. This is why many previous studies are devoted to the validation of satellite estimation (AghaKouchak et al., 2011; AghaKouchak et al., 2012; Amitai et al., 2009).

The primary requirement in precipitation measurement is to know where and how much precipitation is falling at any given time. Such precipitation characteristics may be determined through traditional ground-based rain-gauges and/or advanced satellite precipitation products. Another important aspect deals with the duration of precipitation. In this study, accumulation products have been evaluated daily (derived from accumulation of half-hourly and 3-hourly basis for IMERG, TMPA-3B42 respectively), monthly and seasonally as well.

Radar rainfall may also be used to provide an indirect measurement of rainfall, but then the radar systems need to cover large areas and have appropriate radar rainfall relationships according to the type of precipitation. For most developing countries and even more so for lesser developed countries, radar systems remain too expensive and difficult to maintain and, thus, are not a feasible option for this purpose (Coning, 2013). Furthermore, radar has limited coverage over mountainous areas of terrain, and shading problems as well. Satellite based estimates of rainfall are not as accurate as gauges or radar rainfall, but have the advantage of high temporal resolution and global spatial coverage over oceans and land, particularly mountainous regions and sparsely populated areas. In areas where a sufficiently dense gauge network and radar system is not available, satellite-derived rainfall can be a “critical tool for identifying hazards from smaller-scale rainfall and flood events” (Coning and Poolman, 2011).

2.2.1 Mission Overview of GPM

Global Precipitation Measurement (GPM) constellation satellites are an international mission to provide next generation observations of rain and snow. NASA and the Japanese Aerospace Exploration Agency (JAXA) launched the GPM Core Observatory satellite on 27 February 2014, carrying advanced instruments that will set a new standard for precipitation measurements from space. GPM constellation satellites provided by NASA, the Japanese Aerospace Exploration Agency (JAXA), Eumetsat’s MetOp-B and planned MetOp-C, the NASA-NOAA (American National Oceanic and Atmospheric Administration) Suomi National Polar-orbiting, France and India’s Megha-Tropiques, NOAA’s Polar-orbiting Operational Environmental Satellites, Japan’s first Global Change Observation Mission-Water, U.S. Defense Department meteorological satellites and NOAA’s Joint Polar Satellite System. The data they provide will be used to unify precipitation measurements made by an international network of partner satellites to quantify when, where, and how much it rains or snows around the world. The GPM Core Observatory satellite flies at an altitude of 407 km in a non-sun-synchronous orbit and continues the TRMM sampling strategy and will extend the observations to higher latitudes, covering the globe from the Antarctic Circle to the Arctic Circle (Huffman et al., 2015). However, as you see in Table 2.1, at present, this version covers a latitude from 60°N to 60°S.

Table 2.1.Characteristics of Satellite/Model Precipitation Products

Products	**Temporal Resolution**	**Spatial Resolution**	**Regions**	**Availability Period**
IMERG	half-hourly	0.1 degree	60°N–60°S	March 2014–present
3B42	3-hourly	0.25 degree	50°N–50°S	1997–April 2015
ERA-INTERIM	daily	0.125 degree	90°N–90°S	1979-present

The increased sensitivity of the Dual-frequency Precipitation Radar (DPR) and the high-frequency channels on the GPM Microwave Imager (GMI) will enable GPM to improve forecasting by estimating light rain and falling snow outside the tropics, even in the winter seasons, which other satellites are unable to measure (Huffman et al., 2015).

Researchers and scientists use models for analysis and forecasts of the atmospheric state. The models may have different spatial and temporal resolution. One of the best models, which is used around the world, has been developed by the European Center for Medium Range Weather Forecasts (ECMWF). They have produced a global reanalysis for the last decades of ERA-40 and ERA-Interim, 12-hourly and daily precipitation fields (Dee et al., 2011). Moreover, ERA-Interim is the latest global atmospheric reanalysis produced by ECMWF. The ERA-Interim project was conducted in part to prepare a new atmospheric reanalysis to replace ERA-40, which will extend the data to the early part of the twentieth century. Another tool to determine precipitation at relatively fine temporal and spatial scale is satellite observation. During the last decade, many researchers have evaluated and used satellite data sets and some have found that the TMPA-3B42 post real-time product performed better than other products compared with the rain-gauges (Ashouri et al., 2015; Bao and Zhang, 2013; Javanmard et al., 2010; Moazami et al., 2013; Moazami et al., 2015; Tobin and Bennett, 2010; Yong et al., 2015). One of the disadvantages of TMPA-3B42 was the limited area of observation; it covered only the tropical and subtropical belts. Another disadvantage was the ability to estimate heavy rainfall while light rainfall and snowfall were not detected properly.

As seen in Table 2.1, IMERG is presently available from mid-March 2014 to the present (with access delay in the order of about three months for the final run version). Based on the preliminary analysis during beta testing by Huffman *et al.* (2015), IMERG is smoother than 3B43 over oceans and at higher latitudes. This was a goal for IMERG, which provides estimates every half hour, *versus* the 3-hourly interval for the satellite data contributing to 3B43. Usually, satellite estimation in regions subject to convective precipitation could be difficult whereas they expect that IMERG data sets will be more accurate (Huffman and Bolvin, D. T., Nelkin, E. J., 20 January-2015). Contrary to other satellites, such as TRMM, that could not measure light rain and snowfall, GPM-IMERG uses different sensors from different satellites to detect both light and heavy rain and snowfall. Three critical improvements in GPM are that (1) the orbital inclination has been increased from 35° to 65°, affording coverage of important additional climate zones; (2) the radar has been upgraded to two frequencies, adding sensitivity to light precipitation; and (3) high-frequency channels (165.5 and 183.3 GHz) have been added to the passive microwave (PMW) imager, which are expected to facilitate sensing of light and solid precipitation.

In brief, the input precipitation estimates computed from the various satellite passive microwave sensors are inter-calibrated to the GPM Combined Instrument (GCI, using GMI and DPR), because it is presumed to be the best snapshot GPM estimate, then morphed and combined with microwave precipitation-calibrated geosynchronous earth orbit (geo) infrared (IR) fields, and adjusted with monthly surface precipitation gauge analysis data (where available) to provide half-hourly and monthly precipitation estimates. Precipitation phase is diagnosed using analyses of surface temperature, humidity, and pressure. On the other hand, the TMPA combines microwave data from multiple satellites, each inter-calibrated to the TRMM Combined Instrument (TCI), using TRMM Microwave Imager (TMI) and TRMM Precipitation Radar (PR). Coverage gaps in space and time are filled in with calibrated infrared (IR) data (which are generally available with near-global coverage every 3 hours); coefficients are derived from co-located IR brightness temperatures and the microwave-based precipitation estimates. The final data products reflect scaling the multi-satellite estimates to rain gauge data on a monthly basis, and ensuring that the 3-hourly averages in 3B42 sum to the monthly totals in 3B43 (Huffman and Bolvin, D. T., Nelkin, E. J., 20 January-2015).

Other advantages for using satellite precipitation data in places such as Iran include generally insufficient spatial coverage of *in-situ* data, long delay in data processing and transfer until they become accessible for the public and scientific use, and absence of data sharing in many trans-boundary basins. As a result, this study aims to assess the accuracy of the new generation of satellite precipitation products. To our knowledge, no report exists yet to study the GPM constellation satellites data over Iran.

2.3 Recent Works

kilometers in size around a gauge, whereas rain-gauges can only record what falls in an area some tens of centimeters in diameter (Bell, 2003). However, recently released IMERG is going to reduce this sampling issue such that GPM constellation satellites will have improved spatial and temporal resolutions (*i.e.*, 30 min).

Many attempts have been made to develop and improve global and regional gridded precipitation gauge data sets in recent years (Mitchell and Jones, 2005; New et al., 1999; Schneider et al., Global Precipitation Climatology Centre (GPCC), Deutscher Wetterdienst, Offenbach a. M., Germany, May-2015). However, due to the lack of observational precipitation datasets over land areas for parts of Asia, Yatagai *et al.* (Yatagai et al., 2008; Yatagai et al., 2009) generated a high resolution rain-gauge based daily precipitation grid dataset for the East, Middle East and Russia.

Xie et al., (2007) assessed the performance of five satellite-based rainfall outputs by comparison against gauge analysis: TRMM (3B42-V7, 3B42-RT) of US National Weather Service (NWS), Climate Prediction Center (CPC), Morphing Techniques (CMORPH), Precipitation Estimation from Remotely Sensed Information using Artificial Neural Networks (PERSIANN), and those of Naval Research Laboratory (NRL). They found that all satellite products performed better in wet climate regions and wet seasons, but showed limited skills in estimating precipitation over central Asian arid and semi-arid regions.

Renzullo *et al.* (Renzullo et al., 2011) constructed daily precipitation surfaces for Australia from the post real-time TRMM 3B42 rainfall product. This product has been used in stream flow and flood modeling studies where real-time gauge data is sparse (Hazarika M. K. et al., 2007; Su et al., 2008). Fleming K. et al., (2011) indicated that there is high correlation between TRMM rainfall data and the Australian Bureau of Meteorology monthly grid values data. Regarding the correlation between datasets as a function of climate, the steppe and temperate climate zones show a higher correlation than the tropical and desert zones. The quality of the analysis depends on the density of gauge reports (sparse data imply larger errors), the complexity of the local terrain, *i.e.*, gauges in mountain areas are generally sited in valleys and, therefore, underreport the true areal average rainfall (Huffman et al., 2007).

A strong increase in tropical land precipitation during the past decade is found in ERA-Interim and Global Precipitation Climatology Project 2. While large improvements have been made in terms of temporal homogeneity compared with ERA-40, especially with regard to precipitation, the homogeneity issue still needs to be carefully addressed when interpreting surface flux data from reanalysis or other sources (Chiodo and Haimberger, 2010).

The performance of GPM satellite-based precipitation has not been studied over arid and semi-arid areas in Iran. To address this, in our research, we compare precipitation estimates of GPM-IMERG-final run data sets with meteorological synoptic stations' data over Iran to evaluate the GPM-based precipitation outputs.

2.4 Study Area

To examine the accuracy of satellite observatory precipitation data in different topographic conditions, we selected four study areas in Iran with diverse topography and within different precipitation zones proposed by Modarres (Modarres, 2006) (see Figure 2.1a,b).

Due to Iran's variable topography and climate conditions, we partitioned the study area to cover provinces such as Kermanshah situated in western Iran. Most of the surface of the province lies within the Zagros Mountains, which forms the western periphery of the Iranian Plateau. Running from southeast to northwest, the nearly parallel broken ridges of the Zagros are highest in the east of the province, and elevation drops progressively towards the west, until the vast plains of Iraq fill the horizon (shown in Figure 2.1 in zone G5). The climate of the highlands is mild in summer and cold in winter, with heavy snowfall; only the province's western strip belongs to the warm climate. The average temperatures in Kermanshah City are approximately 0 °C in January and 26 °C in July. The winds blowing from the Mediterranean Sea carry rainclouds, with an annual precipitation of up to 700 mm in the highlands and about 400 mm at Kermanshah City (William B. Fisher, 1968). The second province, namely Guilan, belongs to zone G8 and includes the northwestern end of the Alborz Mountains and the western part of the Caspian lowlands of Iran. The mountainous belt is cut through by the deep transversal valley of the Sefidrud. To the northwest, the highlands stretch over a continuous watershed and, except for at their northern end, they are over 2000 m high, with three spots over 3000 m. Their eastern and northeastern side is deeply carved by parallel streams flowing down towards the Caspian Sea. Prevailing north-south atmospheric currents, humidified over the Caspian, are forced to a vigorous ascent by the mighty barrier of Alborz and thus are responsible for abundant rainfall on both the plain and the northwestern slope of the mountains. Mean annual precipitation varies between 1200 mm and 1800 mm along the shoreline, decreases towards a sub-humid area in the southwestern corner of the plain, and reaches again very high amounts in the lower part of the mountain, up to 1500–2400 mm including convective rainfall during summer. Bushehr (shown in Figure 2.1 in zone G4) is just northwest of the Persian Gulf with an arid and subtropical climate. There are two different regions in Bushehr, which are the plains along the Persian Gulf, and the mountain ranges including the Zagros Mountains. Rainfall in autumn and spring usually occurs in the form of convective precipitation, and during the winter in the form of cyclonic storms. The rest of precipitation is in the form of moderate and light rain. Snowfall was unprecedented in this region. The average annual rainfall in Bushehr is approximately 230 mm and the average temperatures are approximately 24 °C. Tehran (shown in Figure 2.1 in zone G2), the capital, at the southern slopes of Alborz Mountains with a semi-arid climate, represents the remaining study area. Tehran's climate is largely defined by its geographic location, with the towering Alborz Mountains to its north and the central desert to the south. It can be generally described as mild in spring and autumn, hot and dry in summer, and cold in winter. The highest point of the Tehran province is Damavand peak at an altitude of 5678 m and the lower most area of the province being the plains of Varamin, 790 m above sea level and located to the south-east of the province. The hottest months of the year are from mid-July to mid-September when temperatures average around 28–30 °C and the coldest months drop to 1 °C temperature in December to January, and the average annual precipitation is approximately 400 mm, the maximum being during the winter season (see Figure 2.2a,b).

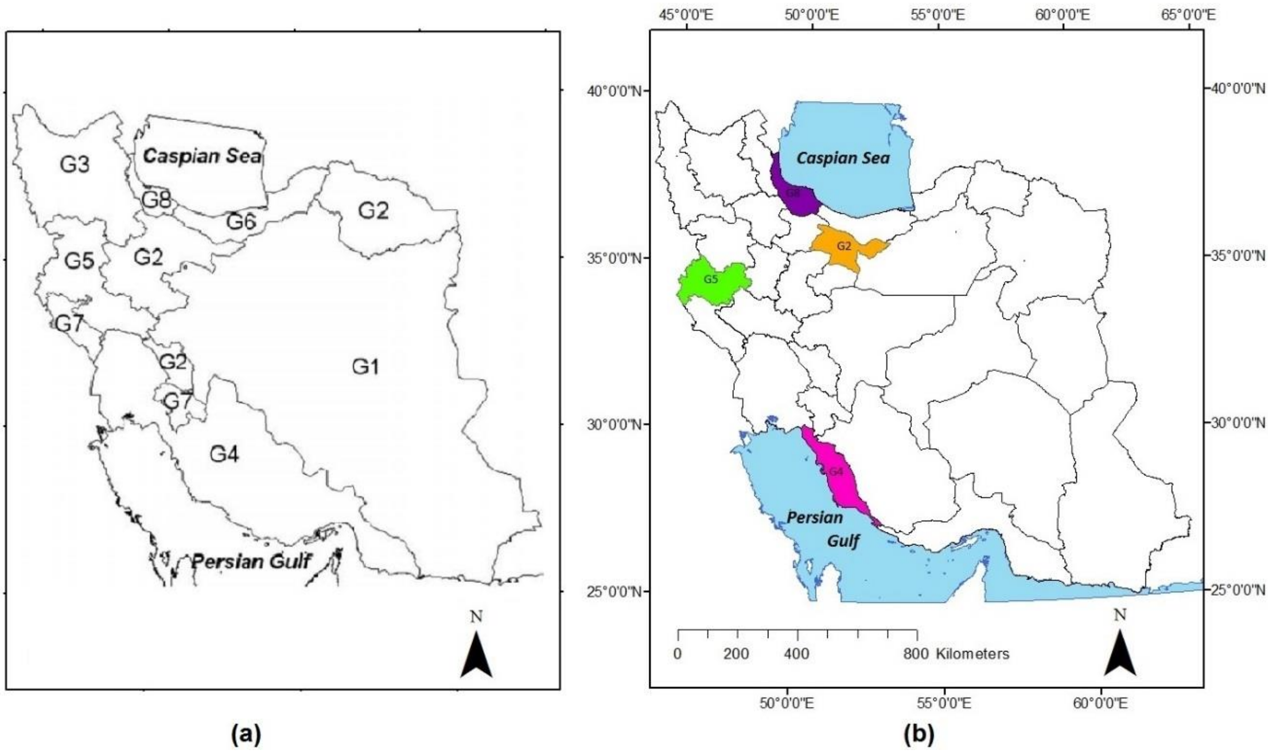

Figure 2.1. (a) Spatial distribution of precipitation zones of Iran (Modarres, 2006); and (b) Provincial map of Iran and the four selected study regions

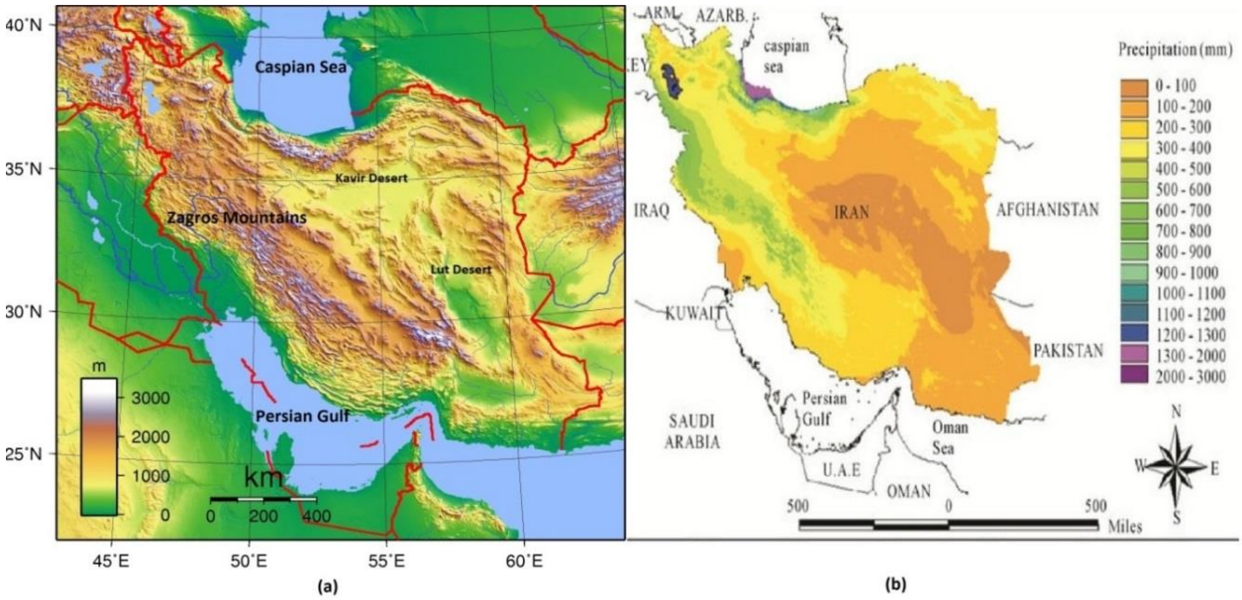

Figure 2.2. (a) Elevation map of Iran; (b) mean annual precipitation (mm) across Iran, 1961–1990 (Javanmard et al., 2010)

2.5 Data and Methodology

2.5.1 Data Sources

In this study, we used only the *in-situ* meteorological synoptic stations within the four study areas that have undergone quality control by the Iran Meteorological Organization (IRIMO). However, the stations with large data gaps were removed. The GPM mission's Precipitation Processing System (PPS) at NASA's Goddard Space Flight Center released the IMERG data to the public in late February, 2015. The data set includes precipitation rates since mid-March 2014. Current and future data sets are freely available to users from NASA Goddard Earth Sciences Data and Information Services Center (GES DISC) website[1]. At present, the IMERG data are available from 12 March 2014 to present, thus providing IMERG-V03D data for March 2014 to February 2015 period. The 3B42-V7 from TRMM and other satellites at GES DISC and ERA-Interim data sets from the European Centre for Medium-Range Weather Forecasts (ECMWF)[2] are available to the public and are free of charge.

We should mention that further works are needed to evaluate the interannual variation of IMERG data relying on larger samples.

The satellite products were compared with the measured precipitation data of 43 meteorological synoptic stations (Figure 2.3) at daily, monthly and seasonal time scales for different climate conditions in Iran. At the time of data analysis, we had access only to this number of stations.

In this research, the data of the nearest grid point in the satellite grid (less than 0.05 degrees off the grid points) is compared with that corresponding to the ground point observation (*i.e.*, the meteorological synoptic station). In cases where the grid points were close to the stations, the comparison was carried out directly between them. However, in cases where the ground station was surrounded by four grid cells but not particularly close to none, an average of the four grid points around the station was used as the basis for comparison. Table 2.1 indicates the characteristics of data sets and Table 2.2 shows the number of stations and pixels in each area as used in this study.

---

[1] http://disc.sci.gsfc.nasa.gov/SSW/ (accessed on 6 June 2015).
[2] http://apps.ecmwf.int/datasets/data/interim-full-daily/ (accessed on 1 July 2015).

Table 2.2. Number of stations and pixels in each area

Products	**Number of Pixels**			
Study Area	No. of Synoptic Stations	IMERG	3B42	ERA-Interim
Guilan (G8)	12	23	23	20
Bushehr (G4)	9	15	18	12
Kermanshah (G5)	12	24	27	18
Tehran (G2)	10	16	22	19

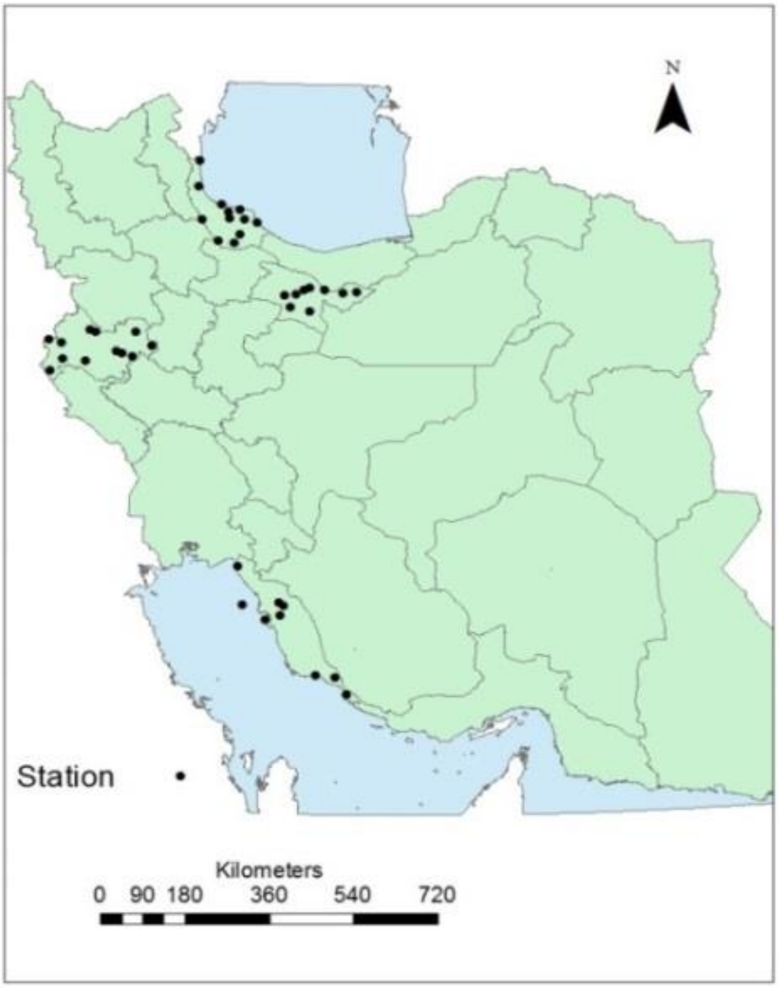

Figure 2.3. Map of meteorological synoptic stations.

2.5.2 Methodology

2.5.2.1 Statistical Analysis

A comprehensive study was performed on the correlation of IMERG, 3B42, and Era-Interim with the station precipitation data over Iran. In the first step, statistical indices such as bias, multiplicative bias (MBias), relative bias (RBias), mean absolute error (MAE), root mean square error (RMSE), and linear correlation coefficient (CC) were determined. The bias is defined as the average difference between *in-situ* observations and satellite/model precipitation estimates (S/M-PE), and can be either positive or negative. A negative bias indicates underestimation by satellite precipitation while a positive bias indicates overestimation.

$$Bias = \frac{\sum_{i=1}^{N}(P_{S_i} - P_{O_i})}{N} \ (mm) \tag{2.1}$$

The multiplicative bias (MBias) is the ratio of S/M-PE over rain-gauge value such that a perfect estimation would result in an Mbias of unity. Underestimation will lead to values less than unity, and overestimation to values greater than unity.

$$MBias = \frac{\sum_{i=1}^{N} P_{S_i}}{\sum_{i=1}^{N} P_{O_i}} \tag{2.2}$$

The relative bias (RBias) describes the systematic bias of satellite-based precipitation and behaves the same as bias.

$$RBias = \frac{\sum_{i=1}^{N}(P_{S_i} - P_{O_i})}{\sum_{i=1}^{N} P_{O_i}} \times 100 \tag{2.3}$$

The mean absolute error (MAE) is used to represent the average magnitude of the error.

$$MAE = \frac{\sum_{i=1}^{N} |P_{S_i} - P_{O_i}|}{N} \ (mm) \tag{2.4}$$

The root mean square error (RMSE), which gives a greater weight to the larger errors relative to MAE, is used to measure the average error magnitude.

$$RMSE = \sqrt{\frac{1}{N}\sum_{i=1}^{N}(P_{S_i} - P_{O_i})^{2}} \ (mm) \tag{2.5}$$

The correlation coefficient (CC) is used to assess the agreement between satellite/model-based precipitation and rain-gauge observations. The value of CC is such that $-1 < CC < +1$. A CC value of +1 indicates a perfect positive fit. If there is no linear correlation or a weak linear correlation, CC is close to zero.

$$CC = \frac{\sum_{i=1}^{N}\left(P_{S_i} - \overline{P}_S\right)\left(P_{O_i} - \overline{P}_O\right)}{\sqrt{\sum_{i=1}^{N}(P_{S_i} - \overline{P}_S)^{2}}\ \sqrt{\sum_{i=1}^{N}(P_{O_i} - \overline{P}_O)^{2}}} \tag{2.6}$$

where P_{S_i} is the value of satellite/model precipitation estimates for the *i*th daily event, P_{O_i} is the value of rain-gauge observation for the *i*th daily event, *N* is the number of observed days, $\overline{P}_S$ is the average value of satellite/model precipitation estimates for *N* observed days over each pixel or grid points.

2.5.2.2 Categorical Technique

Another assessment technique of satellite estimation/model forecast is using a contingency table that reflects the frequency of “Yes” and “No” of the satellite estimation/forecast model (see Table 2.3).

Table 2.3. Contingency table

		Satellite/Model		
		Yes	**No**	total
	Yes	Hits (**a**)	Misses (**c**)	a + c
Rain-Gauge	**No**	False alarms (**b**)	Correct negative (**d**)	b + d
	total	a + b	c + d	**total**

A dichotomous estimates says, “Yes, an event will happen”, or “No, the event will not happen”. By using this table for daily precipitation, a set of statistical indices are shown as follows:

Probability of detection (POD) responds to the question of what fraction of the observed “Yes” events were correctly estimated/forecasted. The perfect score is 1.

$$POD = \frac{a}{a + c} \tag{2.7}$$

False alarm ratio (FAR) deals with the question of what fraction of the estimated/forecasted “Yes” events did not occur. The ideal score is 0.

$$FAR = \frac{b}{a + b} \tag{2.8}$$

Critical success index (CSI) or threat score (TS), answers the question of how well the estimated/forecasted “Yes” events corresponded to the observed “Yes” events. The perfect score is 1.

$$CSI = \frac{a}{a + b + c} \tag{2.9}$$

Accuracy (fraction correct) measures the fraction of correct estimates/forecasts and its perfect score is 1.

$$Accuracy = \frac{a + d}{total} \tag{2.10}$$

Bias (frequency bias) answers the question of how the estimated/forecasted frequency of “Yes” events compared to the observed frequency of “Yes” events. Range of values is 0 to ∞ with a perfect score of 1.

$$Bias = \frac{a + b}{a + c} \tag{2.11}$$

Probability of false detection (POFD) deals with the question of what fraction of observed “No” events were incorrectly estimated/forecasted as “Yes”. The range varies from 0 to 1 and the perfect score is 0.

$$POFD = \frac{b}{d + b} \tag{2.12}$$

Success ratio (SR) responds to the question of what fraction of estimated/forecasted “Yes” events was correctly observed. The range is 0 to 1 and the perfect score is 1.

$$SR = \frac{a}{a + b} \tag{2.13}$$

Equitable threat score (ETS) or Gilbert skill score, answers the question of how well the estimated/forecasted “Yes” events corresponded to the observed “Yes” events. The range is −1/3 to 1 and the perfect score is 1. For rare events, the minimum ETS value is near 0, while the absolute minimum is obtained if the event has a climatological frequency of 0.5, and there are no hits. If the score goes below 0 then the chance forecast is preferred to the actual forecast, and the forecast is said to be unskilled.

$$ETS = \frac{a - a_{random}}{a + b + c - a_{random}} \tag{2.14}$$

Odds ratio (OR) deals with the ratio of the odds of “yes” estimates/forecasts being correct over the odds of “Yes” estimates/forecasts being wrong. Odds ratio range is 0 to ∞, 0 indicates no skill and the perfect score is ∞.

$$OR = \frac{a * d}{c * b} \tag{2.15}$$

Hanssen and Kuiper discriminant (HK) or true skill statistic (TSS) covers the question of how well the estimates/forecast separated the “Yes” events from the “No” events. The range is −1 to 1, while 0 indicates no skill and 1 is the perfect score (Ebert et al., 2007; Thornes and Stephenson, 2001; Wilks Daniel S., 2006).

$$TSS == \frac{a}{a + c} - \frac{b}{b + d} \tag{2.16}$$

$$ORSS = \frac{a * d - c * b}{a * d + c * b} \tag{2.17}$$

where ***a*** represents the number of times that observed rain is correctly detected, ***b*** *is* the number of times that rain is detected but not observed, ***c*** *is* the number of times that observed rain is not detected, ***d*** is the number of times that observed and estimated did not occur and ***total*** is the sample size and

$$a_{random} = \frac{(a + c) * (a + b)}{total} \tag{2.18}$$

2.6 Results and Discussion

This Study for the first time has evaluated daily, monthly and seasonally precipitation estimates (derived from half-hourly precipitation estimates of GPM constellation satellites (IMERG) and 3-hourly precipitation estimates of TRMM and multi satellite precipitation analysis (3B42)) and ERA-Interim precipitation fields from ECMWF in comparison with the corresponding rain-gauge observations according to four different topographic and climatic conditions over parts of Iran. The evaluation results follow.

2.6.1 Daily Evaluation

We start with the evaluation of daily IMERG, TMPA-3B42 and ERA-Interim data against rain-gauge observations. This is based on days with observed precipitation solely. Figure 2.4-Figure 2.6 and Figure 2.7a-c show the scatter plots of average daily precipitation values during March 2014 to February 2015 in four regions. In Figure 2.4 and Table 2.4, all three satellite/model products indicate underestimation according to Bias, Mbias and Rbias values but IMERG shows slight underestimation which means that all three products generate negative systematic errors. 3B42 and ERA-Interim heavily underestimate precipitation in the Guilan region (G8) with respect to Mbias and Rbias. This is more so when the precipitation is above 20 mm according to Figure 2.4c for ERA-Interim. On the basis of RMSE and MAE, ERA-Interim shows better results in comparison with the IMERG and 3B42.

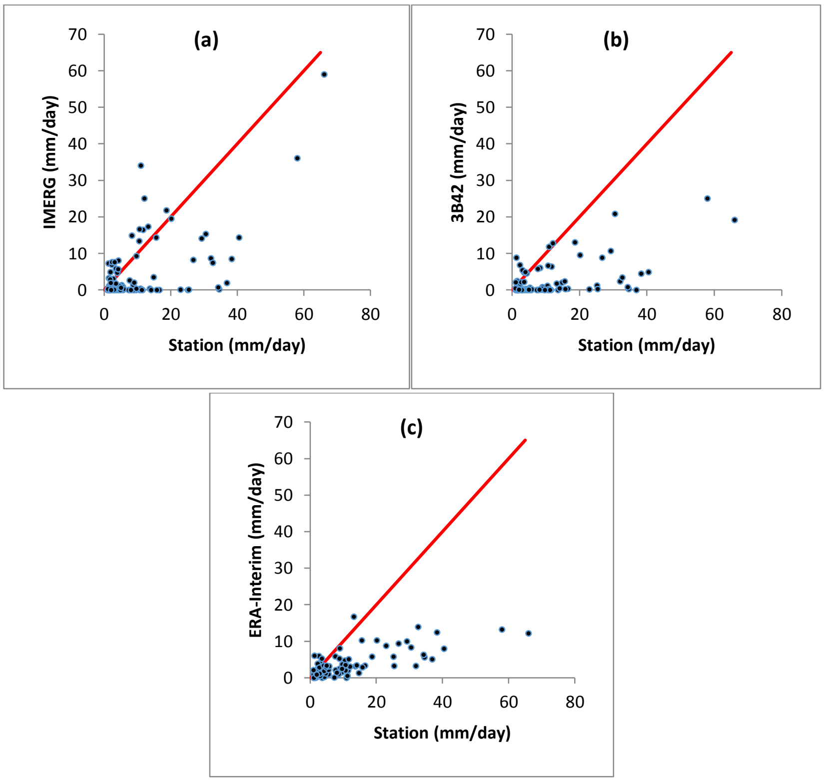

Figure 2.4. Daily precipitation events scatter plots for Guilan of IMERG (a); 3B42 (b) and ERA-Interim (c) against gauge data (mid-March 2014 to February 2015)

As seen in Figure 2.5 and Table 2.5, IMERG, 3B42 and ERA-Interim tend to underestimate while ERA-Interim underestimates heavily when precipitation is above 10 mm in Bushehr (G4). The IMERG yields Bias, Mbias and Rbias better than other products. On the other hand, ERA-Interim provides better values of RMSE and MAE in comparison with 3B42 and IMERG. In all, IMERG indicates a good agreement with the observed data.

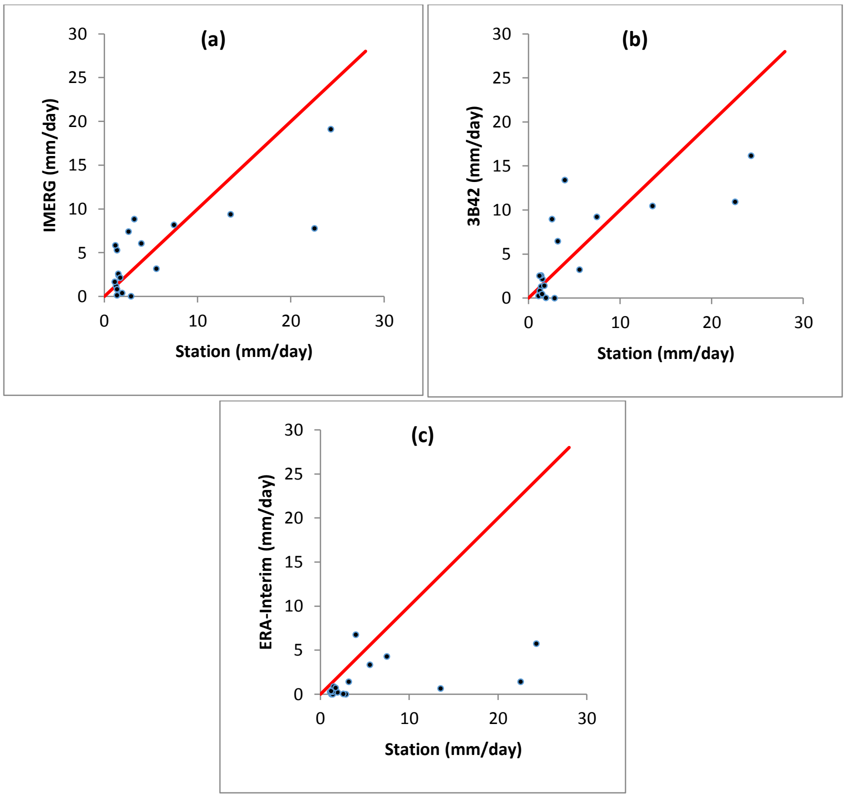

Figure 2.5. Daily precipitation events scatter plots for Bushehr of IMERG (a); 3B42 (b) and ERA-Interim (c) against gauge data (mid-March 2014 to February 2015).

Figure 2.6 presents the scatter plot of daily precipitation over Kermanshah area (G5) where IMERG, 3B42 and ERA-Interim underestimate the observed values. As seen in Table 2.6, IMERG has a better value for RMSE, Bias, Mbias, Rbias and CC in comparison with other data sets while IMERG performs better when precipitation is greater than 10 mm.

As seen in Figure 2.7, for, IMERG, 3B42 and Era-Interim underestimate Tehran (G2) daily precipitation. Furthermore, based on Table 2.7, 3B42 and IMERG show lower bias and better value of Mbias and Rbias in comparison with the other two datasets whereas ERA-Interim yields better in RMSE and MAE.

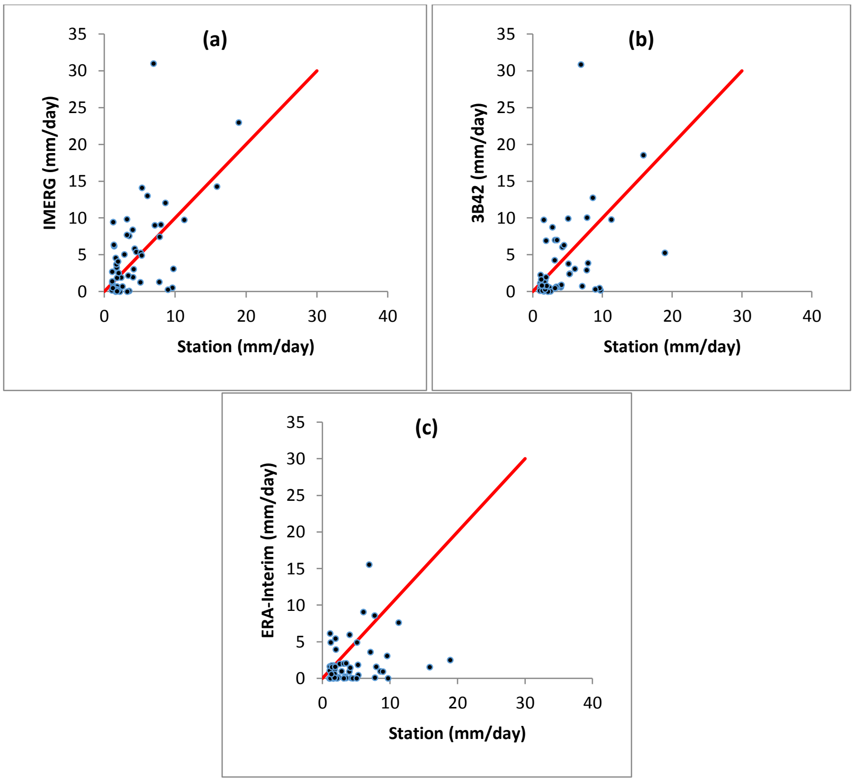

Figure 2.6. Daily precipitation events scatter plots for Kermanshah of IMERG (a); 3B42 (b) and ERA-Interim (c) against gauge data (mid-March 2014 to February 2015).

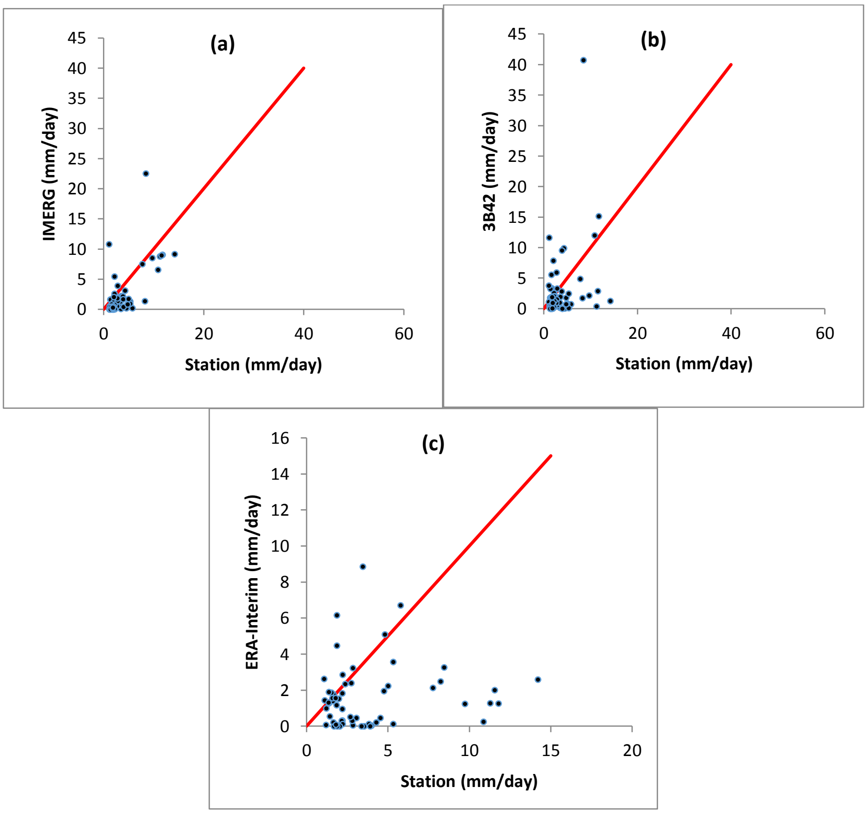

Figure 2.7. Daily precipitation events scatter plots for Tehran of IMERG (a); 3B42 (b) and ERA-Interim (c) against gauge data (mid-March 2014 to February 2015).

Table 2.4. Statistical indices of daily precipitation events in Guilan area (mid-March 2014 to February 2015).

	No. of Events	RMSE (mm)	MAE (mm)	Bias (mm)	Mbias	Rbias	CC
IMERG		19.41	11.59	**−6.41**	**0.62**	**−0.37**	0.40
3B42	105	19.59	11.68	−9.75	0.31	−0.69	0.29
ERA-Interim		**17.59**	**9.88**	−9.06	0.35	−0.65	**0.55**

Table 2.5. Statistical indices of daily precipitation events in Bushehr area (mid-March 2014 to February 2015).

	No. of Events	RMSE (mm)	MAE (mm)	Bias (mm)	Mbias	Rbias	CC
IMERG		13.7	7.92	**−2.52**	**0.90**	**−0.10**	**0.51**
3B42	19	**11.86**	**7.07**	−2.95	0.75	−0.25	0.47
ERA-Interim		14.30	8.04	−7.72	0.22	−0.78	0.40

Table 2.6. Statistical indices of daily precipitation events in Kermanshah area (mid-March 2014 to February 2015).

	No. of events	RMSE (mm)	MAE (mm)	Bias (mm)	Mbias	Rbias	CC
IMERG		**7.10**	4.91	**−0.72**	**0.88**	**−0.12**	**0.52**
3B42	53	7.72	5.39	−1.59	0.75	−0.25	0.42
ERA-Interim		7.35	**4.31**	−3.33	0.52	−0.48	0.38

Table 2.7. Statistical indices of daily precipitation events in Tehran area (mid-March 2014 to February 2015).

	No. of Events	RMSE (mm)	MAE (mm)	Bias (mm)	Mbias	Rbias	CC
IMERG		6.38	4.42	−1.86	0.75	−0.25	**0.46**
3B42	59	7.64	7.74	**−1.47**	**0.78**	**−0.22**	0.27
ERA-Interim		**5.92**	**4.05**	−3.42	0.35	−0.65	0.14

2.6.2 Monthly Evaluation

To evaluate monthly precipitation, we derived IMERG from half-hourly, 3B42 from 3-hourly and ERA-Interim from daily precipitation. As a reference we compared rain-gauge observations with their corresponding grid points on satellites and models for all days of the corresponding months. Figure 2.8 and Table 2.8 show underestimation for monthly scale in all three products but very slightly for IMERG with Bias, Rbias and Mbias of −29.18 mm, 0.98 and −0.02, respectively, which shows a better result in comparison with the other two products. Also, IMERG yields MAE and RMSE of 52.75 mm and 81.43 mm, respectively, in comparison to 59 mm and 102.76 mm for 3B42 while the same for

ERA-Interim are 62.18 mm and 95.41 mm. On the other hand, CC of ERA–Interim indicates better agreement than others in the Guilan region.

As seen in Figure 2.9 and Table 2.9, IMERG and 3B42 tend to overestimate while ERA-Interim underestimates in Bushehr. The 3B42 yields for all indices better results than the other two data sets while ERA-Interim shows significant agreement with a correlation coefficient of 0.95.

Regarding to monthly precipitation over the Kermanshah area, based on Figure 2.10 and Table 2.10, IMERG and 3B42 overestimate and ERA-Interim underestimates the observed values. 3B42 presents lower Bias, MAE and RMSE in comparison with the other two data sets. Furthermore, based on Figure 2.10, ERA-Interim shows a very slight bias during the January, February and March (winter season).

As seen in Figure 2.11 and Table 2.11, 3B42 tends to overestimate Tehran monthly precipitation whereas IMERG and ERA-Interim tend to underestimate. IMERG shows strong overestimates during October while ERA-Interim is almost unbiased in this month. Generally, IMERG represents better value of Bias, Mbias and Rbias while Era-Interim yields a better value for RMSE and MAE.

Table 2.8. Statistical indices of monthly precipitation in Guilan area (mid-March 2014 to February 2015).

	IMERG	**TMPA**	**ERA-Interim**
RMSE (mm)	**81.43**	102.76	95.41
MAE (mm)	**52.75**	59.00	62.18
Bias (mm)	**−29.18**	−35.57	−54.47
Mbias	**0.98**	0.93	0.58
Rbias	**−0.02**	−0.07	−0.42
CC	0.76	0.52	**0.85**

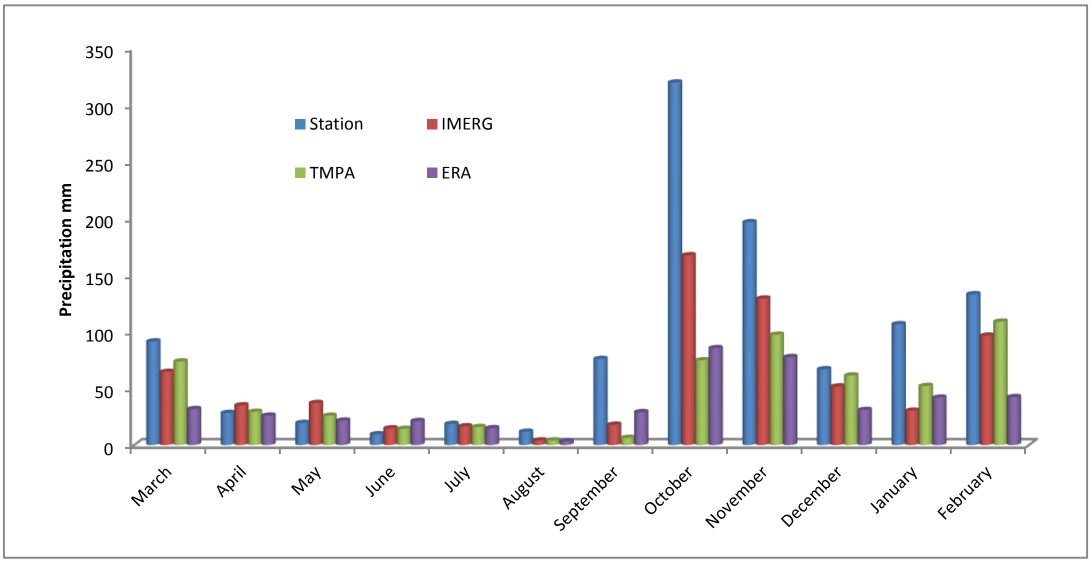

Figure 2.8. Guilan monthly precipitation (mid-March 2014 to February 2015).

Table 2.9. Statistical indices of monthly precipitation in Bushehr area (mid-March 2014 to February 2015).

	IMERG	3B42	ERA-Interim
RMSE (mm)	14.36	**11.88**	16.50
MAE (mm)	7.13	**6.31**	6.39
Bias (mm)	3.84	**1.05**	−5.86
Mbias	1.49	**1.21**	0.39
Rbias	0.71	**0.21**	−0.61
CC	0.82	0.89	**0.95**

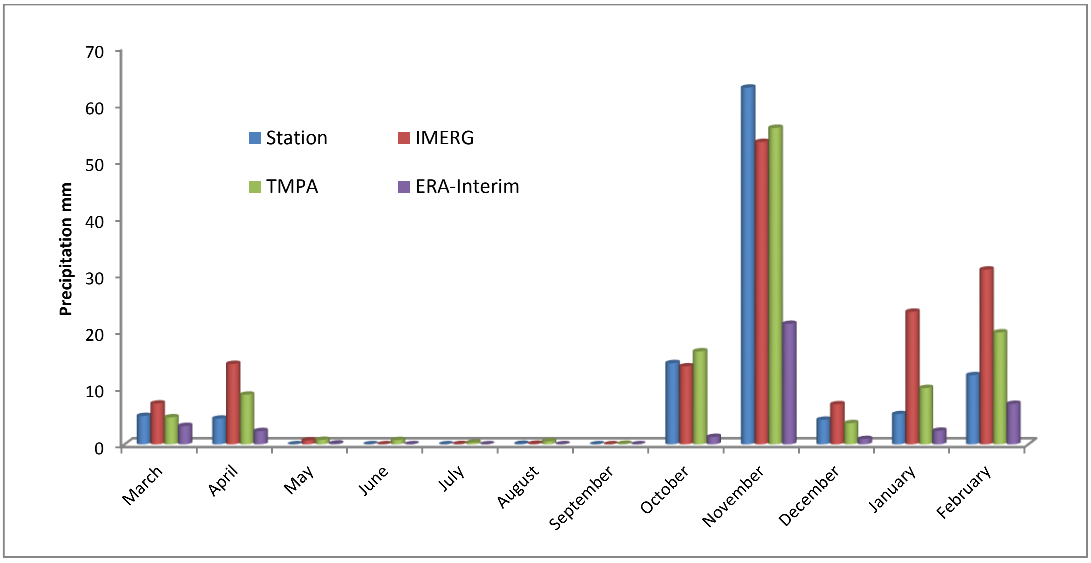

Figure 2.9. Bushehr monthly precipitation (mid-March 2014 to February 2015).

Table 2.10. Statistical indices of monthly precipitation in Kermanshah area (mid-March 2014 to February 2015).

	IMERG	3B42	ERA-Interim
RMSE (mm)	16.94	**15.64**	16.87
MAE (mm)	11.50	**10.31**	10.34
Bias (mm)	7.70	**4.56**	−5.67
Mbias	1.62	1.40	**0.82**
Rbias	0.62	0.57	**−0.18**
CC	**0.88**	0.85	0.84

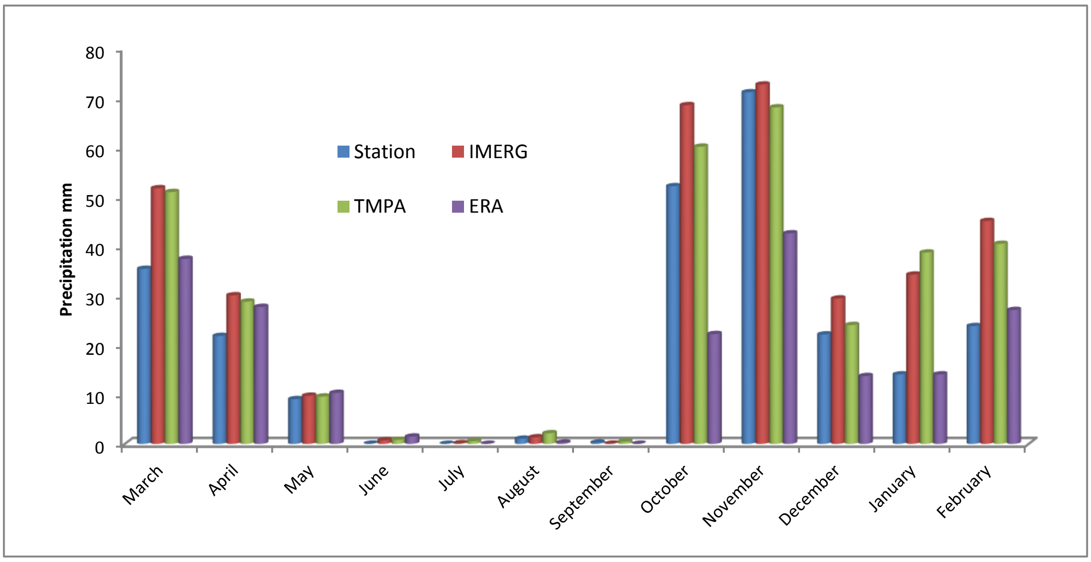

Figure 2.10. Kermanshah monthly precipitation (mid-March 2014 to February 2015).

Table 2.11. Statistical indices of monthly precipitation in Tehran area (mid-March 2014 to February

	IMERG	3B42	ERA-Interim
RMSE (mm)	19.88	20.61	**14.74**
MAE (mm)	14.08	14.55	**11.08**
Bias (mm)	**−5.14**	11.56	−7.34
Mbias	**1.13**	2.03	0.82
Rbias	**0.13**	1.03	−0.18
CC	0.57	0.69	**0.80**

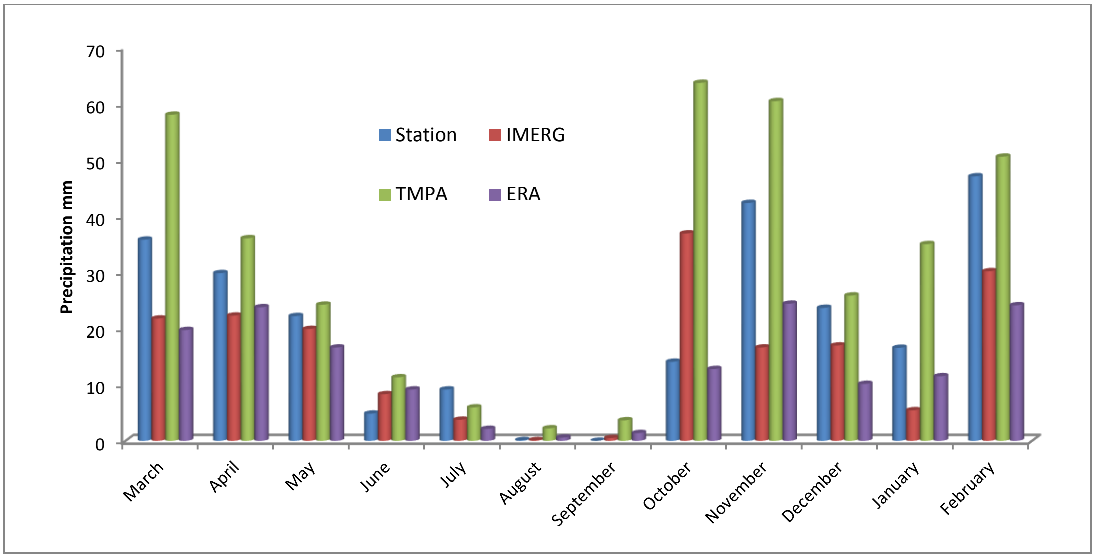

Figure 2.11. Tehran monthly precipitation (mid-March 2014 to February 2015).

2.6.3 Seasonal Evaluation

To evaluate the seasonal precipitation rain-gauge observations with their corresponding grid points on satellites and models, all days of the corresponding seasons are compared. Based on seasonal scale, Figure 2.12 and Table 2.12 indicate that all three products tend to underestimate in all seasons except spring in the Guilan region. IMERG has a better value of Bias, RMSE, Mbias and Rbias while ERA-Interim represents significant agreement.

With respect to Figure 2.13 and Table 2.13, 3B42 shows the best results in Bushehr in comparison with other data sets. IMERG and 3B42 displayed overestimates and ERA-Interim underestimates.

As seen in Figure 2.14 and Table 2.14 , 3B42 and IMERG tend to overestimate while ERA-Interim underestimates in the Kermanshah region. The IMERG yields a correlation coefficient of 0.95 which is a good agreement between satellite estimation and rain-gauge observation and there is no great difference for MAE and Bias among all data sets. In all, ERA-Interim indicates a strong bias during autumn and a slight bias during winter.

Table 2.12. Statistical indices of seasonal precipitation in Guilan area.

	IMERG	**3B42**	**ERA-Interim**
RMSE (mm)	**206.11**	232.06	237.99
MAE (mm)	162.68	**157.28**	179.10
Bias (mm)	**−97.88**	−106.72	−163.03
Mbias	**0.96**	0.93	0.58
Rbias	**−0.04**	−0.07	−0.42
CC	0.85	0.75	**0.93**

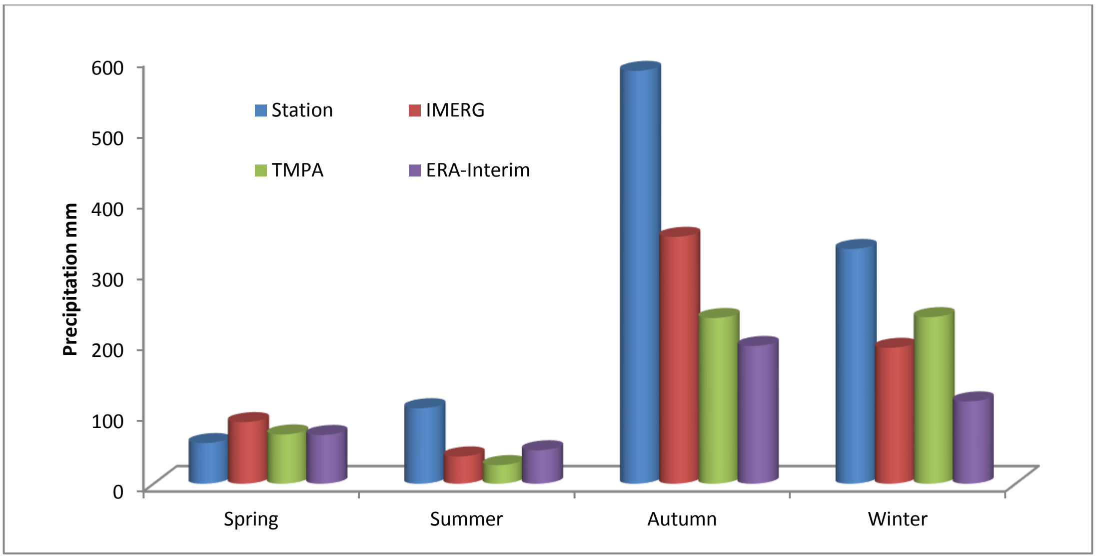

Figure 2.12. Guilan seasonal precipitation

Table 2.13. Statistical indices of seasonal precipitation in Bushehr area.

	IMERG	3B42	ERA-Interim
RMSE (mm)	30.37	**17.81**	30.12
MAE (mm)	22.74	**13.58**	17.99
Bias (mm)	10.46	**3.14**	−17.59
Mbias	1.60	**1.21**	0.39
Rbias	0.60	**0.21**	−0.61
CC	0.83	**0.95**	0.92

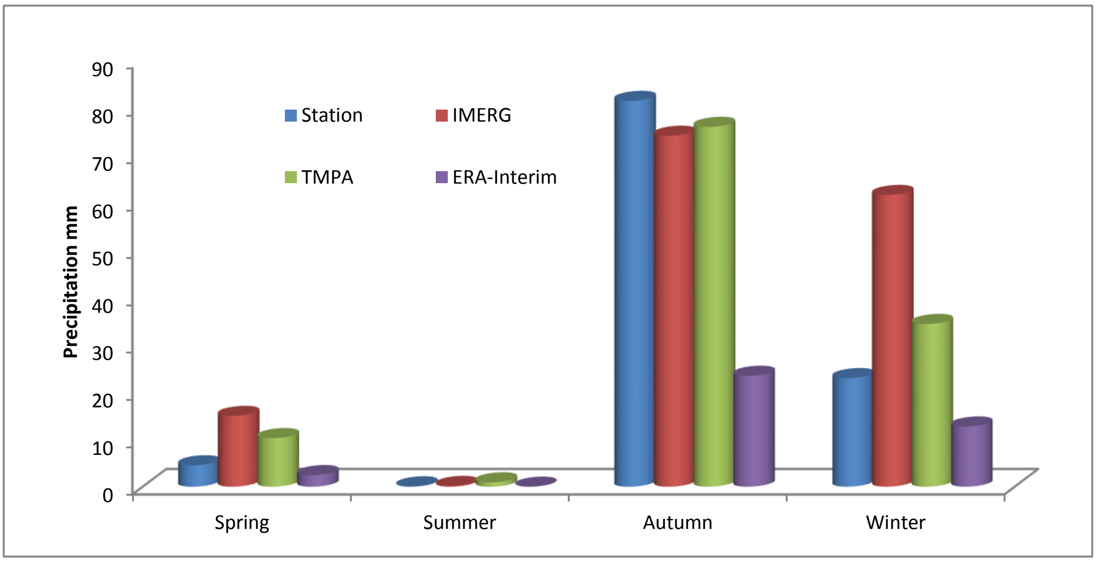

Figure 2.13. Bushehr seasonal precipitation.

Table 2.14. Statistical indices of seasonal precipitation in Kermanshah area.

	IMERG	3B42	ERA-Interim
RMSE (mm)	**34.73**	36.36	39.43
MAE (mm)	27.52	**26.69**	28.00
Bias (mm)	17.87	18.26	**−17.02**
Mbias	1.45	1.56	**0.82**
Rbias	0.64	0.56	**−0.18**
CC	**0.95**	0.92	0.88

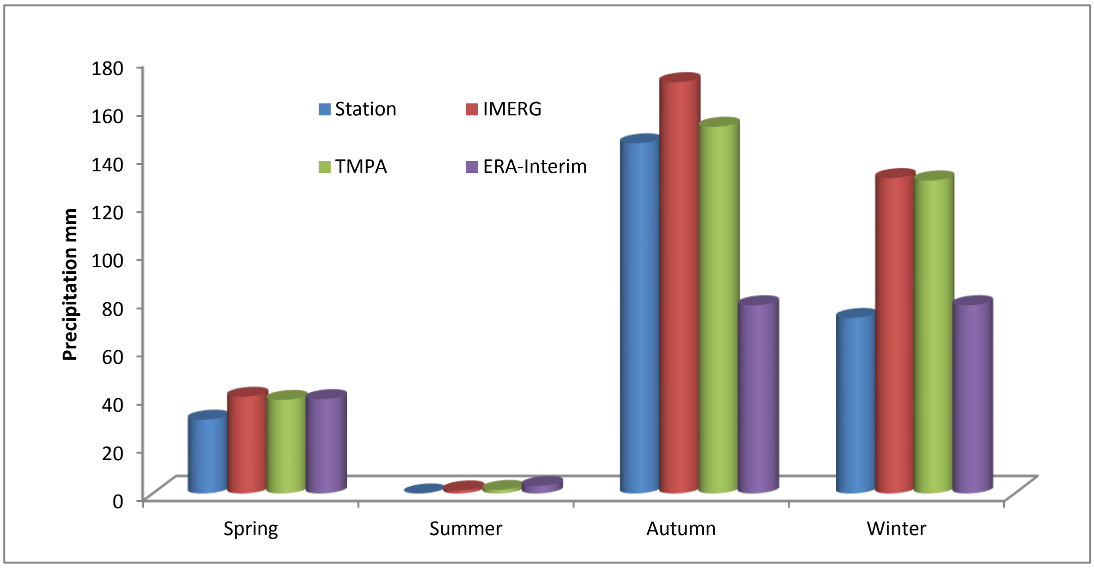

Figure 2.14. Kermanshah seasonal precipitation.

IMERG and ERA-Interim displayed underestimation and 3B42 overestimation over Tehran region. Among these products, IMERG has better results in comparison with the other data sets while ERA-Interim yields a smaller magnitude of error (Figure 2.15 and Table 2.15).

Table 2.15. Statistical indices of seasonal precipitation in Tehran area.

	IMERG	3B42	ERA-Interim
RMSE (mm)	43.68	46.48	**33.18**
MAE (mm)	34.54	35.57	**27.54**
Bias (mm)	**−15.42**	34.67	−22.01
Mbias	**1.13**	2.03	0.82
Rbias	**0.13**	1.03	−0.18
CC	0.84	**0.93**	0.90

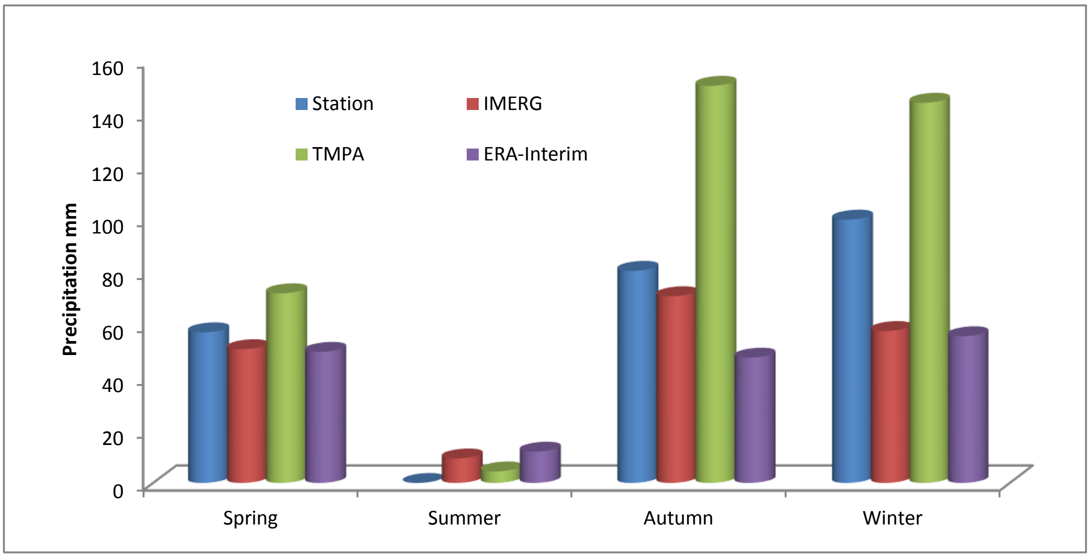

Figure 2.15. Tehran seasonal precipitation.

2.6.4 Evaluation of Dichotomous Estimates/Forecasts

With respect to an evaluation through contingency tables, Figure 2.16a–c and Table 2.16 reveals higher POD (0.74), lower FAR (0.40) and higher CSI (0.49) by ERA-Interim over the North of Iran, Guilan area, compared to other satellite products. High POD may have been influenced by the dominance of convective storms (Nasrollahi). Lower POD for 3B42 and IMERG may be associated with missed precipitation over this region.

The missed precipitation may be caused by snow cover on the ground at higher altitudes over the Alborz Mountains and by the inability to catch warm rain processes, short-lived convective storms, or maritime precipitation along the Caspian Sea.

POD value of IMERG (0.70) seems to be better than other products over Bushehr area while it is quite low for ERA-Interim (0.39). On the other hand, IMERG indicates a high FAR value (0.59) because of rare precipitation events despite high humidity. Figure 2.16.b shows similar results for 3B42 and ERA Interim in Bushehr area as well.

Table 2.16. Spatially averaged POD, FAR and CSI metrics.

		POD			FAR			CSI		
	Number of Daily Events	**IMERG**	**3B42**	**ERA**	**IMERG**	**3B42**	**ERA**	**IMERG**	**3B42**	**ERA**
Guilan (G8)	**105**	0.46	0.39	**0.74**	0.52	0.59	**0.40**	0.29	0.23	**0.49**
Bushehr (G4)	**19**	**0.70**	0.56	0.39	0.59	0.55	**0.54**	**0.35**	0.33	0.28
Kermanshah (G5)	**53**	**0.66**	0.51	0.63	**0.45**	0.57	0.46	**0.42**	0.30	**0.42**
Tehran (G2)	**59**	**0.55**	0.50	0.51	**0.43**	0.71	0.58	**0.37**	0.23	0.30

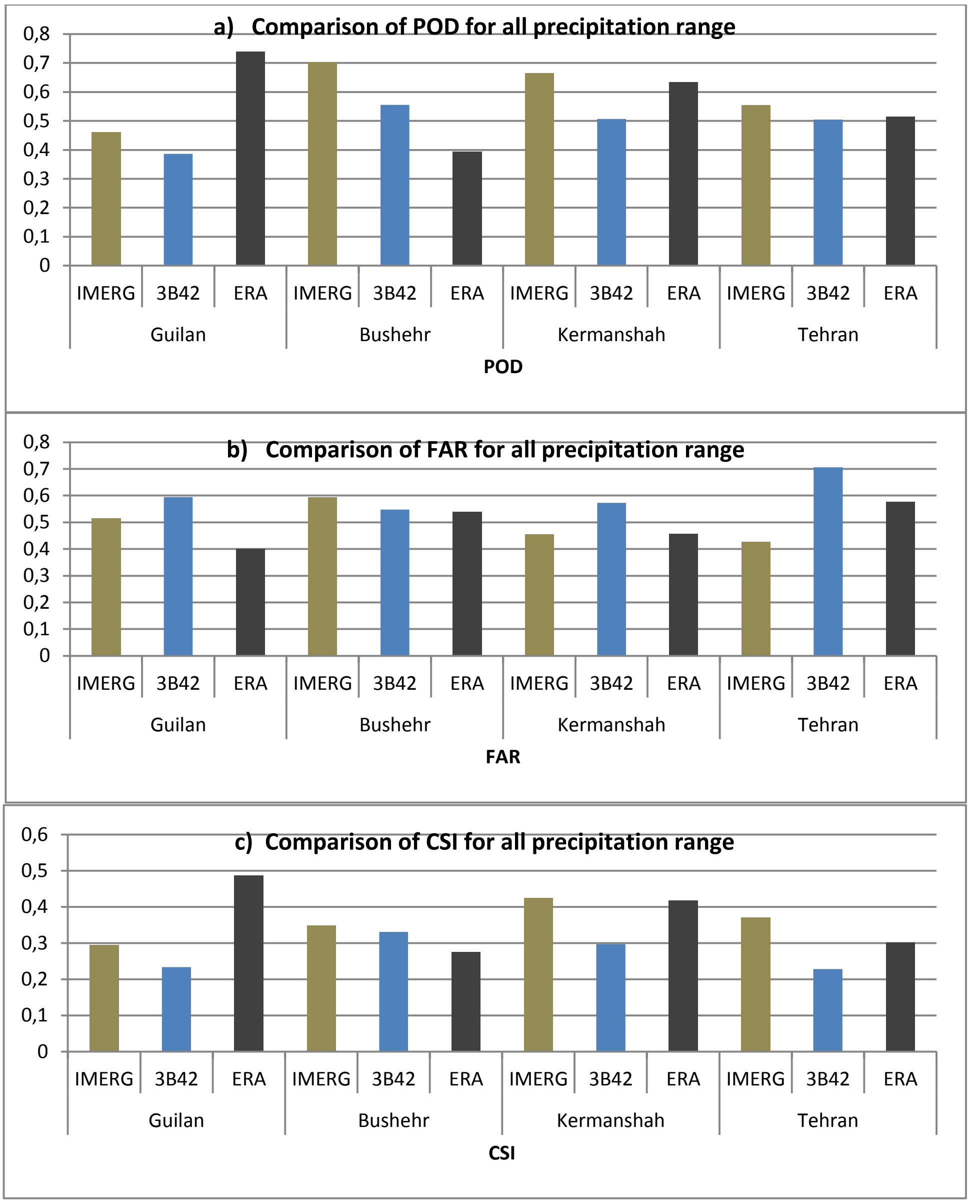

Figure 2.16. (a–c) POD, FAR and CSI, respectively, in the four study regions.

In Kermanshah area, IMERG yields a higher POD and CSI and lower FAR in comparison to 3B42. These results could be due to the inability of TRMM Microwave Imager (TMI) to measure snowfall and light rain over the ground and Zagros Mountains while the main feature of Dual-frequency Precipitation Radar (DPR) based on the GPM is to measure snowfall and light rain. Overall, the ERA-Interim product produced fewer robust results when compared to IMERG.

As Figure 2.16a–c and Table 2.16 indicate, IMERG product performs better than others with higher POD and CSI and lower FAR in Tehran. We should note that precipitation in Tehran is stratiform and orographic.

2.6.5 Evaluation of Dichotomous Estimates/Forecasts for Precipitation below 15 mm

As can be seen in Figure 2.17a–c and Table 2.17, in the Guilan area, ERA-Interim performs better than IMERG and 3B42 for precipitation below 15 mm/day which might be due to high amount of moisture in the atmosphere in this area that the satellites observed, although precipitation did not occur. Whereas, IMERG yields better results in Tehran and Bushehr areas in comparison to the other products. Moreover, in Kermanshah, IMERG and ERA-Interim indicated rather similar behavior, while in all study areas, 3B42 indicated low values of indices for precipitation below 15 mm/day.

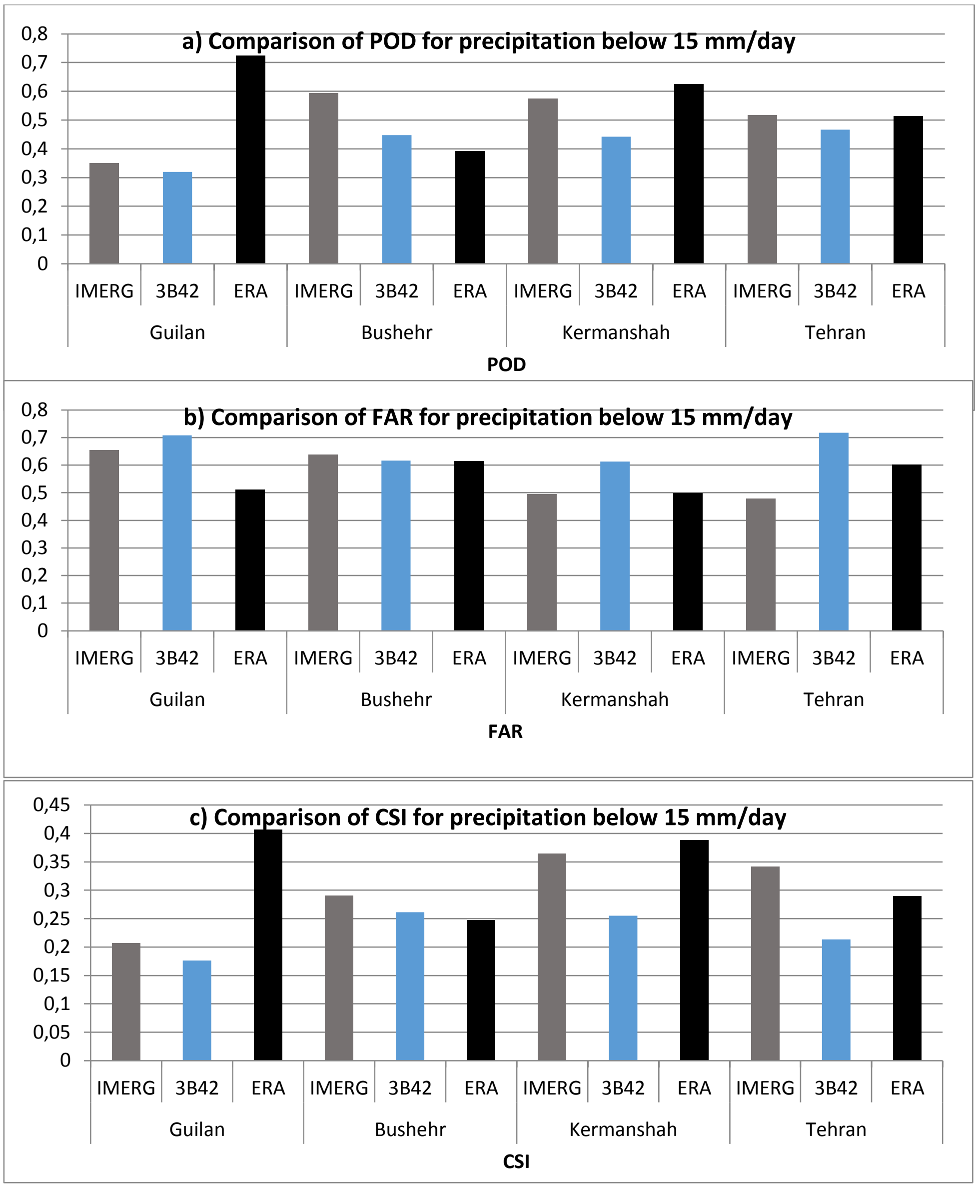

Figure 2.17. (a–c) POD, FAR and CSI, respectively, in four study region for precipitation below 15 mm/day.

Table 2.17. Spatially averaged POD, FAR and CSI metrics for precipitation below 15 mm/day.

		POD			FAR			CSI		
	Number of Precipitation Days <15 mm	**IMERG**	**3B42**	**ERA**	**IMERG**	**3B42**	**ERA**	**IMERG**	**3B42**	**ERA**
Guilan (G8)	**85**	0.35	0.32	**0.72**	0.65	0.71	**0.51**	0.21	0.18	**0.41**
Bushehr (G4)	**17**	**0.59**	0.45	0.39	0.64	0.62	**0.61**	**0.29**	0.26	0.25
Kermanshah (G5)	**51**	0.57	0.44	**0.63**	**0.50**	0.61	**0.50**	0.37	0.25	**0.39**
Tehran (G2)	**57**	**0.52**	0.47	0.51	**0.48**	0.72	0.60	**0.34**	0.21	0.29

2.6.6 Evaluation of Dichotomous Estimates/Forecasts for Precipitation above 15 mm

In contrast, for precipitation above 15 mm/day, IMERG indicates better results for POD and CSI in all case studies while ERA-Interim indicates a very weak value (Figure 2.18a–c and Table 2.18) that could be due to KuPR (Ku-band (13.6 GHz) precipitation radar) instrument that can detect heavy precipitation.

Notice that almost in all study areas the value of FAR for precipitation above 15 mm/day from all products was rather high which could be due to observed liquid water in the atmosphere profiles which did not fall as precipitation due to their small size or evaporation.

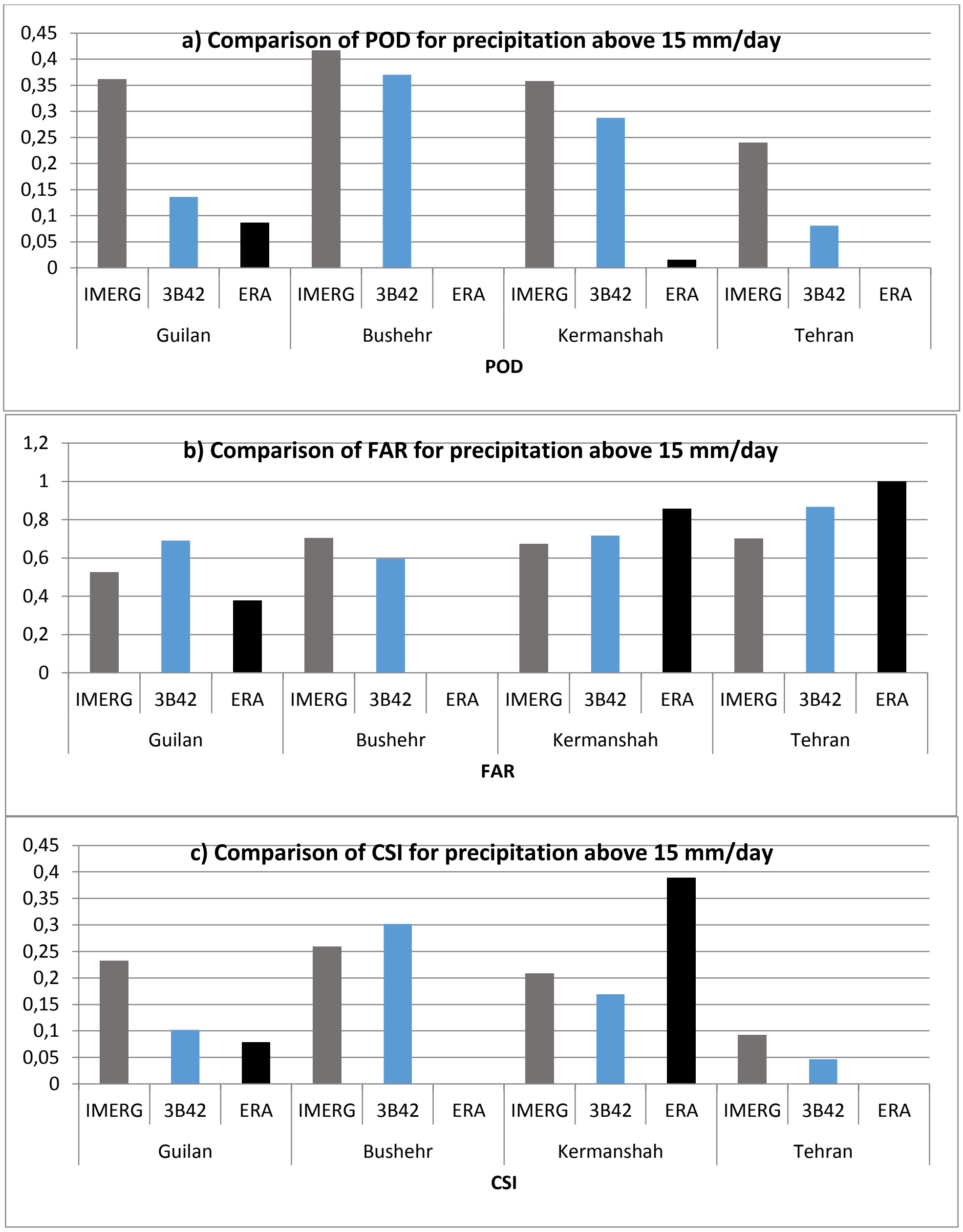

Figure 2.18. (a–c) POD, FAR and CSI, respectively, in four study regions for precipitation above 15 mm/day.

Table 2.18. Spatially averaged POD, FAR and CSI metrics for precipitation above 15 mm/day.

		POD			FAR			CSI		
	Number of precipitation days >15 mm	IMERG	3B42	ERA	IMERG	3B42	ERA	IMERG	3B42	ERA
Guilan (G8)	**20**	**0.36**	0.14	0.09	0.53	0.69	**0.38**	**0.23**	0.10	0.08
Bushehr (G4)	**2**	**0.42**	0.37	0.00	0.70	0.60	-----	0.26	**0.30**	0.00
Kermanshah (G5)	**2**	**0.36**	0.29	0.02	**0.67**	0.72	0.86	0.21	0.17	**0.39**
Tehran (G2)	**2**	**0.24**	0.08	0.00	**0.70**	0.87	1.00	**0.09**	0.05	0.00

2.7 Conclusions

An evaluation of the two recent post real time satellite datasets (IMERG and 3B42) and a common precipitation forecast model dataset (ERA-Interim) in daily, monthly and seasonal scales against rain-gauges for four different topography and climate conditions in Iran from mid-March 2014 to February 2015 shows that IMERG, 3B42 and ERA-Interim lead to underestimation over Iran. Overall, in daily scale (at days with observed precipitation), the results reveal that all three products lead to underestimation but IMERG underestimates precipitation slightly in all four regions. The correlation coefficient between IMERG and the rain-gauge data in daily scale is mostly far superior to those of for Era-Interim and 3B42. On the basis of daily timescale of bias in comparison with the ground data, the IMERG product is better than ERA-Interim and 3B42 products. Based on monthly and seasonal scales (all days), in Guilan (G8) all products in Bushehr (G4) and Kermanshah (G5) ERA-Interim and in Tehran (G2) IMERG and ERA-Interim tend to underestimate. According to the categorical verification technique used in this study, IMERG yields better results for detection of precipitation events on the basis of Probability of Detection (POD), Critical Success Index (CSI) and False Alarm Ratio (FAR) in those areas with stratiform and orographic precipitation such as Tehran and Kermanshah compared with other satellite/model data sets. Moreover, in case of precipitation below 15 mm/day, ERA-Interim and IMERG indicate better results in all study areas, particularly ERA-Interim in Guilan, which shows reasonable results of POD, FAR and CSI. Meanwhile, for heavy precipitation (P >15 mm/day), IMERG is far superior to the other products in all study areas which could be used in the future for early warning of floods *etc*.

Relative to TRMM, GPM is designed to make more accurate and frequent observations of global precipitation, especially over middle and high latitudes (Hou et al., 2014). Although the newly introduced sensors and upgraded calibration algorithms have undoubtedly improved the GPM constellation satellites' accuracy, some challenging issues in satellite retrieval processes will continue to remain open for the satellite community, providing the impetus for more research and development. With respect to the current monitoring skills, it is almost certain that regions characterized by complex terrain and snowy/ice cover will remain to be problematic for multi-satellite retrieval in GPM (Yong et al., 2015). These results will better guide those users who are taking advantage of these satellite-based precipitation data to accommodate their various research and operational applications.

The following conclusions are drawn based on this study:

1. Located in North of Iran, Guilan region enjoys a humid and subtropical climate. Under this climate condition, ERA-Interim performed reasonably on the basis of POD, FAR, CSI, RMSE and MAE indices on the daily scale. Additionally, the GPM constellation satellites' product (IMERG) was superior to the TRMM Multi-satellite Precipitation Satellites (TMPA) product (3B42). Moreover, all three satellite/model products underestimated the precipitation in this region, a similar conclusion by Moazzami *et al.* (Moazami et al., 2015) and Javanmard *et al.* (Javanmard et al., 2010) who tested 3B42 in this region. Such findings may be attributed to local wind and convective precipitation in this region so that satellites could not detect precipitation properly.
2. Along the Zagros Mountains in the West of Iran, the Kermanshah region has a hot Mediterranean subtropical climate. All products, including IMERG, TRMM and ERA-Interim, underestimate the precipitation on the daily scale. With respect to contingency table metrics, IMERG outperformed ERA-Interim on the basis of POD, FAR, RMSE, Bias, Mbias, Rbias and CC (correlation coefficient) while ERA-Interim performed best in terms of MAE values on the daily scale. 3B42 outperformed other products on a monthly scale. Moreover, all three products showed rather the same behavior in seasonal scale but IMERG indicates a better CC.
3. Just northwest of the Persian Gulf, Bushehr region is subject to warm and subtropical arid climate in low latitudes. In this area, on the daily scale, IMERG was more accurate in terms of Bias, Mbias, Rbias and CC while 3B42 was better in RMSE and MAE. Also, 3B42 outperformed other products on monthly and seasonal scales. On the other hand, IMERG showed reasonable results with a POD of 0.70 that could be due to the dual-frequency sensor based on the GPM which can detect light rain.
4. Tehran is located in a semi-arid climate with the towering Alborz Mountains to its North and the central desert to the South. In this region, according to the daily scale precipitation, IMERG outperformed other precipitation products with POD, FAR and CSI.
5. ERA-Interim yields weak results of POD, FAR and CSI for precipitation above 15 mm/day over Iran while IMERG is far superior to the other products in all study areas.

ERA-Interim in Guilan region shows a significant value of POD for precipitation below 15 mm/day.

6. Generally, in Guilan, Kermanshah, Tehran and Bushehr regions, all three products (IMERG, 3B42 and ERA-Interim) underestimate precipitation based on daily scale, which might be due to an inadequate number of gauges which are provided by the Global Precipitation Climatology Centre (GPCC) and used for bias correction in satellite products or/and the inability to measure available water in the air profiles. Moreover, in semi-arid and hot climates, rain drops may evaporate before reaching the ground (Tesfagiorgis et al., 2011).
7. Based on monthly and seasonally scale, in Guilan, all products tend to underestimate while in Bushehr and Kermanshah, IMERG and 3B42, and in Tehran, 3B42 indicated overestimate.

In summary, the overestimation or underestimation over mountainous regions indicates that accurate estimation by satellite-based precipitation products remains a challenge. Such inaccuracy may be rooted in the inadequate number of gauges, provided by the Global Precipitation Climatology Centre (GPCC) and used for bias correction in satellite products or the non-uniform beam filling (NUBF) problem for remote sensing instruments. Another cause might be the spatial resolution of the satellite product, since precipitation within a region may occur in smaller scales than the pixel size of satellites. Overall, this preliminary accuracy assessment highlights that the IMERG product can adequately substitute 3B42 products despite its limited historic record. As more IMERG data become available, more detailed studies of GPM-IMERG applications in water, weather, and climate studies are possible in the near future. We expect that the regional analysis of GPM constellation satellites-based precipitation estimates reported here can give the satellite precipitation users a better understanding of the features associated with currently available IMERG precipitation estimates from a broader perspective.

Published paper:

remote sensing

MDPI

Article

Assessment of GPM-IMERG and Other Precipitation Products against Gauge Data under Different Topographic and Climatic Conditions in Iran: Preliminary Results

Ehsan Sharifi [1,*], Reinhold Steinacker [1] and Bahram Saghafian [2]

[1] Department of Meteorology and Geophysics, University of Vienna, Vienna 1090, Austria; reinhold.steinacker@univie.ac.at

[2] Department of Technical and Engineering, Science and Research Branch, Islamic Azad University, Tehran 1477893855, Iran; b.saghafian@gmail.com

* Correspondence: ehsansharifi83@gmail.com; Tel.: +43-676-976-6304

Academic Editors: Magaly Koch and Prasad S. Thenkabail
Received: 2 November 2015; Accepted: 2 February 2016; Published: 6 February 2016

Abstract: The new generation of weather observatory satellites, namely Global Precipitation Measurement (GPM) constellation satellites, is the lead observatory of the 10 highly advanced earth orbiting weather research satellites. Indeed, GPM is the first satellite that has been designed to measure light rain and snowfall, in addition to heavy tropical rainfall. This work compares the final run of the Integrated Multi-satellitE Retrievals for GPM (IMERG) product, the post real time of TRMM and Multi-satellite Precipitation Analysis (TMPA-3B42) and the Era-Interim product from the European Centre for Medium Range Weather Forecasts (ECMWF) against the Iran Meteorological Organization (IMO) daily precipitation measured by the synoptic rain-gauges over four regions with different topography and climate conditions in Iran. Assessment is implemented for a one-year period from March 2014 to February 2015. Overall, in daily scale the results reveal that all three products lead to underestimation but IMERG performs better than other products and underestimates precipitation slightly in all four regions. Based on monthly and seasonal scale, in Guilan all products, in Bushehr and Kermanshah ERA-Interim and in Tehran IMERG and ERA-Interim tend to underestimate. The correlation coefficient between IMERG and the rain-gauge data in daily scale is far superior to that of Era-Interim and TMPA-3B42. On the basis of daily timescale of bias in comparison with the ground data, the IMERG product far outperforms ERA-Interim and 3B42 products. According to the categorical verification technique in this study, IMERG yields better results for detection of precipitation events on the basis of Probability of Detection (POD), Critical Success Index (CSI) and False Alarm Ratio (FAR) in those areas with stratiform and orographic precipitation, such as Tehran and Kermanshah, compared with other satellite/model data sets. In particular, for heavy precipitation (>15 mm/day), IMERG is superior to the other products in all study areas and could be used in future for meteorological and hydrological models, *etc*.

Keywords: GPM constellation satellites; IMERG; TMPA-3B42; ERA-Interim; satellite precipitation estimates; remote sensing; statistical analysis

1. Introduction

Water is fundamental to life on Earth. Knowing the locations and extents of rain and snowfall is vital to understanding how weather and climate impact our environment and Earth's water and energy cycles, including effects on agriculture, fresh water availability, and response to natural disasters. Since rainfall and snowfall vary greatly on a small scale and over time, satellites can provide a better picture

Remote Sens. **2016**, *8*, 135; doi:10.3390/rs8020135 www.mdpi.com/journal/remotesensing

Chapter 3

3 Multi Time-Scale Evaluation

This chapter has been published as: Sharifi, E., Steinacker, R., Saghafian, B., 2018. Multi time-scale evaluation of high-resolution satellite-based precipitation products over northeast of Austria. *Atmospheric Research* 206, 46-63, https://doi.org/10.1016/j.atmosres.2018.02.020.

3.1 Abstract

Over the years, combinations of different methods that use multi-satellites and multi-sensors have been developed for estimating global precipitation. Recently, studies that have evaluated Integrated Multi-satellite Retrievals for GPM (IMERG) Final-Run (FR) version V-03D and other precipitation products have indicated better performance for IMERG-FR compared to other similar products in different climate regimes. This study comprehensively evaluates the two GPM-IMERG products, specifically IMERG-FR and IMERG-Real-Time (RT) late-run, against a dense station network (62 stations) in northeast Austria from mid-March 2015 to the end of January 2016 using different time-scales. Both products are examined against station data in capturing the occurrence and statistical characteristics of precipitation intensity. With regard to probability density functions (PDFs), the satellite precipitation estimate (SPE) products have detected more heavy and extreme precipitation events than the ground measurements. Both precipitation products at all time-scales, except for IMERG-RT 12-hourly and daily precipitation, capture less occurrence of precipitation than the station dataset for light precipitation. This partially explains the under-detection of precipitation events. For all time-scales, both IMERG products' CDFs (Cumulative Distribution Function) are well above that of the stations' precipitation. For lower precipitation levels, IMERG-RT is slightly below the IMERG-FR whereas IMERG-RT is above IMERG-FR at higher precipitation levels. Furthermore, for entire spectrum precipitation rates ($P \geq 0.1$ mm), 1, 3, 6-hourly, IMERG-FR did not show a clear improvement of the Bias over IMERG-RT, while for 12-hourly and daily precipitation estimates, the bias in IMERG-FR has improved compared to IMERG-RT. In

addition, IMERG-FR shows a considerable improvement in RMSE as compared to IMERG-RT. IMERG-FR, however, systematically underestimates moderate to extreme precipitation and overestimates light precipitation for all time scales against rain-gauges in northeast Austria. When comparing the bias, RMSE, and correlation coefficients, IMERG-FR has outperformed IMERG-RT particularly for 6-hourly, 12-hourly, and daily precipitation. Despite the general low probability of detection (POD) and threat score (TS) and the high false alarm ratio (FAR) within specified precipitation thresholds, the contingency table shows relatively acceptable values of the POD, TS and FAR for precipitation without classification.

3.2 Introduction

Accurate precipitation estimation on fine spatio-temporal resolutions is important for water resources-related applications such as hazards forecast and management, agricultural water use, water resource management for human and industrial use, and understanding the ecosystems (Joyce et al., 2004; Yong et al., 2010). In-situ observations are often limited; however, currently available SPE products can potentially provide the precipitation estimation needed for meteorological and hydrological applications. Moreover, accurate monitoring and prediction of rainfall would help to reduce property damages and potential loss of life that may occur due to flooding (Wong and Chiu, 2008). Hence, for a better understanding of the impact of rainfall on the environment, it is crucial that one has good spatial and high temporal resolution rainfall observations available. This is specifically the case over complex mountainous regions where there is insufficient rain-gauge available and rainfall is distinguished by complex patterns (Gebere et al., 2015; Krakauer et al., 2013).

Over the ocean, microwave emissivity is low and highly polarized, allowing passive microwave (PMW) sensors to (largely) separate the surface radiation signal and the (warm) emission signal arising from liquid hydrometeors. However, over land, the microwave emissivity is higher and more variable because of its complex relationship with a number of highly variable surface characteristics such as soil moisture, roughness, vegetation properties, canopy, and snow cover (Aires et al., 2011). Moreover, the spatial distribution of precipitation within the footprint and the precipitation's microphysical characteristics can significantly impact the quality of PMW rainfall estimates (Carr et al., 2015).

In mountainous regions, rainfall is extremely variable and changes in rainfall distribution can occur over short distances and within short periods of time. The hydrological regime in these areas is extremely variable, characterized by a short duration and high-intensity rainfall events. Since mountain areas are known for their undulating topography, the number of ground-based rain-gauge stations is usually very limited. Therefore, rainfall observation with high spatial and temporal resolution is extremely important to understand the hydrologic processes in these areas (Collier, 2009; Germann et al., 2009; Villarini et al., 2009). However, the interaction between different scales to resolve atmospheric dynamics and land surface hydrology still needs progress. Well-balanced high-resolution precipitation datasets play an essential role in such land-atmosphere interactions (Vila et al., 2009). One of the motivations for this study is the potential use of high-resolution atmospheric datasets for diagnostic and prognostic atmospheric numerical modeling and land surface hydrology studies over the northeast of Austria by combining surface observations with remotely sensed information.

The main requirement in precipitation assessment is to know where and how much precipitation is falling at any given time. Such precipitation attributes may be determined through traditional ground-based rain-gauges and/or advanced SPE products. Ground-based radar is of limited value in areas with large elevation variations due to topographic shading effects (Germann et al., 2006b). Another important aspect deals with the duration of precipitation (Sharifi et al., 2016).

The Global Precipitation Measurement (GPM) constellation satellites are an international mission to provide next-generation observations of rain and snow. GPM was particularly designed to bring together advanced precipitation measurements from research and operational sensors from the partner satellites for providing the next-generation global precipitation data products. As more nations contribute to earth observations from space in the coming years, the long-term vision is that GPM sampling will further benefit from additional microwave sensors. Although a suite of sensors flying on a variety of satellites has been used to estimate precipitation on a global basis, generally speaking, the performance of SPEs over land areas is highly dependent on the rainfall regime and the temporal and spatial scale of the retrievals (Ebert et al., 2007). On the other hand, gauge observations continue to play a critical role in observation systems over global land areas. In addition, when precipitation data from rain-gauges are used as reference data, the main concern is related to uncertainties in the accuracy of areal estimates, which stem from the limited spatial representativeness of the gauges (Dezfuli et al., 2017; Sungmin et al., 2017; Villarini et al., 2008a). Satellite-derived data deviations from ground-based observations may partly be due to the possible lack of spatial representativeness of the observation sites (Hakuba et al., 2014). The spatial representativeness of a surface site greatly depends on the time-scale considered - hours, days, months - as temporal averaging strongly reduces the mismatch between point observation and surrounding area mean (Wang et al., 2012; Zhang et al., 2010). Despite this fact, gauge observations are the only sources obtained from direct measurements. Both radar and satellite estimates are indirect in nature and need to be calibrated or verified using the gauge observations (Xie and Arkin, 1995). Although it is possible to create rainfall estimates using a combination of different satellite data i.e., IMERG (Huffman et al., 2015), climate prediction center (CPC) morphing technique (CMORPH: (Joyce et al., 2004) and Precipitation Estimation from Remotely Sensed Information using Artificial Neural Networks (PERSIANN: (Sorooshian et al., 2000). Researchers have increasingly moved to using “the best of both worlds” to improve accuracy, coverage, and resolution (Vila et al., 2009).

The GPM Core Observatory satellite flies at an altitude of 407 km in a non-sunsynchronous orbit and continues the Tropical Rainfall Measuring Mission (TRMM) sampling strategy and extended the observations to wider latitudes (65°N-S), while TRMM covered roughly latitudes 35°N-S (Huffman et al., 2015). However, as can be seen in Table 1, GPM constellation satellite product, IMERG-V03, covers 60°N-S latitudes. It has a spatial resolution of 0.1° and is updated every 30 min. IMERG consists of three products: IMERG-FR (currently aimed for research), IMERG-RT Early-Run, and IMERG-RT Late-Run. The IMERG products are built upon the widely used TRMM Multi-satellite Precipitation Analysis (TMPA) products and continue to enhance spatial and temporal resolutions and snowfall estimates. The increased sensitivity of the Dual-frequency Precipitation Radar (DPR) and the high frequency channels on the GPM Microwave Imager (GMI) provide a unique capability for GPM to improve the estimate of light rain and snowfall, even in the winter seasons, which other satellites are unable to measure (Hou et al., 2014; Huffman et al., 2015).

Table 3.1. Characteristics of SPE Products

Products	Temporal resolution	Spatial resolution	Regions	Availability Period
IMERG-FR	30 minute	0.1 degree	60^{o}N - 60^{o}S	March 2014 – January 2016
IMERG-RT	30 minute	0.1 degree	60^{o}N - 60^{o}S	March 2015 – Present

Since GPM-IMERG is a rather new satellite product, up to now only a few preliminary comparisons between the GPM-IMERG products and other precipitation products have been carried out in Austria (Sungmin et al., 2017). Therefore, more comprehensive comparisons are still needed to better understand their differences, such as in spatial and temporal domains, at different precipitation rates, over surface types, etc. In this study, the Day-1 IMERG-FR which is the post real-time research product and IMERG near real-time late-run product of GPM-IMERG have been evaluated hourly, 3-hourly, 6-hourly, 12-hourly and daily, derived from the accumulation of half-hourly basis for IMERG V-03D for March 2015–January 2016.

Despite the limited data in the initial release of IMERG, results presented here show that systematic differences between the two products do exist and vary with precipitation rates (Liu, 2016). On the aggregate, it should be mentioned, we expect the direct inclusion of gauge analyses product (IMERG-FR) outperform the climatological adjustment product (IMERG-RT) while both use the same input satellite estimates. In addition, there will be differences in the statistics at the various time resolutions and precipitation classes since the monthly gauge adjustments are essentially being “decomposed” to higher temporal resolutions.

3.3 Study area

To examine the accuracy of satellite-derived precipitation data in the center of Europe, we selected the northeast of Austria, because there is a rather high-density gauge network; moreover, in this area, both stratiform and convective precipitation can occur, and the precipitation pattern is not directly affected by altitude and the topography is moderate.

Austria is located in a temperate climatic zone, and due to the topographical diversity and the relatively large west-east extent there are three quite different climatic regions: the Alpine Region with alpine climate, the eastern part of the country has Pannonian climate with a continental influence and low precipitation, and the remainder of the country, referred to as transient climate is influenced by the Atlantic (in the west) and a continental-Mediterranean influence in the southeast.

Altitude and distance from the rim determines the precipitation pattern; while as seen in Figure 3.1 and Figure 3.2 high-level areas in the Alps may have a high average precipitation > 2000 mm per year, some regions in the east and northeast of Austria have < 600 mm annually (Hiebl et al., 2011). Moreover, according to the Köppen-Geiger Classification-updated by Rubel et al. (Figure 3.3), the climate of Austria can be classified as Cfb; and the climate of the Mountainous Regions can be classified as Dfb and Dfc (Rubel et al., 2017);

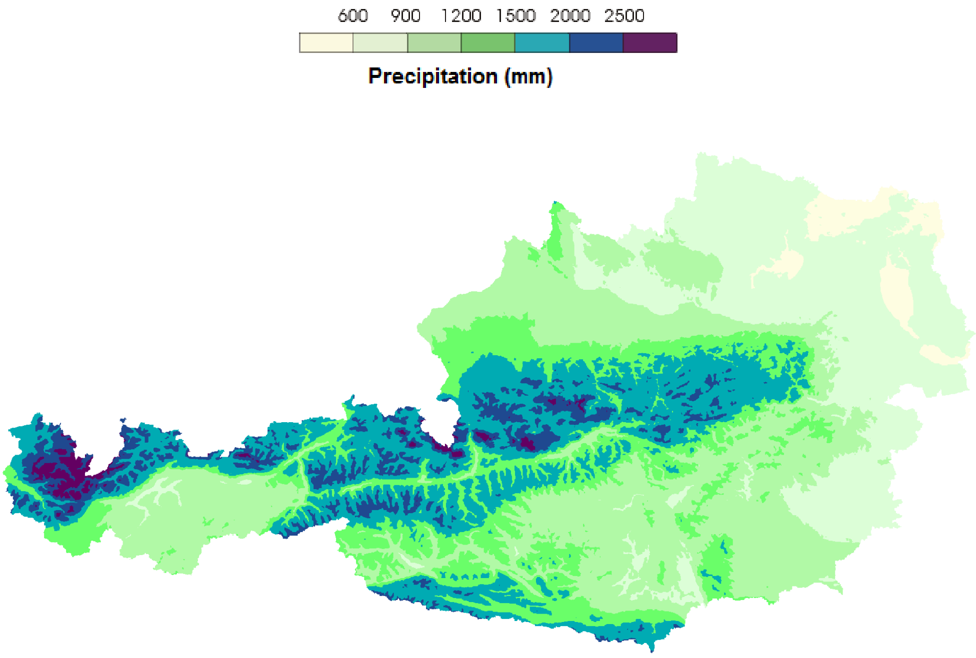

Figure 3.1. Mean annual precipitation of Austria (Hiebl et al., 2011)

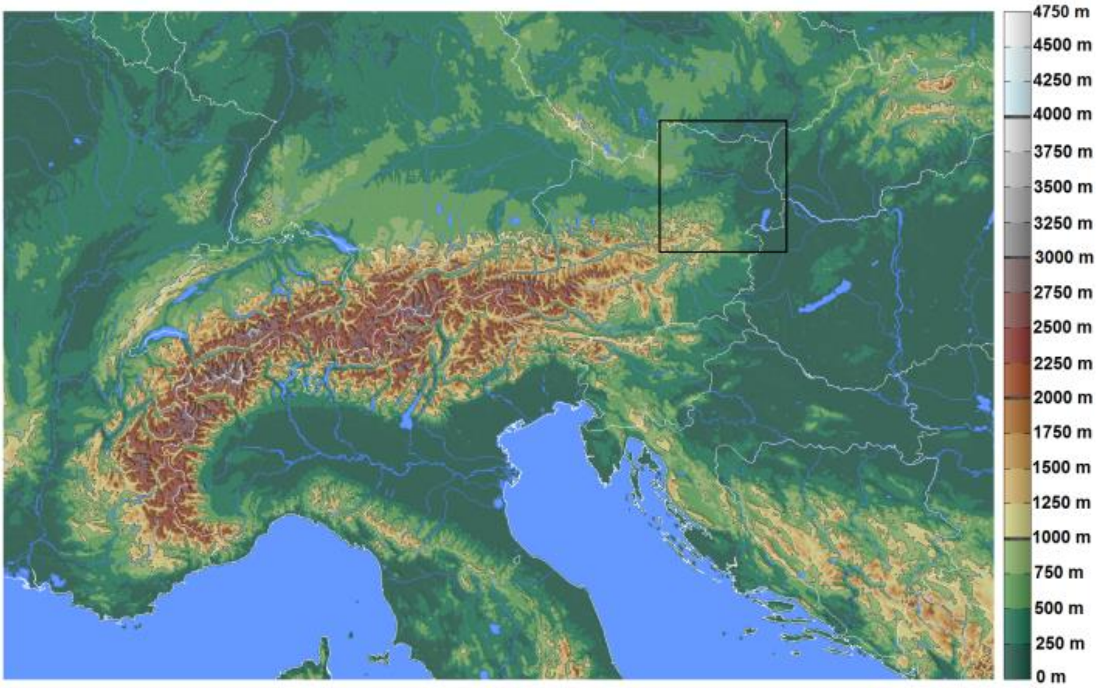

Figure 3.2. Elevation map of Austria

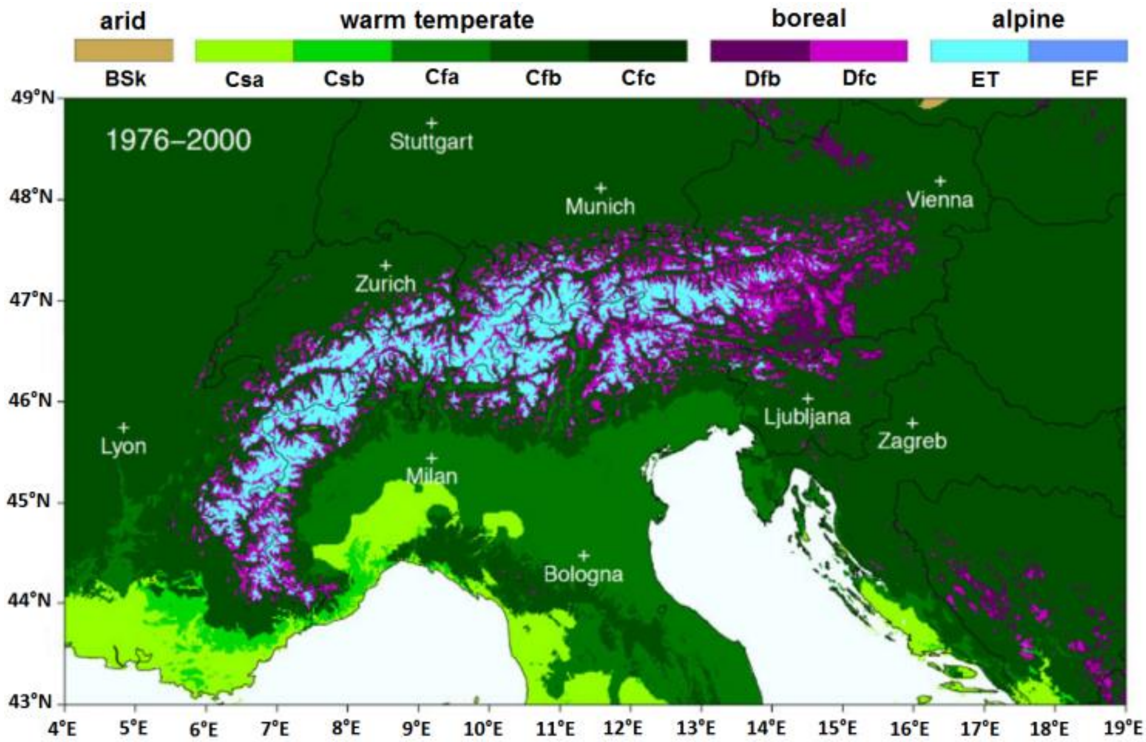

Figure 3.3. Climate of Austria based on Köppen climate classification-update by Rubel et. al. (Rubel et al., 2017)

3.4 Data and methods

3.4.1 Data

3.4.1.1 Stations

In this research, 62 in-situ meteorological synoptic stations with 10-minute time interval observations are used, which have been provided by the Zentralanstalt für Meteorologie und Geodynamik (ZAMG)-Austria. ZAMG operates a network of semi-automatic stations across the country and provides quality-controlled precipitation data. The ZAMG stations have tipping bucket gauges and weighing rain-gauges which are equipped with a heating system (Haiden et al., 2011). Before evaluating these data, we used a second derivative filter to find unrealistic rapid and isolated changes in the time-series of precipitation (edges control). Such a derivative filter is very sensitive to noise, which should be eliminated before using the data for an objective analysis (Shapiro and Stochman, 2001). According to climatology data, the outliers are removed to avoid using these values of rain-gauge precipitation measurements. This affected only four out of the 419,890 hourly data.

3.4.1.2 IMERG-FR (post real-time) V03

The GPM mission's Precipitation Processing System (PPS) at NASA's Goddard Space Flight Center released the IMERG V03 data to the public in late February 2015. The data set includes precipitation rates since mid-March 2014 for IMERG-FR. Ongoing and forthcoming data sets are freely accessible to users from NASA Goddard Earth Sciences Data and Information Services Center (GES DISC) website. Currently, the IMERG-FR V03 is available for the period between 12 March 2014 and January 2016[3].

The IMERG product used in this study is the Level 3 multi-satellite precipitation algorithm of GPM which is intended to inter-calibrate, merge, and interpolate all constellation microwave sensors, IR-based observations from geosynchronous satellites, and monthly gauge precipitation data for the TRMM and GPM eras. The system runs several times for each time of observation, giving a quick measurement at first, and then successively providing better measurement as more data arrive. In the last step, IMERG-FR follows the TMPA approach for infusing monthly gauge information into the fine-scale precipitation

[3] NASA. "GPM_3IMERGHH 03D". Available online: http://disc.sci.gsfc.nasa.gov/SSW/ (accessed on 26 May 2016).

estimates (Huffman et al., 2007). All of the full-resolution multi-satellite estimates are summed in a month to create a monthly multi-satellite-only field. This field is combined with the monthly Global Precipitation Climatology Centre (GPCC) precipitation rain-gauges (over land) to correct the bias of satellite retrievals and create research-level products, when available (Huffman et al., 2015).

3.4.1.3 IMERG-RT late run V03

The data are available to users for the period between 7 March 2015, and the present, thus providing IMERG-RT V03 data for the period 14 March 2015, to January 2016. The IMERG-RT late run, which is the near real-time product in the IMERG series of products, presently runs about 16 h after observation time. It has a climatological calibration to the monthly gauge data (unlike the Final-Run, which uses actual monthly gauge analyses).

It should be mentioned that further work is needed to evaluate the inter-annual variation of IMERG data relying on larger samples, as well as evaluate the newer versions of this product.

3.4.2 Methodology

The satellite products are compared with the measured precipitation data of 62 meteorological synoptic stations (Figure 3.4) at hourly, 3-hourly, 6-hourly, 12-hourly and daily time-scales for the northeast of Austria.

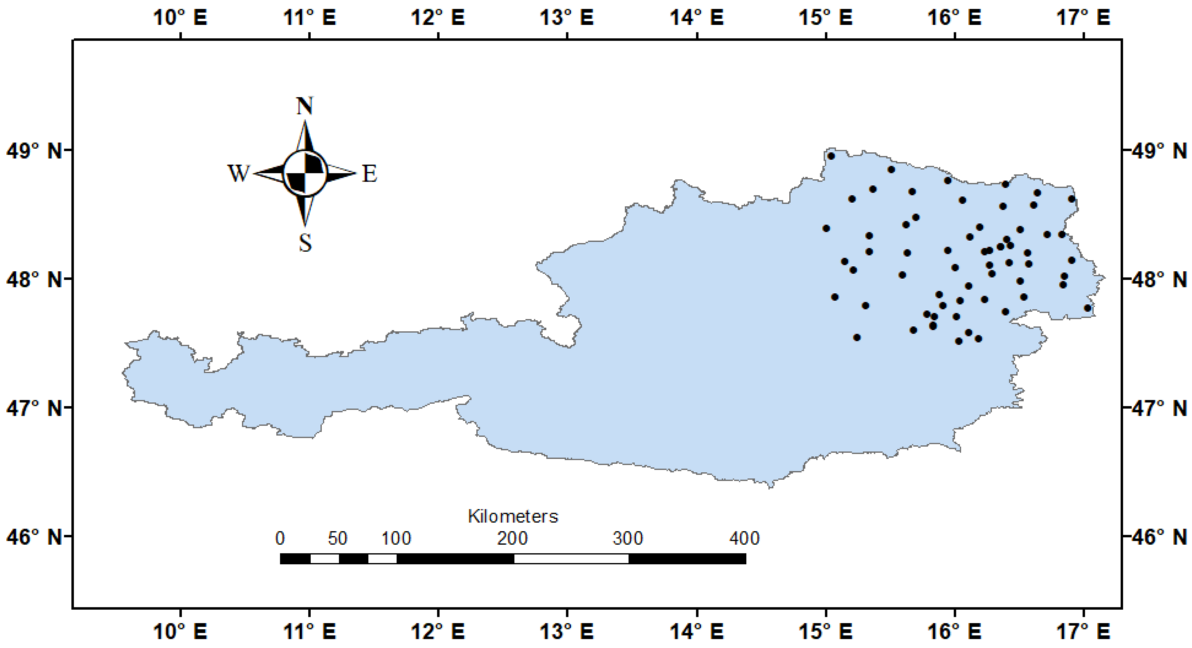

Figure 3.4. Map of meteorological synoptic stations distribution in northeast of Austria

In terms of the independence of the comparison between gauge and satellite-based products, GPCC uses data from 51 Austrian synoptic stations over the northeast of the country, which accounts for a big part of the total gauges (82%) used in our study. In addition, GPM-IMERG research level product (IMERG-FR) is combined with GPCC gauge data at the monthly scale, while the comparison in our study is conducted at sub-daily and daily scales.

In this research, the data of a pixel of the satellite is compared with that corresponding to the ground point observation (i.e., the station). Only the cells where there is at least one reporting station can be selected for computation (Guo et al., 2015). In cases where the stations are within the pixels, the comparison is carried out directly between them. However, in cases where the ground station is close to the edge between two or close to the corner of four pixels (< 0.01° off the edges), an average of the two or four pixels around the station is used as the basis for comparison. Also, for a pixel with two or more rain-gauges, the areal-average precipitation is the arithmetic average of all rain-gauges located within that pixel. In addition, the statistical analysis based on regional events is done and applied to different time-scales such as hourly, 3-hourly, 6-hourly, 12-hourly and daily precipitation from meteorological synoptic stations of ZAMG. In total, there are 419,890 hourly data and 35,835 h with precipitation available. When there is quantitative data with a wide range of possible values, it is beneficial to place these values into categories. In general, three different methods have been used to define different precipitation thresholds: (i) a relative threshold, quantiles, i.e., percentiles (ii) absolute thresholds; or (iii) return period (recurrence) values. As an example of the first case, a daily precipitation event with an amount greater than the 90th percentile of daily precipitation for all wet days can be considered as extreme (Simonović, 2012). To do that the percentile method is used and each class contains an admissible number of values.

Some researchers (Karl et al., 1995; Karl and Knight, 1998) observed a significant positive trend in the frequency of extreme rainfalls (> 50 mm per day) over the last few decades in the USA. For Australia, Suppiah and Hennessy (1996, 1998) showed a significant increase in the 90th and 95th percentiles, while other studies showed increases in the 99th percentile (Hennessy and Suppiah, 1999; Plummer et al., 1999). Variations in total precipitation can be caused by a change in the frequency of precipitation events, in the intensity of precipitation per event, or a combination of both. In order to ensure better understanding of precipitation process in comparison to satellite estimation, multi time-scale precipitation series must be analyzed. In particular, for the studies aimed at comprising stations and SPE products at varied classes which are referred to as light, medium, heavy, very heavy and extreme precipitation respectively, we consider the 50th, 70th, 90th, 98th percentile. Extreme events are particularly interesting as these events cause considerable damage and loss of life worldwide each year.

3.4.2.1 Probability density distribution

To understand the overall characteristics of precipitation, the precipitation frequency with different intensities is equally important as knowing the mean and spatial/temporal variation patterns of precipitation (Sohn et al., 2013; Tian et al., 2007). Because the same rainfall amount in the form of long-lasting light rain or a short-duration storm will yield quite different impacts in natural hazards, e.g., flood and landslide (Li et al., 2013; Shen et al., 2010). In this regard, a probability density function (PDF) can provide detailed information about the frequency of rainfall with different intensities.

In this study, a cumulative distribution function (CDF) is used to measure the number of observations that lie above or below a particular value in a data set. In other words, this is an indication of how often the satellite precipitation measurements are below or above the precipitation from stations (Gebere et al., 2015).

3.4.2.2 Statistical analysis

In the first step, statistical indices such as bias, MBias, MAE, RMSE, and CC for different precipitation thresholds are determined.

3.4.2.3 Multi-category contingency table

Another assessment technique of satellite estimation is using a contingency table (see Table 3.2). In this way, a precipitation event is considered if at least one of the stations available in the region registered precipitation. Otherwise, if none of the stations registered precipitation, a "no-precipitation" event is assigned to the whole area (Ballester and Moré, 2007). Both satellite and station data that are < 0.1 mm are assigned to zero-precipitations, because our stations do not measure precipitation < 0.1 mm. The statistical results are compiled and stratified by a number of criteria, including the number of time intervals (i.e., 1, 3, 6, 12 and 24 h) and particularly by precipitation thresholds. In this step analyses for observed precipitation below or above a particular threshold and satellite estimation below or above the same threshold are determined (Wilks, 2006).

Table 3.2. Contingency table

		Observed		
	I / J	**Yes**	**No**	**Total**
Satellit	**Yes**	*Hit (a)*	*False alarm (b)*	*a + b*
	No	*Miss (c)*	*Correct negative (d)*	*c + d*
	Total	*a + c*	*b + d*	*n = a+b+c+d*

In order to apply these to non-probabilistic estimates that are not dichotomous, it is necessary to collapse the $I = J > 2$ contingency table into a series of 2×2 contingency tables. Each of these 2×2 tables is constructed, as indicated in Table 3.3, by considering the estimated event in distinction to the complementary, not the forecast event. The advantage of this approach is that the nature of the estimation errors can more easily be diagnosed and the disadvantage is that it is more difficult to condense the results into a single number.

Table 3.3. Schematic multi-category contingency table and relationship between counts (letters a–d) of satellite estimate/event pairs for the dichotomous non-probabilistic verification situation as displayed in a 2 x 2 contingency table.

I/J	O_1	O_2	O_3	….
S_1	r	s	t	
S_2	u	v	w	
S_3	x	y	z	
⋮				

a = z	**b** = x+y
c = t+w	**d** = r+s+u+v

a = v	**b** = u+w
c = s+y	**d** = r+t+x+z

a = r	**b** = s+t
c = u+x	**d** = v+w+y+z

By using this table for different time-scale precipitation, a set of statistical indices are shown as follows (see Equations. (3.1-5)):

POD responds to the question of what fraction of the observed "Yes" events is correctly estimated. The perfect score is 1.

$$POD = \frac{hits}{hits\ +\ misses} \tag{3.1}$$

FAR deals with the question of what fraction of the estimated "Yes" events did not occur. The ideal score is 0.

$$FAR = \frac{false\ alarms}{hits\ +\ false\ alarms} \tag{3.2}$$

TS is the fraction between the number of correct "Yes" estimated and the total number of times that event is observed. The perfect score is 1.

$$TS = \frac{hits}{hits\ +\ misses\ +\ false\ alarms} \tag{3.3}$$

Accuracy is the fraction of the total estimated events when the satellite products correctly estimated event and non-event; the perfect skill score is 1.

$$Accuracy = \frac{hits\ + correct\ negatives}{total} \tag{3.4}$$

The frequency bias (Fbias) answers the question of how the estimated frequency of "Yes" events compare to the observed frequency of "Yes" events. The Range of values is 0 to ∞ with a perfect score of 1 which means an unbiased estimation. In other words, the satellite estimates and observations have an occurrence above a given threshold the same number of times. Note that the bias provides no information about the correspondence between the individual forecasts and observations of the event on particular occasions, so that Eq. (3.5) is not an accuracy measure. An Fbias greater than unity indicates that the event is estimated more often than observed, which is called overestimated. Conversely, a bias less than unity indicates that the event is estimated less often than observed, or is underestimated.

$$Frequency\ bias = \frac{hits + \ false\ alarms}{hits\ + misses} \qquad (3.5)$$

3.5 Results

3.5.1 Probability density distribution

With regard to PDFs, both satellite-based precipitation products (IMERG-FR and IMERG-RT) are examined against the reference data (stations) to capture the occurrence of precipitation and statistical characteristics of precipitation intensity in the northeast of Austria from March 2015 to the end of January 2016. The PDFs of hourly, 3-hourly, 6-hourly, 12-hourly and daily precipitation occurrences are computed as a ratio between the number of times the precipitation occurs inside each bin and the total number of times precipitation occurs overall. Then based on percentiles, precipitation intensities (P) are grouped into several bins for each time-scale with regard to the 50th, 70th, 90th, 98th percentile based on gauge data (Figure 3.5a–e).

The PDF of hourly precipitation with different intensities is shown in Figure 3.5a. Both SPE products, IMERG-FR and IMERG-RT, capture less precipitating events than the reference dataset, principally between 0.1 and 0.4 mm/h. For precipitation of 0.4 mm/h and above, the trend is reversed, and more precipitation events are detected by both satellite products. In other words, the SPE products detected more heavy and extreme precipitation events than the ground measurements. This may shift the precipitation distribution spectrum to the higher intensity and cause great differences for the various applications, such as runoff production (Guo et al., 2015).

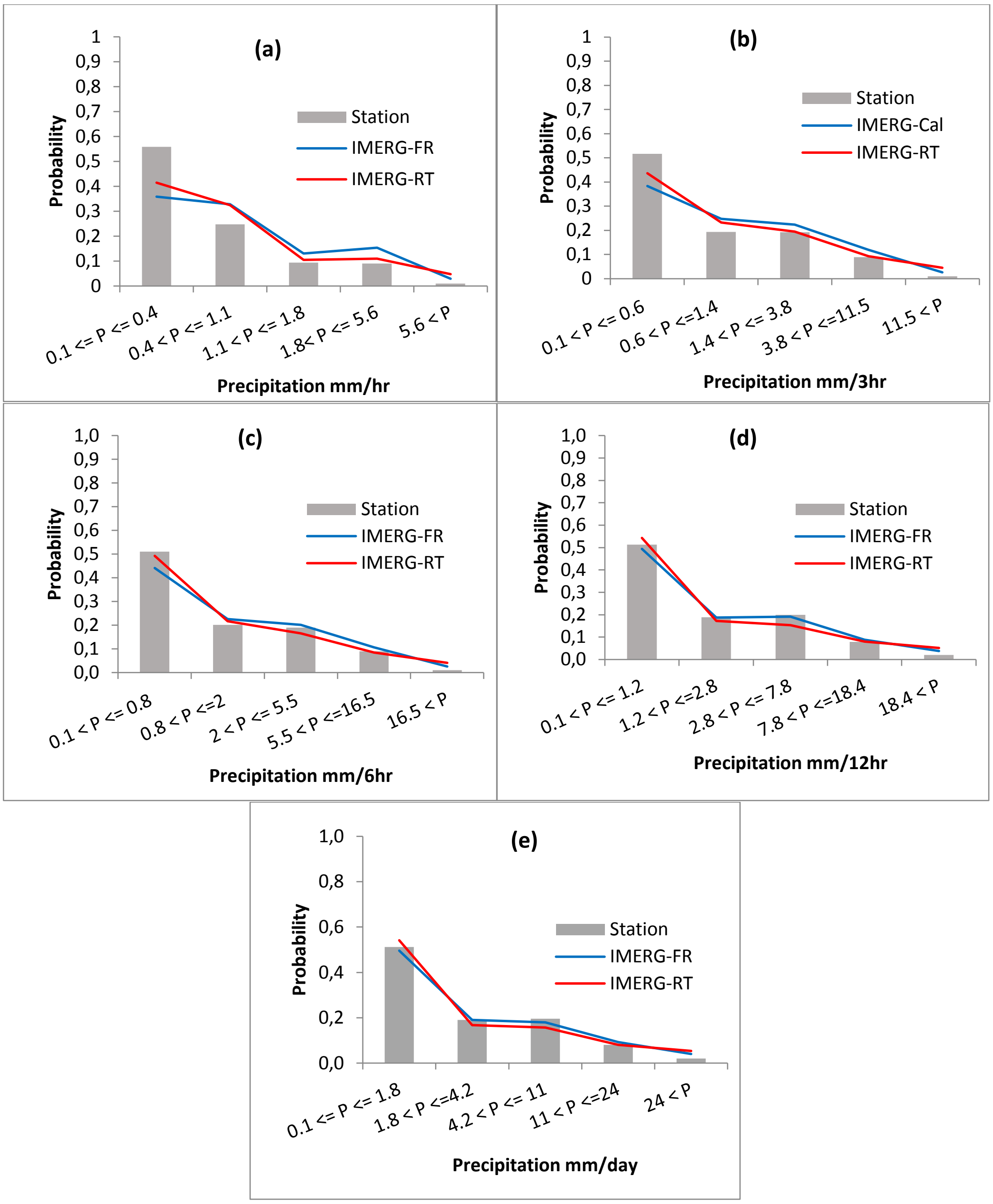

Figure 3.5. PDFs of precipitation events with different intensities a) hourly b) 3-hourly c) 6-hourly d) 12-hourly and e) daily

IMERG-RT outperforms IMERG-FR for the frequency precipitation intensity in the range of 0.1 to 0.4 mm/h when the precipitation rate is in the range of 1.1 to 1.8 mm/h and 1.8 to 5.6 mm/h. IMERG-RT shows the closest performance with stations. IMERG-FR (calibrated with monthly ground rain-gauges) performs even worse than its corresponding original satellite product (IMERG-RT). As demonstrated by the PDF of precipitation, the magnitude of the detected events is reduced at the expense of the missed events, skewing the intensity distribution (Tian et al., 2007). In fact, the gauge adjustment product (IMERG-FR) can modify the precipitation amounts but it cannot modify the occurrence of precipitation (Behrangi et al., 2014; Gosset et al., 2013). Both precipitation products in all time-scales, except for IMERG-RT in 12-hourly and daily precipitation, capture less precipitating events than the station dataset for light precipitation. This partially explains the over-detection of no-precipitation events.

As seen in Figure 3.6a, about 9% is reported by the station dataset in the frequency of precipitation events for an hourly time-scale. In general, both satellite-based precipitation products slightly tend to detect less precipitation events compared to the ground measurements. This indicates that satellite-based precipitation products missed some precipitation cases. Further details about all time-scales are found in Figure 3.6a–e.

These results may be attributed to the following aspects. First, the satellite-based precipitation products, in particular, IMERG-RT, can detect reasonably heavy and convective precipitation events. Second, the bias correction procedures also boost the amplitude of events detected to compensate for the contribution on missed events (Tian et al., 2007).

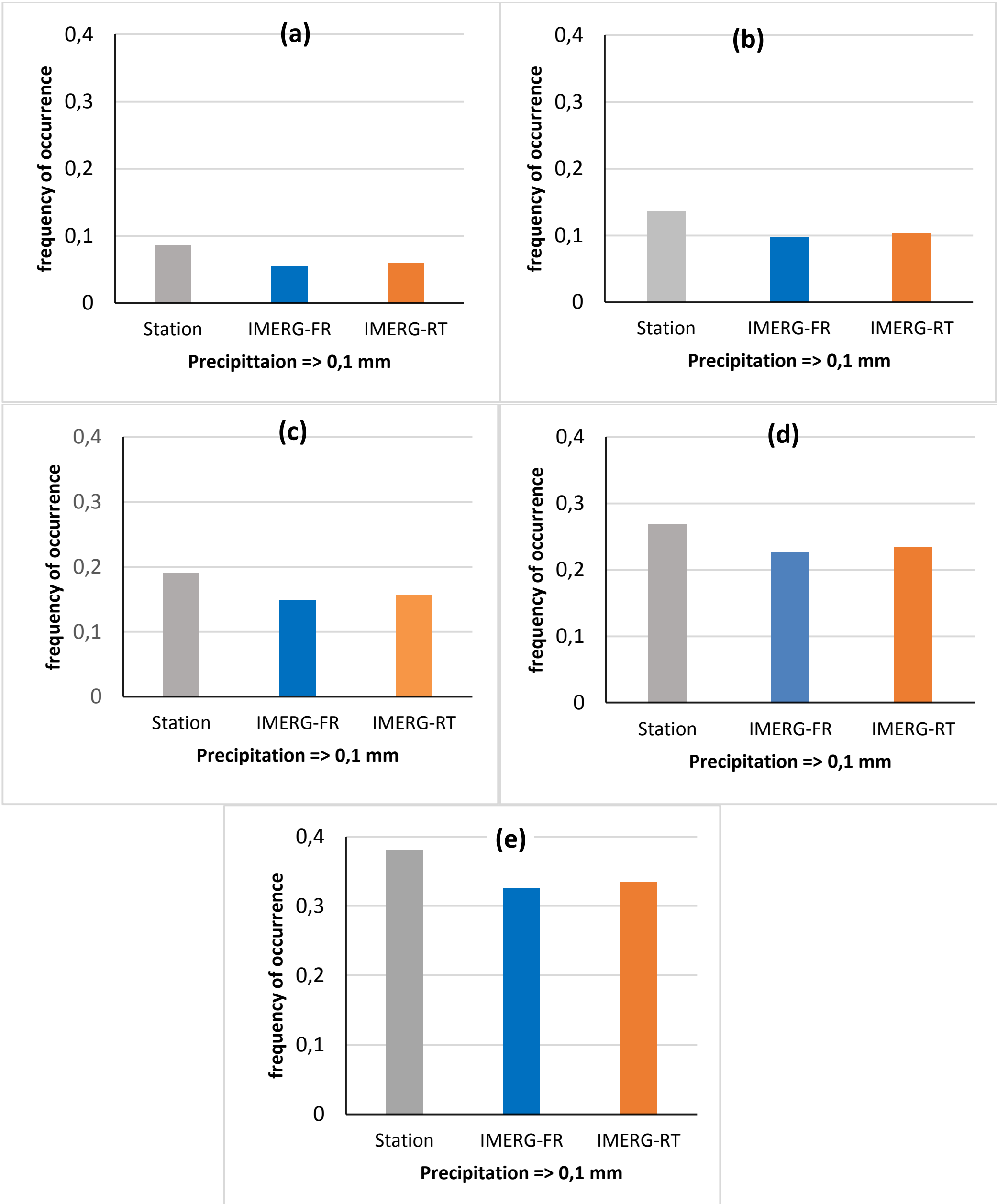

Figure 3.6. Fraction of detected precipitation events a) hourly b) 3-hourly c) 6-hourly d) 12-hourly and e) daily

Figure 3.7a–e shows the CDF of precipitation between both IMERG-FR and IMERG-RT products against the stations. Figure 3.7a for hourly time-scale shows that both IMERG products' CDFs are well above that of the stations' precipitation. However, the 94% frequency level for the ground data at 2.4 mm/h corresponds to only an 88% frequency level for IMERG-FR and IMERG-RT. Below 2.4 mm/h, the IMERG-RT frequency is slightly lower than of IMERG-FR whereas it is above IMERG-FR at higher precipitation levels.

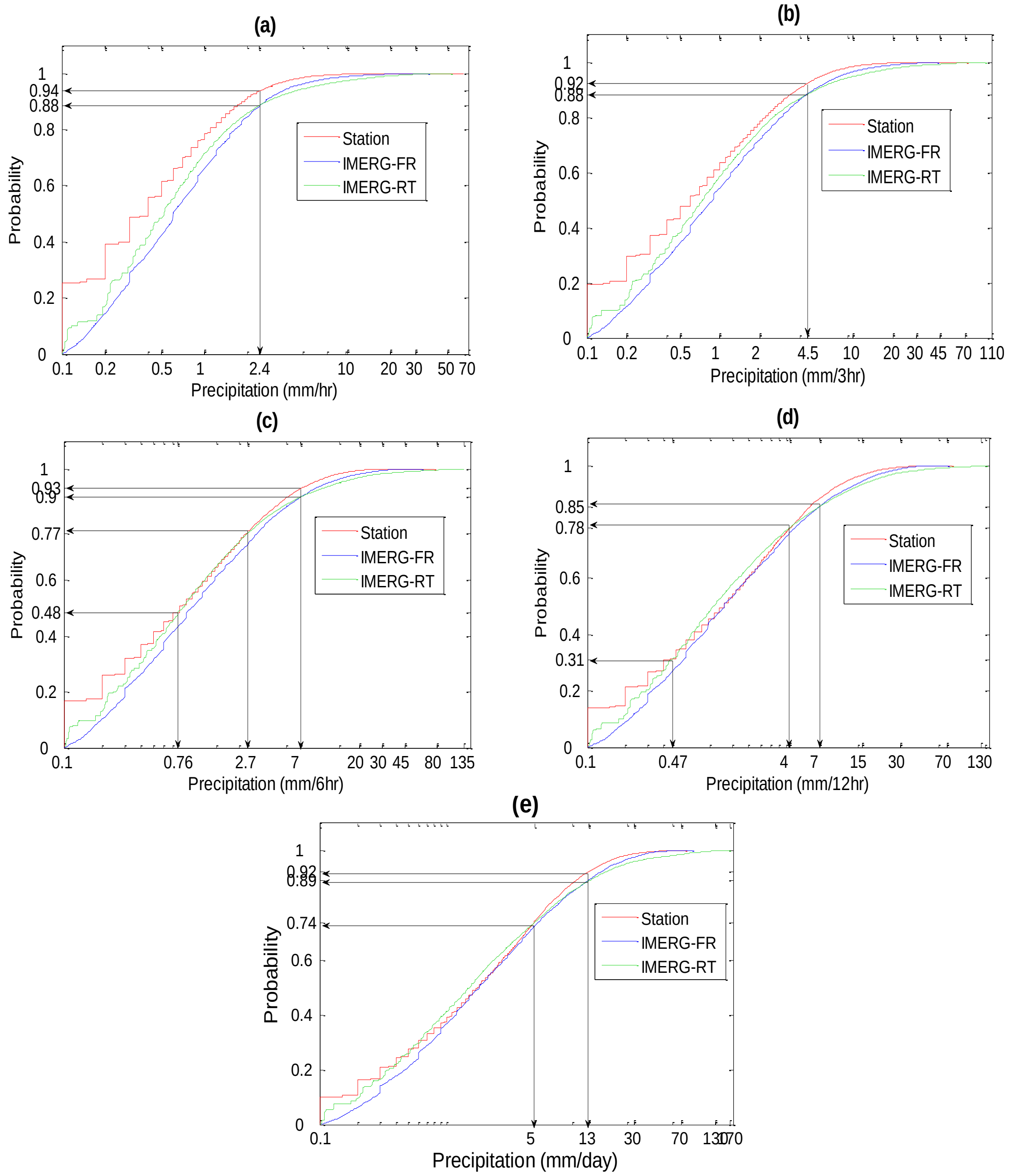

Figure 3.7. CDFs of precipitation events with different intensities a) hourly b) 3-hourly c) 6-hourly d) 12-hourly and e) daily

Moreover, the finding for the 3-hourly precipitation is almost the same as for the hourly time-scale; but, the difference between them is that for the 3-hourly time-scale at 92% frequency level stations, precipitation is < 4.5 mm/3 h. This is the case for only 88% of IMERG-FR and IMERG-RT. However, until 4.5 mm/3 h, the IMERG-RT frequency is slightly lower than the IMERG-FR frequency, and above this value, the IMERG-RT frequency is higher than of IMERG-FR. This indicates that the IMERG-FR observation is closer to the station values until a 4.5 mm/3 h precipitation rate is reached. This result shows an overestimated frequency of precipitation by both IMERG-FR and IMERG-RT (see Figure 3.7b).

In order to evaluate the 6-hourly precipitation, as can be seen in Figure 3.7c, the result shows that the CDF of IMERG-FR is above that of the stations' precipitation at every point. However, IMERG-RT is above the station values until the 48% frequency level and almost at the same frequency level of ground data till the 77% frequency level when the precipitation rate is 2.7 mm/6 h. After this frequency level, IMERG-RT is again below the station value. This shows an overestimated frequency of precipitation by both IMERG-FR and IMERG-RT except for IMERG-RT in the medium precipitation range. Here it is more or less in the same frequency range as the stations are.

As shown in Figure 3.7d for the 12-hourly time-scale, the CDF of IMERG-FR is above that of the stations' precipitation whereas the IMERG-RT is above the ground data until the 31% frequency level. This corresponds to a precipitation of < 0.47 mm/12 h. For higher precipitation intensities in the range of heavy precipitation, the IMERG-RT is below the frequency of stations at the level of 78% frequency. This corresponds to a ground precipitation of < 4 m m/12 h. It dips below the frequency of IMERG-FR at the 85% frequency level, corresponding to a precipitation of < 7 mm/12 h. Furthermore, an overestimation of the frequency of IMERG-FR in comparison to IMERG-RT can be observed when the precipitation rate is lower than 4.5 mm/12 h and there is an underestimation above a precipitation rate of 4.5 mm/12 h.

Figure 3.7e shows that for daily precipitation the IMERG-FR product's CDF is above that of the stations' precipitation whereas the IMERG-RT is above only until the 74% frequency level when station data are < 5 mm/day. For higher precipitation intensities in the range of heavy precipitation, the IMERG-RT drops below the frequency of stations at the level of 74%, corresponding to ground precipitation < 5 mm/day. It even dips below the frequency of IMERG-FR at the 89% frequency level, corresponding to a precipitation of < 13 mm/day. In other words, IMERG-FR underestimates the frequency of precipitation in comparison to IMERG-RT when the precipitation rate is above 13 mm/day.

In general, with respect to CDFs of 3-hourly, 6-hourly and 12-hourly precipitation, the CDFs of IMERG-RT is slightly lower than the IMERG-FR whereas IMERG-RT is above IMERG-FR at higher precipitation levels.

It should be noted that the results in Figure 3.5 -Figure 3.6Figure 3.7 are according to all stations and they are not based on an individual station.

3.5.2 Statistical analysis

To evaluate the IMERG precipitation products comprehensively, ten metrics are selected. These can be divided into three categories: the first category includes the CC, describing the agreement between satellite estimates and gauge observations; the second category includes the MAE, the MBias and the RMSE, which are used to describe the error and bias of satellite estimates compared with gauge observations; and, the third category includes the POD, the FAR, TS, accuracy and frequency Bias, which are used to describe the contingency of SPEs (Yong et al., 2010). All metrics are illustrated in Table Aa–e.

In Table B.1, the statistical summary of the metrics for IMERG-FR and IMERG-RT products at hourly, 3-, 6-, 12-hourly and daily resolution at different thresholds over northeast Austria is shown. According to the results (Table B.1a), precipitation shows a weak correlation to both products at the hourly time-scale for all precipitation classifications. Only precipitation without classification ($P \geq 0.1$ mm/h) yields values of 0.30 and 0.29 for IMERG-FR and IMERG-RT respectively, showing a better agreement than for all other precipitation classes. At a 3-hourly time-scale (Table B.1b), a correlation value of 0.46 and 0.40 for IMERG-FR and IMERG-RT respectively in the range of equal or above 0.1 mm/3 h is documented while in other classified precipitation values, the correlations are rather weak. The 6-hourly correlation coefficients (Table B.1c) for the precipitation amount at different thresholds vary from 0.06 to 0.55, indicating that nearly all the classified precipitation considered in this time-scale is not homogenous. In the range of precipitation rates $P \geq 0.1$ mm/6 h, IMERG-FR and IMERG-RT show a correlation of 0.55 and 0.21 respectively. Moreover, in the range of heavy precipitation (5.5 mm/6 h $< P \leq$ 16.5 mm/6 h) the correlation to the values of 0.38 and 0.29 for IMERG-FR and IMERG-RT respectively are higher than for other thresholds. Also, as shown in Table B.1d–e, the value of the CC in the range of light and moderate rain is low while in the entire range of precipitation ($P \geq 0.1$ mm/12 h or $P \geq 0.1$ mm/24 h) it is higher than for other classified thresholds for both 12-hourly and daily precipitation with the corresponding values of 0.61 and 0.49 for 12-hourly and 0.65 and 0.51 for daily precipitation for IMERG-FR and IMERG-RT.

Generally, the CC of IMERG-FR yields rather better than IMERG-RT due to the fact that the general performance of the CC is rather weak for different thresholds and time-scales. Several factors could contribute to the relatively low CC of IMERG products over such areas: (1) the topography and climate of this area is partly complex, posing a great challenge for accurate SPE (Dinku et al., 2007); (2) the gauges are used for the production of GPCC through monthly gauge analyses while our evaluation is on a daily and sub-daily time-scale, resulting in the quality of IMERG products being potentially degraded; and (3) rain-gauge measurement error.

Generally, IMERG-FR and IMERG-RT overestimate hourly precipitation in the range of light rain and with a slight trend to underestimate medium, heavy, very heavy and extreme precipitation over northeast Austria (Figure 3.8, Table B.1a). Maximum values of RMSE can reach up to 5.97 mm/h for IMERG-FR for extreme precipitation intensity and the minimum value is close to 0 mm for IMERG-RT for precipitation without defined classification ($P \geq 0.1$ mm/h). As shown in Table Aa and Figure 3.9a, the RMSE value can be as high as 9.07 mm/h for IMERG-RT in the range of extreme precipitation and 1.02 mm/h for IMERG-FR for light precipitation.

3-hourly light precipitation indicates rather an overestimation for both products while only IMERG-FR shows an underestimation for other intensities (Table B.1b and Figure 3.8b). IMERG-FR has a total bias of +0.17 mm/3 h in comparison to +0.25 mm/3 h for IMERG-RT in the range of light precipitation intensity with a tendency to underestimate precipitation at higher intensities. In addition, in the range of extreme precipitation ($P > 11.5$ mm/3 h), IMERG-FR has a larger negative total bias (−8.50 mm/3 h) in comparison to IMERG-RT (−2.28 mm/3 h). However, MAE and RMSE of IMERG-RT, 14.79 mm/3 h and 18.92 mm/3 h respectively show larger/higher values in comparison to IMERG-FR of 10.66 mm/3 h and 12.89 mm/3 h respectively.

As shown in Table B.1c and Figure 3.8c, for 6-hourly precipitation and in the range of extreme precipitation, IMERG-FR underestimates precipitation with the highest Bias (−8.02 mm/6 h) and the lowest Mbias (0.64 mm/6 h) in comparison to IMERG-RT. This overestimates precipitation with a Bias and Mbias of 3.42 mm/6 h and 1.15 mm/6 h respectively. Meanwhile, MAE and RMSE for IMERG-FR and IMERG-RT correspondingly increase from light to extreme precipitation intensities (Figure 3.9c). On the other hand, based on Bias and Mbias indices, IMERG-FR tends to underestimate from light to extreme precipitation while IMERG-RT tends to underestimate from light to heavy precipitation and overestimate from very heavy to extreme precipitation.

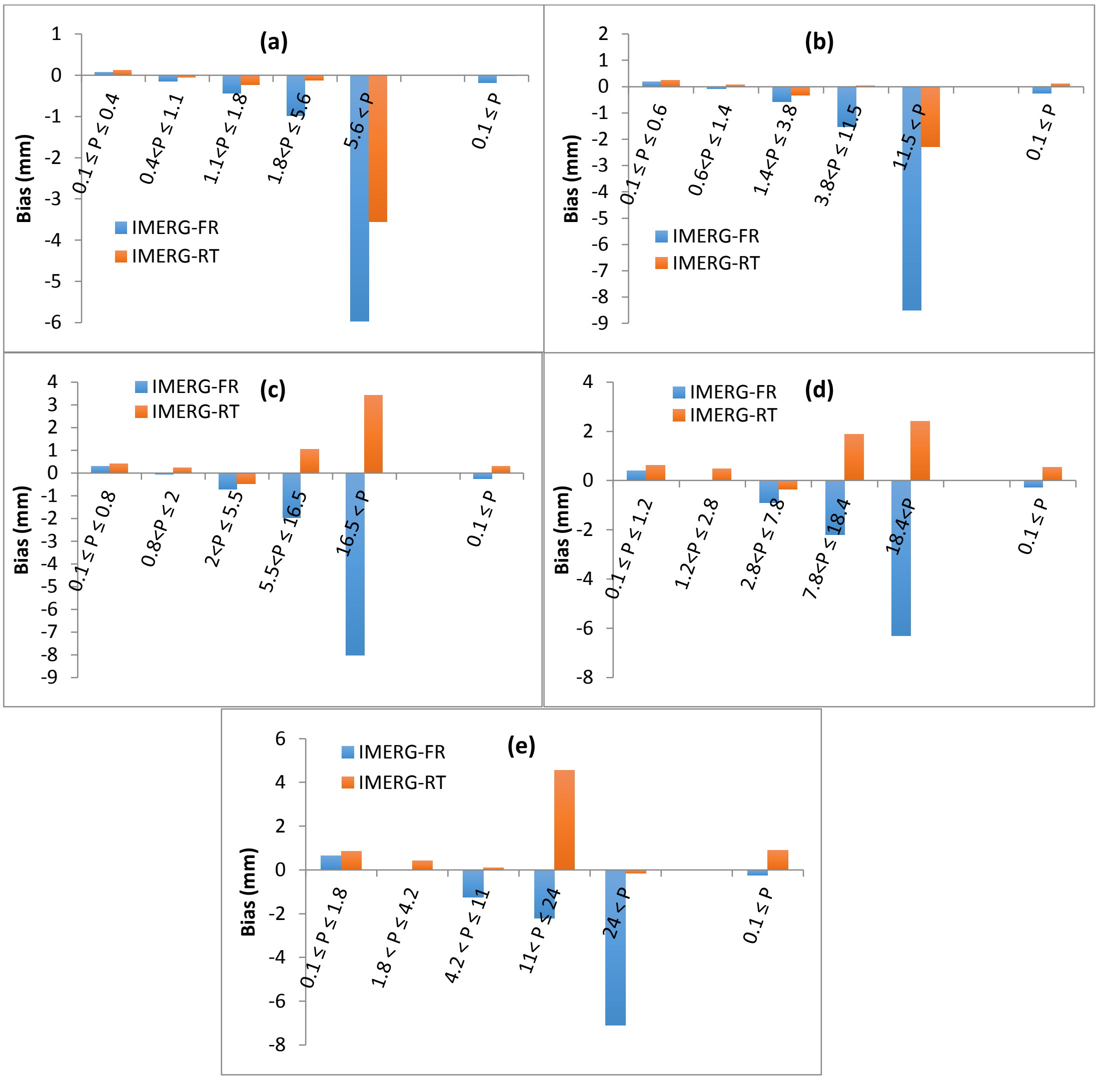

Figure 3.8. The bias of precipitation events for different time-scale and intensities a) hourly b) 3-hourly c) 6-hourly d) 12-hourly and e) daily over northeast Austria for the period March 2015 to January 2016.

Based on metrics of Table B.1d, at 12-hourly time-scale precipitation, the performance of both satellite products can be compared. They vary between each other and for different thresholds. For instance, both products overestimate at the lowest precipitation intensity range (0.1 mm/12 h ≤ P ≤ 0.8 mm/12 h) and underestimate at precipitation intensities of 2 mm/12 h < P ≤ 5.5 mm/12 h (Figure 3.8).

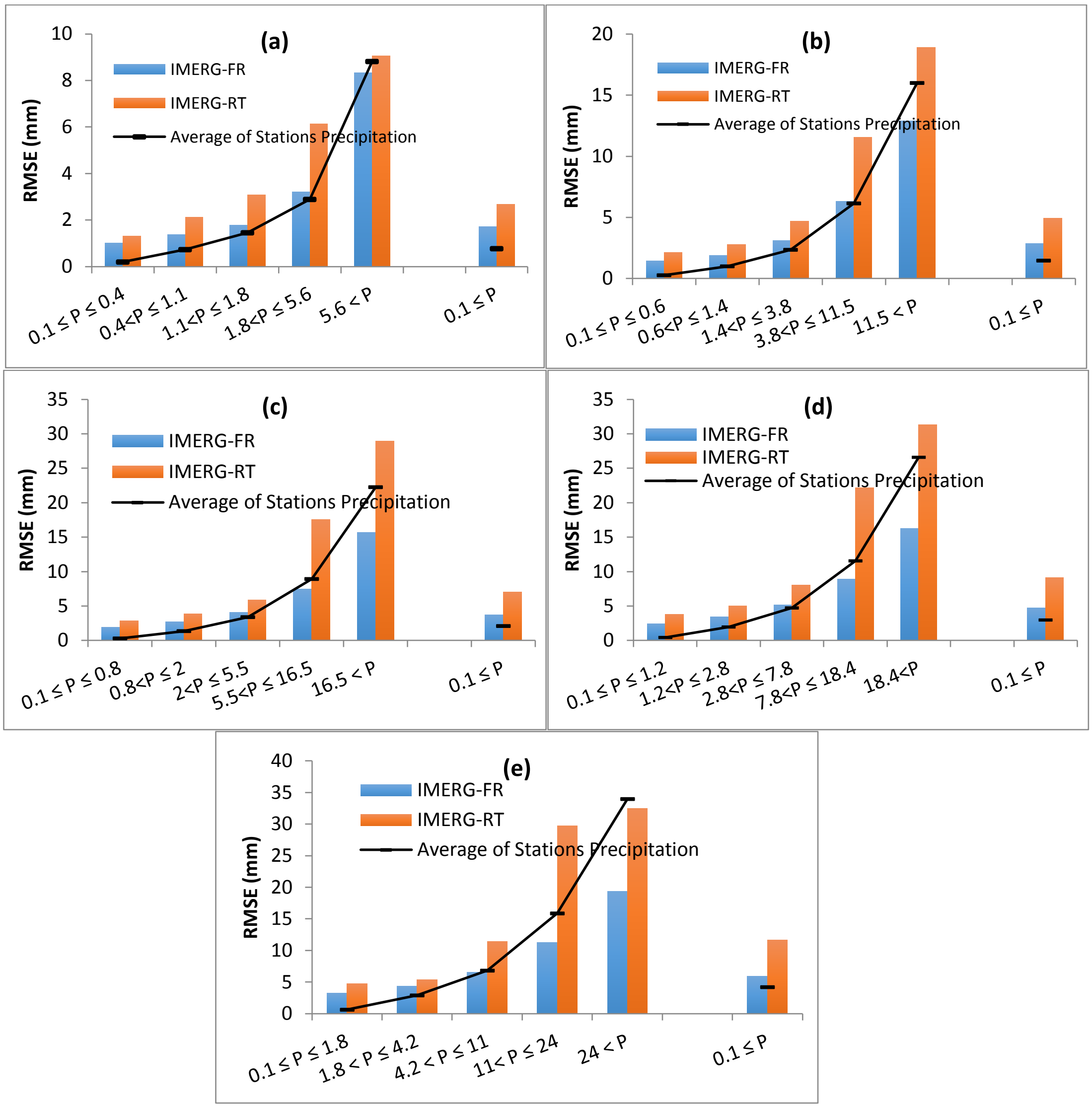

Figure 3.9. RMSE of precipitation events for different time-scale and intensities a) hourly b) 3-hourly c) 6-hourly d) 12-hourly and e) daily over northeast Austria for period March 2015 to January 2016.

Moreover, for the daily time-scale, IMERG-FR shows a smaller/lower RMSE than IMERG-RT particularly for heavy and extreme precipitation over northeast Austria, which is consistent with Table B.1e and Figure 3.9e. As seen in Figure 3.8e, the total bias and its components show that IMERG-FR has a total bias to the extent of 0.64 mm/day in comparison to 0.85 mm/day for IMERG-RT in the range of light precipitation intensity.

This is higher than that for medium precipitation intensity. In addition, in the range of extreme precipitation (P > 24 mm/day), IMERG-FR has a larger negative total bias (−7.09 mm/day) in contrast to IMERG-RT (−0.17 mm/day). However, MAE of IMERG-RT (23.76 mm/day) shows a larger value in comparison to IMERG-FR (15.37 mm/day). The low Bias compared to MAE is probably caused by the cancellation of positive/negative values.

Next, an analysis of observed precipitation above or between particular thresholds and satellite estimation above or between the same thresholds are carried out (Wilks, 2006). Multi-category contingency table evaluation (Table B.1a and Table B.2 and Figure 3.10a) for hourly precipitation reveals a low POD, a lower TS and high FAR for both products in all precipitation intensity classes, meaning both products are not able to detect many events on an hourly time-scale. The low POD may have been influenced by the dominance of convective storms and missed precipitation over this region (Nasrollahi; Sharifi et al., 2016). However, relatively high FAR values for classified precipitation might be due to spurious events detected by satellites (Blacutt et al., 2015) and/or disability of satellite products to detect precipitation in their exact precipitation categories. However, they may detect the amount of precipitation somewhat lower or higher than the specified intensities. Moreover, a frequency bias of light, moderate and heavy precipitation less than unity (< 1) for both products indicate that satellite estimation underestimates the frequency, while for extreme precipitation (P > 5.6 mm/h) an overestimation is shown. Despite this, at this time-scale, the accuracy values of both products are similar in each intensity and they show nearly a perfect skill score in the range of extreme precipitation.

With respect to the 3-hourly time-scale with different precipitation intensities (Table B.1b and Table B.3 and Figure 3.10b), IMERG-RT shows better POD than IMERG-FR with 0.46 and 0.34 for IMERG-RT and 0.32 and 0.24 for IMERG-FR in the range of heavy and extreme precipitation. FAR values of both products are relatively high and there is no meaningful difference between the two products. Lower POD and high FAR may be associated with systematic errors of the products algorithms, missed precipitation over this region, poor performance to detect short-lived convective precipitation, and precipitation over the surface covered by snow. Moreover, in the range of extreme precipitation intensity, IMERG-FR and IMERG-RT both tend to overestimate the number of events with a bias frequency of 1.9 and 3.4 respectively, but the value of IMERG-FR is close to unity, even in the range of heavy precipitation. IMERG-FR with the bias frequency value of 0.96 outperformed IMERG-RT with a value of 0.79.

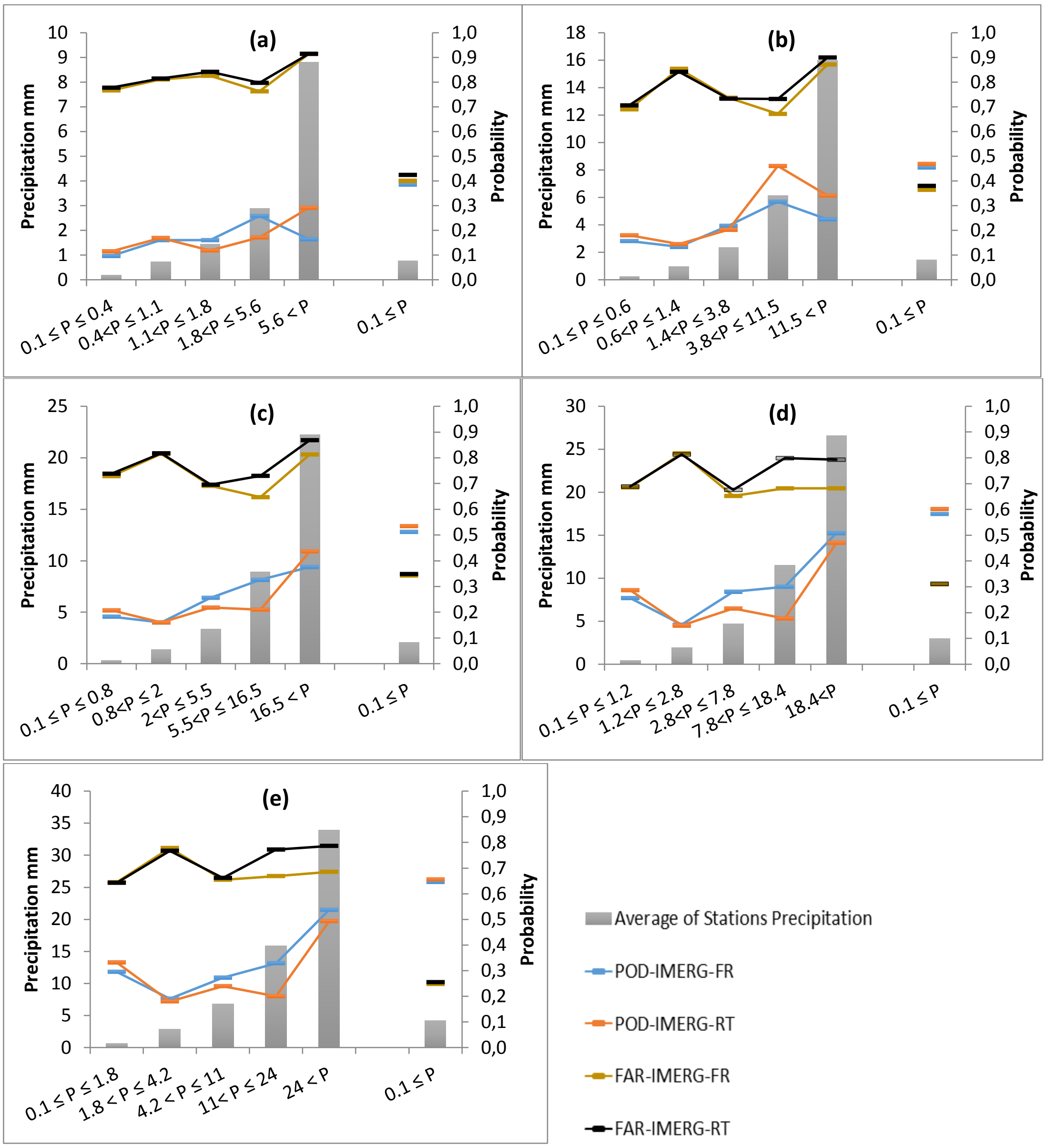

Figure 3.10. Verification statistics (POD and FAR) between IMERG-FR / IMERG-RT and observed gauge observation for different time-scale and intensities a) hourly b) 3-hourly c) 6-hourly d) 12-hourly and e) daily over northeast Austria for period March 2015 to Januar

Table B.1c and Table B.4 and Figure 3.10c show the 6-hourly precipitation statistical analysis and details. With respect to the contingency table in the range of light to very heavy precipitation, the behavior of both products is similar and shows a low POD and TS and a high FAR, while the POD of extreme precipitation intensity (P > 16.5 mm/6 h) yields relatively high values for both products. However, IMERG-RT yields better results than IMERG-FR for the POD values of 0.44 and 0.38 respectively. Nevertheless, in general, indices related to the contingency table show high POD and TS and a low FAR but they underestimate the frequency of events for precipitation equal or above 0.1 mm/6 h. It is notable that there is no meaningful difference between both products.

For 12-hourly precipitation, IMERG-FR and IMERG-RT tended to underestimate the number of events corresponding to light, moderate, heavy and very heavy precipitation while they tended to slightly overestimate the extreme precipitation with the bias frequency of 1.6 and 2.27 for IMERG-FR and IMERG-RT respectively. Moreover, again both products yield relatively poor results with respect to POD, TS and FAR for light, moderate, heavy and very heavy precipitation. Instead, extreme precipitation (P > 18.4 mm/12 h) yields better. However, in this threshold, IMERG-FR yields better than IMERG-RT to detect precipitation with higher POD and TS and lower FAR, 0.51, 0.24 and 0.68 in contrast to 0.47, 0.17 and 0.79 for IMERG-FR and IMERG-RT respectively (see Table B.1d and Table B.5 and Figure 3.10d).

With respect to different precipitation intensities for the daily time-scale (Table B.1e and Table B.6 and Figure 3.10e), IMERG-FR generally reveals better results than IMERG-RT in all precipitation categories. However, in the range of extreme precipitation (P > 24 mm/day) and precipitation with no classified intensity (P ≥ 0.1 mm/day) both products show a relatively high POD with 0.54 and 0.65 for IMERG-FR and 0.49 and 0.66 for IMERG-RT. The FAR values of both products are relatively high for precipitation with classified intensities and low for no classified precipitation and indicate 0.25 and 0.26 for IMERG-FR and IMERG-RT, respectively (Figure 3.10e). It is notable that there is no big difference between the FAR values of the two products.

The advantage of the multi-category contingency table approach is that the nature of the forecast errors can more easily be diagnosed but the disadvantage is that it is more difficult to condense the results into a single number. Despite this, in this study, a low POD and TS, and a high FAR for classified precipitation means that satellite products are not able to detect precipitation in their exact precipitation categories, but they are able to detect the amount of precipitation somewhat lower or higher than the specified intensities. Moreover, as for the other time-scale evaluations in the range of extreme precipitation intensity

($P > 24$ mm/day), both IMERG-FR and IMERG-RT tend to overestimate the number of events with a bias frequency of 1.7 and 2.31 respectively. For more information about the frequency of events with different intensities see Appendix Table B.2Table B.6.

3.6 Conclusions

Accurate high-resolution multi-satellite precipitation estimates have wide applications in hydrology, meteorology, water resource management and numerical weather prediction model verification. In this study, a comprehensive assessment has been performed to examine the performance of the Day-1 IMERG-FR and IMERG-RT late-run version V03 against 62 meteorological synoptic station data on a multi time-scale such as daily and sub-daily time resolution over northeast Austria from mid-March 2015 till end of January 2016. IMERG-FR uses monthly Global Precipitation Climatology Centre (GPCC) gauge data over land for bias correction; and the IMERG-RT late-run product also uses a coefficient of monthly climatology data.

It is found that in general for hourly precipitation and for entire precipitation rate ($P \geq 0.1$), both products indicate a negative bias. However, for other time steps, IMERG-FR tends to underestimate while IMERG-RT tends to overestimate precipitation over the study area.

Based on the entire range of precipitation, hourly, 3- and 6-hourly IMERG-FR did not show a clear improvement of the bias over IMERG-RT while for 12-hourly and daily precipitation estimates, the bias in IMERG-FR has improved compared to IMERG-RT. In addition, IMERG-FR shows a considerable improvement in RMSE compared to IMERG-RT. However, IMERG-FR systematically underestimates moderate to extreme and overestimates light precipitation for the entire range of precipitation intensities ($P \geq 0.1$ mm/time interval). When comparing the bias, RMSE, and correlation coefficients, IMERG-FR outperforms IMERG-RT particularly for 6-hourly, 12-hourly and daily precipitation. Despite the generally low POD and TS and high FAR skill scores within specified precipitation thresholds, the multi-categorical contingency table shows relatively good values of the POD, TS and FAR for precipitation without classification. This means these two satellite products are relatively well able to detect precipitation without classification but they have poor results to detect precipitation in their exact precipitation categories over northeast Austria.

Also, in agreement with earlier studies, there is a different statistical relation between satellite and in-situ precipitation depending on elevation, land surface characteristics and snow-rain phase of precipitation. Therefore, further work on these issues is needed. This research is to our knowledge one of the first studies to evaluate GPM-IMERG products over Austria. Further intensive detailed studies are needed when improved and fully GPM-IMERG retrospectively processed data starting from 1998 to 2000 become available to understand inter-annual variability which is very important because sensors and satellites used in multi-satellite products can be out of service and new sensors can be added at any time (Prakash et al., 2016).

In summary, although the newly introduced sensors and upgraded calibration algorithms have undoubtedly improved the GPM constellation satellites' accuracy, some challenging issues in satellite retrieval processes will continue to remain open for the satellite community, providing the impetus for more research and development.

The overestimation or underestimation over forest areas indicates that accurate estimation by satellite-based precipitation products even though they are improved still remains a challenge particularly for short-time precipitation (i.e., hourly precipitation). Such inaccuracy may be rooted in the following possible causes of uncertainty of evaluation of SPEs against rain-gauges:

1. The spatial resolution of the satellite product, since precipitation within a region, may occur on smaller scales than the pixel size of satellites.

2. An inadequate number of gauges, provided by the GPCC and used for bias correction in satellite products.

3. Short-time precipitation (i.e., daily and sub-daily accumulation) is much more variable than monthly precipitation and regional effects like topography and local circulation play an important role in rainfall generation. Accordingly, monthly precipitation from GPCC which are used for the calibration of IMERG-FR would not be well smoothed if sub-daily precipitation fields are used.

4. Algorithm error

5. Rain-gauge measurements error due to wind-induced undercatching, precipitation type and particle falling velocities, rainfall intensity and the aerodynamic properties of a particular type of gauge

As more IMERG data become available, more detailed studies of GPM-IMERG applications in water, weather, and climate studies are possible in the near future. We expect that the regional analysis of GPM constellation satellite-based precipitation estimates reported here can give users a better understanding of the features associated with currently available IMERG precipitation estimates and a broader perspective.

Published paper:

Atmospheric Research 206 (2018) 46–63

Contents lists available at ScienceDirect

Atmospheric Research

journal homepage: www.elsevier.com/locate/atmosres

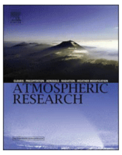

Multi time-scale evaluation of high-resolution satellite-based precipitation products over northeast of Austria

Ehsan Sharifi[a,*], Reinhold Steinacker[a], Bahram Saghafian[b]

[a] Department of Meteorology and Geophysics, University of Vienna, Austria
[b] Department of Technical and Engineering, Science and Research Branch, Islamic Azad University, Tehran 1477893855, Iran

ARTICLE INFO

Keywords:
Satellite precipitation products
GPM constellation satellite
IMERG
Statistical analysis

ABSTRACT

Over the years, combinations of different methods that use multi-satellites and multi-sensors have been developed for estimating global precipitation. Recently, studies that have evaluated Integrated Multi-satellite Retrievals for GPM (IMERG) Final-Run (FR) version V-03D and other precipitation products have indicated better performance for IMERG-FR compared to other similar products in different climate regimes. This study comprehensively evaluates the two GPM-IMERG products, specifically IMERG-FR and IMERG-Real-Time (RT) late-run, against a dense station network (62 stations) in northeast Austria from mid-March 2015 to the end of January 2016 using different time-scales. Both products are examined against station data in capturing the occurrence and statistical characteristics of precipitation intensity. With regard to probability density functions (PDFs), the satellite precipitation estimate (SPE) products have detected more heavy and extreme precipitation events than the ground measurements. Both precipitation products at all time-scales, except for IMERG-RT 12-hourly and daily precipitation, capture less occurrence of precipitation than the station dataset for light precipitation. This partially explains the under-detection of precipitation events. For all time-scales, both IMERG products' CDFs (Cumulative Distribution Function) are well above that of the stations' precipitation. For lower precipitation levels, IMERG-RT is slightly below the IMERG-FR whereas IMERG-RT is above IMERG-FR at higher precipitation levels. Furthermore, for entire spectrum precipitation rates ($P \geq 0.1$ mm), 1, 3, 6-hourly, IMERG-FR did not show a clear improvement of the Bias over IMERG-RT, while for 12-hourly and daily precipitation estimates, the bias in IMERG-FR has improved compared to IMERG-RT. In addition, IMERG-FR shows a considerable improvement in RMSE as compared to IMERG-RT. IMERG-FR, however, systematically underestimates moderate to extreme precipitation and overestimates light precipitation for all time scales against rain-gauges in northeast Austria. When comparing the bias, RMSE, and correlation coefficients, IMERG-FR has outperformed IMERG-RT particularly for 6-hourly, 12-hourly, and daily precipitation. Despite the general low probability of detection (POD) and threat score (TS) and the high false alarm ratio (FAR) within specified precipitation thresholds, the contingency table shows relatively acceptable values of the POD, TS and FAR for precipitation without classification.

1. Introduction

Accurate precipitation estimation on fine spatio-temporal resolutions is important for water resources-related applications such as hazards forecast and management, agricultural water use, water resource management for human and industrial use, and understanding the ecosystems (Joyce et al., 2004; Yong et al., 2010). In-situ observations are often limited; however, currently available SPE products can potentially provide the precipitation estimation needed for meteorological and hydrological applications. Moreover, accurate monitoring and prediction of rainfall would help to reduce property damages and potential loss of life that may occur due to flooding (Wong and Chiu, 2008). Hence, for a better understanding of the impact of rainfall on the environment, it is crucial that one has good spatial and high temporal resolution rainfall observations available. This is specifically the case over complex mountainous regions where there is insufficient rain-gauge available and rainfall is distinguished by complex patterns (Gebere et al., 2015; Krakauer et al., 2013).

Over the ocean, microwave emissivity is low and highly polarized, allowing passive microwave (PMW) sensors to (largely) separate the surface radiation signal and the (warm) emission signal arising from liquid hydrometeors. However, over land, the microwave emissivity is

* Corresponding author.
E-mail addresses: ehsan.sharifi@univie.ac.at (E. Sharifi), reinhold.steinacker@univie.ac.at (R. Steinacker), b.saghafian@gmail.com (B. Saghafian).

https://doi.org/10.1016/j.atmosres.2018.02.020
Received 4 July 2017; Received in revised form 8 February 2018; Accepted 21 February 2018
Available online 24 February 2018
0169-8095/

Chapter 4

4 Uncertainty Analysis and Bias Correction

This chapter has been accepted as: Sharifi, E., Saghafian, B., Steinacker, R., 2019. Copula-based Stochastic Uncertainty Analysis of Satellite Precipitation Products. *Journal of Hydrology*, accepted: January 13, 2019.

4.1 Abstract

Satellite products, like all datasets, are subject to errors and uncertainties. Due to inherent biases embedded in satellite precipitation estimates, we present an error-adjustment approach based on the statistical differences between satellite precipitation products and in-situ observations (observed errors) employing two widely-used error models, namely that additive and the multiplicative error models, in an attempt to assess their suitability for the error correction of satellite-based daily precipitation estimates over northeast Austria. An error-adjustment technique based on the concept of the copula is adopted and applied to correct the supplied precipitation fields. It was found that IMERG precipitation estimates improved after error adjustment when compared to original satellite precipitation estimate (OSPE). The additive error model resulted in a better improvement by fitting the entire range of data when compared with the multiplicative error model. Moreover, the additive error model extracted the error with more accuracy and produced a better estimation of their characteristics, while the method based on the multiplicative error was less robust. However, the overall spatial dependence of the observed errors is reasonably preserved as that of the generated errors by copula. In addition, the validation results implied that the simulated realizations error-adjusted band, encompassed the observed data reasonably. Moreover, the copula-based simulations associated with the additive error model performed much better in comparison to the multiplicative error model. Overall, by using the t-copula model with an emphasis on the additive error model and imposing the simulated error fields on the OSPE, one may generate multiple realizations of precipitation fields.

4.2 Introduction

The quantification of precipitation and its spatio-temporal variability is very important for understanding hydrological processes. Precipitation characteristics may be captured through traditional ground-based rain-gauges, radars and/or satellite precipitation estimate (SPE) products. High-resolution SPEs provide an effective source of data (i.e., uninterrupted effectively global coverage) for hydro-meteorological applications and water resource management, particularly over economically developing regions where there is often a lack of or very sparse ground-based observations. In order to understand the hydrological processes and their associated uncertainties in ungauged catchments, the development of hydrological models is vital (Abimbola et al., 2017). The uncertainties, vagueness, and inaccuracy of hydro-meteorological data results from errors in the measurement equipment and precipitation estimation models. Such errors indicate that hydrological studies may potentially be unreliable, leading to water allocations using hydrologic data being inaccurate for future studies (Khazaei and Hosseini, 2015).

The high costs related to the set-up and maintenance of hydro-meteorological monitoring networks constraints the number of conventional (i.e. in-situ) stations that can be established. Despite improved technology, the quality and reliability of measured hydro-meteorological data are not always assured and the accompanying uncertainty is often significant. (Behrangi et al., 2011) used precipitation products as input to a rainfall-runoff model to generate streamflow at different time-scales over the mid-size Illinois River basin. They found that the bias-adjusted satellite precipitation products agreed well with gauge-adjusted radar, compared with their counterparts with no bias-adjustment, particularly in capturing the timing, occurrence and magnitude of precipitation events. Sharifi et al., (2018) evaluated daily and sub-daily IMERG data against rain-gauge observation in northeast Austria. They showed IMERG-FR, systematically underestimates moderate to extreme precipitation and overestimates light precipitation for different time scales when compared to rain-gauges in this region.

Reliable precipitation is essential for hydrologists and meteorologists, as the uncertainties associated with precipitation estimates propagate through related modeling predictions (AghaKouchak et al., 2011). Therefore, bias correction procedures are often applied to produce local-scale information before it can be employed in decision-making activities. Previous studies have confirmed that efforts are needed to assess the accuracy of SPEs and their associated uncertainty, as they are of great significance to research and applications in hydrology and climate studies (e.g., Ciach et al. (2007); Hossain and Huffman (2008); Habib et al. (2009a); Villarini et al. (2008b); Dong et al. (2005); and Sharifi et al. (2018)). However, satellite products are subject to errors and uncertainties due to the indirect nature of their estimates. Accordingly, this study is focused on the error correction and uncertainty analysis of the highest resolution Integrated Multi-satellitE Retrievals for GPM (Global Precipitation Measurement, a joint Japanese Space Agency/NASA mission), also known as IMERG, over northeast Austria.

The GPM constellation satellite product, IMERG, covers latitudes 60°N-S. It has a spatial resolution of 0.1 degrees and is updated every 30 minutes. IMERG consists of three products: IMERG-FR (currently aimed at research activities), IMERG-RT Early-Run, and IMERG-RT Late-Run. The IMERG algorithm is intended to inter-calibrate, merge, and interpolate entire satellite microwave precipitation estimates, together with microwave-calibrated infrared (IR) satellite estimates and precipitation gauge analysis.

The need to quantify the uncertainties in such precipitation products is gaining strength, especially as the volume of accessible data is rapidly increasing, leading the scientific community to focus more on the degree of data reliability. Precipitation uncertainty affects many research fields such as climate change, the hydrological cycle, and weather/climate prediction data assimilation, as well as the calibration and validation of Earth-observing instruments. The assessment of uncertainty greatly depends on the adopted error model. To evaluate the uncertainties in precipitation measurements, two types of error models have been broadly adopted: the additive and the multiplicative. The applicability of different error models results in different interpretations of uncertainty, which may potentially impede direct comparisons between datasets and mislead end users (Tian et al., 2013).

The accuracy of SPEs has been assessed over different spatio-temporal resolutions in a number of studies (AghaKouchak et al., 2011; 2011; Dezfuli et al., 2017; Gebere et al., 2015; Guo et al., 2015; Khodadoust et al., 2016; Mahmud et al., 2015; Moazami et al., 2013; Prakash et al., 2016; Sharifi et al., 2016, 2018; Sungmin et al., 2016; Tian et al., 2009). Although, the application of SPEs to hydro-meteorological predictions and water resource management has been intensified in recent years, the accuracy evaluation of SPEs at the required spatio-temporal resolution is needed before use. The variability in precipitation is often represented by the error in the amount of precipitation over space and time. In addition to the magnitude of precipitation, the general pattern and its location are also important (AghaKouchak et al., 2011; Foufoula-Georgiou and Vuruputur, 2001).

Hydrological and meteorological phenomena are known to be multidimensional and thus require multivariate analyses as well as knowledge of the conditional probability distributions among variables. Classic families of multivariate distributions are frequently used for modeling joint probability distributions of multiple random variables. Multivariate distributions, such as bivariate normal, log-normal and gamma, are built with several model parameters that illustrate the behavior of each random variable as well as the joint probability distribution itself. The main disadvantage of such methods is that modeling the dependence structure among variables is not independent of the choice of the marginal distributions (Dupuis, 2007; Genest and Favre, 2007). Therefore, using such models may lead to unrealistic simulations (Germann et al., 2006a).

As the spatial correlation of satellite and radar rainfall error is significant (Ciach et al., 2007; Habib et al., 2009a), the error term is assumed to be spatially correlated and copulas may be used to describe the dependence structure. In general, in-situ precipitation data, employed as the reference, are collected from high-density gauge networks in the study region in order to quantify the SPEs error.

Using different members of the copula family in multivariate data, extreme value analysis and modeling dependence structure has become popular in hydro-meteorological analysis. Kelly and Krzysztofowicz, (1997) employed a meta-Gaussian approach to bivariate rainfall analysis and pointed out that the meta-Gaussian distribution is independent of marginals and hence may be applied to represent the dependence structure of bivariate variables. Michele and Salvadori, (2003) modeled the intensity-duration of rainfall events utilizing copulas. Favre et al., (2004) used copulas in multivariate hydrological frequency analysis. Bárdossy (2006), and Bárdossy and Li (2008) applied the concept of copulas to the interpolation of groundwater quality criterions. Using the Gaussian copula, Renard and Lang (2007) investigated multivariate extreme value analysis and its application to hydrology. Schölzel and Friederichs (2008) modeled multivariate non-Gaussian random variables with copulas. Kuhn et al., (2007) described the spatio-temporal dependence of weekly precipitation extremes using copulas. Serinaldi, (2008) and Villarini et al., (2008b) presented a model for radar rainfall estimation uncertainties by using bivariate mixed distributions and a copula-based Markov approach. (AghaKouchak, 2014) introduced a drought indicator to predict drought conditions over the United States. Balistrocchi et al., (2017) identified the dependence structure between peak flow discharge and flood volume featuring hydrographs forcing a flood control reservoir by using copula function. (Liu et al., 2017) developed a copula-based hydrological uncertainty processor for probabilistic flood forecasting. Pham (2016) developed a framework that allowed for generating coupled precipitation and evaporation time series based on vine copulas. Major developments in the theory and implementation of copulas may be found in Schweizer (1991), Salvadori and de-Michele (2007), and Dall'aglio et al. (1991).

One way to evaluate the spatio-temporal uncertainty of SPE products is to simulate an ensemble of precipitation fields containing a large number of realizations, with each realization standing for a possible rainfall event (AghaKouchak, 2010). Hossain and Anagnostou (2005) expanded a two-dimensional satellite rainfall error model for satellite rain fields ensemble simulations. They reported the joint spatial probability of the successful delineation of rainy and non-rainy areas using Bernoulli uniform distribution experiments with a correlated structure generated according to Gaussian random fields. They also simulated SPEs random error fields by Monte Carlo simulations of any given realization. Bellerby and Sun (2005) designed a methodology to quantify the uncertainty of high-resolution SPEs by generating probabilistic and ensemble representations of the measured precipitation field. An extensive copula-based simulation study for applications involving up to 100 variables was presented by Dong and Patton (2015). Teo and Grimes (2007) characterized an approach for uncertainty estimation of satellite-based rainfall values utilizing ensemble generation of rainfall fields according to a stochastic calibration. They obtained the spatial correlation structure within each ensemble member via geostatistical sequential simulations.

In all of the studies noted above, geostatistical approaches and Monte Carlo simulations were used in order to generate spatially correlated random fields and ensemble members of the precipitation estimation error. The ensemble-based model is selected because it can provide a better quantification of the precipitation uncertainty in comparison to single best estimates; however, geostatistical-based methods (e.g., a simple variogram model or a covariance matrix) have limitations. For instance, the data is assumed to display three main features: dependency, stationarity, and Gaussian distribution (Johnston, 2004). In addition, the spatial dependence structure of daily precipitation is too complex to be modelled by a simple correlation coefficient over the range of observed values. Where the observed values are low, they tend to be scattered and intermittent, exhibiting a poor spatial dependency. By contrast, where precipitation is high, it tends to be spatially and temporally more dependent. Such interdependence, which is related to the amount of precipitation, requires an appropriate quantification technique (Bárdossy and Pegram, 2009). Multivariate copulas may be a suitable choice, hence in this work, copulas representing joint cumulative distribution functions (CDF) are employed to describe the dependence structure of variables, as well as to model multivariate random variables with different marginal distributions. Indeed, one of the most attractive features of copulas is their ability to describe the dependence structure of a dataset, independent of the marginal distribution (Joe, 1997; Nelsen, 2006). In recent years, several studies dealing with application of different families of copula in hydrological and meteorological processes have been carried out (AghaKouchak et al., 2010b; AghaKouchak et al., 2010a; Grimaldi and Serinaldi, 2006; Renard and Lang, 2007; Wang et al., 2010; Zhang and Singh, 2007).

In this study, a bias-corrected IMERG product using a copula-based ensemble generation approach is generated. A multivariate t-copula is employed to describe the dependence structure and to simulate multivariate satellite precipitation error fields. Error is measured against observed daily precipitation events over 48 $0.1° \times 0.1°$ pixels within the study region. The methodology presented here is similar to that of Moazami et al. (2014) who used copulas to generate an ensemble of precipitation realizations. However, Moazami et al. (2014) used a gaussian copula-based additive error model in order to generate an ensemble of precipitation realizations, while in this study, an error correction model for the IMERG product is developed by adopting/comparing both additive and multiplicative error models based on t-copula. Overall, by analyzing the error characteristics of precipitation algorithms, the objective of this study goes beyond the mere validation of the IMERG product.

This chapter is organized into six sections. In the following sections, after a brief review of copula theory in section 4.3, the t-copula family used in this study is introduced in more detail. Section 4.4 introduces the study area and data resources used; The methodology is described in section 4.5; section 4.6 details the results and discussion; and section 4.7 summarizes the conclusions and remarks.

4.3 Copulas

4.3.1 Concept of copula

Copulas are joint CDFs that describe dependency among variables regardless of their marginal distribution (Joe, 1997; Nelson, 2006). The relationship among random variables is defined through their joint distribution function as follows:

$$C^n(u_1, \dots, u_n) = P_r(U_1 \leq u_1, \dots, U_n \leq u_n) \tag{4.1}$$

where function C^n is called a copula, which is an *n*-dimensional joint CDF of a multivariate random variables $\mathrm{U}(U_1, \dots, U_n)$, such that $\mathrm{u}(u_i, \dots, u_n)$ represent one realization, and P_r is the probability of the variables. The copula is therefore a function that links the multivariate distribution $F(x_1, \dots, x_n)$ to its univariate marginal $F_{X_i}(x_i)$. Sklar (1959) demonstrated that:

$$C^n\big(F_{X_1}(x_1), \dots, F_{X_n}(x_n)\big) = F(x_1, \dots, x_n) \tag{4.2}$$

where a copula *C* of *n* random variables is defined as a multivariate CDF (*F*) on the *n*-dimensional unit cube with uniform marginals:

$$C : [0,\ 1]^{\,n} \rightarrow [0, 1] \tag{4.3}$$

In the copula model defined in Eq. (4.2), it is possible to integrate different families of probability distributions. This is the main advantage of this approach compared to standard multivariate models used in practice (Favre et al., 2004). In addition, copula can preserve the dependency among variables that are described with a correlation *n*-by-*n* matrix, where *n* is the number of variables.

The Sklar theorem indicates that for multivariate distributions, the multivariate dependence structure and the univariate marginal distributions may be separated, and hence, the dependence structure can be represented by a copula, independent of the marginals. For proof and derivations, interested readers are referred to Sklar (1996).

There are numerous families of copulas developed within different practical contexts. Each copula family has a number of parameters. The main difference associated with different copulas is in the detail of the dependence they represent. In this study, an elliptical copula, in particular a t-copula, is used for simulations. For additional information regarding the different copula families, the readers are referred to Joe (1997) and Nelson (2006).

4.3.2 T-copula

The t-copula, also known as Student copula, is an elliptical copula based on the Student distribution. For modeling the dependencies of extremes, the application of the gaussian copula may not be an appropriate choice while the tail dependence is observed in the data. Thus the t-copula may be more appropriate (Moazami et al., 2013). The asymptotic dependent behavior of t-copula is expected even when the variables are negatively correlated (Embrechts et al., 2001). The t-copula is expected to specify different ranks of correlation between the marginals. The t-copula copula is suitable when more than two dimensions (variables) are used (Demarta and McNeil, 2004; Renard and Lang, 2007). A number of studies have reported on the application of the t-copula to describe the dependence between variables in multivariate distributions (AghaKouchak et al., 2010a; AghaKouchak, 2014; Daneshkhah et al., 2016; Madsen, 2009; Song, 2000; Song et al., 2009). In principle, the choice of a suitable copula for modeling a data set is not straightforward, especially if the data set is not informative enough to provide relevant indications about the asymptotic dependence properties (Renard and Lang, 2007). The simulation of multivariate random fields may be performed based on any given copula. Interested readers are referred to (Salvadori and de-Michele, 2007).

Consequently, in this study, as a first attempt to quantify and bias-correct IMERG data over northeast Austria, a multivariate t-copula is employed to simulate multivariate satellite precipitation error fields. As noted before, since a copula is invariant to monotonic transformations of the variables, the simulated random variables will have the same spatial dependence structure as that of the input data. This is one of the main interesting features of using copulas for the simulation of spatially-dependent random fields. In the current study, the copula parameter is estimated based on the observed errors in each pixel.

4.4 Study Area and Dataset

4.4.1 Study Area

Austria is situated in a temperate climatic zone, under the influence of the Atlantic climate. Altitude determines the precipitation pattern, as shown by Figure 4.1 where the central parts towards the west of the country may experience an average precipitation of over 2000 mm/year, while regions in east and northeast of Austria are drier with less than 600 mm in annual precipitation (Hiebl et al., 2011). Moreover, according to the Köppen-Geiger classification, updated by Rubel et al. (Figure 4.2), the Cfb (warm temperate, No dry season and warm summer) and Dfb (boreal, No dry season and warm summer) are the prevailing climates in northern and eastern Austria (Rubel et al., 2017).

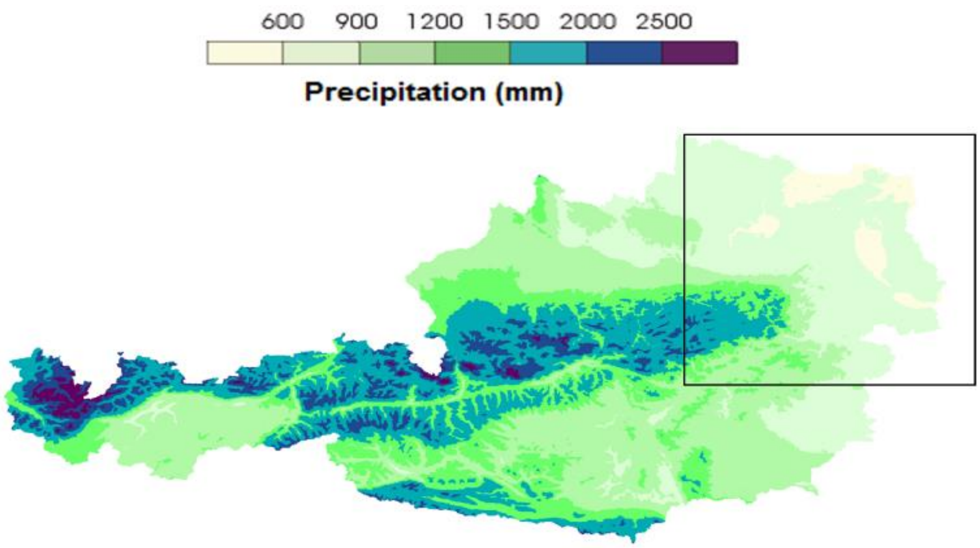

Figure 4.1. Mean annual precipitation map of Austria (Hiebl et al., 2011)

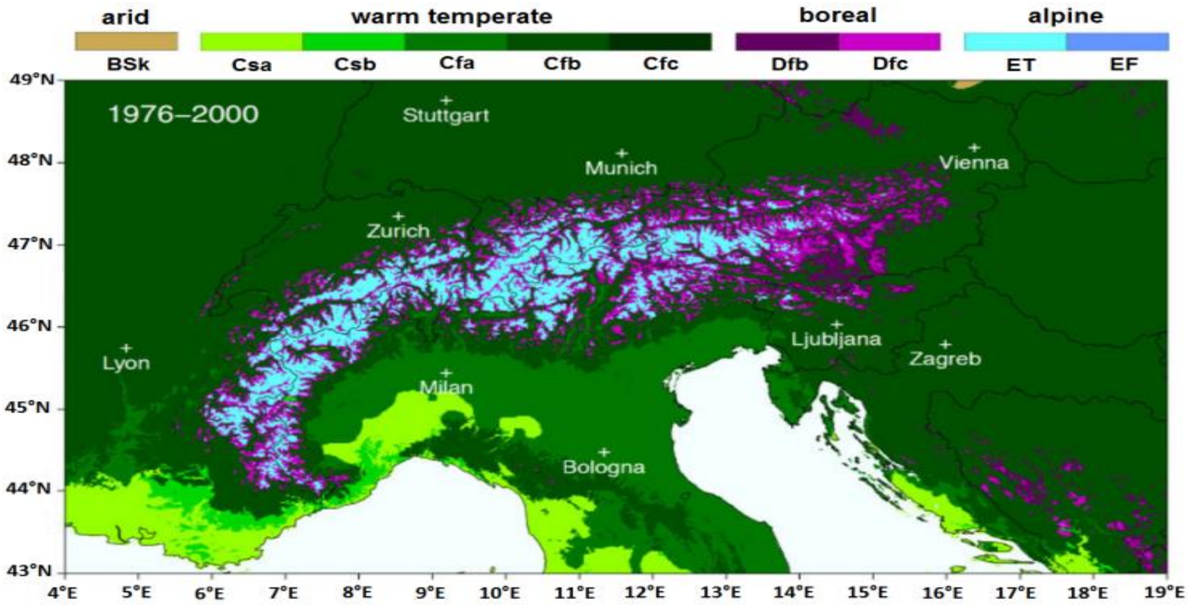

Figure 4.2. Climate map of Austria based on Köppen climate classification, updated by Rubel et. al. (2017)

Northeast Austria consists of about 290 0.1° × 0.1° IMERG pixels. There are 55 operating synoptic stations across the study area (Figure 4.3), falling within 48 IMERG pixels. The study period covers March 2015 to January 2016. 52 daily precipitation events which occurred across the region were identified such that all stations simultaneously recorded precipitation. Consequently, the analyses were carried out for 52 daily events over 48 pixels in the study area.

4.4.2 Dataset

The reference dataset employed in the present study is based on daily rain-gauge meteorological observations provided by the Zentralanstalt für Meteorologie und Geodynamik (ZAMG)-Austria. ZAMG operates a network of semi-automatic stations across the country and provides quality-controlled precipitation data. The ZAMG stations have tipping bucket gauges and weighting rain-gauges equipped with a heating system (Haiden et al., 2011). Before evaluating the precipitation data, we used a second derivative filter to identify unrealistic rapid and isolated changes in the precipitation time series. Such a derivative filter is quite sensitive to noise which should be eliminated before using the data for analysis (Shapiro and Stochman, 2001). Furthermore, the outliers that were removed make up only four out of the 419,890 hourly data points.

The rain-gauge precipitation data was therefore derived from the 55 synoptic stations during the 52 days with precipitation between 15 March, 2015 and 31 January, 2016 (Figure 4.3). The resolution of the rain-gauge data is 0.1 mm, so that any observation less than this threshold was taken to be a dry day. Comparisons were made between the ground precipitation data with the corresponding IMERG pixel precipitation. It is notable that in this area, the precipitation pattern is not directly affected by altitude and the topography is moderate. In cases where two or more stations fall within a single pixel, the reference ground precipitation was obtained based on the average precipitation of the stations.

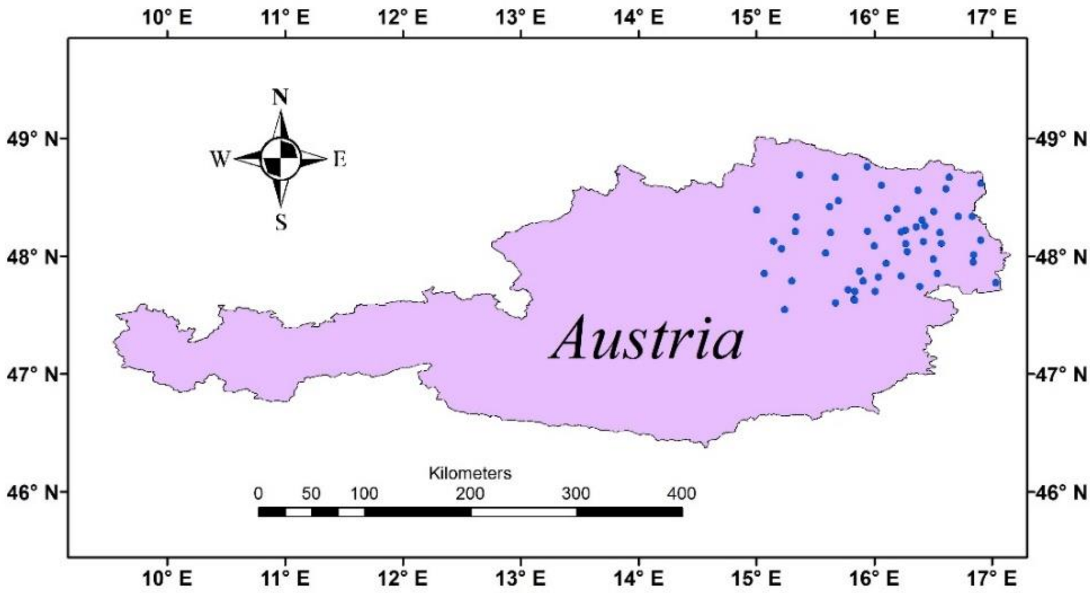

Figure 4.3. Distribution of precipitation stations

The SPE product used in this study is taken from IMERG-FR version 04 aggregated to daily accumulation from its original half-hourly dataset. IMERG is based on components from three prior multi-satellite algorithms, namely the Tropical Rainfall Measuring Mission (TRMM) Multi-Satellite Precipitation Analysis (TMPA: (Huffman et al., 2007), the Climate Prediction Center (CPC) Morphing Technique (CMORPH: (Joyse et al., 2004), and the Precipitation Estimation from Remotely Sensed Information using Artificial Neural Networks (PERSIANN: (Sorooshian et al., 2000) products. IMERG-V04 covers the global latitude belt from 60°N to 60°S. Interested readers are referred to (Huffman et al., 2017a;

Huffman et al., 2017b; Precipitation Processing System at NASA GSFC, 2015) for further details on the IMERG product specifications.

4.5 Methodology

In this study, the error fields associated with SPEs are simulated on the basis of two error models (described above) using copula-based random generators. Then, in order to obtain an ensemble of error-adjustment SPE (EASPE), the simulated error fields are imposed over the original satellite precipitation estimate (OSPE) before any adjustments are made. A general overview of the proposed approach is presented as follows. First, SPEs daily event errors over selected pixels using additive and multiplicative error models are derived. Consequently, a multivariate t-copula is fitted to those (observed) errors and random ensembles of error fields are generated. Afterwards, generated error fields are imposed over OSPEs to produce ensembles of EASPEs and, eventually, the accuracy of simulated ensembles is assessed.

The procedure is presented as follows:

Step 1) 49 (94%) out of 52 precipitation events over 48 pixels are employed randomly in order to calibrate the ensembles of error fields while another 3 events (6%) are left to validate the predictive skill of the simulation model.

Step 2) The difference between station measurements, used as the reference precipitation data, and the SPE in the corresponding pixel represents the so-called “observed error”. Using these observed error values, a 49-by-48 matrix is formed.

Step 3) The best probability distribution function (PDF) is fitted to the observed error values in each pixel; subsequently, the CDFs of the observed errors are computed for each pixel.

Step 4) The n-dimensional multivariate t-copula is fitted to the CDFs from the previous step. Since the error in each pixel is assumed to be a variable, the dimension (n) of the t-copula is 48. In other words, the spatial dependence structure of the error values among the 48 pixels is captured by the copula. The marginal PDF is constructed empirically for each pixel using the Anderson–Darling goodness-of-fit test to statistically examine whether or not data is sampled from the fitted distribution at 5% significance level. This criterion has demonstrated its usefulness in hydrological applications (Laio, 2004).

Step 5) The t-copula is employed to randomly generate an ensemble of error CDFs.

Step 6) Ensembles of error fields, i.e., the inverse of randomly generated CDFs, are obtained.

Step 7) Outlier data of the randomly generated ensembles are identified and removed.

Step 8) The simulated multiple random error fields are imposed over the OSPEs. This step results in 49 ensembles of error-adjusted realizations of SPEs. Indeed, each ensemble member represents a possible realization precipitation.

Step 9) The significance of the 49 simulated ensembles is measured and the best-simulated ensembles are identified.

Step 10) The best-simulated ensemble from the previous step is employed to validate the performance of the model for the three remaining daily events. All three simulated realizations are evaluated using bias and root mean square error (RMSE) statistical indices (AghaKouchak, 2010 and Moazami et al. 2014).

Outlier identification is important in many multivariate analysis applications, either because there is some specific interest in finding anomalous observations, or as a pre-processing task before the application of some multivariate method, in order to preserve the results from the possible negative influence of those observations. It should be mentioned that in step 7, outlier data, i.e., data that are located rather far from the center of the data distribution, are identified using a multivariate outlier detection technique and subsequently removed from the generated error fields. Several distance measures may be implemented for such a task. In this study, the Mahalanobis distance (also known as the generalized squared distance) is adopted to detect multivariate outliers. The Mahalanobis distance relies on the estimated parameters of the multivariate distribution. Interested readers are referred to Ben-Gal (2010); Hodge and Austin (2004) and Werner (2003) for extensive review and details of this procedure.

After the outliers are detected and removed, the generated errors are imposed on the OSPE in order to obtain an ensemble of EASPEs. Moreover, with respect to step 3, instead of fitting a standard distribution function to the data, the empirical CDF of observed error is applied to the uniformly simulated error values so that the simulated error values will have the same CDF as that of the observed. This significant improvement helps to avoid overshoot (simulating unrealistically large values) which typically happens when a standard distribution function is fitted and used for simulations.

Two types of error models have been extensively adopted in dealing with uncertainty of precipitation estimation: the additive error model and the multiplicative error model (Eqs. 4.4 and 4.5). In this study, we assessed the applicability of both error models in the quantification of satellite-based daily precipitation uncertainty. Many studies on SPE products have used the additive error model (Ebert et al., 2007; Habib et al., 2009a; Moazami et al., 2014; Shrestha, 2011) as expressed by:

$$Additive\ error = \frac{1}{N}\sum_{i=1}^{N}\left(P_{O_i} - P_{S_i}\right) \tag{4.4}$$

where P_{O_i} is the value of a rain-gauge observation for the *i*th daily event, P_{S_i} is the value of satellite precipitation estimates for the *i*th daily event, and N is the number of observed days.

Other studies (Ciach et al., 2007; Hossain and Anagnostou, 2005; Villarini et al., 2008b) have used the multiplicative error model to quantify/simulate errors in radar or satellite-based measurements. This model is expressed as follows:

$$Multiplicative\ error = \frac{\frac{1}{N}\sum_{i=1}^{N} P_{S_i}}{\frac{1}{N}\sum_{i=1}^{N} P_{O_i}} \tag{4.5}$$

In fact, the use of different error models leads to different quantification of uncertainties (Tian et al., 2013). Essentially, the additive error model explains the error as the difference between the satellite value and the corresponding station value, while the multiplicative error model defines the error as the ratio of the two.

Eqs. 4.6 and 4.7 describe the general error-adjustment formulations associated with additive and multiplicative error models, respectively:

$$EASPE_{i,add} = OSPE_i + Error_i \tag{4.6}$$

$$EASPE_{i,mlt} = OSPE_i \times Error_i \tag{4.7}$$

where $EASPE_{i,add}$ and $EASPE_{i,mlt}$ are ensembles of the EASPE in the *i*th pixel, according to additive and multiplicative error model, where $OSPE_i$ is the OSPE in *i*th pixel, and $Error_i$ is the randomly generated error fields in *i*th pixel.

In the current study framework, for a single "hit" event (both rain-gauge and satellite report non-zero precipitation, over P ≥ 0.1 mm threshold), one can correct the satellite estimation by using both additive and multiplicative models. However, for a single "miss" event (rain-gauge reports non-zero precipitation while satellite reports no precipitation), the multiplicative model leads to an indeterminate form (0/0). Therefore, in the case of "miss" events, the additive model is more practical for the estimation of error-adjusted precipitation. In this study, we only evaluated the "hit" events, i.e., both station and satellite reporting a precipitation depth of 0.1 mm/day (threshold precipitation) or more. Furthermore, following the previous studies, if a precipitation value becomes negative after error adjustment, it would be set to zero.

In this study, the ensemble approach is adopted to address the uncertainty associated with the EASPE. The output uncertainty based on the additive error model is quantified by the 60 percentage prediction uncertainty (PPU) band, enveloped by 20% lower and 80% upper limits of the simulated ensemble. The 60 PPU and 75 PPU bands associated with additive and multiplicative error models are used, respectively. As a result, some 40% and 25% of inappropriate simulations corresponding to 60 PPU and 75 PPU bands were ignored, respectively, expecting that the ground observation data fall within the selected bands. The 60 PPU and 75 PPU band were found appropriate after conduction a sensitivity analysis within the additive and multiplicative error model frameworks.

The prediction uncertainty band may be evaluated by *P-factor* and *d-factor* indices (Abbaspour et al., 2007). In this study, the *P-factor* is the percentage of pixels bracketed by the 60 PPU and 75 PPU bands, corresponding to the additive and multiplicative error models, respectively. For example, a *P-factor* of 50% indicates that the 60 PPU band of the simulated ensemble brackets the observed values of 24 pixels (the total number of studied pixels is 48). In other words, 24 rain-gauge values fall within the 60 PPU band. The maximum value of *P-factor* is 100% that ideally brackets all the observed data in the 60 PPU band.

The *d-factor* is determined by:

$$d - factor = \frac{\frac{1}{n}\sum_{i=1}^{n}(Q_{i,80\%} - Q_{i,20\%})}{\sigma_{obs}} \tag{4.8}$$

where $Q_{i,80\%}$ and $Q_{i,20\%}$ represent the upper and lower boundary of the 60 PPU in each pixel, *n* is the number of pixels (here 48), and σ_{obs} stands for the standard deviation of the observed precipitation of a single daily event for all 48 pixels. The *d-factor* represents the ratio between the average thickness of the simulated band (60 PPU and 75 PPU) and the standard deviation of the observed data. It expresses the width of the uncertainty interval. The smaller the *d-factor*, the closer the simulations are to the observations. Indeed, the *d-factor* denotes the strength of the simulation and ideally may be smaller than unity; however, in the practical cases, a reasonable value for *d-factor* is unity, demonstrating that the simulated fields reproduce the standard deviation of observed data.

The goodness of calibration and prediction uncertainty is considered based on how close the average value of *P-factor* is to 100% and the *d-factor* to 1 (Schuol et al., 2008). As a greater *P-factor* leads to a greater *d-factor*, often a trade-off between the two must be sought.

It is noted that both the *P-factor* and *d-factor* are determined for a simulated ensemble of EASPE associated with a single daily event. Within the framework presented here, the procedure is implemented for several sets of randomly generated error fields; consequently, for each set of generated errors, the average values of the *P-factor* and *d-factor* for 49 simulated ensembles are computed. Therefore, several pairs of averaged *P-* and *d-factors* are obtained. Then, an appropriate set among different sets of randomly generated errors is selected based on the best values of both the *P-* and *d-factors*. In fact, the selected set can simulate an ensemble of EASPE that has two features simultaneously: the *PPU* band brackets most of the observed data (*P-factor* approaching 100%) (Abbaspour et al., 2007), and the average distance between the upper and lower parts of the *60 PPU* (*75 PPU*) at 80% (87.5%) and 20% (12.5%) level corresponding to additive (multiplicative) error model(s) is as small as permissible, indicating a better correspondence between simulation and observation fields.

One of the advantage of the proposed methodology lies in its easily application to other geographical regions. Moreover, the proposed methodology, beside the spatially downscaled precipitation may be applied for fulfilling the needs of various application such as natural hazard, hydro-meteorology, agricultural and climate change studies where the need for more reliable precipitation data is of paramount importance.

4.6 Results and Discussion

The results are presented in three parts: 1) evaluation of the EASPEs, 2) spatial dependency analysis, and 3) copula-based uncertainty analysis and assessing suitability of error models.

4.6.1 Evaluation of the EASPEs

In order to assess the accuracy of the simulated ensembles, Bias and RMSE statistical indices were used on OSPE and EASPE satellite precipitation products by denoting the station observations as reference data. Note that the Bias and RMSE indices are computed for 49 out of 52 daily events over 48 pixels.

As discussed before, an ensemble of EASPE of any given daily non-zero event is simulated by imposing copula-based randomly generated error fields over the OSPE of the same event. Thus, for 49 selected daily events, a set of 49 ensembles are simulated, each of which consists of a large number of realizations. Each realization represents a possible daily precipitation event that may occur over the study domain.

In Figure 4.4 and Figure 4.5, the OSPE and EASPE indices represent the average bias and RMSE values for all 49 daily non-zero events in each pixel. It may be observed that the IMERG product is improved after error adjustment. The additive error model with a bias and RMSE of -0.03 mm and 8.09 mm, respectively, performed better by fitting the overall range of the data, compared with the multiplicative error model with 0.78 mm and 7.58 mm for the same indices, respectively.

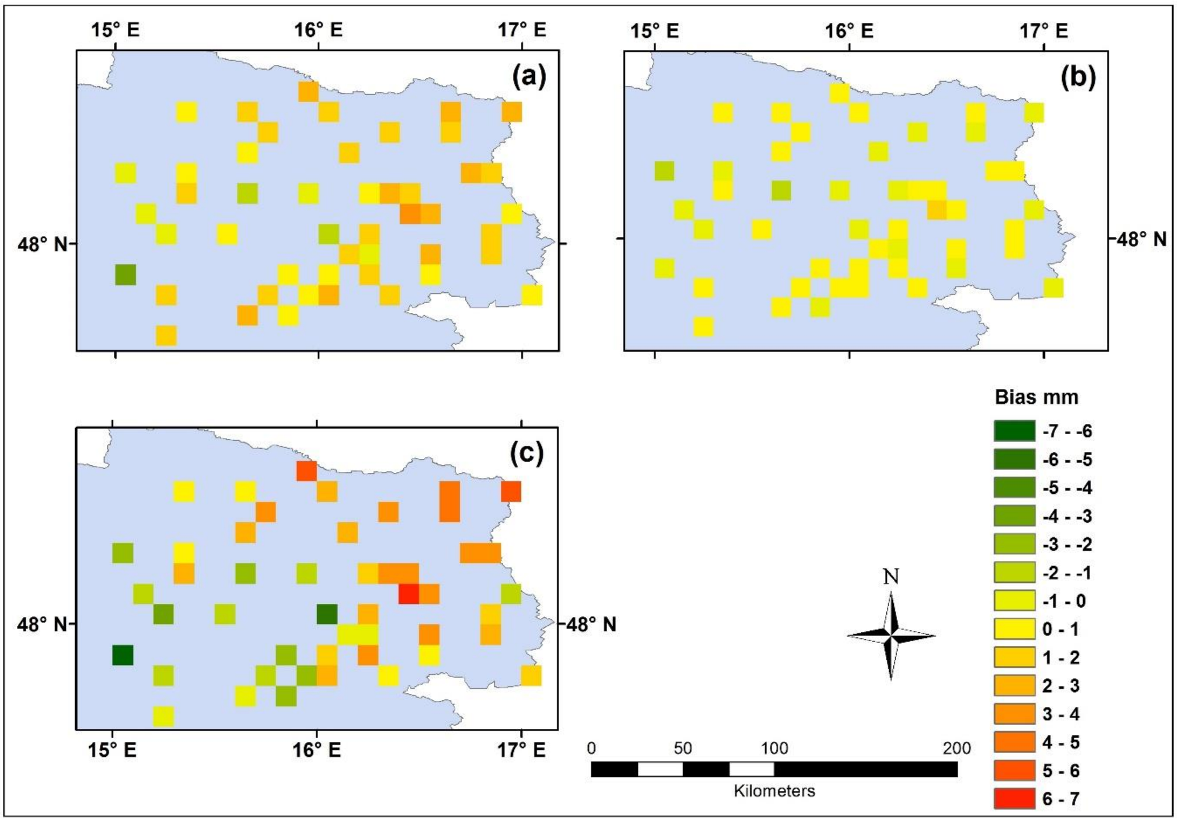

Figure 4.4. Average Bias of 49 daily precipitation events over 48 IMERG pixels for a) OSPE, , b) $EASPE_{add}$ and c) $EASPE_{mlt}$

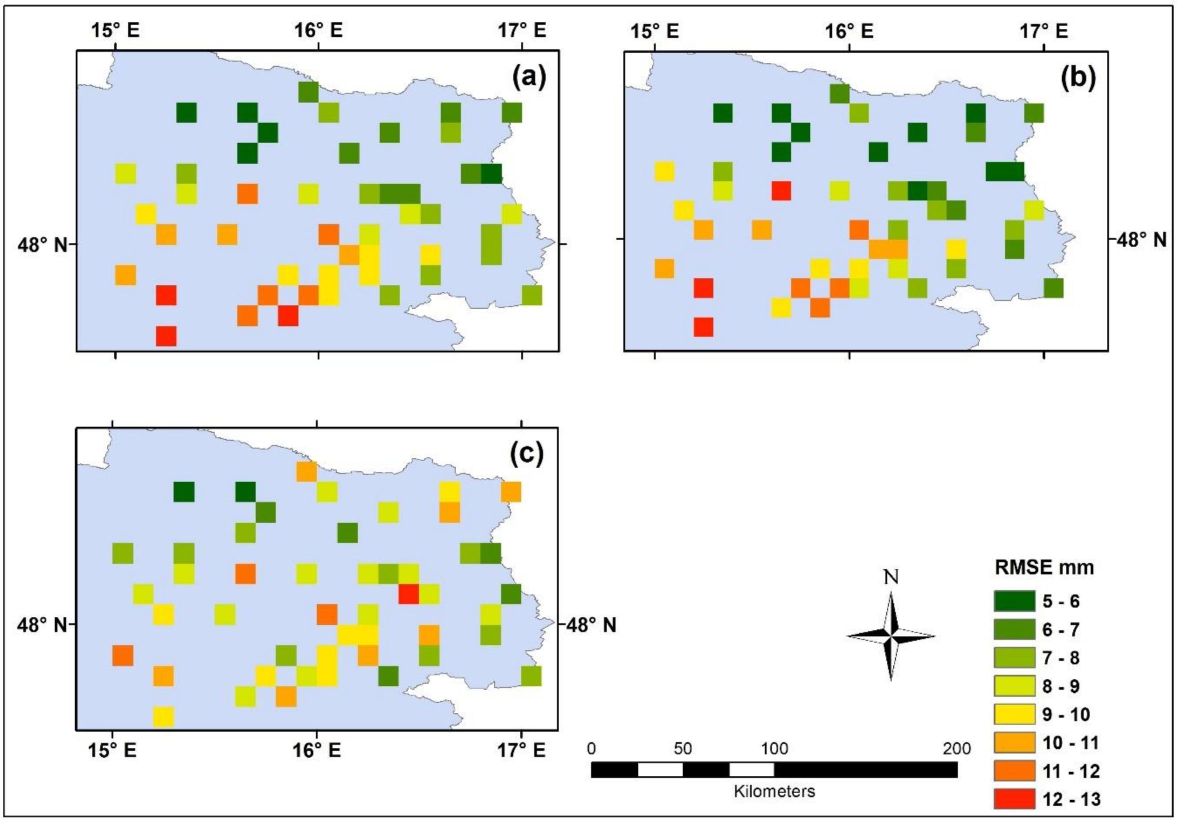

Figure 4.5. Average RMSE of 49 daily precipitation events over 48 IMERG pixels for a) OSPE, , b) $EASPE_{add}$ and c) $EASPE_{mlt}$

4.6.2 Spatial Dependency

Since copulas are invariant to monotonic transformations, the simulated random errors will have the same spatial dependence structure as that of the observed errors. It should be mentioned that although CC is a measure of linear dependency between a pair of random variables, numerous studies argued that estimation of the CC suffers from several shortcomings specially for precipitation analysis. For example, Willmott (1984) proposed that CC is insensitive to additive and proportional differences that may exist between the two variables, which causes a problem if CC is used as a performance measure. Legates and Davis (1997) stated that the existence of extreme events will lead to a high estimate of CC that may obscure the true relationship over most of the range of observations. Therefore, correlation estimates for precipitation patterns observed via a variety of sources may be affected by the distribution of the data and sample size effects. Another problem with the correlation analysis comes from the fact that extreme events are characterized by short intense precipitation periods often associated with localized convective cells.

However, in this study the CC has been used to examine whether the spatial dependency is preserved by the copula. Therefore, a comparison between all pair pixels of the observed error and simulated random error was conducted.

Scatterplots of the copula-based randomly generated and observed errors for pair pixels with the highest and lowest correlation coefficients are displayed in Figure 4.6. With respect to the additive error model, the highest CC values between each pixel pair (pixels 36 and 38) were 0.94 and 0.93, while the lowest CCs -0.24 and -0.10 (pixels 2 and 48), corresponding to the observed and generated errors, respectively. However, for the multiplicative error model, similar values were 0.84 and 0.85 (pixels 24 and 25) while, the lowest CCs (pixels 1 and 11) were -0.10 and -0.26 for the observed and generated errors, respectively.

As seen in Figure 4.6, the correlations between the observed errors (marked with orange symbols) are reasonably preserved by the generated errors (marked with blue symbols) for both the highest and lowest CC values between the pairs of pixels mentioned above. Furthermore, the scatterplots of the error values between previously mentioned pixels for the three validation events are presented and marked with black symbols. Note that the values of CC associated with the three validation set in Fig. 4.6.a-d are 0.30 and -0.05 for additive and 0.22 and 0.09 for multiplicative error models respectively.

The simulated error fields will be spatially dependent due to the dominance of the underlying spatial dependence structure of SPEs. It is notable that in this model, the satellite estimates are agitated with error fields and thus the dependence structure of the satellite estimates will be preserved within the simulated fields. To illustrate this, the Spearman correlation matrix is employed to assess the dependence structure of the simulated precipitation fields (Figure 4.7a-f). Figure 4.8a-f compare the spatial correlation structure of observed and copula-based simulated errors corresponding to both error models. In this figure, the 48×48 dimensional CC matrices are shown. The copula simulation is performed properly as the correlations are similar to those of the observations.

The lack of a true representation of precipitation in space and time causes most error models to particularly neglect the spatial dependency inherent in satellite precipitation error fields. A visual comparison of Figure 4.7 confirms that the spatial correlation of error is significant

(Ciach et al., 2007 and Habib et al., 2008) and adequate spatial correlation structure within each ensemble is preserved via the t-copula copula simulation.

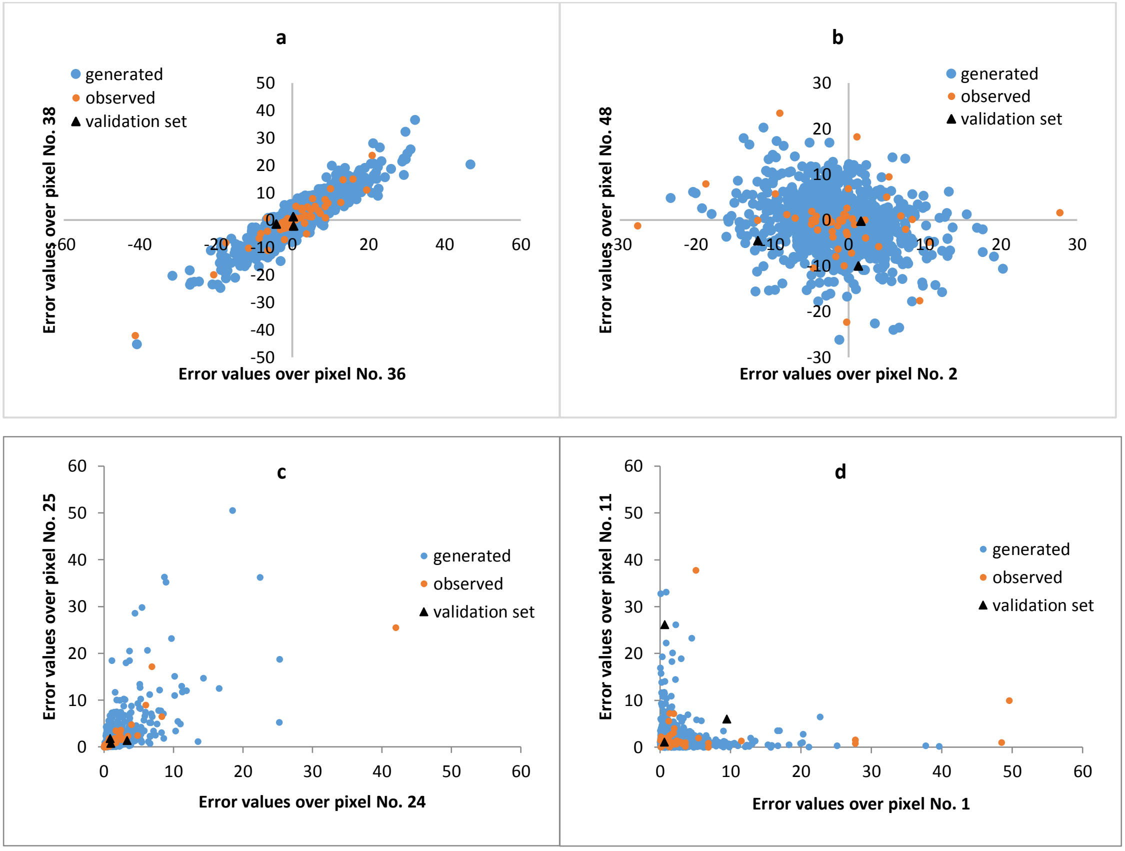

Figure 4.6. Scatterplot of error pairs related to a) highest values of CC b) lowest values of CC for the additive error model; and c) highest values of CC and d) lowest values of CC for the multiplicative error models over two pixels. Three validation events are indicated by black triangles, copula-generated errors indicated by blue symbols, and 49 observed events indicated by orange symbols.

Figure 4.7a shows the correlation matrices of 49 observed errors, Figure 4.7b presents one set of simulated error fields and Figure 4.7c shows the difference between the observed and simulated precipitation error fields using the t-copula model (based on additive error model). Furthermore, Figure 4.7d displays the correlation matrices of 49 precipitation observed errors, Figure 4.7e shows one set of simulated errors and Figure 4.7f shows the difference between the observed and simulated precipitation error fields using the t-copula model (based on the multiplicative error model). It may be noted that there is a robust spatial correlation of error using the additive error model in comparison with the multiplicative error model. However, as may be seen in Fig. 4.7, there is scatter in correlation variation among different pair pixels and the estimated values become more biased, likely due to sample-size effect (Habib et al., 2001).

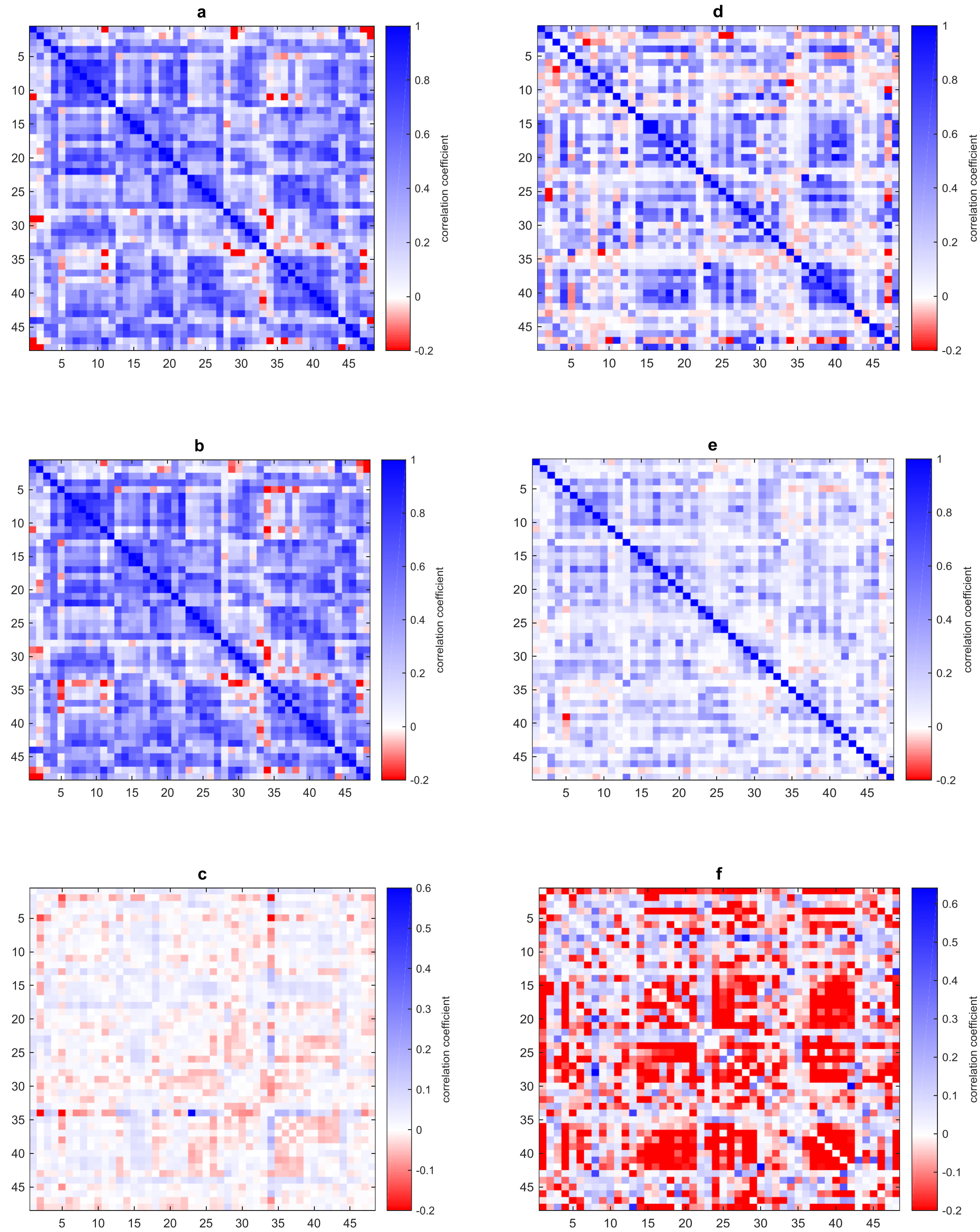

Figure 4.7. CC matrix values of error among 48 IMERG pixels corresponding to 49 a) observed, b) one thousand simulations, c) difference between the observed and simulated precipitation error fields for the additive error model, and d) observed, e) one thousand simulations and f) difference between the observed and simulated precipitation error fields for the multiplicative error model.

Generally, one can argue that a reasonable representation of dependence structure may be required to generate an ensemble of precipitation data with similar dependence structures as that of the precipitation estimates. However, it may not be possible to obtain multiple generated precipitation fields with the exact correlation matrix as that of the original field data. Nonetheless, in accurate models the general dependence structure of the simulated fields should be similar to the dependence structure of the observed precipitation fields. The reason for this is that if some neighboring pixels show high dependence in the precipitation map, the same pixels in the simulated precipitation fields should also exhibit a similar form of dependence.

The presented model is also evaluated with respect to the distribution function of the OSPE and EASPE. Figure 4.8a-b show the empirical CDF of the daily gauge measurements (blue), OSPEs (green) and EASPEs (red). As shown in Figure 4.8a, the CDF of the gauge measurements is closer to the CDF of the $EASPE_{add}$ compared with OSPE, particularly for light/moderate precipitation, and after the 68% frequency level, the CDF of $EASPE_{add}$ is moving above the gauge's CDF. Moreover, the OSPE's CDF is well above that of the gauge precipitation. In contrast, as may be seen in Figure 4.8b, the result shows that the CDF of rain-gauges' precipitation up to the 60% frequency level when the precipitation rate is 7 mm, lies below those of the OSPE and $EASPE_{mlt}$ while beyond the 60% frequency, the $EASPE_{mlt}$'s CDF would be almost the same as that of the gauge CDF. In addition, this result shows an overestimated frequency of precipitation by OSPE, $EASPE_{add}$ when the precipitation rate is above ~ 8 mm and $EASPE_{mlt}$ before the precipitation rate is around 7 mm.

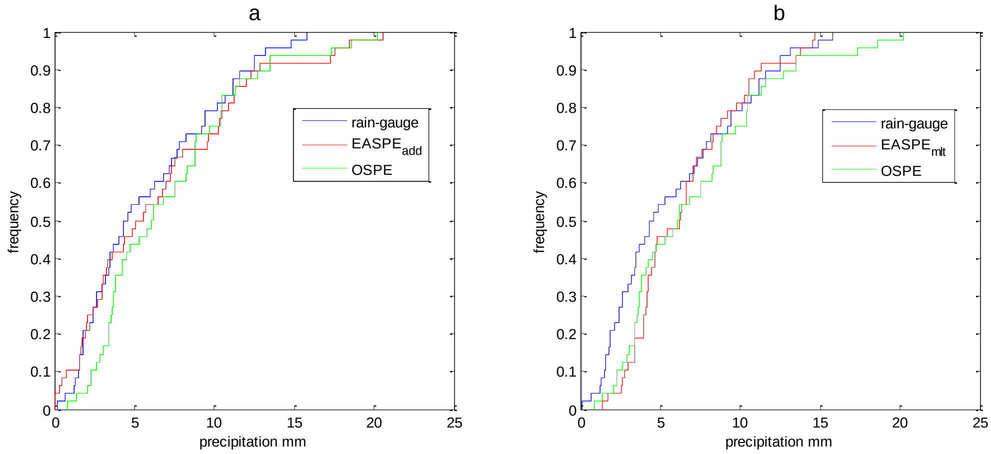

Figure 4.8. Empirical CDF of daily precipitation for rain-gauges, OSPE and EASPE corresponding to a) additive and b) multiplicative error models.

4.6.3 Copula-based uncertainty analysis and assessing suitability of error models

The reliability of the copula-based error adjustment model proposed in this study is evaluated for three daily precipitation events that were not used in the ensembles simulation. For this purpose, an appropriate set of generated errors (among all 49 events) was imposed on the OSPE associated with the three events in order to simulate three EASPE ensembles. It is noted that the average values of the *P*- and *d-factors* for the selected set of generated errors were 79% and 0.36 for the additive error model, and 67% and 0.21 for the multiplicative error model, respectively (see Table 4.1). As Figure 4.9 illustrates, for each event, the simulated ensemble is compared with the station observations. In Figure 4.10a and Figure 4.10b, the average values of the Bias and RMSE of the three validated events over each pixel are illustrated. In addition, the error values associated with the validated events in each pixel for both error models are exhibited in Appendix Table C.1. The OSPE and EASPE error indices were obtained in comparison with the station data. Note that the EASPE indices are computed based on the 50% quantile of simulated ensembles. Clearly, the indices are improved after error adjustment of the satellite estimates.

In Figure 4.9, solid blue lines, solid red lines, gray areas, and solid green lines denote the OSPEs, the station precipitation, the 60 PPU and 75 PPU bands corresponding to additive and multiplicative error models of simulated realizations of EASPEs, and the 50% quantiles of simulated realizations, respectively. As seen in Figure 4.9, the simulated realizations of events 1, 2 and 3 yielded a *P-factor* of 75%, 65% and 98% for $EASPE_{add}$ and 65%, 52% and 83% for $EASPE_{mlt}$, respectively. This figure indicates that the 60 PPU and 75 PPU band of the simulated ensemble bracketed the observed values of 36, 31 and 47 pixels for $EASPE_{add}$ and 31, 25 and 40 pixels for $EASPE_{mlt}$, respectively. Similarly, *d-factor* values of 0.59 and 0.33 for events 2 and 3, respectively, demonstrate reasonable agreement for $EASPE_{add}$. Moreover, the simulations via the additive error model perform much better in comparison with the multiplicative error model. Table 1 also summarizes the averages of bias, RMSE, *P*- and *d-factors* of the three validation events based on additive and multiplicative error models over all 48 pixels. The multiplicative error model produces larger errors for higher precipitation depths, thus leading to unrealistic magnitude for the higher precipitation events. However, for each validation event, there are a number of pixels where observed data fall outside of the simulated ensembles.

Figure 4.10a-b presents the average bias and RMSE values of $OSPE$, $EASPE_{add}$ and $EASPE_{mlt}$, corresponding to three validation events, respectively. These indices are computed for the three daily events over the 48 pixels. It is notable that the values of bias and RMSE associated with the OSRE, and EASPEs are the average values of the three daily events over each pixel. As a result, the estimates from the IMERG satellite product are improved after error-adjustment.

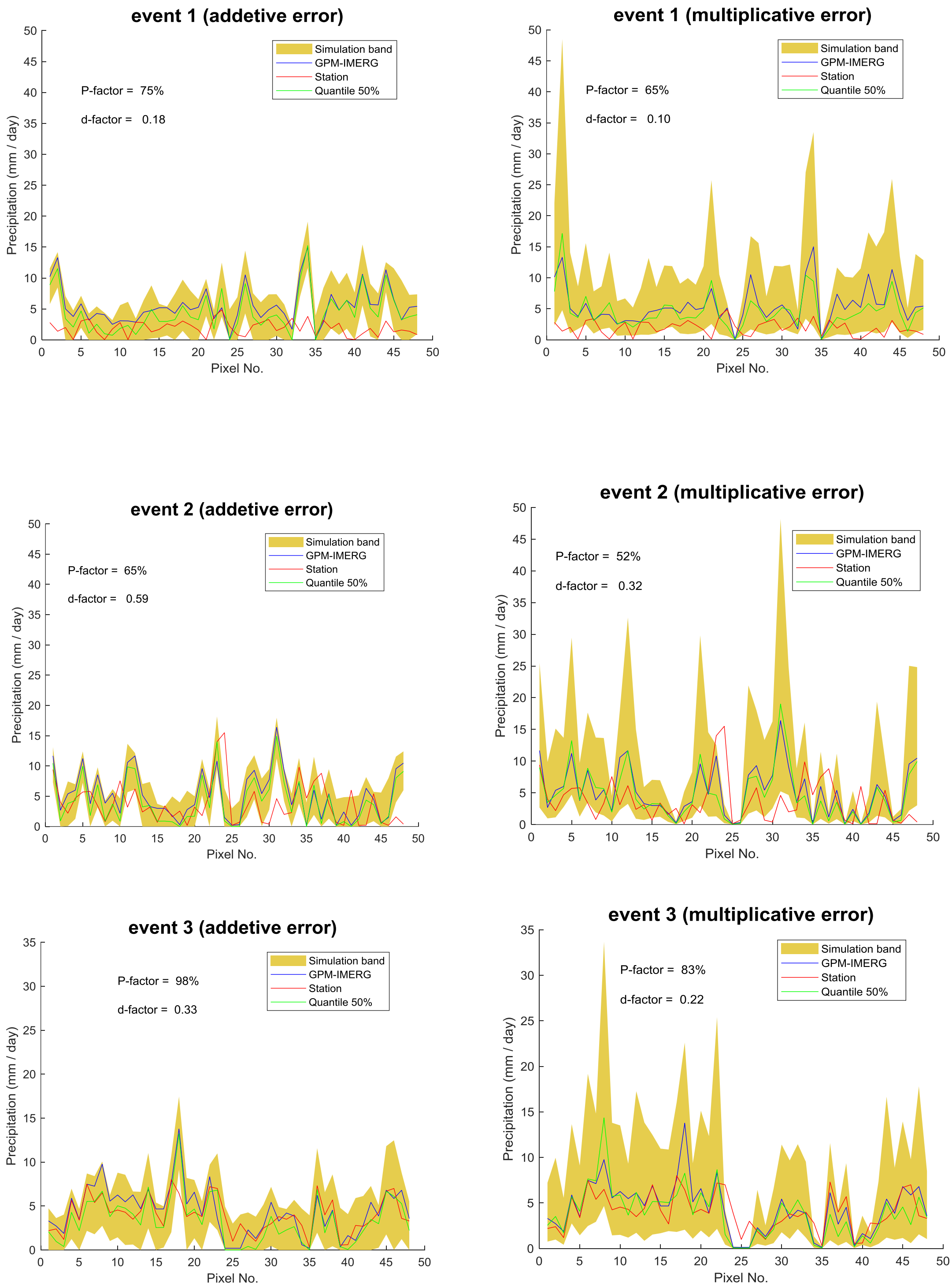

Figure 4.9. Comparison between OSPE (blue line), rain-gauge observations (red line), and 60% and 75% confidence band associated with EASPE (gray band) of the three validated daily events over 48 pixels associated with additive- (left) and multiplicative (right) error models.

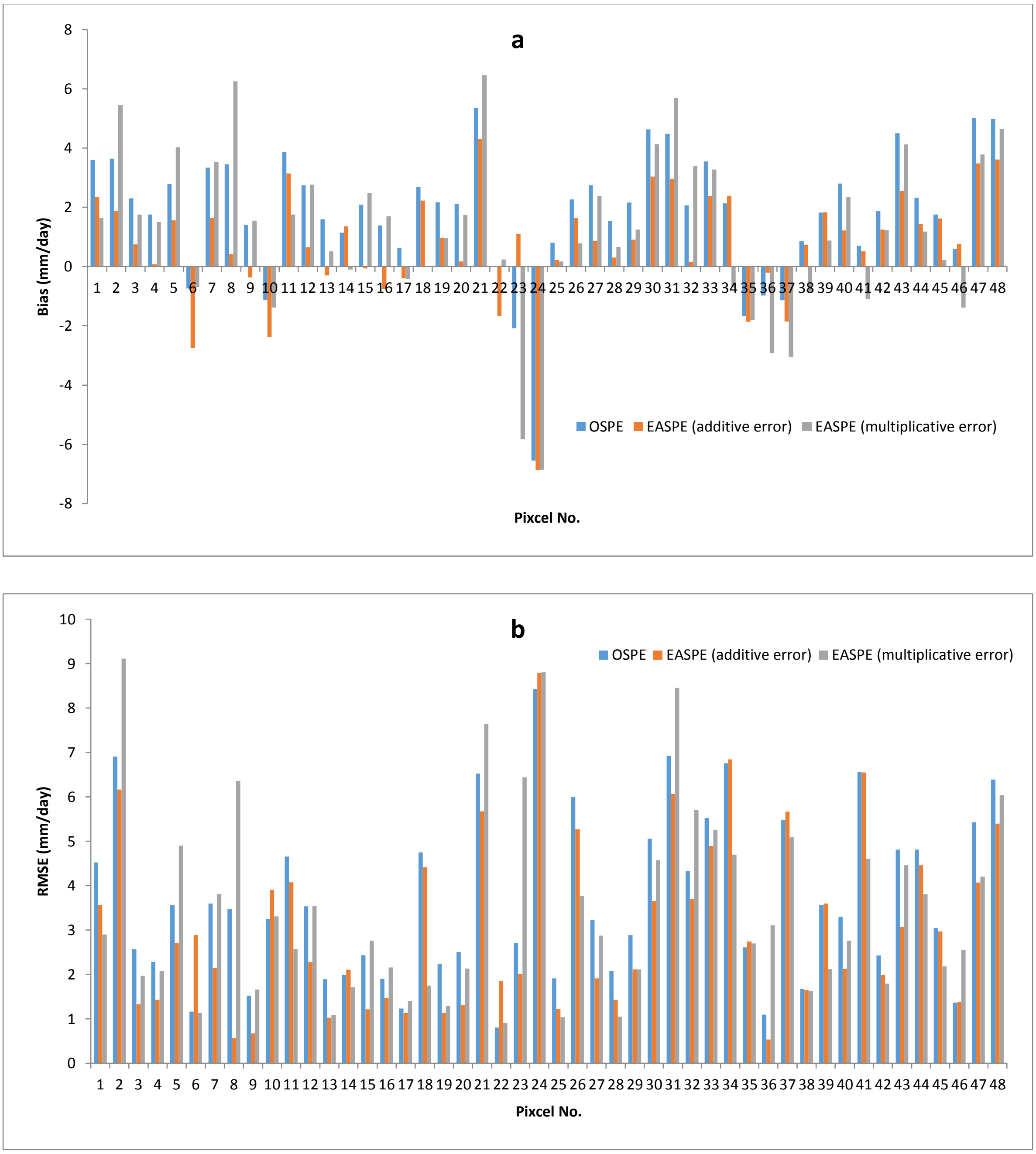

Figure 4.10. Average values of a) Bias and b) RMSE corresponding to OSPE (blue), $EASPE_{add}$ (orange) and $EASPE_{mlt}$ (gray) error models for three daily validation events over each pixel

Table 4.1. Comparison of average statistical indices of three daily validation events over 48 pixels

	Bias mm	RMSE mm	P-factor	d-factor
OSPE	1,82	3,86	-----	-----
$EASPE_{add}$	0,77	3,39	79%	0,36
$EASPE_{mlt}$	1,19	3,89	67%	0,21

4.7 Conclusions

The quantification of precipitation and its spatio-temporal variability is very important for reliable hydro-meteorological modeling. However, there are uncertainties in the precipitation values used as key input data in the models, and these uncertainties will propagate throughout the employed hydro-meteorological models. In-situ observations are often limited over highlands, remote areas and oceans, however, currently available satellite precipitation products can potentially provide the precipitation estimation needed for hydro-meteorological applications. Unlike traditional gauge measurements, remotely sensed precipitation estimates capture the patterns of precipitation spatial variability, although they are subject to various errors from different sources.

One way to assess spatial uncertainty of SPE products is to simulate an ensemble of precipitation fields consisting of a large number of realizations. As precipitation varies over space and time, similarities in the spatial structure between generated and observation fields can be an important feature of precipitation simulation models. Therefore, a copula-based model that preserves the spatial dependency among variables independent of their marginals would be a useful tool in the simulation of multivariate random precipitation fields.

In this study, the uncertainties associated with a high resolution SPE product (IMERG-FR V04) were quantified through a copula-based model linked with additive and multiplicative error models. In order to measure the robustness of the EASPE simulated realizations, *P-* and *d-factors* were computed for each simulated ensemble in light of observed data. Using *P-* and *d-factors,* one can quantitatively predict the uncertainty associated with the EASPEs. Furthermore, since each set of randomly generated errors resulted in an individual pair of *P-* and *d-factors* for simulated ensemble, 49 sets of error fields were generated randomly, while the most suitable set was selected based on the best pair of P- and d-factor values. This procedure may lead to a more accurate simulation of ensembles. Based on Bias and RMSE error indices, the presented framework was able to improve the SPEs considerably. In addition, the validation stage implied that the error-adjusted band of the simulated realizations encompassed the observed data reasonably. Moreover, by fitting the whole data range, the simulations associated with the additive error model performed much better than the multiplicative error model. The results also confirmed that the spatial correlation of error was not negligible. Adequate spatial correlation structures within each ensemble are preserved via the t-copula. In addition, the results demonstrated that the additive error model was superior to the multiplicative error model. Overall, the results presented here indicate that by using a t-copula copula-based model with an emphasis on an additive error model, one can generate multiple realizations of precipitation fields through the simulation of error fields.

It is notable that in the presented copula-based model, instead of fitting a standard distribution function to the data, the empirical CDF of the observed error is applied to the uniformly simulated error values so that the simulated error values will have the same CDF as that of the observed. This avoids the effect of marginal distribution functions on copulas which typically happens when a standard distribution function is fitted (Alidoost et al., 2017). In addition, in ideal situations, more than one gauge per single SPE pixel should be used to provide reliable estimates of the error. Having only one gauge per pixel produces the point-area effect, which may be significant in highly variable events (Habib et al., 2009b). Such a limitation may be addressed through downscaling.

We need to emphasize that the presented model is meant to describe random error (stochastic sources of uncertainty) associated with the SPEs and does not address systematic error (bias) involved in the quantification of precipitation uncertainty. Precipitation data may be subject to physical biases and may require further attempts to remove/correct physical biases (AghaKouchak et al., 2010a).

Moreover, as the number of events decline, the sample size of the observed error decreases. This may, though not necessarily, result in a narrower range of error. One can intuitively conclude that any change in the error range and thus the distribution of error will also affect the estimated uncertainty. In other words, an insufficient precipitation sample size will lead to lower EASPE robustness (Berg et al., 2012; Boé et al., 2007). Another cause might be due to seasonality in the data as well as the precipitation types. Therefore, it is expected that improved accuracy may be warranted in adopting a denser station network and/or using satellite products of finer spatial resolution with longer time series data availability. In addition, rain-gauge measurement errors due to rainfall intensity, wind-induced undercatch, precipitation type and particle falling velocities and the aerodynamic properties of a particular type of gauge could be other causes of uncertainty of SPEs when faired against rain-gauge values. An interesting issue for future research, which may potentially improve the presented framework, is to investigate the dependence of precipitation uncertainty on precipitation regime (e.g., convective, stratiform) in different topographic regions. Finally, the presented models are to be investigated for their robustness and transferability over different time-scales.

Chapter 5

5 Downscaling of Satellite Precipitation Products

This chapter has been submitted as: Sharifi, E., Saghafian, B., Steinacker, R., 2019. Downscaling Satellite Precipitation Estimates With Multiple Linear Regression, Artificial Neural Networks, and Spline Interpolation Techniques. *Journal of Geophysical Research: Atmosphere*, 124, https://doi.org/10.1029/2018JD028795.

5.1 Abstract

Satellite Precipitation Estimates (SPEs) have been widely used in various applications. However, when applied to small basins and regions, the spatial resolution of SPEs is too coarse. In this study, we present three downscaling algorithms based upon the relationships between SPEs and cloud optical and microphysical properties in northeast Austria. Different downscaling techniques, namely multiple linear regression, artificial neural networks and spline interpolation, were adopted for the downscaling of Integrated Multi-satellitE Retrievals for GPM (IMERG) precipitation data. In this respect, linear and non-linear relationship among IMERG data and different cloud variables; such as cloud effective radius, cloud optical thickness, and cloud water path were evaluated. Downscaled SPEs, as well as the original IMERG product, were subsequently validated using 54 rain-gauges at a daily time-scale. According to the results, all downscaled products were more accurate than the original IMERG data. Furthermore, all downscaling techniques captured the spatial patterns of precipitation reasonably well with more detailed information when compared with the original IMERG precipitation. However, the spline interpolation slightly outperformed the other techniques, followed by multiple linear regression and artificial neural network, respectively. Moreover, the proposed methods, which consistently showed increased correlation (e.g., from 0.30 to 0.56 for spline interpolation) and reduced mean absolute error and root mean square error (e.g., from 10.14 to 6.55 mm and 13.5 to 8.76 mm, respectively) for average of all events, can more accurately produce downscaled precipitation data.

5.2 Introduction

Precipitation measurements are traditionally performed using rain-gauges. Rain-gauges are the most reliable source of precipitation observations and are used in most studies as a reference to compare and validate satellite data (Sorooshian et al., 2000). However, they have limited and irregular spatial coverage. Ground-based radar systems are also very valuable, but are not feasible for most developing and less-developed countries due to high upfront cost and maintenance difficulties.

Given a network of rain-gauges, regional precipitation patterns may be determined using geospatial interpolation techniques. However, interpolation using a sparse rain-gauge network does not reflect the actual precipitation pattern (Steinacker et al., 2006). Accordingly, remote sensing techniques significantly improve our knowledge on spatial and temporal variation of precipitation that enhances the accuracy of hydro-meteorological applications, such as flood and drought forecasting, numerical weather prediction and climatological changes. As a result, Satellite Precipitation Estimates (SPEs) are attractive sources of geospatial data.

The accuracy of SPEs has been assessed at different spatio-temporal resolutions in a number of studies in recent years (Manz et al., 2017; Moazami et al., 2014; Prakash et al., 2016; Sharifi et al., 2016, 2018; Tian et al., 2009). In certain applications, the variability of precipitation is often represented by the precipitation error in space and time. Since precipitation within a region may occur at finer scales compared with the pixel size of satellites, satellite data should be sufficiently accurate before being used as inputs to the hydro-meteorological and water management models (Sharifi et al., 2016). Therefore, downscaling of SPEs is necessary for various applications. Moreover, fine-resolution SPEs can be produced through spatial interpolation techniques which are widely used to produce continuous precipitation surfaces (Dorninger et al., 2008).

Downscaling techniques are classified into statistical and dynamical. Dynamical downscaling relies on a regional climate model (RCMs) or numerical weather model (NWMs) to provide high-resolution precipitation and other climate variables by simulating the physical processes of the coupled land-atmosphere system at the expense of often large computational resources. The resolution in most RCMs ranges from 20 to 60 km. In contrast, statistical downscaling methods aim to model the statistical relationships between small and large-scale covariates (He et al., 2016; Rummukainen, 2010; Tang et al., 2016). In such techniques, auxiliary data (e.g., vegetation index, elevation, and cloud properties) are adopted. A low-resolution image is enhanced to a finer resolution using another higher resolution data product via a regression procedure (Fang et al., 2013; Immerzeel et al., 2009; Park, 2013).

During the last decade, diverse statistical downscaling techniques have been developed with widespread of applications. The analogs and weather typing, weather generators, and regressions are the three categories of the statistical downscaling procedures (Gutiérrez et al., 2013). The regression approach forms an attractive alternative to dynamical downscaling methods due to its simplicity and lower computationally demands. However, it is not yet clear which method provides the most reliable estimates of daily precipitation. Nevertheless, due to high potential for complex, nonlinear, and time-varying input-output mapping, the nonlinear regression methods, such as artificial neural networks (ANNs), raise interest. With respect to ANN, the distinctive structure of the network and the nonlinear transfer function related to each hidden and output node allows ANNs to estimate highly nonlinear relationships even without considering their complex interactions. Moreover, while other regression techniques assume a functional form, ANNs allow the data to define the functional form (Coulibaly et al., 2005; Pasini, 2015).

Most studies for downscaling of low-resolution precipitation products have used topography and a Normalized Difference Vegetation Index (NDVI) as high-resolution auxiliary variables (Immerzeel et al., 2009; Jia et al., 2011). These environmental variables, derived from high-resolution satellite data, are closely related to precipitation only in arid areas where the precipitation patterns are affected by elevation. Timescale is an important downscaling consideration in order to select the auxiliary data type. For example, when using an auxiliary index for the greenness of the Earth’s surface, which represents the vegetation in a certain area, the response of this index to a precipitation event lags on the order of a few weeks (Cheema et al., 2011). Moreover, the region with high precipitation reaches the saturation point and more precipitation does not mean a higher NDVI. Therefore, due to precipitation timescales (i.e., daily and monthly), NDVI is more suitable for downscaling on a monthly basis, whereas using cloud properties might be a suitable means of downscaling and may be investigated at a daily or subdaily scale. In addition, most studies on downscaling for precipitation data have been done on a monthly or yearly scale. This approach neglects to consider short-term, extreme precipitation events which have large implications for local heavy precipitation forecasting. Short-term and extreme precipitation over the ocean and flat terrain is more reliant on local weather conditions (i.e., lifting mechanisms) than on topography and vegetation (Park et al., 2016). On the other hand, precipitation extremes near elevated topography is correlated more closely with topography.

The interactions between cloud properties and precipitation have been studied extensively during the last decade. Kobayshi and Masuda (2009) found considerable scatter from the 1:1 line between cloud optical thickness (COT) and rain rate on a global scale. They indicated that the COT increases with rain rate for weak rain while it is almost independent of rain rate for rain stronger than a few millimeters per hour. vanZanten et al., (2005) showed that higher precipitation rates are not due to a change in shape of the drizzle drop distribution but are mainly caused by more frequent occurrence of larger drizzle drops in the right tail end of the distribution, as a consequence of a higher total number of drizzle drops. There are many factors (e.g., drop size distribution) that specify growing the intensity of a precipitation event, time duration, and the amount of precipitation it will finally produce. In order to precisely determine the amount of precipitation in a precipitation event, assessment of the ratio of large drops to smaller drops is needed. When the cloud water mixing ratio reaches a certain constant value, cloud droplets might transform to raindrops (Berry and Reinhardt, 1974). The COT is a function of the liquid density in and the thickness of the cloud which actually represents the passage of light through the cloud. As cloud thickness and the density of liquid water in the cloud increases, the occurrence of precipitation and its amount is expected to increase (Kobayshi and Masuda, 2009; Platnick et al., 2003). The Moderate Resolution Imaging Spectroradiometer (MODIS) onboard Terra and Aqua satellites, provides unique spectral and spatial capability for retrieving cloud optical properties and it has a number of additional spectral channels, relative to previous generation global imagers, that provide cloud microphysical information. Cloud optical and microphysical properties such as COT, cloud effective radius (CER), and integrated cloud water path (CWP) of both liquid water and ice clouds, are produced for pixels by the cloud mask during the daytime portions of each orbit (Platnick et al., 2015). Ham et al., (2009) evaluated the accuracy of MODIS cloud products. They indicated that the COTs at band 2-4 were reasonably accurate with comparison to observation data. Moreover, when multilayered clouds are present larger errors were observed.

The Global Precipitation Measurement (GPM) mission constellation is implemented as an international satellite mission, and transitioned critical measurements begun by Tropical Rainfall Measurements Mission (TRMM) to fill the gaps of precipitation monitoring from ground-based gauges. One of the attractive precipitation products of this constellation is the Integrated Multi-satellitE Retrievals for GPM (IMERG), which covers 60°N-S latitude with a spatial resolution of 0.1° and it is updated every 30 minutes (Gebregiorgis et al., 2018; Huffman et al., 2015; Huffman et al., 2017a). Although IMERG belongs to the highest spatio-temporal resolution satellite precipitation-based products category, its major limitation might be the spatial resolution of the product, since each pixel represents the mean precipitation over the pixel area.

Since, in our study, there is not a priori relationship between precipitation and cloud optical and microphysical properties, both multilinear and ANN models for regression and spatial spline interpolation techniques have been implemented on the native resolution of the IMERG data (Dorninger et al., 2008; Zheng and Zhu, 2014). Further in this research, the possibilities of using cloud products for downscaling IMERG images are assessed. The idea of using cloud products as auxiliary data for daily downscaling of SPEs is rooted in the idea that there should be a mutual relationship between the existence of clouds and precipitation; in other words, clouds are a prerequisite for precipitation occurrence.

5.3 Study area and data

5.3.1 Study area

To assess the accuracy of SPE data in central Europe, northeast of Austria was selected owing to the fact that this region enjoys a rather high-density gauge network. Fifty-four operating synoptic stations across the study area were used to quantitatively evaluate the presented downscaling scheme in 2015. Moreover, since topography of the region is moderate, the precipitation pattern is not greatly affected by altitude while both stratiform and convective precipitation types do occur. In general, northeast of Austria receives less than 600 mm of average annual precipitation (Figure 5.1).

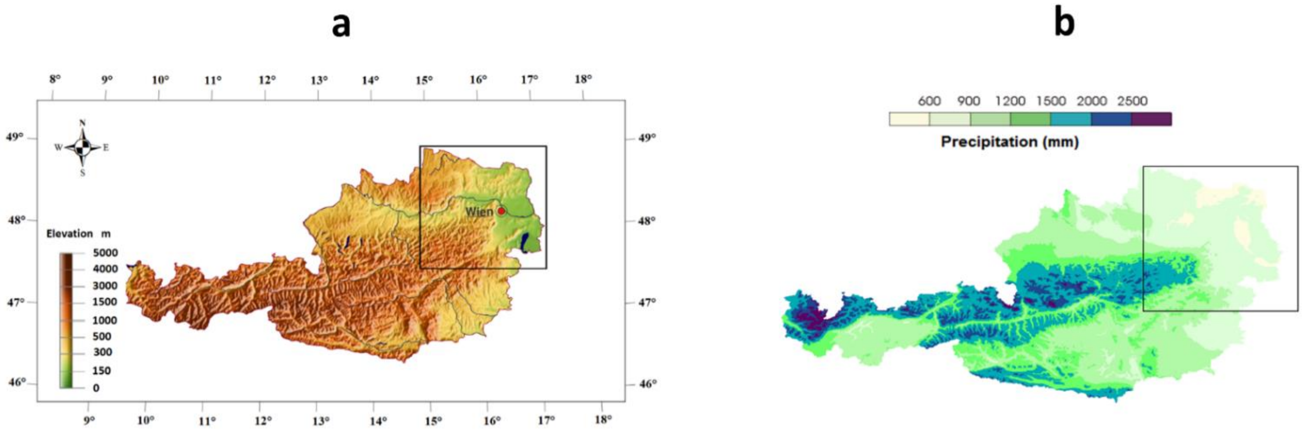

Figure 5.1. a) elevation map of Austria and b) mean annual precipitation map of Austria

5.3.2 Station data

Precipitation data of some 54 in-situ meteorological synoptic stations with 10-min time resolution, provided by the Central Institute for Meteorology and Geodynamics (ZAMG)-Austria, were used in this study. ZAMG operates a network of semi-automatic weather stations across the country and provides quality-controlled precipitation data. These stations (tipping bucket gauges and weighing rain-gauges) are equipped with heating systems (Haiden et al., 2011). To demonstrate the proposed downscaling methodology, five specific heavy precipitation events with the rain intensity above 30 mm/day, which occurred in 2015 over the study area were chosen.

5.3.3 IMERG-FR V05B

The IMERG V05B final-run product is provided by GPM mission's Precipitation Processing System at NASA’s Goddard Space Flight Center. The data set includes precipitation rates with the half-hourly temporal resolution and 0.1º × 0.1º (11 × 11 km) spatial resolution since mid-March 2014. After inter-calibrate, merge and interpolate all constellation microwave and IR-based sensors, this product is calibrated with monthly gauge precipitation data. This process converts these data into a more accurate product relative to the other two early- and late-run products that are calibrated based on climatological monthly gauge data (unlike the final-run). IMERG final-run currently is produced almost 3 months after the date of preliminary records and mainly used for research purposes. Contrary to other satellites, such as TRMM, three critical improvements in GPM, as the core of GPM constellation satellites, are that (1) increased the inclination of nonsun-synchronous orbit from 35º to 65º, affording coverage of important additional climate zones; (2) the radar aboard the GPM satellite has been upgraded and composed of two precipitation radars (Ku-band [13.6 GHz] and Ka-band [35.5 GHz]), increased sensitivity for light rain and snowfall; and (3) GPM Microwave Imager (GMI) has been equipped with higher frequency channels (165.5 and 183.3 GHz), which are expected to improve the estimation accuracy of light and snow. Moreover, the preliminary analysis of the IMERG product for detecting heavy precipitation events at a daily time scale showed a considerable improvement over TMPA as compared to rain-gauge observations. The users can freely access the data sets from NASA Goddard Earth Sciences Data and Information Services Center (GES DISC) website. Interested readers are referred to Huffman et al., (2015c; 2017b) for more information.

5.3.4 MODIS

MODIS on Terra and Aqua satellites is a Level 2 product that provides unique spectral and spatial capability for retrieving cloud optical and microphysical properties by merging both infra-red and visible techniques in order to measure different cloud properties. One to four images may be available daily. This product (MOD06 and MYD06 for Terra and Aqua MODIS, respectively) which combines infrared and visible techniques consist of pixel-level retrievals of both cloud physical and optical properties (optical thickness, effective particle radius and water path for both liquid water and ice clouds) with spatial resolutions ranging from 1 to 5 km (Platnick et al., 2015). These high-resolution cloud parameters (1 km) obtained from solar reflectance channels (Cloud Optical Properties and Cirrus Reflectance).

The first and second MODIS instruments were launched aboard Terra (1999) and Aqua (2002) platforms respectively. In the morning Terra passes from north to south, while in the afternoon Aqua passes from south to north across the equator. The entire Earth's surface can be observed through the MODIS instruments onboard both Terra and Aqua every 1 to 2 days, obtaining data from different wavelength (36 spectral bands) ranging from 0.4 to 14.4 µm. The aim to design the twin-MODIS was to enhance cloud imaging, particularly during the morning and afternoon sunlight by reducing the optical effects of shadows and glare that occur within these times. The data are freely accessible to users from the Level 1 and Atmosphere Archive & Distribution System (LAADS) website[4].

5.4 Methodology

During the last several years, numerous statistical downscaling techniques have been developed at the regional scale to downscale the satellite-based precipitation dataset. The downscaling algorithms, that being marked by a favorable outcome, have improved the spatial resolution mainly on the basis of relationships between precipitation and for example, cloud top temperature, NDVI and elevation as predictors (Verlinde, 2011). The multiple linear regression (MLR) and ANN models have mainly performed well in different climatic and topographic regions by using various combinations of predictors. Along with the aforementioned models, spline interpolation technique is employed to downscale the IMERG data. In this study, these statistical techniques for downscaling SPEs are conducted and validated against rain-gauges (Retalis et al., 2017; Schoof and Pryor, 2001; Shi et al., 2015; Xu et al., 2015). The approach is based upon the assumption that the statistical relationship between the cloud optical and microphysical predictive variables and precipitation at a coarse scale is maintained at a finer scale to generate more detail in the precipitation grids. In order to find a regression relationship between the 1-km cloud properties and the 0.1° (approximately 11-km) IMERG precipitation data, the cloud property variables were consistently resampled using the bilinear technique in order to match the IMERG native grid size (Gharabeigli, 2013). Consequently, the statistical relationships between original IMERG precipitation estimates and cloud variables at a coarse scale were derived via ANN and MLR models.

The overall MLR model may be written as follows:

$$P = a + x_1 * COT + x_2 * CER + x_3 * CWP \tag{5.1}$$

where P is predicted precipitation , a is intercept value and x_1, x_2 and x_3 are the estimated regression coefficients of respective variables.

[4] https://ladsweb.modaps.eosdis.nasa.gov/search/order/1/MOD06_L2--61

While linear regressions are dominant, non-linear methods, such as ANN, have also been applied. ANNs are information processing systems that are inspired by the way biological neural networks, such as the brain. ANNs have the ability to model the complex relationships that exist between input and output by simulating human learning. The basic processing elements of an ANN are the neurons. A neuron has five components including: input, weight, summation function, activation function, and output. Weights interconnect the neuron units to form a network. The multi-layer ANN model is typically composed of three parts: input, one or more hidden layers, and one or more output layers (Alexakis and Tsanis, 2016; Lee and Evangelista, 2006; Vu et al., 2016). The weights, adjust as learning proceeds, are connections between neurons. The neurons then apply activation functions to the sum of weighs that might be linear or non-linear algebraic functions. Neural networks provide a learning rule for modifying their weights and neurons based on the input/output patterns. A particular output is derived when a pattern is provided to the network so that weights and neurons are adjusted. During the last years, ANNs have been used for variety of tasks such as spatial data interpolation to overcoming some challenges presented by traditional techniques (Rigol et al., 2010).

In general, ANN may be mathematically presented as follows:

$$Network_j \; = \sum_{k=1}^{n} w_{kj} O_k^j \tag{5.2}$$

where w_{kj} and O_k^j are matrices of weights between nodes *k* and *j* associated with inputs to the node and outputs, respectively.

The activation function, such as a nonlinear sigmoid function, is applied to hidden as well as to output layers of a neural network. The output is then fed to other units linked to it. In this study, training that determines the weights of the network was carried out via feed forward back-propagation. A set of examples of associated input (COT, CER, and CWP) and output (IMERG) values are used to train the network by the back-propagation training algorithm. In this algorithm, if desired output is not satisfactory, weights between layers are modified until the error is minimal (Sen et al., 2008). A three-layer network consisting of an input layer (three neurons), one hidden layer (number of neurons are differing from case to case) and one output layer was used as a network structure.

The ANN model in this study is implemented through the following steps:

1) The inputs and the output (P_11km) data were randomly divided into three subsets: 70% comprise the training subset, 15% the validation subset, and the remaining 15% for testing subset.
2) Various ANN architectures with one hidden layer were designed and examined.
3) The back-propagation algorithm trains the network by the gradient descent optimization algorithm to adjust the weight of neurons between the output and the target (IMERG) values of the network. The network used a feed-forward procedure for the entire data set, after the completion of the training.
4) The model producing the highest performance (i.e. the model with the minimum mean square error) was selected.

It is notable that there is no universal form for building ANNs such that each network should be investigated individually. For example to explore how many nodes are needed to downscale each daily precipitation event the specific network should build/examine based on the particular input/output variables (Retalis et al., 2017). However, the presented ANN model was produced in MATLAB software. The MATLAB users are able to import, create, and export data and neural networks. The properties of the Network used in this study are as follows:

- Network inputs: COT, CER and CWP
- Network target: IMERG
- Network type: Feed-Forward Back-Propagation
- Training function: TRAINLM
- Adaption learning function: LEARNGDM
- Performance function: Mean Square Error (MSE)
- Number of hidden layers: 1

A scheme of a network used in this study is presented in Figure 5.2.

For detailed information of ANN, interested readers are referred to Lee and Evangelista (2006) and deep learning documentation with MATLAB.

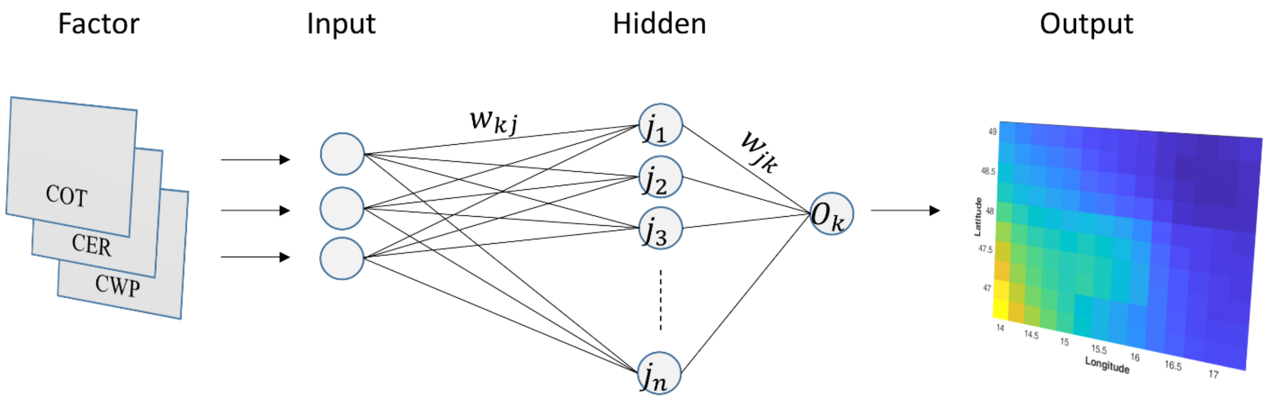

Figure 5.2. Architecture of a multi-layer feed-forward back-propagation with 3 input layer, 1 hidden layer and 1 output layer

5.4.1 Downscaling model

As part of precipitation variability may not be explained by the ANN and MLR models, the difference between the predicted values (P_{11km}) and the original $IMERG_{11km}$ values were spatially interpolated to form residual maps at 1-km resolution using a bilinear resampling technique (Alexakis and Tsanis, 2016; Gharabeigli, 2013; Park, 2013). By adding the residuals at 1-km resolution to the predicted terms, one obtains the following:

$$Residual_{11km} = IMERG_{11km} - P_{11km} \tag{5.3}$$

$$P_{1km-Res} = P_{1km} + Residual_{1km} \tag{5.4}$$

Then, spline interpolation is applied to both $P_{1km-Res}$ derived from ANN and MLR techniques to produce the final downscaled product (P_{final}) from pixel to point.

The effectiveness of downscaling method was measured via the following metrics: the root mean squared error (RMSE), bias, the mean absolute error (MAE), the correlation coefficient (CC), as well as the index of agreement (IA) which is a standardized measure of the degree of model performance and evaluates measured observation against model performance. The range of this skill varies from 0 to 1, and the perfect score is 1, which indicates perfect agreement.

$$RMSE = \sqrt{\frac{1}{N}\sum_{i=1}^{n}(P_{S_i} - P_{O_i})^{\,2}} \quad (mm) \tag{5.5}$$

$$Bias = \frac{\sum_{i=1}^{n}(P_{S_i} - P_{O_i})}{N} \quad (mm) \tag{5.6}$$

$$MAE = \frac{\sum_{i=1}^{N} |P_{S_i} - P_{O_i}|}{N} \ (mm) \tag{5.7}$$

$$CC = \frac{\sum_{i=1}^{N}(P_{S_i} - \overline{P}_S)\,(P_{O_i} - \overline{P}_O)}{\sqrt{\sum_{i=1}^{N}(P_{S_i} - \overline{P}_S)^{2}}\ \sqrt{\sum_{i=1}^{N}(P_{O_i} - \overline{P}_O)^{2}}} \tag{5.8}$$

$$IA = \quad 1 - \frac{\sum_{i=1}^{n}\left(P_{S_i} - P_{O_i}\right)^2}{\sum_{i=1}^{n}\left(|P_{S_i} - \overline{P_O}| + |P_O - \overline{P_O}|\right)^2} \tag{5.9}$$

where P_{S_i} and P_{O_i} are the value of SPEs and the value of rain-gauge observations, respectively, *i* is the index of the station number and N the total number of stations, $\overline{P}_S$ and $\overline{P}_O$ are the average value of SPEs and rain-gauge observations for *N* stations over the study area.

It should be noted that the analyses were carried out for five daily heavy precipitation events in 2015 over 54 IMERG pixels in the study area.

The presented downscaling scheme is shown in Figure 5.3.

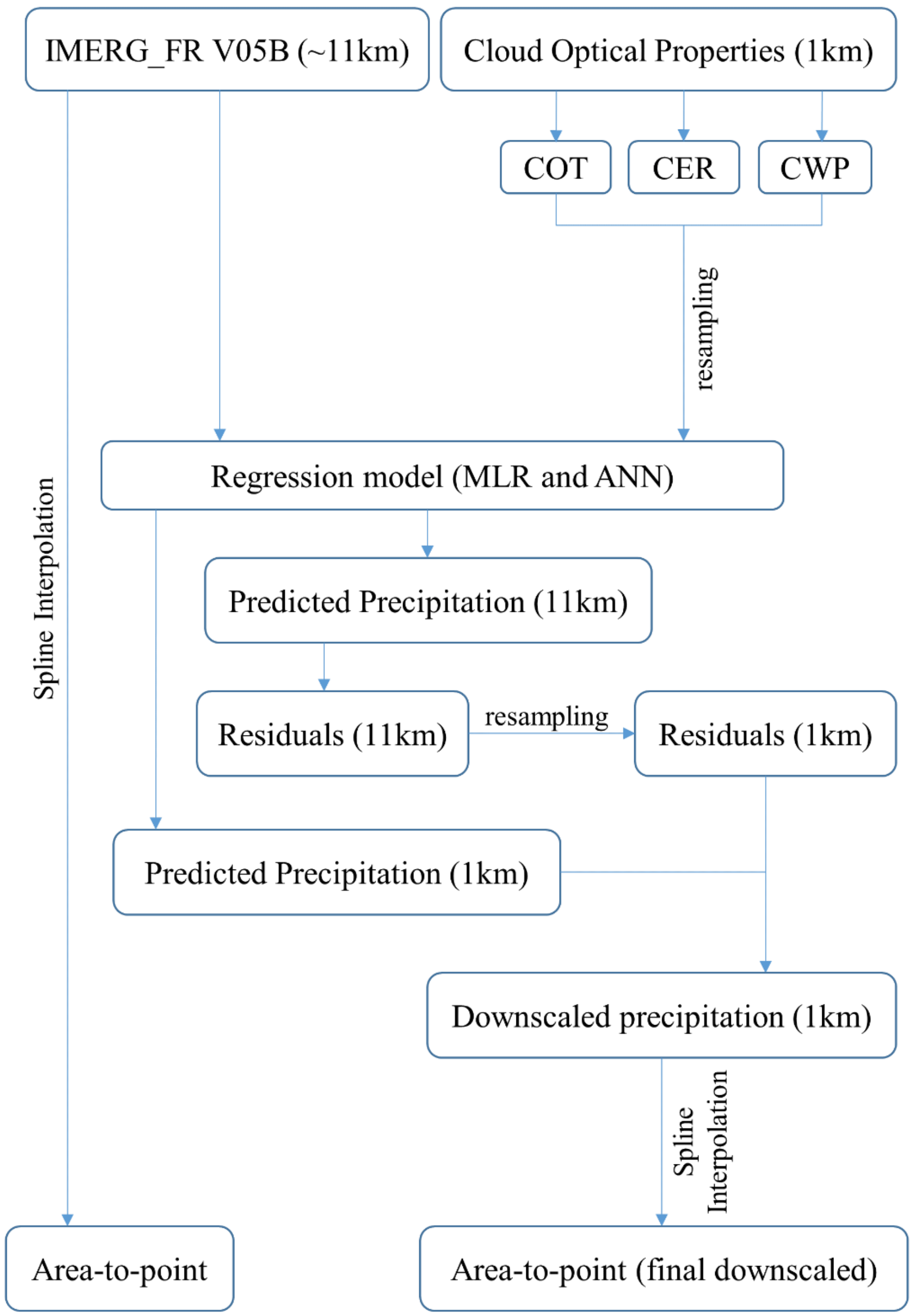

Figure 5.3. Workflow for statistical downscaling of coarse IMERG precipitation data

5.5 Results and discussions

In this study, a hybrid downscaling method was formed using regression MLR and ANN models with residual correction. First, linear and non-linear regression analysis was applied to derive statistical relationships between precipitation and three cloud variables at original IMERG resolution. For this analysis, COT, CER, and CWT were upscaled to 0.1° resolution via bilinear resampling. The downscaling method was based on the assumption that the models (ANN and MLR) correlating the IMERG precipitation with cloud properties at coarse spatial scale (0.1° × 0.1°) are equally effective at fine scale (1 km × 1 km; Jing et al., 2016; Zhang et al., 2018). Besides regression models, spline interpolation as a common precipitation spatial interpolation technique was implemented on IMERG native spatial resolution.

The regression model in northeast Austria revealed a meaningful and significant relationship between IMERG and cloud variables. A p-value of less than 0.05 indicates that one may reject the null hypothesis. It should be noted that with respect to the MLR model, in some events, CWP did not show a relationship with precipitation; therefore, for those events CWP was not involved in the MLR model.

The downscaled results were validated using observation records of 54 rain-gauges over the study area for five heavy precipitation events in 2015. The downscaled results before and after residual correction were also validated to assess the impact of residual correction. After validation, predicted precipitation at fine scale corresponding to MLR, ANN and spline spatial interpolation, before ($P_{1km}MLR$ and $P_{1km}ANN$) and after ($P_{final}MLR$ and $P_{final}ANN$) residual corrections, proved to have varying accuracy. All downscaling approaches, as well as the original IMERG data, were compared against the rain-gauges observations. The results of linear and non-linear regression models are presented in Table 5.1, and Figs. 4-8. The residual maps indicate the areas where part of the precipitation cannot be solely explained by cloud variables. Negative residual values depict areas where influence of some of the variables is more than expected.

Although the results of downscaling methods after residual correction were rather close, some differences were observed among events. Table 5.1 shows the Bias, MAE, RMSE, CC and IA estimated by different models for each individual and the average of all the events. On average, Original IMERG yielded the highest bias (6.06 mm), MAE (10.14 mm) and RMSE (13.50 mm). Spline interpolation, $P_{final}MLR$ and $P_{final}ANN$ models produced on average the lowest bias, MAE, RMSE and the highest CC and IA, respectively.

Table 5.1. Evaluation statistics for the downscaled models for five daily heavy precipitation events over northeast Austria

		17/04/2015	23/05/2015	03/09/2015	25/09/2015	07/10/2015	**Average**
IMERG	**Bias (mm)**	2.27	-10.84	-8.98	9.85	-1.29	6.06
Spline		1.82	-7.67	-4.28	-0.31	-7.90	1.82
$P_{final}ANN$		2.25	-8.82	-3.88	2.52	-4.64	2.38
$P_{final}MLR$		-1.36	-7.88	-4.29	-0.20	-7.63	-1.36
$P_{1km}MLR$		-0.15	-10.99	-3.58	2.55	3.39	1.93
$P_{1km}ANN$		0.59	-12.20	-2.39	0.82	1.60	1.1
IMERG	**MAE (mm)**	4.26	12.58	9.86	13.07	10.96	10.14
Spline		3.93	10.68	5.39	4.83	7.93	6.55
$P_{final}ANN$		4.98	11.21	5.75	12.86	7.90	8.54
$P_{final}MLR$		4.03	10.92	5.68	5.09	9.83	7.11
$P_{1km}MLR$		4.65	12.08	8.08	9.60	8.88	8.66
$P_{1km}ANN$		5.28	13.07	7.26	14.41	10.29	10.06
IMERG	**RMSE (mm)**	6.28	15.15	12.97	17.37	15.76	13.50
Spline		5.72	12.77	7.74	7.17	10.40	8.76
$P_{final}ANN$		6.74	13.60	7.92	17.84	10.07	11.24
$P_{final}MLR$		5.53	13.09	7.97	7.20	12.13	9.18
$P_{1km}MLR$		6.07	15.13	10.47	11.73	14.09	11.50
$P_{1km}ANN$		7.12	15.91	9.45	20.37	12.45	13.06
IMERG	**CC**	0.65	0.51	0.25	0.16	-0.07	0.30
Spline		0.67	0.43	0.73	0.75	0.20	0.56
$P_{final}ANN$		0.56	0.43	0.69	0.13	-0.01	0.36
$P_{final}MLR$		0.66	0.42	0.71	0.75	-0.07	0.49
$P_{1km}MLR$		-0.15	0.15	-0.05	-0.01	-0.02	-0.02
$P_{1km}ANN$		0.14	0.19	0.30	0.15	-0.04	0.15
IMERG	**IA**	0.75	0.57	0.51	0.46	0.26	0.51
Spline		0.78	0.59	0.79	0.83	0.47	0.69
$P_{final}ANN$		0.70	0.58	0.78	0.44	0.40	0.58
$P_{final}MLR$		0.78	0.58	0.78	0.83	0.39	0.67
$P_{1km}MLR$		0.15	0.47	0.36	0.27	0.19	0.29
$P_{1km}ANN$		0.47	0.47	0.50	0.44	0.37	0.45

As far as validation is concerned, the RMSE values associated with $P_{final}MLR$ and $P_{final}ANN$ models ranged from 5.53 to 13.09 mm and 6.74 to 17.84 mm, respectively for 03.09.2015 as an example. Concerning bias, in a few cases values were negative, indicating precipitation underestimation. Among the models that were used to downscale IMERG product, spline interpolation and $P_{final}MLR$ seem to outperform $P_{final}ANN$ with mean CC values of 0.56, 0.49 and 0.36, respectively. In contrast to traditional statistical method and spline interpolation, $P_{final}ANN$ provides higher bias on average (2.38 mm). Regarding bias validation, all models resulted in positive values on average (except $P_{final}MLR$), meaning that precipitation is generally overestimated. In northeast Austria, $P_{final}ANN$ has optimal performance in terms of bias only for the 03.09.2015 and 07.10.2015 events in comparison with $P_{final}MLR$ and spline interpolation (Table 5.1).

Figure 5.4 and Figure 5.5 show the downscaled results using three algorithms over the study area, in the case of the 03.09.2015 event. The original IMERG-FR V05B and spline interpolation are also displayed to compare each of the ANN and MLR methods to them (Figure 5.4a-b and Figure 5.5a-b). The results of MLR and ANN before residual correction (Figure 5.4c and Figure 5.5c respectively) show significantly different spatial distribution patterns compared to that of the original IMERG, whereas the final downscaled results of MLR, ANN and spline interpolation have spatial distribution patterns similar to that of the IMERG.

The residuals were calculated using the approach described previously. Figure 5.4d and Figure 5.5d show the residuals for MLR and ANN respectively. The spatial distribution of the residuals corresponding to MLR and ANN models indicate that they tend to underestimate IMERG precipitation over the northwestern and slightly overestimate over the southeastern regions of the study area. The residual of both models had similar distribution patterns.

Figure 5.4f and Figure 5.5f show the downscaled precipitation after residual correction based on MLR and ANN algorithms respectively. These were obtained by adding the high resolution predictive (P_{1km}) daily precipitation data (Figure 5.4e and Figure 5.5e) to the high resolution residual obtained above. Compared to the predicted results without residual correction (Figure 5.4e and Figure 5.5e), the downscaled results after residual correction (Figure 5.4f and Figure 5.5f), are more likely to show a spatial distribution pattern similar to that of the original IMERG (Figure 5.4a and Figure 5.5a). Consequently, to reach the optimum scale and increase the resolution of downscaled precipitation from area-to-point, the spline interpolation technique was applied to obtain the final downscaled precipitation data $P_{final}MLR$ and $P_{final}ANN$ (Figure 5.4g and Figure 5.5g).

Higher precipitation values were particularly observed mainly in the northwestern parts while lighter precipitation was detected in southeast of the study area. Downscaled IMERG product relying on cloud optical and microphysical predictive variables could reasonably describe the spatial patterns of precipitation with sufficient detail when compared with the original IMERG precipitation.

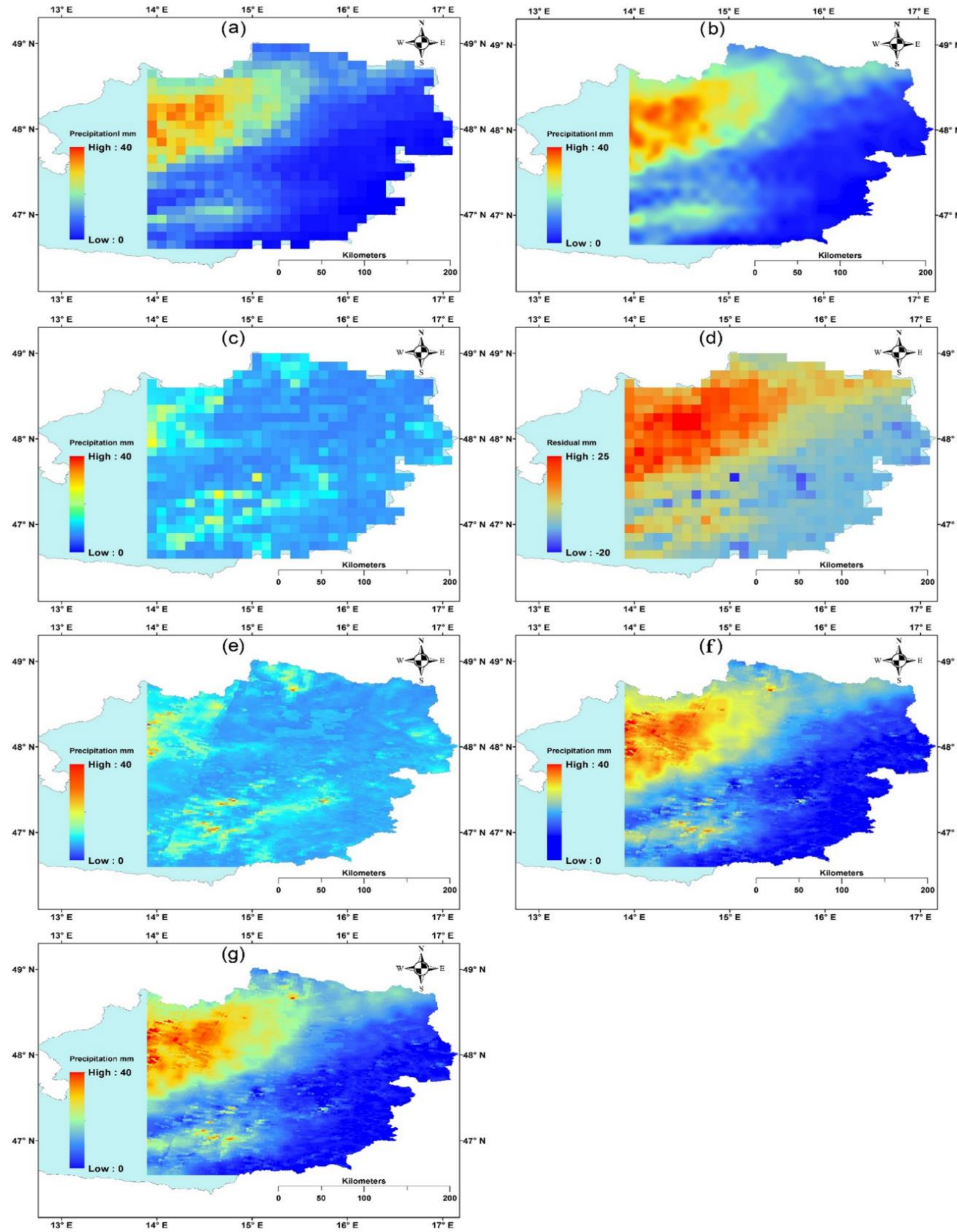

Figure 5.4. a) Original IMERG, b) Spline interpolation, c) predicted precipitation based on MLR (P_{11km}), d) $Residual_{11km}$ e) predicted precipitation (P_{1km}), f) downscaled residual corrected and g) final downscaled precipitation for 3 September 2015 event over northeast of Austria

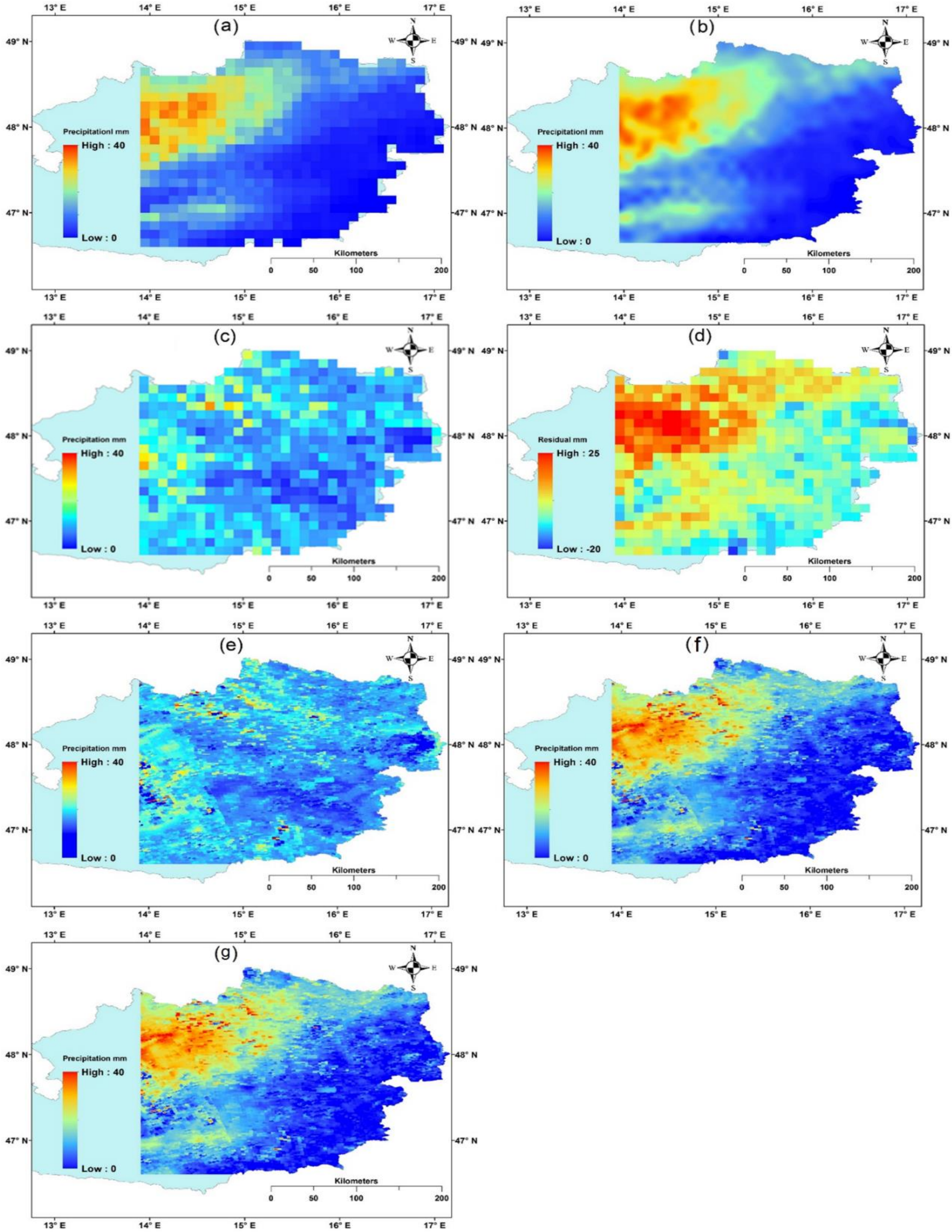

Figure 5.5. a) Original IMERG, b) Spline interpolation, c) predicted precipitation based on ANN (P_{11km}), d) $Residual_{11km}$ e) predicted precipitation (P_{1km}), f) downscaled residual corrected, and g) final downscaled precipitation for 3 September 2015 event over northeast of Austria

The overall model performance (spline, $P_{final}MLR$ and $P_{final}ANN$) was almost similar. In all cases, significant improvements (in terms of spatial distribution) were achieved, such that the downscaled product could capture the precipitation pattern around the alpine mountains in the northwestern area.

However, from Figure 5.5f and g, it is evident that the spatial distribution of precipitation by ANN downscaling contained systematic anomalies, with values clearly greater than neighboring area, included more variations and a lager portion of the errors compared with neighboring pixels. However, the MLR and spline interpolation downscaled results showed continuous spatial variations with a gradual trend without outliers. This indicates that probably, in extreme cases, the ANN model fails to place the precipitation in the correct area (Retalis et al., 2017).

5.5.1 Validation Analysis

Figure 5.6 and Figure 5.7 display the scatterplots and quantitative comparison of each algorithm respectively, before and after residual correction, between observed gauge data (reference object), original IMERG and downscaled daily precipitation corresponding to the 03.09.2015 event. As seen in Figure 5.6a, IMERG has difficulty in estimating higher precipitation values, while the precipitation spatial pattern is mostly unaffected by complex terrain. Spline interpolation, $P_{final}MLR$ and $P_{final}ANN$ performed much better with improved CC, MAE, RMSE and IA values over the original IMERG. The lower bias of $P_{1km}MLR$ and $P_{1km}ANN$ compared to other models is caused by the cancelation of positive/negative values (Figure 5.6c and d). The original IMERG indicated relatively low CC values and points scattered far from the 1:1 line. Moreover, it tended to highly underestimate daily precipitation (Bias = -8.98 mm), while other downscaled models produced smaller underestimation. This indicates that the residual correction model can effectively improve the CC, RMSE, Bias, MAE and IA and smooth out extreme precipitation. Such a conclusion is supported by the average results of all events shown in Table 5.1.

According to the validation results, spline interpolation was the most accurate (CC = 0.73, MAE = 5.39 mm, RMSE = 7.74 mm) compared with the other algorithms. The $P_{final}MLR$ algorithm ranked second with CC = 0.71, MAE = 5.68 mm and RMSE = 7.97 mm, the

$P_{final}ANN$ followed (CC = 0.69, MAE = 5.75 mm, RMSE = 7.92 mm), while ANN and MLR before residual correction ($P_{1km}MLR$ and $P_{1km}ANN$, respectively) produced the poorest results (Figure 5.6c and d). In general, significant improvement was achieved by residual correction.

However, according to Figure 5.7, original IMERG significantly underestimates precipitation and predicts some no-precipitation events despite rain-gauges recording precipitation, while other downscaled products slightly underestimate. In addition, $P_{1km}MLR$ reported rather uniform precipitation over the area. This may be partially due to the fact that the residual correction algorithms smooth the precipitation events by identifying more no-precipitation as precipitation events and consequently reducing the magnitude of extreme precipitation events.

In order to determine which downscaled model better estimates precipitation over the study area, a Taylor diagram was plotted for all events (Taylor, 2001). For each individual event, the final downscaled results were well correlated with the observations, as evidenced in their respective Taylor diagram (Figure 5.8).

Smaller distances between the in -situ observation as reference, lie on the x- axis and downscaled precipitation patterns on a Taylor diagram indicate a closer agreement. As shown in Figure 5.6Figure 5.8, spline, $P_{final}MLR$ and $P_{final}ANN$ predicted results are much closer to the observed values compared with the original IMERG, $P_{1km}MLR$, and $P_{1km}ANN$. This indicates that the residual-corrected models and spline interpolation with higher CC and lower RMSE are clearly superior to other models.

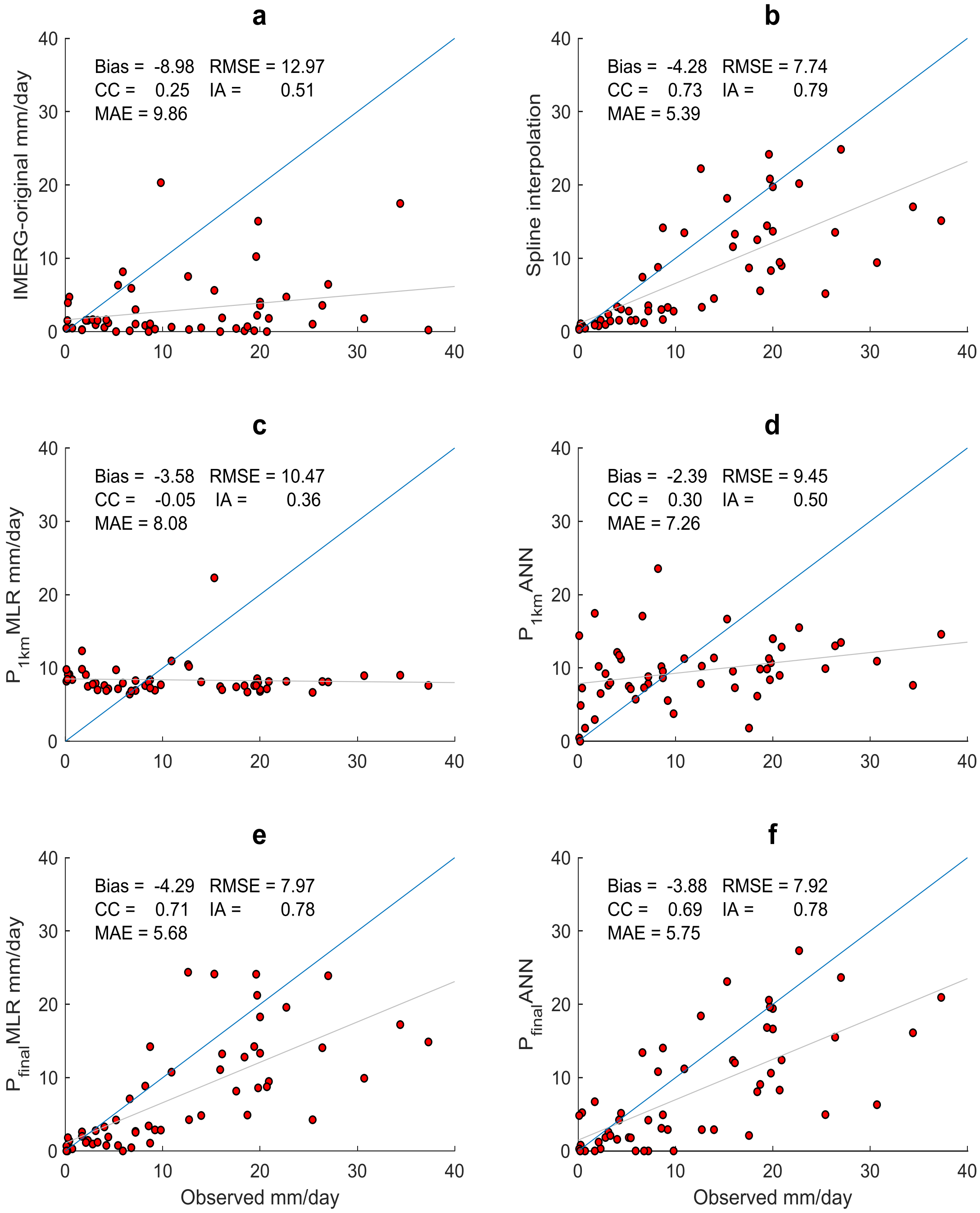

Figure 5.6. Scatterplots for (a) original IMERG, (b) spline interpolation technique, (c and d) predicted precipitation by MLR and ANN regression model ($P_{1km}MLR$ and $P_{1km}ANN$, respectively) before residual correction and (e and f) final downscaled precipitation after residual correction (MLR and ANN, respectively) for 3 September 2015. event.

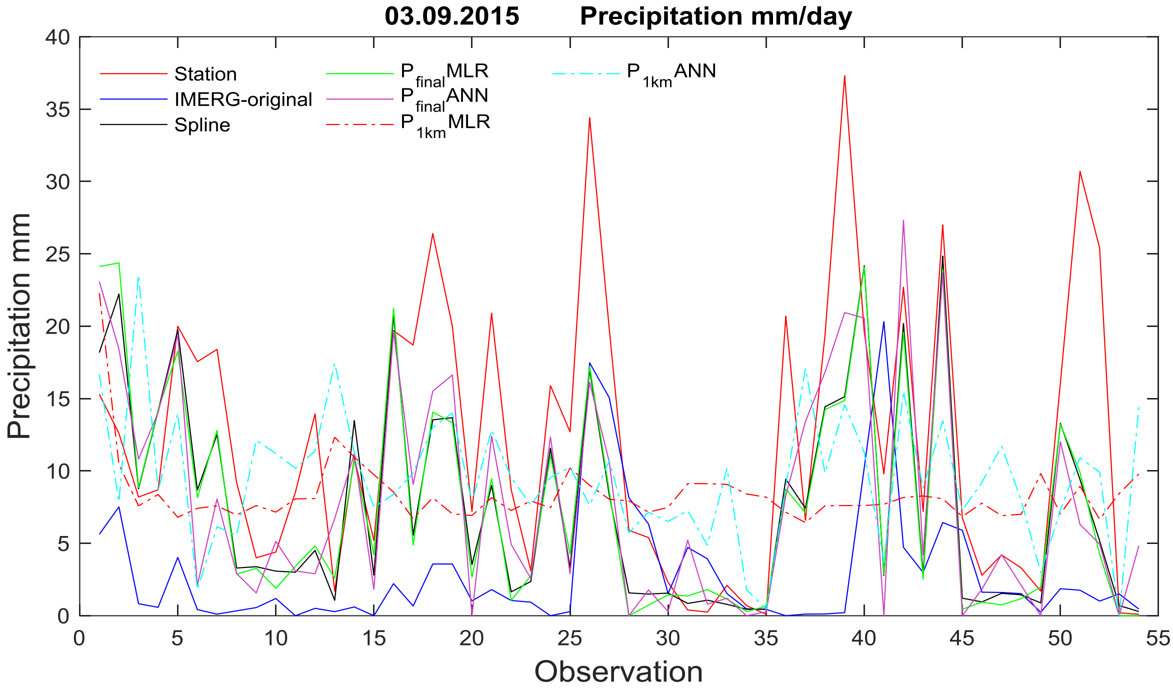

Figure 5.7. Comparison of precipitation values of all data sets for 3 September 2015.

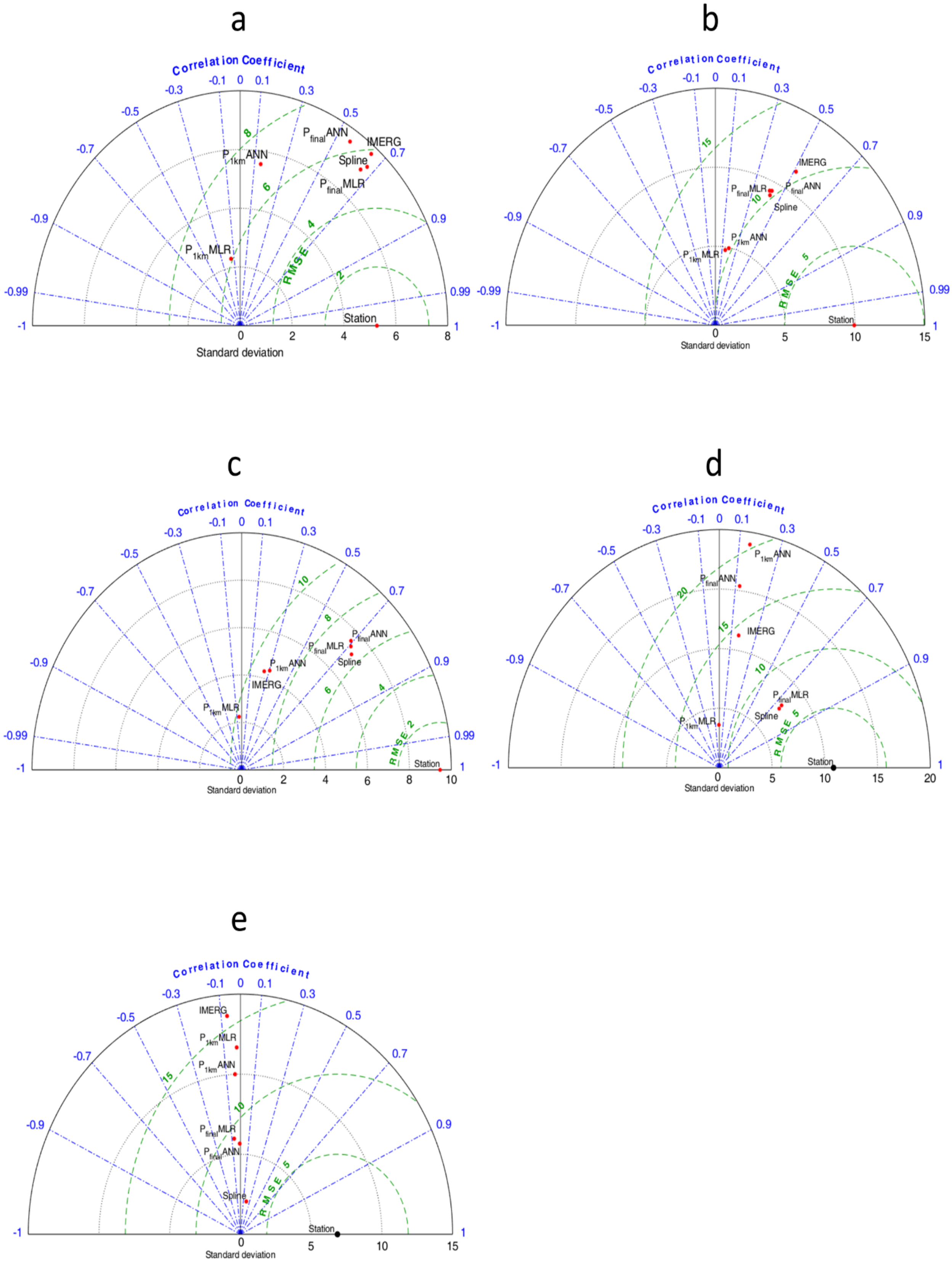

Figure 5.8. Taylor diagram for precipitation events on (a) 17 April 2015, (b) 23 May 2015, (c) 3 September 2015, (d) 25 September 2015, and (e) 7 October 2015.

5.6 Conclusions

The objective of this research was to downscale, while maintaining accuracy, GPM-IMERG final-run V05B product to a spatial resolution meaningful for applications in hydro-meteorology and water resource studies. The various downscaling procedures on IMERG-FR V05B product were conducted over five heavy daily precipitation events (P > 30 mm/day) in 2015. The downscaling procedure adopted high-resolution MODIS-MOD06 cloud optical and microphysical as the predictor variables (including COT, CER, and CWP) in order to map daily precipitation product to a fine spatial resolution over northeast Austria. The main contribution of our research is the development of two integrated downscaling methodologies, as well as the improvement of precipitation spatial resolution and incorporation of freely-distributed satellite MODIS data in the downscaling process.

All techniques considerably improved the accuracy of GPM-IMERG precipitation product compared with the original coarse resolution IMERG product. The extracted area-to-point resolution is suitable for hydro-meteorological modeling at the catchment scale. However, in contrast to NDVI-based downscaling methods, the cloud optical and microphysical properties variables not only are applicable to land surfaces but also may be implemented to water bodies and urban areas.

The following specific conclusions are drawn from this study:

- There was not a robust agreement between the original IMERG daily precipitation and the recorded gauge measurements for the selected heavy precipitation events. This is most likely due to the difference in spatial scale of the two, and the bias in the satellite products.
- Using COT, CER and CWP, a relation between cloud optical and microphysical properties with IMERG precipitation can be established.
- None of the cloud products, or any other sensor, can individually quantify cloud conditions leading to a precipitation event. However, use of a set of cloud properties may be able to explain precipitation occurrence.
- Residual correction algorithms significantly improved the accuracy of final downscaled satellite precipitation.

- Although outperforming $P_{final}ANN$, no significant difference between direct IMERG interpolation and $P_{final}MLR$ models was detected in this study.
- The spline interpolation technique improved precipitation estimation slightly better than other models. That could be due to the fact that the precipitation pattern in our study area is not affected by altitude. However, the performance of spline interpolation alone in complex terrain must be further evaluated.
- Incorporation of MODIS cloud optical and microphysical products for daily precipitation downscaling purposes proved effective. However, due to the possibility of precipitation occurrence before or after satellite passage time over the study area, one may expect some error in the regression relationships.
- One of the limitations of using cloud optical and microphysical properties is that data are available only for daytime.

The advantage of the proposed methodology lies in the application of auxiliary (input) data that are freely available with global coverage. Thus, the methodology can easily be applied to other geographical regions. Moreover, the proposed methodology may be applied for fulfilling the needs of general downscaling applications, for example, in natural hazard, hydrometeorology, and agricultural and climate change studies where the need for spatially downscaled precipitation data is of paramount importance. Despite its easy adaptation to other geographical locations or other downscaling applications, use of the neural network model should be preceded by elaborate experimentation with various architectures, input combinations and data selection.

The new downscaled products could be considered as input for hydro-meteorological applications due to their high spatial resolution. Moreover, the proposed methodology provides the capability for future updates to downscaled precipitation maps due to ongoing IMERG and MODIS missions. Future work could also embrace an inter-comparison of various downscaling methodologies, particularly machine learning methodology, with emphasis on extremes, outliers, and interannual evaluation of such methods. Furthermore, the exclusive use of MODIS data in the downscaling process illustrated the potential of fine-resolution freely distributed satellite data.

Published paper:

AGU100 ADVANCING EARTH AND SPACE SCIENCE

JGR Atmospheres

RESEARCH ARTICLE

10.1029/2018JD028795

Key Points:
- The artificial neural networks, multiple linear regression, and spline interpolation downscaling techniques improved the accuracy compared with the original coarse resolution IMERG product
- Residual correction algorithms significantly improved the accuracy of final downscaled satellite precipitation
- Incorporation of MODIS cloud optical and microphysical products for daily precipitation downscaling purposes proved effective

Correspondence to:
E. Sharifi,
ehsan.sharifi@univie.ac.at

Citation:
Sharifi, E., Saghafian, B., & Steinacker, R. (2019). Downscaling satellite precipitation estimates with multiple linear regression, artificial neural networks, and spline interpolation techniques. *Journal of Geophysical Research: Atmospheres*, *124*. https://doi.org/10.1029/2018JD028795

Received 9 APR 2018
Accepted 5 JAN 2019
Accepted article online 11 JAN 2019

Author Contributions:
Conceptualization: B. Saghafian, R. Steinacker
Supervision: B. Saghafian, R. Steinacker
Writing – review & editing: B. Saghafian, R. Steinacker

Downscaling Satellite Precipitation Estimates With Multiple Linear Regression, Artificial Neural Networks, and Spline Interpolation Techniques

E. Sharifi[1], B. Saghafian[2], and R. Steinacker[1]

[1]Department of Meteorology and Geophysics, University of Vienna, Vienna, Austria, [2]Department of Technical and Engineering, Science and Research Branch, Islamic Azad University, Tehran, Iran

Abstract Satellite precipitation estimates (SPEs) have been widely used in various applications. However, when applied to small basins and regions, the spatial resolution of SPEs is too coarse. In this study, we present three downscaling algorithms based upon the relationships between SPEs and cloud optical and microphysical properties in northeast Austria. Different downscaling techniques, namely, multiple linear regression, artificial neural networks, and spline interpolation, were adopted for the downscaling of Integrated Multi-satellitE Retrievals for GPM (IMERG) precipitation data. In this respect, linear and nonlinear relationship among IMERG data and different cloud variables, such as cloud effective radius, cloud optical thickness, and cloud water path, was evaluated. Downscaled SPEs, as well as the original IMERG product, were subsequently validated using 54 rain gauges at a daily timescale. According to the results, all downscaled products were more accurate than the original IMERG data. Furthermore, all downscaling techniques captured the spatial patterns of precipitation reasonably well with more detailed information when compared with the original IMERG precipitation. However, the spline interpolation slightly outperformed the other techniques, followed by multiple linear regression and artificial neural network, respectively. Moreover, the proposed methods, which consistently showed increased correlation (e.g., from 0.30 to 0.56 for spline interpolation) and reduced mean absolute error and root-mean-square error (e.g., from 10.14 to 6.55 mm and 13.5 to 8.76 mm, respectively) for average of all events, can more accurately produce downscaled precipitation data.

1. Introduction

Precipitation measurements are traditionally performed using rain gauges. Rain gauges are the most reliable source of precipitation observations and are used in most studies as a reference to compare and validate satellite data (Sorooshian et al., 2000). However, they have limited and irregular spatial coverage. Ground-based radar systems are also very valuable but are not feasible for most developing and less developed countries due to high upfront cost and maintenance difficulties.

Given a network of rain gauges, regional precipitation patterns may be determined using geospatial interpolation techniques. However, interpolation using a sparse rain gauge network does not reflect the actual precipitation pattern (Steinacker et al., 2006). Accordingly, remote sensing techniques significantly improve our knowledge on spatial and temporal variation of precipitation that enhances the accuracy of hydrometeorological applications, such as flood and drought forecasting, numerical weather prediction, and climatological changes. As a result, satellite precipitation estimates (SPEs) are attractive sources of geospatial data.

The accuracy of SPEs has been assessed at different spatiotemporal resolutions in a number of studies in recent years (Manz et al., 2017; Moazami et al., 2014; Prakash et al., 2016; Sharifi et al., 2016, 2018; Tian et al., 2009). In certain applications, the variability of precipitation is often represented by the precipitation error in space and time. Since precipitation within a region may occur at finer scales compared with the pixel size of satellites, satellite data should be sufficiently accurate before being used as inputs to the hydrometeorological and water management models (Sharifi et al., 2016). Therefore, downscaling of SPEs is necessary for various applications. Moreover, fine-resolution SPEs can be produced through spatial interpolation techniques that are widely used to produce continuous precipitation surfaces (Dorninger et al., 2008).

Chapter 6

6 Summary and Conclusions

The comprehensive assessment of satellite-based precipitation products over the different topography and climate conditions constitute the focus of this work. The study has also sought to develop the error-adjustment model and downscaling techniques over northeast Austria, to address a number of open questions on the basis of hydro-meteorological activities, in particular, in the northeast of Austria and different parts of Iran. It is worthy to mention that, up to the authors' knowledge, this is the first study of IMERG products over these regions. Although other studies might effort to evaluate the accuracy of satellite-based precipitation over the regions but neither evaluated the newest generation satellite-based precipitation products (IMERG) nor comprehensively assessed the SPEs.

To accomplish our goals, we primarily for the first time have evaluated the daily, monthly and seasonal precipitation estimates (derived from half-hourly precipitation estimates of IMERG and 3-hourly precipitation estimates of TMPA 3B42 and ERA-Interim precipitation fields) with the corresponding rain-gauge observations according to four different topographic and climatic conditions over parts of Iran (Chapter 2).

Then, a comprehensive assessment has been undertaken to examine the performance of the Day-1 IMERG-FR and IMERG-RT late-run version V03 against 62 meteorological synoptic station data on a multi timescale such as daily and sub-daily time resolution over northeast Austria from mid-March 2015 till end of January 2016 (Chapter 3).

In the next step (Chapter 4), uncertainty analysis and bias correction of the IMERG has been done with a copula-based model that preserves the spatial dependency among pixels independent of their marginal and then the simulation of multivariate random precipitation fields. However, the uncertainties associated with high resolution SPE product (IMERG-FR V04) were quantified through above mentioned model associated with additive and multiplicative error models. In order to measure the robustness of the EASPE simulated realizations, P- and d-factors were computed for each simulated ensemble in light of observed data.

In the last phase of this study (Chapter 5), we developed an operational method to downscale GPM-IMERG final-run V05B product to a spatial resolution being meaningful for applications in hydrology and water management.

6.1 Accuracy Assessment of GPM-IMERG Product over Different Topography and Climate Condition

As first topic, an evaluation of the two recent post real time satellite datasets (IMERG and 3B42) and a common precipitation forecast model dataset (ERA-Interim) in daily, monthly and seasonal scales against rain-gauges for four different topography and climate conditions in Iran from mid-March 2014 to February 2015 shows that IMERG, 3B42 and ERA-Interim lead to an underestimation over Iran. Overall, on the daily scale (at days with observed precipitation), the results reveal that all three products lead to an underestimation but IMERG underestimates precipitation only slightly in all four regions. The correlation coefficient between IMERG and the rain-gauge data in daily scale is mostly far superior to those of for Era-Interim and 3B42. On the basis of a daily timescale of biases in comparison with the ground data, the IMERG product is better than ERA-Interim and 3B42 products. Based on monthly and seasonal scales (all days), in Guilan (G8) all products tend to underestimate while in Bushehr (G4) and Kermanshah (G5) IMERG and 3B42, and in Tehran, 3B42 indicate an overestimation. According to the categorical verification technique used in this study, IMERG yields better results for detection of precipitation events on the basis of Probability of Detection (POD), Critical Success Index (CSI) and False Alarm Ratio (FAR) in those areas with stratiform and orographic precipitation such as Tehran and Kermanshah compared with other satellite/model data sets. Moreover, in case of precipitation below 15 mm/day, ERA-Interim and IMERG indicate better results in all study areas, particularly ERA-Interim in Guilan, which shows reasonable results of POD, FAR and CSI. Meanwhile, for heavy precipitation (>15 mm/day), IMERG is far superior to the other products in all study areas which could be used in the future eventually for early warning of floods. With respect to the current monitoring skills, it is almost certain that regions characterized by complex terrain and snowy/ice cover will remain to be problematic for multi-satellite retrieval in GPM. These results will better guide those users who are taking advantage of these satellite-based precipitation data to accommodate their various research and operational applications.

The following conclusions are drawn based on this study:

1. Located in the North of Iran, the Guilan region enjoys a humid and subtropical climate. Under this climate condition, ERA-Interim performed reasonably on the basis of POD, FAR, CSI, RMSE and MAE indices on a daily scale. Additionally, the GPM constellation satellites' product (IMERG) was superior to the TRMM Multi-satellite Precipitation Satellites (TMPA) product (3B42). Moreover, all three satellite/model products underestimated the precipitation in this region, a similar conclusion by Moazzami *et al.* (Moazami et al., 2015) and Javanmard *et al.* (Javanmard et al., 2010) who tested 3B42 in this region. Such findings may be attributed to local wind and convective precipitation in this region so that satellites could not detect precipitation properly.
2. Along the Zagros Mountains in the West of Iran, the Kermanshah region has a hot Mediterranean subtropical climate. All products, including IMERG, TRMM and ERA-Interim, underestimate the precipitation on the daily scale. With respect to contingency table metrics, IMERG outperformed ERA-Interim on the basis of POD, FAR, RMSE, Bias, Mbias, Rbias and CC (correlation coefficient) while ERA-Interim performed best in terms of MAE values on the daily scale. 3B42 outperformed other products on a monthly scale. All three products showed rather the same behavior on the seasonal scale but IMERG indicates a better CC.
3. Just northwest of the Persian Gulf, the Bushehr region is subject to warm and subtropical arid climate in low latitudes. In this area, on the daily scale, IMERG was more accurate in terms of Bias, Mbias, Rbias and CC while 3B42 was better in RMSE and MAE. Also, 3B42 outperformed other products on monthly and seasonal scales. On the other hand, IMERG showed reasonable results with a POD of 0.70 that could be due to the dual-frequency sensor based on the GPM which can detect light rain.
4. Tehran is located in a semi-arid climate with the towering Alborz Mountains to its North and the central desert to the South. In this region, according to the daily scale precipitation, IMERG outperformed other precipitation products with POD, FAR and CSI.
5. ERA-Interim yields weak results of POD, FAR and CSI for precipitation above 15 mm/day over Iran while IMERG is far superior to the other products in all study

areas. ERA-Interim in Guilan region shows a significant value of POD for precipitation below 15 mm/day.

6. Generally, in Guilan, Kermanshah, Tehran and Bushehr regions, all three products (IMERG, 3B42 and ERA-Interim) underestimate precipitation based on a daily scale, which might be due to an inadequate number of gauges which are provided by the Global Precipitation Climatology Centre (GPCC) and used for bias correction in satellite products or/and the inability to measure available water in the air profiles. Moreover, in semi-arid and hot climates, rain drops may evaporate before reaching the ground (Tesfagiorgis et al., 2011).

6.2 Multi Time-Scale Evaluation

In chapter 3, the performance of the Day-1 IMERG-FR and IMERG-RT late-run version V03 against 62 meteorological synoptic station data has been examined on a multi timescale such as daily and sub-daily time resolution over northeast Austria from mid-March 2015 till end of January 2016. IMERG-FR uses monthly GPCC gauge data over land for bias correction; and the IMERG-RT late-run product also uses a coefficient of monthly climatology data. In general, for hourly precipitation and for entire precipitation rate ($P \geq 0.1$), both products indicate a negative bias. However, for other time steps, IMERG-FR tends to underestimate while IMERG-RT tends to overestimate precipitation over the study area. Based on the entire range of precipitation, hourly, 3- and 6-hourly IMERG-FR did not show a clear improvement of the bias over IMERG-RT while for 12-hourly and daily precipitation estimates, the bias in IMERG-FR has improved compared to IMERG-RT. In addition, IMERG-FR shows a considerable improvement in RMSE compared to IMERGRT. However, IMERG-FR systematically underestimates moderate to extreme and overestimates light precipitation for the entire range of precipitation intensities ($P \geq 0.1$ mm/time interval). When comparing the bias, RMSE, and correlation coefficients, IMERG-FR outperforms IMERG-RT particularly for 6-hourly, 12-hourly and daily precipitation. Despite the generally low POD and TS and high FAR skill scores within specified precipitation thresholds, the multi-categorical contingency table shows relatively good values of the POD, TS and FAR for precipitation without classification. This means these two satellite products are relatively well able to detect precipitation without classification but they have poor results to detect precipitation in their exact precipitation categories over northeast Austria. However, further intensive detailed studies are needed when improved and fully GPM-IMERG retrospectively processed data starting from 1998 become available to understand inter-annual variability which is very important because sensors and satellites used in multi-satellite products can be out of service and new sensors can be added at any time.

In summary, although the newly introduced sensors and upgraded calibration algorithms have undoubtedly improved the GPM constellation satellites' accuracy, some challenging issues in satellite retrieval processes will continue to remain open for the satellite community, providing the impetus for more research and development. The overestimation or underestimation over forest areas indicates that accurate estimation by satellite-based precipitation products even though they are improved still remains a challenge particularly for short-time precipitation (i.e., hourly precipitation).

Such inaccuracy may be rooted in the following possible causes of uncertainty of evaluation of SPEs against rain-gauges:

- The spatial resolution of the satellite product, since precipitation within a region, may occur on smaller scales than the pixel size of satellites.
- An inadequate number of gauges, provided by the Global Precipitation Climatology Centre (GPCC) and used for bias correction in satellite products.
- Short-time precipitation (i.e., daily and sub-daily accumulation) is much more variable than monthly precipitation and regional effects like topography and local circulation play an important role in rainfall generation. Accordingly, monthly precipitation from GPCC which are used for the calibration of IMERG-FR would not be well smoothed if sub-daily precipitation fields are used.
- Algorithm error.
- Rain-gauge measurements error due to wind-induced undercatching, precipitation type and particle falling velocities, rainfall intensity and the aerodynamic properties of a particular type of gauge.

6.3 Uncertainty Analysis and Bias Correction

In chapter 4, based on Bias and RMSE error indices, the presented framework was able to improve the SPEs considerably. In addition, the validation stage implied that the error-adjusted band of the simulated realizations encompassed the observed data reasonably. Moreover, by fitting the whole data range, the simulations associated with the additive error model performed much better than the multiplicative error model. The results also confirmed that the spatial correlation of error was not negligible. Adequate spatial correlation structures within each ensemble are preserved via the t-copula. In addition, the results demonstrated that the additive error model was superior to the multiplicative error model. Overall, the results presented here indicate that by using a t-copula model with an emphasis on an additive error model, one can generate multiple realizations of precipitation fields through the simulation of error fields.

We need to emphasize that the presented model is meant to describe random error (stochastic sources of uncertainty) associated with the SPEs and does not address systematic error (bias) involved in the quantification of precipitation uncertainty. Precipitation data may be subject to physical biases and may require further attempts to remove/correct physical biases. Moreover, it is pointed out that as the number of events declines, the sample size of the observed error decreases. This may, but not necessarily, result in a narrower range of error.

One can intuitively conclude that any change in the error range and thus the distribution of error will also affect the estimated uncertainty. In other words, an insufficient precipitation sample size will lead to lower EASPE robustness (Berg et al., 2012; Boé et al., 2007). Another cause might be due to seasonality in the data as well as the precipitation types. Therefore, it is expected that improved accuracy may be warranted in adopting a denser station network and/or using satellite products of finer spatial resolution with longer time series data availability.

6.4 Downscaling of Satellite Precipitation Products

In chapter 5, we have presented two downscaling algorithms on the basis of the relationships between SPEs and cloud optical and microphysical properties alongside with spline interpolation over five heavy daily precipitation events ($P > 30$ mm/day) in 2015 in northeast Austria. The downscaling procedure adopted high-resolution MODIS-MOD06 cloud optical and microphysical predictor variables (including COT, CER and CWP) in order to map daily precipitation product to a fine spatial resolution. The main contribution of our research is the development of two integrated downscaling methodologies, as well as the improvement of precipitation spatial resolution and incorporation of freely-distributed satellite MODIS data in the downscaling process.

The following specific conclusions are drawn from this study:

- There was not a robust agreement between the original IMERG daily precipitation and the recorded gauge measurements for the selected heavy precipitation events. This is most likely due to the difference in spatial scale of the two, and the bias in the satellite products.
- Using COT, CER and CWP, a relation between cloud optical and microphysical properties with IMERG precipitation can be established.
- None of the cloud products, or any other sensor, can individually quantify cloud conditions leading to a precipitation event. However, use of a set of cloud properties may be able to explain precipitation occurrence.
- Residual correction algorithms significantly improved the accuracy of final downscaled satellite precipitation.
- Although outperforming $P_{final}ANN$, no significant difference between direct IMERG interpolation and $P_{final}MLR$ models was detected in this study.
- The spline interpolation technique improved precipitation estimation slightly better than other models. That could be due to the fact that the precipitation pattern in our study area is not affected by altitude. However, the performance of spline interpolation alone in complex terrain must be further evaluated.
- Incorporation of MODIS cloud optical and microphysical products for daily precipitation downscaling purposes proved effective. However, due to the possibility of precipitation occurrence before or after satellite passage time over the study area, one may expect some error in the regression relationships.
- One of the limitations of using cloud optical and microphysical properties is that data is available only for daytime.

In summary, although the accuracy of the recently released satellite-based precipitation product (IMERG) significantly improved compared with the previous products, but the overestimation or underestimation over mountainous regions indicates that accurate estimation by original coarse resolution IMERG product still remains a challenge, particularly in sub-daily time-scale. However, the bias-adjusted and downscaling improved the accuracy and spatial resolution of the product and could be considered as input for hydro-meteorological applications.

Appendix A.

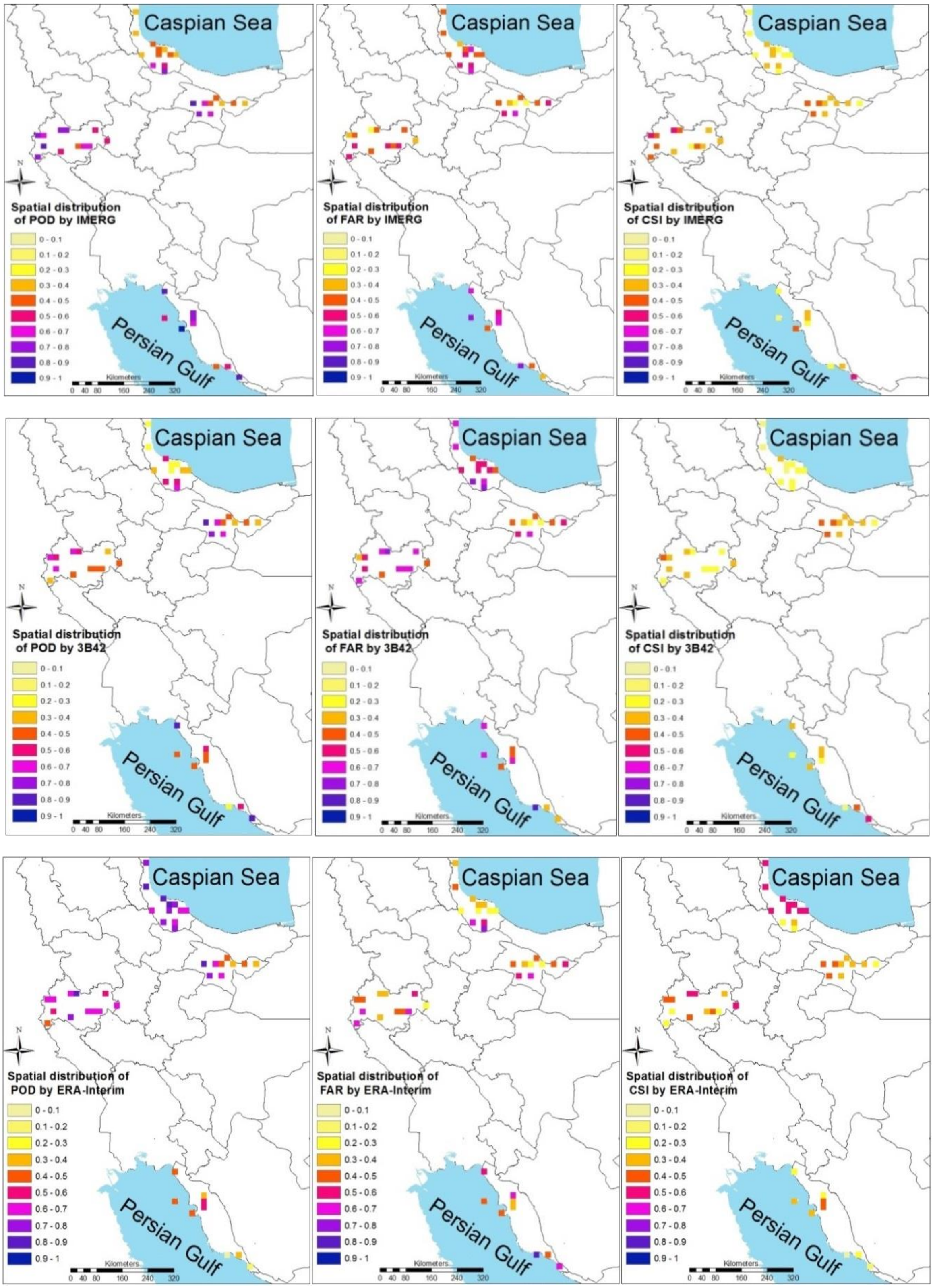

Figure A.1. Spatial distribution of POD, FAR and CSI over four study areas in Iran for entire precipitation range.

Table A.1. Summary of all statistical indices for daily, monthly and seasonal precipitation over four study regions of Iran.

Daily	**IMERG**						**3B42**						**ERA-Interim**					
	RMSE mm	**MAE mm**	**Bias mm**	**Mbias**	**Rbias**	**CC**	**RMSE mm**	**MAE mm**	**Bias mm**	**Mbias**	**Rbias**	**CC**	**RMSE mm**	**MAE mm**	**Bias mm**	**Mbias**	**Rbias**	**CC**
Guilan (G8)	19.41	11.59	**-6.41**	**0.62**	**-0.37**	0.40	19.59	11.68	-9.75	0.31	-0.69	0.29	**17.59**	**9.88**	-9.06	0.35	-0.65	**0.55**
Bushehr (G4)	13.7	7.92	**-2.52**	**0.90**	**-0.10**	**0.51**	**11.86**	**7.07**	-2.95	0.75	-0.25	0.47	14.30	8.04	-7.72	0.22	-0.78	0.40
Kermanshah (G5)	**7.10**	4.91	**-0.72**	**0.88**	**-0.12**	**0.52**	7.72	5.39	-1.59	0.75	-0.25	0.42	7.35	**4.31**	-3.33	0.52	-0.48	0.38
Tehran (G2)	6.38	4.42	-1.86	0.75	-0.25	**0.46**	7.64	7.74	**-1.47**	**0.78**	**-0.22**	0.27	**5.92**	**4.05**	-3.42	0.35	-0.65	0.14

Monthly	**IMERG**						**3B42**						**ERA-Interim**					
	RMSE mm	**MAE mm**	**Bias mm**	**Mbias**	**Rbias**	**CC**	**RMSE mm**	**MAE mm**	**Bias mm**	**Mbias**	**Rbias**	**CC**	**RMSE mm**	**MAE mm**	**Bias mm**	**Mbias**	**Rbias**	**CC**
Guilan (G8)	**81.91**	**53.00**	**-29.21**	**0.98**	**-0.02**	0.76	102.76	58.96	-35.45	0.93	-0.07	0.52	95.27	62.07	-54.34	0.58	-0.42	**0.85**
Bushehr (G4)	14.36	7.13	3.84	1.49	0.71	0.82	**11.88**	**6.31**	**1.05**	**1.21**	**0.21**	0.89	16.50	6.39	-5.86	0.39	-0.61	**0.95**
Kermanshah (G5)	16.94	11.50	7.70	1.62	0.62	**0.88**	**15.64**	**10.31**	**4.56**	1.40	0.57	0.85	16.87	10.34	-5.67	**0.82**	**-0.18**	0.84
Tehran (G2)	19.88	14.09	**-5.14**	**1.13**	**0.13**	0.57	20.61	14.55	11.56	2.03	1.03	0.69	**14.74**	**11.08**	-7.34	0.82	-0.18	**0.80**

Seasonally	**IMERG**						**3B42**						**ERA-Interim**					
	RMSE mm	**MAE mm**	**Bias mm**	**Mbias**	**Rbias**	**CC**	**RMSE mm**	**MAE mm**	**Bias mm**	**Mbias**	**Rbias**	**CC**	**RMSE mm**	**MAE mm**	**Bias mm**	**Mbias**	**Rbias**	**CC**
Guilan (G8)	**207.02**	163.29	**-97.95**	**0.97**	**-0.03**	0.85	232.45	**157.45**	-106.36	0.93	-0.07	0.75	237.58	178.71	-163.03	0.58	-0.42	**0.93**
Bushehr (G4)	30.52	22.85	10.55	1.60	0.60	0.83	**17.81**	**13.58**	**3.14**	**1.21**	**0.21**	**0.95**	30.12	17.99	-17.59	0.39	-0.61	0.92
Kermanshah (G5)	37.07	27.52	23.10	1.62	0.62	**0.95**	**36.36**	26.69	18.26	1.56	0.56	0.92	39.43	28.00	**-17.02**	**0.82**	**-0.18**	0.88
Tehran (G2)	43.68	34.54	**-15.42**	**1.13**	**0.13**	0.84	46.48	35.57	34.67	2.03	1.03	**0.93**	**33.18**	27.54	-22.01	0.82	-0.18	0.90

Table A.2. Summary of spatially-averaged metrics based on contingency tables for all precipitation ranges.

	Guilan (G8)			**Bushehr (G4)**			**Kermanshah (G5)**			**Tehran (G2)**		
	IMERG	**3B42**	**ERA**	**IMERG**	**3B42**	**ERA**	**IMERG**	**3B42**	**ERA**	**IMERG**	**3B42**	**ERA**
POD	0.46	0.39	**0.74**	**0.70**	0.56	0.39	**0.66**	0.51	0.63	**0.55**	0.50	0.51
FAR	0.52	0.59	**0.40**	0.59	0.55	**0.54**	**0.45**	0.57	0.46	**0.43**	0.71	0.58
CSI	0.29	0.23	**0.49**	**0.35**	0.33	0.28	**0.42**	0.30	**0.42**	**0.37**	0.23	0.30
Accuracy	0.77	0.74	**0.84**	0.95	0.96	**0.97**	**0.90**	0.86	**0.90**	**0.89**	0.80	0.86
Bias	**1.02**	1.06	1.36	1.86	1.30	**0.83**	1.24	1.24	**1.21**	**1.03**	1.73	1.23
POFD	**0.13**	0.15	**0.13**	0.04	0.02	**0.01**	**0.07**	0.10	**0.07**	**0.05**	0.17	0.09
SR	0.48	0.41	**0.60**	0.41	0.45	**0.46**	**0.55**	0.43	0.54	**0.57**	0.29	0.42
ETS	0.19	0.13	**0.38**	**0.33**	0.31	0.26	**0.37**	0.24	0.36	**0.32**	0.15	0.24
TSS	0.33	0.24	**0.61**	**0.67**	0.53	0.38	**0.60**	0.41	0.57	**0.50**	0.34	0.42
OR	7.48	4.12	**20.59**	**118.43**	77.74	56.28	**34.84**	13.62	30.16	**30.51**	6.00	11.74

Appendix B.

Table B.1. Summary of evaluation metrics for IMERG-FR and IMERG-RT products at a)hourly, b)3-hourly, c)6-hourly, d)12-hourly and e)daily time-scales over northeast Austria. The metrics are calculated based on all hours of all stations.

(a)

	0.1≤P≤0.4		0.4<P≤1.1		1.1<P≤1.8		1.8<P≤5.6		5.6<P		0.1≤P	
	IMERG-FR	IMERG-RT	IMERG-FR	IMERG-RT	IMERG-FR	IMERG-RT	IMERG-FR	IMERG-RT	IMERG-FR	IMERG-RT	IMERG-FR	IMERG-RT
RMSE mm	1.02	1.31	1.38	2.11	1.77	3.08	3.20	6.14	8.33	9.07	1.72	2.67
MAE mm	0.35	0.40	0.79	0.90	1.24	1.56	2.31	3.35	6.76	7.35	0.79	0.97
Bias mm	0.07	0.12	-0.14	-0.05	-0.44	-0.23	-0.99	-0.11	-5.97	-3.56	-0.18	-0.01
Mbias	1.37	1.64	0.81	0.93	0.70	0.84	0.66	0.96	0.32	0.60	0.76	0.99
CC	0.09	0.07	0.09	0.07	0.05	0.06	0.15	0.14	0.00	0.05	0.30	0.29
POD	0.10	0.11	0.16	0.17	0.16	0.12	0.26	0.17	0.16	0.29	0.39	0.40
FAR	0.77	0.78	0.81	0.81	0.83	0.84	0.76	0.80	0.91	0.91	0.40	0.43
TS	0.07	0.08	0.09	0.10	0.09	0.07	0.14	0.10	0.06	0.07	0.31	0.31
Accuracy	0.94	0.94	0.97	0.97	0.99	0.99	0.99	0.99	1.00	1.00	0.93	0.92
Frequency bias	0.41	0.52	0.85	0.91	0.92	0.75	1.09	0.85	1.92	3.39	0.64	0.70

(b)

	0.1≤P≤0.6		0.6<P≤1.4		1.4<P≤3.8		3.8<P≤11.5		11.5<P		0.1≤P	
	IMERG-FR	IMERG-RT	IMERG-FR	IMERG-RT	IMERG-FR	IMERG-RT	IMERG-FR	IMERG-RT	IMERG-FR	IMERG-RT	IMERG-FR	IMERG-RT
RMSE mm	1.43	2.13	1.88	2.79	3.11	4.68	6.33	11.55	12.89	18.92	2.88	4.93
MAE mm	0.52	0.60	1.15	1.32	2.11	2.53	4.48	6.48	10.66	14.79	1.39	1.80
Bias mm	0.17	0.25	-0.08	0.08	-0.58	-0.33	-1.52	0.03	-8.50	-2.28	-0.24	0.12
Mbias	1.68	2.00	0.92	1.08	0.75	0.86	0.75	1.01	0.47	0.86	0.83	1.08
CC	0.11	0.07	0.08	0.09	0.14	0.12	0.26	0.22	-0.01	0.05	0.46	0.40
POD	0.16	0.18	0.13	0.15	0.22	0.20	0.32	0.46	0.24	0.34	0.45	0.47
FAR	0.69	0.71	0.85	0.84	0.74	0.73	0.67	0.73	0.87	0.90	0.36	0.38
TS	0.12	0.13	0.08	0.08	0.14	0.13	0.19	0.13	0.09	0.08	0.36	0.36
Accuracy	0.93	0.93	0.96	0.96	0.96	0.96	0.98	0.98	1.00	1.00	0.89	0.89
Frequency bias	0.51	0.61	0.92	0.91	0.83	0.76	0.96	0.79	1.90	3.40	0.71	0.76

(c)

	0.1≤P≤0.8		0.8<P≤2		2<P≤5.5		5.5<P≤16.5		16.5<P		0.1≤P	
	IMERG-FR	IMERG-RT	IMERG-FR	IMERG-RT	IMERG-FR	IMERG-RT	IMERG-FR	IMERG-RT	IMERG-FR	IMERG-RT	IMERG-FR	IMERG-RT
RMSE mm	1.97	2.89	2.67	3.82	4.07	5.90	7.51	17.53	15.68	28.96	3.75	7.04
MAE mm	0.69	0.80	1.60	1.86	2.90	3.45	5.95	9.87	12.72	21.21	1.88	2.53
Bias mm	0.29	0.41	-0.05	0.22	-0.72	-0.49	-1.96	1.04	-8.02	3.42	-0.25	0.29
Mbias	1.92	2.31	0.97	1.16	0.79	0.86	0.78	1.12	0.64	1.15	0.88	1.14

CC	0.11	0.09	0.06	0.06	0.15	0.13	0.38	0.29	0.06	0.20	0.55	0.21
POD	0.18	0.21	0.16	0.16	0.26	0.22	0.33	0.21	0.38	0.44	0.51	0.53
FAR	0.73	0.74	0.82	0.82	0.69	0.70	0.65	0.73	0.81	0.87	0.34	0.35
TS	0.12	0.13	0.09	0.09	0.16	0.15	0.20	0.13	0.14	0.11	0.40	0.42
Accuracy	0.87	0.87	0.94	0.94	0.95	0.95	0.98	0.98	1.00	0.99	0.86	0.86
Frequency bias	0.67	0.79	0.87	0.88	0.83	0.72	0.92	0.78	2.02	3.33	0.78	0.82

(d)

	0.1≤P≤1.2		**1.2<P≤2.8**		**2.8<P≤7.8**		**7.8<P≤18.4**		**18.4<P**		**0.1≤P**	
	IMERG-FR	**IMERG-RT**	**IMERG-FR**	**IMERG-RT**	**IMERG-FR**	**IMERG-RT**	**IMERG-FR**	**IMERG-RT**	**IMERG-FR**	**IMERG-RT**	**IMERG-FR**	**IMERG-RT**
RMSE mm	2.44	3.80	3.45	5.05	5.18	8.04	8.93	22.14	16.23	31.29	4.71	9.14
MAE mm	0.91	1.11	2.18	2.71	3.87	4.83	7.26	12.92	12.69	21.40	2.48	3.49
Bias mm	0.41	0.62	-0.01	0.47	-0.90	-0.35	-2.19	1.88	-6.32	2.41	-0.27	0.53
Mbias	1.96	2.43	0.99	1.24	0.81	0.93	0.81	1.16	0.76	1.09	0.91	1.18
CC	0.14	0.11	0.06	0.01	0.15	0.10	0.36	0.23	0.12	0.17	0.61	0.49
POD	0.26	0.29	0.15	0.15	0.28	0.22	0.30	0.18	0.51	0.47	0.58	0.60
FAR	0.68	0.69	0.82	0.81	0.65	0.68	0.68	0.80	0.68	0.79	0.31	0.31
TS	0.16	0.18	0.09	0.09	0.18	0.15	0.18	0.10	0.24	0.17	0.46	0.47
Accuracy	0.82	0.81	0.92	0.92	0.93	0.93	0.97	0.97	0.99	0.99	0.82	0.82
Frequency bias	0.81	0.93	0.84	0.80	0.81	0.67	0.95	0.88	1.60	2.27	0.84	0.87

(e)

	0.1≤P≤1.8		**1.8<P≤4.2**		**4.2<P≤11**		**11<P≤24**		**24<P**		**0.1≤P**	
	IMERG-FR	**IMERG-RT**	**IMERG-FR**	**IMERG-RT**	**IMERG-FR**	**IMERG-RT**	**IMERG-FR**	**IMERG-RT**	**IMERG-FR**	**IMERG-RT**	**IMERG-FR**	**IMERG-RT**
RMSE mm	3.25	4.77	4.35	5.37	6.52	11.40	11.28	29.68	19.39	32.49	5.95	11.63
MAE mm	1.32	1.54	2.88	3.39	5.15	6.88	9.29	18.41	15.37	23.76	3.30	4.75
Bias mm	0.64	0.85	0.01	0.41	-1.24	0.10	-2.21	4.56	-7.09	-0.17	-0.24	0.90
Mbias	2.00	2.34	1.00	1.14	0.82	1.01	0.86	1.29	0.79	1.00	0.94	1.21
CC	0.17	0.15	0.13	0.12	0.19	0.17	0.27	0.15	0.14	0.28	0.65	0.51
POD	0.30	0.33	0.19	0.18	0.27	0.24	0.33	0.20	0.54	0.49	0.65	0.66
FAR	0.64	0.64	0.78	0.77	0.65	0.66	0.67	0.77	0.69	0.79	0.25	0.26
TS	0.19	0.21	0.11	0.11	0.18	0.16	0.20	0.12	0.25	0.17	0.53	0.54
Accuracy	0.76	0.75	0.89	0.90	0.91	0.91	0.96	0.95	0.99	0.98	0.78	0.78
Frequency bias	0.83	0.93	0.86	0.77	0.79	0.70	0.99	0.88	1.70	2.31	0.86	0.88

Table B.2. Frequency of events with different intensities in corresponding to GPM-IMERG products a) IMERG-FR and b) IMERG-RT for hourly precipitation

(a)

		IMERG-FR						
		P<0.1	**0.1≤P≤0.4**	**0.4<P≤1.1**	**1.1<P≤1.8**	**1.8<P≤5.6**	**5.6<P**	**Total**
Station	**P<0.1**	374858	4697	3011	729	645	115	384055
	0.1≤P≤0.4	14827	1928	1916	644	595	98	20008
	0.4<P≤1.1	4921	987	1425	697	754	98	8882
	1.1<P≤1.8	1362	304	610	437	587	66	3366
	1.8<P≤5.6	866	311	541	427	834	246	3225
	5.6<P	52	28	50	59	107	58	354
	Total	396886	8255	7553	2993	3522	681	**419890**

(b)

		IMERG-RT						
		P<0.1	**0.1≤P≤0.4**	**0.4<P≤1.1**	**1.1<P≤1.8**	**1.8<P≤5.6**	**5.6<P**	**Total**
Station	**P<0.1**	373435	5953	3099	711	656	201	384055
	0.1≤P≤0.4	14468	2296	1955	542	557	190	20008
	0.4<P≤1.1	4851	1268	1503	535	528	197	8882
	1.1<P≤1.8	1296	473	735	337	377	148	3366
	1.8<P≤5.6	814	333	741	424	553	360	3225
	5.6<P	39	28	64	57	63	103	354
	Total	394903	10351	8097	2606	2734	1199	**419890**

Table B.3. Frequency of events with different intensities in corresponding to GPM-IMERG products a) IMERG-FR and b) IMERG-RT for 3-hourly precipitation

(a)

		IMERG-FR						
		P<0.1	**0.1≤P≤0.6**	**0.6<P≤1.4**	**1.4<P≤3.8**	**3.8<P≤11.5**	**11.5<P**	**Total**
Station	**P<0.1**	115980	2850	1267	645	152	44	120938
	0.1≤P≤0.6	6851	1281	889	602	179	30	9832
	0.6<P≤1.4	1886	534	491	540	198	18	3667
	1.4<P≤3.8	1358	429	533	802	487	54	3663
	3.8<P≤11.5	291	113	165	416	530	165	1680
	11.5<P	11	10	18	37	66	46	188
	Total	126377	5217	3363	3042	1612	357	**139968**

(b)

		IMERG-RT						
		P<0.1	**0.1≤P≤0.6**	**0.6<P≤1.4**	**1.4<P≤3.8**	**3.8<P≤11.5**	**11.5<P**	**Total**
Station	**P<0.1**	115464	5953	3099	711	656	201	384055
	0.1≤P≤0.6	14468	2296	1955	542	557	190	20008
	0.6<P≤1.4	4851	1268	1503	535	528	197	8882
	1.4<P≤3.8	1296	473	735	337	377	148	3366
	3.8<P≤11.5	814	333	741	424	553	360	3225
	11.5<P	39	28	64	57	63	103	354
	Total	394903	10351	8097	2606	2734	1199	**419890**

Table B.4. Frequency of events with different intensities in corresponding to GPM-IMERG products a) IMERG-FR and b) IMERG-RT for 6-hourly precipitation

(a)

		IMERG-FR						
		P<0.1	**0.1≤P≤0.8**	**0.8<P≤2**	**2<P≤5.5**	**5.5<P≤16.5**	**16.5<P**	**Total**
Station	**P<0.1**	53090	2397	726	344	71	17	56645
	0.1≤P≤0.8	4357	1241	665	408	108	23	6802
	0.8<P≤2	1238	487	432	374	140	17	2688
	2<P≤5.5	760	350	389	645	347	31	2522
	5.5<P≤16.5	154	98	128	295	389	130	1194
	16.5<P	3	8	5	18	49	50	133
	Total	59602	4581	2345	2084	1104	268	**69984**

(b)

		IMERG-RT						
		P<0.1	**0.1≤P≤0.8**	**0.8<P≤2**	**2<P≤5.5**	**5.5<P≤16.5**	**16.5<P**	**Total**
Station	**P<0.1**	52822	2792	639	266	110	16	56645
	0.1≤P≤0.8	4196	1412	663	342	156	33	6802
	0.8<P≤2	1183	550	431	330	153	41	2688
	2<P≤5.5	689	523	438	551	221	100	2522
	5.5<P≤16.5	140	115	189	304	251	195	1194
	16.5<P	2	3	9	21	40	58	133
	Total	59032	5395	2369	1814	931	443	**69984**

Table B.5. Frequency of events with different intensities in corresponding to GPM-IMERG products a) IMERG-FR and b) IMERG-RT for 12-hourly precipitation

(a)

		IMERG-FR						
		P<0.1	**0.1≤P≤1.2**	**1.2<P≤2.8**	**2.8<P≤7.8**	**7.8<P≤18.4**	**18.4<P**	**Total**
Station	**P<0.1**	23135	1859	379	160	43	14	25590
	0.1≤P≤1.2	2741	1236	459	300	65	21	4822
	1.2<P≤2.8	692	391	271	322	77	16	1769
	2.8<P≤7.8	423	351	296	528	238	42	1878
	7.8<P≤18.4	66	78	77	190	224	111	746
	18.4<P	2	6	8	18	58	95	187
	Total	27059	3921	1490	1518	705	299	34992

(b)

		IMERG-RT						
		P<0.1	**0.1≤P≤1.2**	**1.2<P≤2.8**	**2.8<P≤7.8**	**7.8<P≤18.4**	**18.4<P**	**Total**
Station	**P<0.1**	23022	2106	280	123	46	13	25590
	0.1≤P≤1.2	2633	1387	393	259	117	33	4822
	1.2<P≤2.8	654	454	265	236	118	42	1769
	2.8<P≤7.8	396	425	366	407	181	103	1878
	7.8<P≤18.4	62	90	108	208	132	146	746
	18.4<P	2	4	9	23	61	88	187
	Total	26769	4466	1421	1256	655	425	34992

Table B.6. Frequency of events with different intensities in corresponding to GPM-IMERG products a) IMERG-FR and b) IMERG-RT for daily precipitation

(a)

		IMERG-FR						
		P<0.1	**0.1≤P≤1.8**	**1.8<P≤4.2**	**4.2<P≤11**	**11<P≤24**	**24<P**	**Total**
Station	**P<0.1**	9426	1145	174	65	20	6	10836
	0.1≤P≤1.8	1756	1007	380	207	44	19	3413
	1.8<P≤4.2	364	354	242	250	53	9	1272
	4.2<P≤11	217	272	230	354	201	27	1301
	11<P≤24	21	48	59	132	176	100	536
	24<P	2	4	6	16	36	74	138
	Total	11786	2830	1091	1024	530	235	17496

(b)

		IMERG-RT						
		P<0.1	**0.1≤P≤1.8**	**1.8<P≤4.2**	**4.2<P≤11**	**11<P≤24**	**24<P**	**Total**
Station	**P<0.1**	9342	1290	119	62	18	5	10836
	0.1≤P≤1.8	1712	1133	284	175	83	26	3413
	1.8<P≤4.2	355	381	229	201	87	19	1272
	4.2<P≤11	206	310	248	311	137	89	1301
	11<P≤24	23	52	93	149	107	112	536
	24<P	2	3	9	19	37	68	138
	Total	11640	3169	982	917	469	319	17496

Appendix C.

Table C.1. Average bias of the three validation events over 48 pixels, comparison between the OSPE and EASPEs according to additive- and multiplicative error models

	event 1			event 2			event 3		
Pixel No.	OSPE error	$EASPE_{add}$ error	$EASPE_{mlt}$ error	OSPE error	$EASPE_{add}$ error	$EASPE_{mlt}$ error	OSPE error	$EASPE_{add}$ error	$EASPE_{mlt}$ error
1	7.42	6.09	4.99	2.27	1.04	-0.41	1.11	-0.12	0.35
2	11.89	10.13	15.74	-1.30	-3.06	-0.52	0.33	-1.43	1.12
3	3.02	1.43	2.32	3.20	1.61	2.44	0.69	-0.80	0.51
4	3.73	2.02	3.47	1.30	-0.41	1.00	0.24	-1.37	0.04
5	2.78	1.62	3.87	5.51	4.25	7.53	0.06	-1.20	0.69
6	-0.20	-2.31	-0.29	-2.01	-3.97	-1.93	-0.01	-1.97	0.14
7	3.02	1.29	3.08	5.13	3.50	5.47	1.86	0.13	2.04
8	4.02	0.95	5.86	3.07	0.10	5.04	3.26	0.19	7.84
9	0.77	-1.00	0.84	2.15	0.38	2.31	1.31	-0.46	1.48
10	0.29	-0.94	0.10	-5.35	-6.68	-5.58	1.71	0.48	1.33
11	3.02	2.30	1.93	7.38	6.66	3.96	1.18	0.46	-0.63
12	0.02	-1.97	0.09	5.46	3.37	5.53	2.77	0.58	2.67
13	1.68	-0.18	0.70	2.80	0.84	1.58	0.30	-1.56	-0.73
14	3.45	3.64	2.21	0.10	0.29	-0.68	-0.13	0.16	-1.84
15	3.50	1.28	3.91	2.30	0.18	2.60	0.47	-1.65	0.93
16	2.60	0.39	2.90	-0.40	-2.51	-0.16	1.97	-0.14	2.34
17	2.09	1.07	1.10	0.20	-0.82	-0.21	-0.40	-1.42	-2.15
18	3.01	2.46	0.51	-2.25	-2.55	-2.37	7.32	6.77	1.81
19	2.48	1.29	1.12	2.60	1.46	1.93	1.44	0.15	-0.17
20	3.67	1.66	3.21	0.40	-1.51	0.22	2.28	0.37	1.82
21	8.21	7.14	9.46	7.76	6.69	9.21	0.06	-0.91	0.71
22	-0.35	-2.04	-0.21	-0.73	-2.42	-0.54	1.13	-0.56	1.46
23	0.35	3.47	-2.68	-3.20	0.02	-9.36	-3.40	-0.18	-5.45
24	-2.00	-2.20	-2.14	-14.00	-14.57	-14.62	-3.65	-3.85	-3.82
25	3.21	1.86	1.53	0.00	-0.20	-0.07	-0.80	-1.00	-0.94
26	10.00	8.59	5.80	-0.40	-0.70	-0.52	-2.80	-3.00	-2.94
27	3.15	1.27	2.76	4.60	2.72	4.13	0.49	-1.39	0.26
28	0.81	-0.42	0.08	3.49	2.26	1.82	0.31	-0.92	0.08
29	1.57	0.32	0.55	4.74	3.49	3.60	0.17	-1.08	-0.39

30	4.13	2.53	3.68	7.34	5.74	6.72	2.43	0.83	2.00
31	2.18	0.59	2.66	11.78	10.29	14.40	-0.51	-2.00	0.02
32	-1.76	-3.50	-1.29	7.25	5.22	9.62	0.71	-1.22	1.84
33	9.48	8.37	9.03	1.30	0.09	1.12	-0.13	-1.34	-0.32
34	11.20	11.45	5.65	-2.60	-2.35	-5.34	-2.20	-1.95	-2.42
35	-0.40	-0.60	-0.54	-4.50	-4.70	-4.64	-0.10	-0.30	-0.24
36	-0.34	0.49	-1.43	-1.50	-0.67	-3.78	-1.10	-0.42	-3.55
37	5.51	4.79	1.73	-7.60	-8.32	-8.21	-1.32	-2.04	-2.69
38	2.12	2.08	0.50	1.60	1.46	-0.36	-1.17	-1.31	-2.76
39	6.16	6.21	3.60	-0.47	-0.52	-0.61	-0.23	-0.18	-0.37
40	5.17	3.59	4.31	2.20	0.62	1.92	1.04	-0.54	0.79
41	9.61	9.43	4.84	-5.80	-6.00	-5.95	-1.71	-1.89	-2.20
42	3.89	3.27	2.77	1.60	0.98	1.33	0.11	-0.51	-0.42
43	5.25	3.30	4.86	6.11	4.16	5.75	2.13	0.18	1.75
44	8.28	7.40	6.28	-0.90	-1.78	-1.67	-0.43	-1.31	-1.09
45	5.27	5.14	3.10	-0.10	-0.23	-0.30	0.10	-0.03	-2.14
46	1.62	1.68	-0.23	1.30	1.46	0.46	-1.14	-0.88	-4.38
47	3.87	2.35	2.98	7.95	6.43	6.32	3.20	1.68	2.04
48	4.58	3.22	4.28	10.07	8.71	9.55	0.28	-1.08	0.10
Average	3.60	2.52	2.70	1.46	0.42	0.99	0.40	-0.63	-0.11

7 References

Abbaspour, K.C., Yang, J., Maximov, I., Siber, R., Bogner, K., Mieleitner, J., Zobrist, J., Srinivasan, R., 2007. Modelling hydrology and water quality in the pre-alpine/alpine Thur watershed using SWAT. Journal of Hydrology 333 (2-4), 413–430.

Abimbola, O.P., Wenninger, J., Venneker, R., Mittelstet, A.R., 2017. The assessment of water resources in ungauged catchments in Rwanda. Journal of Hydrology: Regional Studies 13, 274–289.

AghaKouchak, A., 2010. Simulation of Remotely Sensed Rainfall Fields Using Copulas. doctoral thesis, Universität Stuttgart-Stuttgart, 175 pp.

AghaKouchak, A., 2014. A baseline probabilistic drought forecasting framework using standardized soil moisture index: Application to the 2012 United States drought. Hydrol. Earth Syst. Sci. 18 (7), 2485–2492.

AghaKouchak, A., Bárdossy, A., Habib, E., 2010a. Copula-based uncertainty modelling: Application to multisensor precipitation estimates. Hydrol. Process. 15 (4), n/a-n/a.

AghaKouchak, A., Habib, E., Bárdossy, A., 2010b. A comparison of three remotely sensed rainfall ensemble generators. Atmospheric Research 98 (2-4), 387–399.

AghaKouchak, A., Mehran, A., Norouzi, H., Behrangi, A., 2012. Systematic and random error components in satellite precipitation data sets. Geophys. Res. Lett. 39 (9), n/a-n/a.

AghaKouchak, A., Nasrollahi, N., Li, J., Imam, B., Sorooshian, S., 2011. Geometrical Characterization of Precipitation Patterns. J. Hydrometeor 12 (2), 274–285.

Aires, F., Prigent, C., Bernardo, F., Jiménez, C., Saunders, R., Brunel, P., 2011. A Tool to Estimate Land-Surface Emissivities at Microwave frequencies (TELSEM) for use in numerical weather prediction. Q.J.R. Meteorol. Soc. 137 (656), 690–699.

Alexakis, D.D., Tsanis, I.K., 2016. Comparison of multiple linear regression and artificial neural network models for downscaling TRMM precipitation products using MODIS data. Environ Earth Sci 75 (14), 606.

Alidoost, F., Stein, A., Su, Z., Sharifi, A., 2017. Three novel copula-based bias correction methods for daily ECMWF air temperature data. Hydrol. Earth Syst. Sci. Discuss., 1–27.

Amitai, E., Llort, X., Sempere-Torres, D., 2009. Comparison of TRMM Radar Rainfall Estimates with NOAA Next-Generation QPE. JMSJ 87A, 109–118.

Ashouri, H., Hsu, K.-L., Sorooshian, S., Braithwaite, D.K., Knapp, K.R., Cecil, L.D., Nelson, B.R., Prat, O.P., 2015. PERSIANN-CDR: Daily Precipitation Climate Data Record from Multisatellite Observations for Hydrological and Climate Studies. Bull. Amer. Meteor. Soc. 96 (1), 69–83.

Balistrocchi, M., Orlandini, S., Ranzi, R., Bacchi, B., 2017. Copula-Based Modeling of Flood Control Reservoirs. Water Resour. Res. 53 (11), 9883–9900.

Ballester, J., Moré, J., 2007. The representativeness problem of a station net applied to the verification of a precipitation forecast based on areas. Met. Apps 14 (2), 177–184.

Bao, X., Zhang, F., 2013. Evaluation of NCEP–CFSR, NCEP–NCAR, ERA-Interim, and ERA-40 Reanalysis Datasets against Independent Sounding Observations over the Tibetan Plateau. J. Climate 26 (1), 206–214.

Bárdossy, A., 2006. Copula-based geostatistical models for groundwater quality parameters. Water Resour. Res. 42 (11), 342.
Bárdossy, A., Li, J., 2008. Geostatistical interpolation using copulas. Water Resour. Res. 44 (7), 357.
Bárdossy, A., Pegram, G., 2009. Copula based multisite model for daily precipitation simulation. Hydrol. Earth Syst. Sci. Discuss. 6 (3), 4485–4534.
Behrangi, A., Khakbaz, B., Jaw, T.C., AghaKouchak, A., Hsu, K., Sorooshian, S., 2011. Hydrologic evaluation of satellite precipitation products over a mid-size basin. Journal of Hydrology 397 (3-4), 225–237.
Behrangi, A., Tian, Y., Lambrigtsen, B.H., Stephens, G.L., 2014. What does CloudSat reveal about global land precipitation detection by other spaceborne sensors? Water Resour. Res. 50 (6), 4893–4905.
Bell, T.L., 2003. Comparing satellite rainfall estimates with rain gauge data: Optimal strategies suggested by a spectral model. J. Geophys. Res. 108 (D3), 10.
Bellerby, T., Sun, J., 2005. Probabilistic and Ensemble Representations of the Uncertainty in an IR/Microwave Satellite Precipitation Product. Journal of Hydrometeorology 6, 1032–1044.
Ben-Gal, I., 2010. Outlier Detection, in: Maimon, O., Rokach, L. (Eds.), Data Mining and Knowledge Discovery Handbook. Springer.
Berg, P., Feldmann, H., Panitz, H.-J., 2012. Bias correction of high resolution regional climate model data. Journal of Hydrology 448-449, 80–92.
Berry, E.X., Reinhardt, R.L., 1974. An analysis of cloud drop growth by collection: Part 2. Single initial distributions. Journal of the Atmospheric Sciences, 1825–1831.
Blacutt, L.A., Herdies, D.L., de Gonçalves, Luis Gustavo G., Vila, D.A., Andrade, M., 2015. Precipitation comparison for the CFSR, MERRA, TRMM3B42 and Combined Scheme datasets in Bolivia. Atmospheric Research 163, 117–131.
Boé, J., Terray, L., Habets, F., Martin, E., 2007. Statistical and dynamical downscaling of the Seine basin climate for hydro-meteorological studies. Int. J. Climatol. 27 (12), 1643–1655.
Carr, N., Kirstetter, P.-E., Hong, Y., Gourley, J.J., Schwaller, M., Petersen, W., Wang, N.-Y., Ferraro, R.R., Xue, X., 2015. The Influence of Surface and Precipitation Characteristics on TRMM Microwave Imager Rainfall Retrieval Uncertainty. J. Hydrometeor 16 (4), 1596–1614.
Cheema, M.J.M., Bastiaanssen, W.G.M., Rutten, M.M., 2011. Validation of surface soil moisture from AMSR-E using auxiliary spatial data in the transboundary Indus Basin. Journal of Hydrology 405 (1-2), 137–149.
Chen, F., Liu, Y., Liu, Q., Li, X., 2014. Spatial downscaling of TRMM 3B43 precipitation considering spatial heterogeneity. International Journal of Remote Sensing 35 (9), 3074–3093.
Chen, F., Warner, T.T., Manning, K., 2001. Sensitivity of Orographic Moist Convection to Landscape Variability: A Study of the Buffalo Creek, Colorado, Flash Flood Case of 1996. J. Atmos. Sci. 58 (21), 3204–3223.
Chiodo, G., Haimberger, L., 2010. Interannual changes in mass consistent energy budgets from ERA-Interim and satellite data. J. Geophys. Res. 115 (D2).

Ciach, G.J., Krajewski, W.F., Villarini, G., 2007. Product-Error-Driven Uncertainty Model for Probabilistic Quantitative Precipitation Estimation with NEXRAD Data. J. Hydrometeor 8 (6), 1325–1347.
Collier, C.G., 2009. On the propagation of uncertainty in weather radar estimates of rainfall through hydrological models. Met. Apps 16 (1), 35–40.
Coning, E. de, 2013. Optimizing Satellite-Based Precipitation Estimation for Nowcasting of Rainfall and Flash Flood Events over the South African Domain. Remote Sensing 5 (11), 5702–5724.
Coning, E. de, Poolman, E., 2011. South African Weather Service operational satellite based precipitation estimation technique: Applications and improvements. Hydrol. Earth Syst. Sci. 15 (4), 1131–1145.
Coulibaly, P., Dibike, Y.B., Anctil, F., 2005. Downscaling Precipitation and Temperature with Temporal Neural Networks. J. Hydrometeor 6 (4), 483–496.
Dall'aglio, G., Kotz, S., Salinetti, G. (Eds.), 1991. Advances in Probability Distributions with Given Marginals: Beyond the Copulas, 1st ed. Springer Netherlands.
Daneshkhah, A., Remesan, R., Chatrabgoun, O., Holman, I.P., 2016. Probabilistic modeling of flood characterizations with parametric and minimum information pair-copula model. Journal of Hydrology 540, 469–487.
Dee, D.P., Uppala, S.M., Simmons, A.J., Berrisford, P., Poli, P., Kobayashi, S., Andrae, U., Balmaseda, M.A., Balsamo, G., Bauer, P., Bechtold, P., Beljaars, A.C.M., van de Berg, L., Bidlot, J., Bormann, N., Delsol, C., Dragani, R., Fuentes, M., Geer, A.J., Haimberger, L., Healy, S.B., Hersbach, H., Hólm, E.V., Isaksen, L., Kållberg, P., Köhler, M., Matricardi, M., McNally, A.P., Monge-Sanz, B.M., Morcrette, J.-J., Park, B.-K., Peubey, C., Rosnay, P. de, Tavolato, C., Thépaut, J.-N., Vitart, F., 2011. The ERA-Interim reanalysis: Configuration and performance of the data assimilation system. Q.J.R. Meteorol. Soc. 137 (656), 553–597.
Demarta, S., McNeil, A.J., 2004. The t Copula and Related Copulas, Department of Mathematics, Federal Institute of Technology, Zurich, 20 pp.
Dezfuli, A.K., Ichoku, C.M., Huffman, G.J., Mohr, K.I., Selker, J.S., van de Giesen, N., Hochreutener, R., Annor, F.O., 2017. Validation of IMERG Precipitation in Africa. J. Hydrometeor. 18 (10), 2817–2825.
Dinku, T., Ceccato, P., Grover-Kopec, E., Lemma, M., Connor, S.J., Ropelewski, C.F., 2007. Validation of satellite rainfall products over East Africa's complex topography. International Journal of Remote Sensing 28 (7), 1503–1526.
Dong, H.O., Patton, A.J., 2015. Modelling Dependence in High Dimensions with Factor Copulas. FEDS 2015 (051), 1–41.
Dong, J., Walker, J.P., Houser, P.R., 2005. Factors affecting remotely sensed snow water equivalent uncertainty. Remote Sensing of Environment 97 (1), 68–82.
Dorninger, M., Schneider, S., Steinacker, R., 2008. On the interpolation of precipitation data over complex terrain. Meteorol Atmos Phys 101 (3-4), 175–189.
Dupuis, D., 2007. Using Copulas in Hydrology: Benefits, Cautions, and Issues. JOURNAL OF HYDROLOGIC ENGINEERING 12 (4).
Ebert, E.E., Janowiak, J.E., Kidd, C., 2007. Comparison of Near-Real-Time Precipitation Estimates from Satellite Observations and Numerical Models. Bull. Amer. Meteor. Soc. 88 (1), 47–64.

Embrechts, P., Lindskog, F., McNeil, A., 2001. Modelling Dependence with Copulas and Applications to Risk Management, Department of Mathematics, Federal Institute of Technology, Zurich.

Fang, J., Du, J., Xu, W., Shi, P., Li, M., Ming, X., 2013. Spatial downscaling of TRMM precipitation data based on the orographical effect and meteorological conditions in a mountainous area. Advances in Water Resources 61, 42–50.

Favre, A.-C., El Adlouni, S., Perreault, L., Thiémonge, N., Bobée, B., 2004. Multivariate hydrological frequency analysis using copulas. Water Resour. Res. 40 (1), 2825.

Fleming K., Awange J.L., Kuhn M., Featherstone W. E., 2011. Evaluating the TRMM 3B43 monthly precipitation product using gridded raingauge data over Australia. Australian Meteorological and Oceanographic Journal 61, 171–184.

Foufoula-Georgiou, E., Vuruputur, V. (Eds.), 2001. Spatial Patterns in Catchment Hydrology: Observations and Modelling. Patterns and Organisation in Precipitation. Cambridge University Press.

Garcia-Martino, A.R., Warner, G.S., Scatena, F.N., Civco, D.L., 1996. Rainfall, Runoff and Elevation Relationships in the Luquillo Mountains of Puerto Rico. Caribbean Journal of Science 32 (4), 413–424.

Gebere, S., Alamirew, T., Merkel, B., Melesse, A., 2015. Performance of High Resolution Satellite Rainfall Products over Data Scarce Parts of Eastern Ethiopia. Remote Sensing 7 (9), 11639–11663.

Gebregiorgis, A.S., Kirstetter, P.-E., Hong, Y.E., Gourley, J.J., Huffman, G.J., Petersen, W.A., Xue, X., Schwaller, M.R., 2018. To What Extent is the Day 1 GPM IMERG Satellite Precipitation Estimate Improved as Compared to TRMM TMPA-RT? J. Geophys. Res. Atmos. 53 (8), 4434.

Genest, C., Favre, A.C., 2007. Everything You Always Wanted to Know about Copula Modeling but Were Afraid to Ask. JOURNAL OF HYDROLOGIC ENGINEERING 12 (4), 347–368.

Germann, U., Berenguer, M., Sempere-Torres, D., Salvade, G. (Eds.), 2006a. Ensemble radar precipitation — a new topic on the radar horizon.

Germann, U., Berenguer, M., Sempere-Torres, D., Zappa, M., 2009. REAL-Ensemble radar precipitation estimation for hydrology in a mountainous region. Q.J.R. Meteorol. Soc. 135 (639), 445–456.

Germann, U., Galli, G., Boscacci, M., Bolliger, M., 2006b. Radar precipitation measurement in a mountainous region. Q. J. R. Meteorol. Soc. 132 (618), 1669–1692.

Gharabeigli, F., 2013. Downscaling of TRMM rainfall data and its comparison with doppler meteorological radar data in the coastal areas of the Caspian Sea. Master Thesis, Guilan.

Gosset, M., Viarre, J., Quantin, G., Alcoba, M., 2013. Evaluation of several rainfall products used for hydrological applications over West Africa using two high-resolution gauge networks. Q.J.R. Meteorol. Soc. 139 (673), 923–940.

Grimaldi, S., Serinaldi, F., 2006. Asymmetric copula in multivariate flood frequency analysis. Advances in Water Resources 29 (8), 1155–1167.

Guo, H., Chen, S., Bao, A., Hu, J., Gebregiorgis, A., Xue, X., Zhang, X., 2015. Inter-Comparison of High-Resolution Satellite Precipitation Products over Central Asia. Remote Sensing 7 (12), 7181–7211.

Gutiérrez, J.M., San-Martín, D., Brands, S., Manzanas, R., Herrera, S., 2013. Reassessing Statistical Downscaling Techniques for Their Robust Application under Climate Change Conditions. J. Climate 26 (1), 171–188.
Habib, E., Aduvala, A.V., Meselhe, E.A., 2008. Analysis of radar-rainfall error characteristics and implications for streamflow simulation uncertainty. Hydrological Sciences Journal 53 (3), 568–587.
Habib, E., Henschke, A., Adler, R.F., 2009a. Evaluation of TMPA satellite-based research and real-time rainfall estimates during six tropical-related heavy rainfall events over Louisiana, USA. Atmospheric Research 94 (3), 373–388.
Habib, E., Krajewski, W.F., Ciach, G.J., 2001. Estimation of Rainfall Interstation Correlation. J. Hydrometeor 2 (6), 621–629.
Habib, E., Larson, B.F., Graschel, J., 2009b. Validation of NEXRAD multisensor precipitation estimates using an experimental dense rain gauge network in south Louisiana. Journal of Hydrology 373 (3-4), 463–478.
Haiden, T., Kann, A., Wittmann, C., Pistotnik, G., Bica, B., Gruber, C., 2011. The Integrated Nowcasting through Comprehensive Analysis (INCA) System and Its Validation over the Eastern Alpine Region. Wea. Forecasting 26 (2), 166–183.
Hakuba, M.Z., Folini, D., Sanchez-Lorenzo, A., Wild, M., 2014. Spatial representativeness of ground-based solar radiation measurements-Extension to the full Meteosat disk. J. Geophys. Res. Atmos. 119 (20), 12.
Ham, S.-H., Sohn, B.-J., Yang, P., Baum, B.A., 2009. Assessment of the Quality of MODIS Cloud Products from Radiance Simulations. J. Appl. Meteor. Climatol. 48 (8), 1591–1612.
Hazarika M. K., Kafle T.P., Sharma R., Karki S., Shrestha R. M., Samarkoon L., 2007. STATISTICAL APPROACH TO DISCHARGE PREDICTION FOR FLOOD FORECASTS USING TRMM DATA.
He, X., Chaney, N.W., Schleiss, M., Sheffield, J., 2016. Spatial downscaling of precipitation using adaptable random forests. Water Resour. Res. 52 (10), 8217–8237.
Hennessy, K.J., Suppiah, R., 1999. Australian rainfall changes, 1910–1955. Australian Meteorology Magazine 48, 1–13.
Hiebl, J., Reisenhofer, S., Auer, I., Böhm, R., Schöner, W., 2011. Multi-methodical realisation of Austrian climate maps for 1971–2000. Adv. Sci. Res. 6, 19–26.
Hodge, V., Austin, J., 2004. A Survey of Outlier Detection Methodologies. Artificial Intelligence Review 22 (2), 85–126.
Hossain, F., Anagnostou, E.N., 2005. Numerical investigation of the impact of uncertainties in satellite rainfall estimation and land surface model parameters on simulation of soil moisture. Advances in Water Resources 28 (12), 1336–1350.
Hossain, F., Huffman, G.J., 2008. Investigating Error Metrics for Satellite Rainfall Data at Hydrologically Relevant Scales. J. Hydrometeor 9 (3), 563–575.
Hou, A.Y., Kakar, R.K., Neeck, S., Azarbarzin, A.A., Kummerow, C.D., Kojima, M., Oki, R., Nakamura, K., Iguchi, T., 2014. The Global Precipitation Measurement Mission. Bull. Amer. Meteor. Soc. 95 (5), 701–722.
Huffman, G.J., Bolvin, D.T., Braithwaite, D., Hsu, K., Joyce R., 2015. Algorithm Theoretical Basis Document (ATBD) Version 4.5: NASA Global Precipitation Measurement (GPM) Integrated Multi-satellitE Retrievals for GPM (IMERG), 30 pp.

Huffman, G.J., Bolvin, D.T., Nelkin, E.J., 2017a. Integrated Multi-satellitE Retrievals for GPM (IMERG) Technical Documentation. https://pmm.nasa.gov/sites/default/files/document_files/IMERG_doc.pdf, 54 pp.

Huffman, G.J., Bolvin, D.T., Nelkin, E.J., Stocker, E.F., 2017b. V04 IMERG Final Run Release Notes. IMERG Tech Document.

Huffman, G.J., Bolvin, D.T., Nelkin, E.J., Wolff, D.B., Adler, R.F., Gu, G., Hong, Y., Bowman, K.P., Stocker, E.F., 2007. The TRMM Multisatellite Precipitation Analysis (TMPA): Quasi-Global, Multiyear, Combined-Sensor Precipitation Estimates at Fine Scales. J. Hydrometeor 8 (1), 38–55.

Huffman, G.J., Bolvin, D. T., Nelkin, E. J., 20 January-2015. Day 1 IMERG Final Run Release Notes: for the NASA Global Precipitation Measurement (GPM) Integrated Multi-satellitE Retrievals for GPM (I-MERG). GPM Project, 9 pp.

Immerzeel, W.W., Rutten, M.M., Droogers, P., 2009. Spatial downscaling of TRMM precipitation using vegetative response on the Iberian Peninsula. Remote Sensing of Environment 113 (2), 362–370.

Javanmard, S., Yatagai, A., Nodzu, M.I., BodaghJamali, J., Kawamoto, H., 2010. Comparing high-resolution gridded precipitation data with satellite rainfall estimates of TRMM_3B42 over Iran. Adv. Geosci. 25, 119–125.

Jia, S., Zhu, W., Lű, A., Yan, T., 2011. A statistical spatial downscaling algorithm of TRMM precipitation based on NDVI and DEM in the Qaidam Basin of China. Remote Sensing of Environment 115 (12), 3069–3079.

Jing, W., Yang, Y., Yue, X., Zhao, X., 2016. A Comparison of Different Regression Algorithms for Downscaling Monthly Satellite-Based Precipitation over North China. Remote Sensing 8 (12), 835.

Joe, H., 1997. Multivariate Models and Dependence Concepts. Chapman and Hall, London.

Johnston, K., 2004. ArcGIS 9: using ArcGIS geostatistical analyst.

Joyce, R.J., Janowiak, J.E., Arkin, P.A., Xie, P., 2004. CMORPH: A Method that Produces Global Precipitation Estimates from Passive Microwave and Infrared Data at High Spatial and Temporal Resolution. Journal of Hydrometeorology 5.

Karl, T.R., Knight, R.W., 1998. Secular Trends of Precipitation Amount, Frequency, and Intensity in the United States. Bull. Amer. Meteor. Soc. 79 (2), 231–241.

Karl, T.R., Knight, R.W., Plummer, N., 1995. Trends in high-frequency climate variability in the twentieth century. Nature 377, 217–220.

Kelly, K.S., Krzysztofowicz, R., 1997. A bivariate meta-Gaussian density for use in hydrology. Stochastic Hydrol Hydraul 11 (1), 17–31.

Khazaei, B., Hosseini, S.M., 2015. Improving the performance of water balance equation using fuzzy logic approach. Journal of Hydrology 524, 538–548.

Khodadoust, S.S., Saghafian, B., Moazami, S., 2016. Comprehensive evaluation of 3-hourly TRMM and half-hourly GPM-IMERG satellite precipitation products. International Journal of Remote Sensing 38 (2), 558–571.

Kobayshi, T., MASUDA, K., 2009. Changes in Cloud Optical Thickness and Cloud Drop Size Associated with Precipitation Measured with TRMM Satellite. JMSJ 87 (4), 593–600.

Krakauer, N., Pradhanang, S., Lakhankar, T., Jha, A., 2013. Evaluating Satellite Products for Precipitation Estimation in Mountain Regions: A Case Study for Nepal. Remote Sensing 5 (8), 4107–4123.

Kuhn, G., Khan, S., Ganguly, A.R., Branstetter, M.L., 2007. Geospatial–temporal dependence among weekly precipitation extremes with applications to observations and climate model simulations in South America. Advances in Water Resources 30 (12), 2401–2423.

Laio, F., 2004. Cramer-von Mises and Anderson-Darling goodness of fit tests for extreme value distributions with unknown parameters. Water Resour. Res. 40 (9), 1323.

Lee, S., Evangelista, D.G., 2006. Earthquake-induced landslide-susceptibility mapping using an artificial neural network. Nat. Hazards Earth Syst. Sci. 6 (5), 687–695.

Legates, D.R., Davis, R.E., 1997. The continuing search for an anthropogenic climate change signal: Limitations of correlation-based approaches. Geophys. Res. Lett. 24 (18), 2319–2322.

Li, Z., Yang, D., Hong, Y., 2013. Multi-scale evaluation of high-resolution multi-sensor blended global precipitation products over the Yangtze River. Journal of Hydrology 500, 157–169.

Liang, S., Li, X., Wang, J. (Eds.), 2012. Advanced Remote Sensing: Soil Moisture Content. Academic Press, Boston.

Liang, X., Guo, J., Leung, L.R., 2004. Assessment of the effects of spatial resolutions on daily water flux simulations. Journal of Hydrology 298 (1-4), 287–310.

Liu, Z., 2016. Comparison of Integrated Multisatellite Retrievals for GPM (IMERG) and TRMM Multisatellite Precipitation Analysis (TMPA) Monthly Precipitation Products: Initial Results. J. Hydrometeor 17 (3), 777–790.

Liu, Z., Guo, S., Xiong, L., Xu, C.-Y., 2017. Hydrological uncertainty processor based on a copula function. Hydrological Sciences Journal 63 (1), 74–86.

Madsen, L., 2009. Maximum likelihood estimation of regression parameters with spatially dependent discrete data. JABES 14 (4), 375–391.

Mahmud, M., Numata, S., Matsuyama, H., Hashim, M., Hosaka, T., 2015. Assessment of Effective Seasonal Downscaling of TRMM Precipitation Data in Peninsular Malaysia. Remote Sensing 7 (4), 4092–4111.

Manz, B., Páez-Bimos, S., Horna, N., Buytaert, W., Ochoa-Tocachi, B., Lavado-Casimiro, W., Willems, B., 2017. Comparative Ground Validation of IMERG and TMPA at Variable Spatiotemporal Scales in the Tropical Andes. J. Hydrometeor. 18 (9), 2469–2489.

Mao, G., Vogl, S., Laux, P., Wagner, S., Kunstmann, H., 2015. Stochastic bias correction of dynamically downscaled precipitation fields for Germany through Copula-based integration of gridded observation data. Hydrol. Earth Syst. Sci. 19 (4), 1787–1806.

Michele, C. de, Salvadori, G., 2003. A Generalized Pareto intensity-duration model of storm rainfall exploiting 2-Copulas. J. Geophys. Res. 108 (D2), 225.

Mitchell, T.D., Jones, P.D., 2005. An improved method of constructing a database of monthly climate observations and associated high-resolution grids. Int. J. Climatol. 25 (6), 693–712.

Moazami, S., Golian, S., Hong, Y., Sheng, C., Kavianpour, M.R., 2015. Comprehensive evaluation of four high-resolution satellite precipitation products over diverse climate conditions in Iran. Hydrological Sciences Journal, 150527103244004.

Moazami, S., Golian, S., Kavianpour, M.R., Hong, Y., 2013. Comparison of PERSIANN and V7 TRMM Multi-satellite Precipitation Analysis (TMPA) products with rain gauge data over Iran. International Journal of Remote Sensing 34 (22), 8156–8171.
Moazami, S., Golian, S., Kavianpour, M.R., Hong, Y., 2014. Uncertainty analysis of bias from satellite rainfall estimates using copula method. Atmospheric Research 137, 145–166.
Modarres, R., 2006. Regional precipitation climates of Iran. Journal of Hydrology (NZ) 45 (1), 13–27.
Nasrollahi, N. False Alarm in Satellite Precipitation Data, 7 pp.
Nelson, R., 2006. An Introduction to Copulas. Springer, New York,
New, M., Hulme, M., Jones, P., 1999. Representing Twentieth-Century Space–Time Climate Variability: Part I: Development of a 1961-90 Mean Monthly Terrestrial Climatology. American Meteorological Society, Journal of Climate 12, 829–856.
Park, N.-W., 2013. Spatial Downscaling of TRMM Precipitation Using Geostatistics and Fine Scale Environmental Variables. Advances in Meteorology 2013 (11), 1–9.
Park, N.-W., Hong, S., Kyriakidis, P.C., Lee, W., Lyu, S.-J., 2016. Geostatistical downscaling of AMSR2 precipitation with COMS infrared observations. International Journal of Remote Sensing 37 (16), 3858–3869.
Pasini, A., 2015. Artificial neural networks for small dataset analysis. Journal of thoracic disease 7 (5), 953–960.
Petty, G.W., Krajewski, W.F., 1997. Satellite estimation of precipitation over land. Hydrological Sciences Journal 41 (4), 433–451.
Pham, M.T., 2016. Copula-based Stochastic Modelling of Evapotranspiration Time Series Conditioned on Rainfall as Design Tool in Water Resources Management, Ghent University, Ghent.
Platnick, S., King, D.M., Meyer, G.K., Wind, G., Amarasinghe, N., Marchant, B., Arnold, T., Zhang, Z., Hubanks, A.P., Ridgway, B., Riedi, J., 2015. MODIS Cloud Optical Properties: User Guide for the Collection 6 Level-2 MOD06/MY06 Product and Associated Level-3 Datasets, 145 pp.
Platnick, S., King, M.D., Ackerman, S.A., Menzel, W.P., Baum, B.A., Riedi, J.C., Frey, R.A., 2003. The MODIS cloud products: Algorithms and examples from terra. IEEE Trans. Geosci. Remote Sensing 41 (2), 459–473.
Plummer, N., Salinger, M.J., Nicholls, N., 1999. Changes in Climate Extremes Over the Australian Region and New Zealand During the Twentieth Century. Climatic Change 42, 183–202.
Prakash, S., Mitra, A.K., AghaKouchak, A., Liu, Z., Norouzi, H., Pai, D.S., 2016. A preliminary assessment of GPM-based multi-satellite precipitation estimates over a monsoon dominated region. Journal of Hydrology.
Precipitation Processing System at NASA GSFC, 2015. GPM merged radiometer global .1 x.1 deg half-hourly precipitation retrieval, 9 pp.
Qu, J.J., Powell, A.M., Siva Kumar, M.V.K., 2013. Satellite-based applications on climate change. Springer, Dordrecht, London.
Renard, B., Lang, M., 2007. Use of a Gaussian copula for multivariate extreme value analysis: Some case studies in hydrology. Advances in Water Resources 30 (4), 897–912.

Renzullo, L., Chappell, A., Raupach, T., Dyce, P., Li, M., Shao, Q., 2011. An Assessment of Statistically Blended Satellite-Gauge Precipitation Data for Daily Rainfall Analysis in Australia.
Retalis, A., Tymvios, F., Katsanos, D., Michaelides, S., 2017. Downscaling CHIRPS precipitation data: An artificial neural network modelling approach. International Journal of Remote Sensing 38 (13), 3943–3959.
Rigol, J.P., Jarvis, C.H., Stuart, N., 2010. Artificial neural networks as a tool for spatial interpolation. International Journal of Geographical Information Science, 323–343.
Rubel, F., Brugger, K., Haslinger, K., Auer, I., 2017. The climate of the European Alps: Shift of very high resolution Köppen-Geiger climate zones 1800–2100. metz 26 (2), 115–125.
Rummukainen, M., 2010. State-of-the-art with regional climate models. WIREs Climate Change 1 (1), 82–96.
Salvadori, G., de-Michele, C., 2007. On the Use of Copulas in Hydrology: Theory and Practice. Journal of Hydrologic Emgineering 12 (4). https://doi.org/10.1061/(ASCE)1084-0699(2007)12:4(369).
Schneider, U., Ziese, M., Becker, A., Meyer-Christoffer, A., Finger, P., Global Precipitation Climatology Centre (GPCC), Deutscher Wetterdienst, Offenbach a. M., Germany, May-2015. Global Precipitation Analysis Products of the GPCC, 14 pp.
Schölzel, C., Friederichs, P., 2008. Multivariate Non-Normally Distributed Random Variables in Climate Research – Introduction to the Copula Approach. Nonlinear Processes Geophysics 15 (5). https://www.nonlin-processes-geophys.net/15/761/2008/.
Schoof, J.T., Pryor, S.C., 2001. Downscaling temperature and precipitation: A comparison of regression-based methods and artificial neural networks. Int. J. Climatol. 21 (7), 773–790.
Schuol, J., Abbaspour, K.C., Yang, H., Srinivasan, R., Zehnder, A.J.B., 2008. Modeling blue and green water availability in Africa. Water Resour. Res. 44 (7), 413.
Schweizer, B. (Ed.), 1991. Thirty years of copulas. In: Advance in Probability Distributions with Given Marginals, 1st ed. Springer Netherlands.
Sen, A., Gümüsay, M.U., Kavas, A., Bulucu, U., 2008. Programming an Artificial Neural Network Tool for Spatial Interpolation in GIS - A Case Study for Indoor Radio Wave Propagation of WLAN. Sensors (Basel, Switzerland) 8 (9), 5996–6014.
Sene, K., 2013. Precipitation Measurement, in: Sene, K. (Ed.), Flash Floods. Springer Netherlands, Dordrecht, pp. 33–70.
Serinaldi, F., 2008. Analysis of inter-gauge dependence by Kendall's τK, upper tail dependence coefficient, and 2-copulas with application to rainfall fields. Stoch Environ Res Risk Assess 22 (6), 671–688.
Shapiro, L., Stochman, G. (Eds.), 2001. Computer Vision: Filtering and Enhancing Images. Prentice Hall PTR Upper Saddle River, NJ, USA, 61 pp.
Sharifi, E., Steinacker, R., Saghafian, B., 2016. Assessment of GPM-IMERG and Other Precipitation Products against Gauge Data under Different Topographic and Climatic Conditions in Iran: Preliminary Results. Remote Sensing 8 (2), 135.
Sharifi, E., Steinacker, R., Saghafian, B., 2018. Multi time-scale evaluation of high-resolution satellite-based precipitation products over northeast of Austria. Atmospheric Research 206, 46–63.

Shen, Y., Xiong, A., Wang, Y., Xie, P., 2010. Performance of high-resolution satellite precipitation products over China. J. Geophys. Res. 115 (D2).

Shi, Y., Song, L., Xia, Z., Lin, Y., Myneni, R., Choi, S., Wang, L., Ni, X., Lao, C., Yang, F., 2015. Mapping Annual Precipitation across Mainland China in the Period 2001–2010 from TRMM3B43 Product Using Spatial Downscaling Approach. Remote Sensing 7 (12), 5849–5878.

Shrestha, M.S., 2011. Bias-Adjustment of Satellite-Based Rainfall Estimates over the Central Himalayas of Nepal for Flood Prediction. Doctor of Engineering Thesis, Japan, 164 pp.

Simonović, P.S., 2012. Floods in a changing climate. Risk management, 1st ed. Cambridge Univ. Press, Cambridge.

Sklar, A., 1959. Fonctions de répartition à n dimensions et leurs marges. Publications de l'Institut de Statistique de L'Universit'e de: Paris 8, 229–231.

Sklar, A., 1996. Random Variables, Distribution Functions, and Copulas: A Personal Look Backward and Forward. Lecture Notes-Monograph Series 28, 1–14. https://www.jstor.org/stable/pdf/4355880.pdf.

Sohn, B.J., Ryu, G.-H., Song, H.-J., Ou, M.-L., 2013. Characteristic Features of Warm-Type Rain Producing Heavy Rainfall over the Korean Peninsula Inferred from TRMM Measurements. Mon. Wea. Rev. 141 (11), 3873–3888.

Song, X.-K.P., 2000. Multivariate Dispersion Models Generated From Gaussian Copula. Scand J Stat 27 (2), 305–320.

Song, X.-K.P., Li, M., Yuan, Y., 2009. Joint regression analysis of correlated data using Gaussian copulas. Biometrics 65 (1), 60–68.

Sorooshian, S., Hsu, K.-L., Gao, X., Gupta, H.V., Imam, B., Braithwaite, D., 2000. Evaluation of PERSIANN System Satellite–Based Estimates of Tropical Rainfall. Bull. Amer. Meteor. Soc. 81 (9), 2035–2046.

Steinacker, R., Ratheiser, M., Bica, B., Chimani, B., Dorninger, M., Gepp, W., Lotteraner, C., Schneider, S., Tschannett, S., 2006. A Mesoscale Data Analysis and Downscaling Method over Complex Terrain. Mon. Wea. Rev. 134 (10), 2758–2771.

Su, F., Hong, Y., Lettenmaier, D.P., 2008. Evaluation of TRMM Multisatellite Precipitation Analysis (TMPA) and Its Utility in Hydrologic Prediction in the La Plata Basin. J. Hydrometeor 9 (4), 622–640.

Sungmin, O., Foelsche, U., Kirchengast, G., Fuchsberger, J., 2016. Validation and correction of rainfall data from the WegenerNet high density network in southeast Austria. Journal of Hydrology.

Sungmin, O., Foelsche, U., Kirchengast, G., Fuchsberger, J., Tan, J., Petersen, W.A., 2017. Evaluation of GPM IMERG Early, Late, and Final rainfall estimates with WegenerNet gauge data in southeast Austria. Hydrol. Earth Syst. Sci. Discuss., 1–21.

Tang, J., Niu, X., Wang, S., Gao, H., Wang, X., Wu, J., 2016. Statistical downscaling and dynamical downscaling of regional climate in China: Present climate evaluations and future climate projections. J. Geophys. Res. Atmos. 121 (5), 2110–2129.

Tapiador, F.J., Turk, F.J., Petersen, W., Hou, A.Y., García-Ortega, E., Machado, L.A.T., Angelis, C.F., Salio, P., Kidd, C., Huffman, G.J., Castro, M. de, 2012. Global precipitation measurement: Methods, datasets and applications. Atmospheric Research 104-105, 70–97.

Taylor, K.E., 2001. Summarizing multiple aspects of model performance in a single diagram. J. Geophys. Res. 106 (D7), 7183–7192.
Teo, C.-K., Grimes, D.I.F., 2007. Stochastic modelling of rainfall from satellite data. Journal of Hydrology 346 (1-2), 33–50.
Tesfagiorgis, K., Mahani, S.E., Krakauer, N.Y., Khanbilvardi, R., 2011. Bias correction of satellite rainfall estimates using a radar-gauge product – a case study in Oklahoma (USA). Hydrol. Earth Syst. Sci. 15 (8), 2631–2647.
Thornes, J.E., Stephenson, D.B., 2001. How to judge the quality and value of weather forecast products. Meteorol. Appl. 8 (3), 307–314.
Tian, Y., Huffman, G.J., Adler, R.F., Tang, L., Sapiano, M., Maggioni, V., Wu, H., 2013. Modeling errors in daily precipitation measurements: Additive or multiplicative? Geophys. Res. Lett. 40 (10), 2060–2065.
Tian, Y., Peters-Lidard, C.D., Choudhury, B.J., Garcia, M., 2007. Multitemporal Analysis of TRMM-Based Satellite Precipitation Products for Land Data Assimilation Applications. J. Hydrometeor 8 (6), 1165–1183.
Tian, Y., Peters-Lidard, C.D., Eylander, J.B., Joyce, R.J., Huffman, G.J., Adler, R.F., Hsu, K.-L., Turk, F.J., Garcia, M., Zeng, J., 2009. Component analysis of errors in satellite-based precipitation estimates. J. Geophys. Res. 114 (D24), 1377.
Tobin, K.J., Bennett, M.E., 2010. Adjusting Satellite Precipitation Data to Facilitate Hydrologic Modeling. J. Hydrometeor 11 (4), 966–978.
vanZanten, M.C., Stevens, B., Vali, G., Lenschow, D.H., 2005. Observations of Drizzle in Nocturnal Marine Stratocumulus. J. Atmos. Sci. 62 (1), 88–106.
Verlinde, J., 2011. TRMM Rainfall Data Downscaling: In the Pangani Basin in Tanzania. Master thesis, Delft.
Vila, D.A., de Goncalves, Luis Gustavo G., Toll, D.L., Rozante, J.R., 2009. Statistical Evaluation of Combined Daily Gauge Observations and Rainfall Satellite Estimates over Continental South America. J. Hydrometeor 10 (2), 533–543.
Villarini, G., Krajewski, W.F., Ciach, G.J., Zimmerman, D.L., 2009. Product-error-driven generator of probable rainfall conditioned on WSR-88D precipitation estimates. Water Resour. Res. 45 (1), n/a-n/a.
Villarini, G., Mandapaka, P.V., Krajewski, W.F., Moore, R.J., 2008a. Rainfall and sampling uncertainties: A rain gauge perspective. J. Geophys. Res. 113 (D11), 385.
Villarini, G., Serinaldi, F., Krajewski, W.F., 2008b. Modeling radar-rainfall estimation uncertainties using parametric and non-parametric approaches. Advances in Water Resources 31 (12), 1674–1686.
Vu, M.T., Aribarg, T., Supratid, S., Raghavan, S.V., Liong, S.-Y., 2016. Statistical downscaling rainfall using artificial neural network: Significantly wetter Bangkok? Theor Appl Climatol 126 (3-4), 453–467.
Wang, K., Augustine, J., Dickinson, R.E., 2012. Critical assessment of surface incident solar radiation observations collected by SURFRAD, USCRN and AmeriFlux networks from 1995 to 2011. J. Geophys. Res. 117 (D23), n/a-n/a.
Wang, X., Gebremichael, M., Yan, J., 2010. Weighted likelihood copula modeling of extreme rainfall events in Connecticut. Journal of Hydrology 390 (1-2), 108–115.
Werner, M., 2003. Identification of Multivariate Outliers in Large Data Sets. Doctor of Philosophy Thesis, Denver, 241 pp.

Wilks Daniel S., 2006. Statistical Methods in the Atmospheric Sciences, Second Edition ed. Elsevier, NY-USA, 649 pp.
William B. Fisher, 1968. THE CAMBRIDGE HISTORY OF IRAN: Climate. Ganji, Moḥammad Ḥasan. University Press, Cambridge, 804 pp.
Willmott, C.J., 1984. On the Evaluation of Model Performance in Physical Geography, in: Gaile, G.L., Willmott, C.J. (Eds.), Spatial Statistics and Models. Springer Netherlands, Dordrecht, pp. 443–460.
Wong, W.F.J., Chiu, L.S., 2008. Spatial and Temporal Analysis of Rain Gauge Data and TRMM Rainfall Retrievals in Hong Kong. Annals of GIS 14 (2), 105–112.
Xie, P., Arkin, P.A., 1995. An Intercomparison of Gauge Observation and Satellite Estimates of Monthly Precipitation. Journal of Applied Meteorology 34.
Xie, P., Chen, M., Yang, S., Yatagai, A., Hayasaka, T., Fukushima, Y., Liu, C., 2007. A Gauge-Based Analysis of Daily Precipitation over East Asia. J. Hydrometeor 8 (3), 607–626.
Xu, G., Xu, X., Liu, M., Sun, A., Wang, K., 2015. Spatial Downscaling of TRMM Precipitation Product Using a Combined Multifractal and Regression Approach: Demonstration for South China. Water 7 (12), 3083–3102.
Yatagai, A., Arakawa, O., Kamiguchi, K., Kawamoto, H., Nodzu, M.I., Hamada, A., 2009. 44 Year Daily Gridded Precipitation Dataset for Asia Based on a Dense Network of Rain Gauges. SOLA 5, 137–140.
Yatagai, A., Xie, P., Alpert, P., 2008. Development of a daily gridded precipitation data set for the Middle East. Adv. Geosci. 12, 165–170.
Yong, B., Liu, D., Gourley, J.J., Tian, Y., Huffman, G.J., Ren, L., Hong, Y., 2015. Global View Of Real-Time Trmm Multisatellite Precipitation Analysis: Implications For Its Successor Global Precipitation Measurement Mission. Bull. Amer. Meteor. Soc. 96 (2), 283–296.
Yong, B., Ren, L.-L., Hong, Y., Wang, J.-H., Gourley, J.J., Jiang, S.-H., Chen, X., Wang, W., 2010. Hydrologic evaluation of Multisatellite Precipitation Analysis standard precipitation products in basins beyond its inclined latitude band: A case study in Laohahe basin, China. Water Resour. Res. 46 (7), n/a-n/a.
Zhang, L., Singh, V.P., 2007. Bivariate rainfall frequency distributions using Archimedean copulas. Journal of Hydrology 332 (1-2), 93–109.
Zhang, Y., Li, Y., Ji, X., Luo, X., Li, X., 2018. Fine-Resolution Precipitation Mapping in a Mountainous Watershed: Geostatistical Downscaling of TRMM Products Based on Environmental Variables. Remote Sensing 10 (1), 119.
Zhang, Y., Long, C.N., Rossow, W.B., Dutton, E.G., 2010. Exploiting diurnal variations to evaluate the ISCCP-FD flux calculations and radiative-flux-analysis-processed surface observations from BSRN, ARM, and SURFRAD. J. Geophys. Res. 115 (D15), 38.
Zheng, X., Zhu, J., 2014. A methodological approach for spatial downscaling of TRMM precipitation data in North China. International Journal of Remote Sensing 36 (1), 144–169.

Curriculum Vitae

Personal Information

Full name	Ehsan Sharifi
Date of Birth	17 March 1983, in Iran
Address	Department of Meteorology and Geophysics (IMGW), University of Vienna, Althanstrasse 14, UZA II, 2D506, 1090 Vienna, Austria
Phone	+43-676-976-6304; +43-1-4277-53737
Email	ehsan.sharifi@univie.ac.at ; ehsansharifi83@gmail.com
Homepage	https://www.researchgate.net/profile/Ehsan_Sharifi4 https://orcid.org/0000-0001-7181-8406

Education

2013-2019	Ph.D. in Meteorology, University of Vienna, Vienna, Austria.
2006-2009	M.Sc. in Agricultural Engineering, Islamic Azad University (IAU), Borujerd Branch, Iran
2001-2005	B.Sc. in Agricultural Engineering, Islamic Azad University (IAU), Kermanshah Branch, Iran

Research

2016-2017	University of Vienna - Department of Meteorology and Geophysics, Project Title: Satellite-based Precipitation Analysis. Advisor: Reinhold Steinacker
2017-2018	University of Vienna - Department of Meteorology and Geophysics, Project Title: Mechanismen des durchgreifens großräumiger strömungen ins Aichfeld, Detektion von typischen stromungsmustern, unterschungen der stabilitat und ausbreitungsbedingungen unter dem Aichfeld

Advisor: Manfred Dorninger

2018-Present BOKU University - Department of Water - Atmosphere - Environment, Project Title: SERBian-Austrian-Italian (SAI) partnership FORcing EXCELLence in ecosystem research

Advisor: Josef Eitzinger

Publication

Pre-review Publication

Sharifi, **E.**, Steinacker, R., Saghafian, B., **2019**. Downscaling Satellite Precipitation Estimates with Multiple Linear Regression, Artificial Neural Networks and Spline Interpolation. *Journal of Geophysical Research: Atmospheres*, 124. https://doi.org/10.1029/2018JD028795.

Sharifi, **E.**, Saghafian, B., Steinacker, R., **2019**. Copula-based Stochastic Uncertainty Analysis of Satellite Precipitation Products. *Journal of Hydrology*, accepted: January 13, 2019, HYDROL28354.

Sharifi, **E.**, Steinacker, R., Saghafian, B., **2018**. Multi time-scale evaluation of high-resolution satellite-based precipitation products over northeast of Austria. *Atmospheric Research*, 206, 46-63, https://doi:10.1016/j.atmosres.2018.02.020.

Sharifi, **E.**, Steinacker, R., Saghafian, B., **2016**. Assessment of GPM-IMERG and Other Precipitation Products against Gauge Data under Different Topographic and Climatic Conditions in Iran: Preliminary Results. Remote Sensing 8 (2), 135, https://doi.org/10.3390/rs8020135.

Recent conference contribution

Oral presentation:

Sharifi, **E.**, Steinacker, R., Saghafian., B., **2016**: Performance Evaluation of the Newest Generation Satellite-Based Precipitation Product with high Spatio-Temporal Resolution. 6th National Conference on Water Resources Management, University of Kurdistan-Iran; 04/2016

Poster presentation:

Sharifi, **E**., Saghafian, B., Steinacker, R., **2019**: Using a Machine Learning Algorithm for Spatial Downscaling of Satellite Precipitation Products. European Geosciences Union (EGU) General Assembly 2019, Vienna, Austria.

Sharifi, **E**., Steinacker, R., Saghafian., B., **2018**: One Dimensional Satellite-based Precipitation Products Downscaling. European Geosciences Union (EGU) General Assembly 2018, Vienna, Austria.

Sharifi, **E**., Saghafian., B., Steinacker, R., **2018**: Bias Correction of Satellite Precipitation Products based on Concept of Copula. European Geosciences Union (EGU) General Assembly 2018, Vienna, Austria.

Sharifi, **E**., Steinacker, R., Saghafian., B., **2017**: Hourly Comparison of GPM-IMERG-Final-Run and IMERG-Real-Time (V-03) over a Dense Surface Network in Northeastern Austria. European Geosciences Union (EGU) General Assembly 2017, Vienna, Austria.

Sharifi, **E**., Steinacker, R., Saghafian., B., **2016**: Data Analysis of GPM Constellation Satellites-IMERG and ERA-Interim precipitation products over West of Iran. European Geosciences Union (EGU) General Assembly 2016, Vienna, Austria.

Experience

Teaching

Atmospheric Systems, University of Vienna, summer semesters 2017, 2018 and 2019.

Employments

Expert of cereal research department- Dryland Agricultural Research Sub-Institute (DARSI) Kermanshah-Iran.

Researcher at the University of Vienna, Department of Meteorology and Geophysics (IMGW), Vienna, Austria.

Researcher at the University of Natural Resources and Life Sciences (BOKU), Department of Water - Atmosphere - Environment (WAU), Vienna, Austria.

Reviewer at peer-reviewed journals

Journal of Geophysical Research-Atmosphere (JGR) from American Geophysical Union (AGU) Publication.

Remote Sensing Journal from MDPI publication.

Journal of Mountain Science (JMS) published by Science Press China, and distributed by Springer.

Atmospheric Research Journal from ELSEVIER Publication.

Workshop

2018 Holding a scientific-educational workshop entitled "Introducing the new Precipitation Satellite Products and how to use their data", Islamic Azad University, Science and Research Branch, Tehran, Iran.

2018 Holding a scientific-educational workshop entitled "Introduction to Remote Sensing: Monitoring Precipitation", Razi University, Kermanshah, Iran.

Conference contribution

Board Member of Panel for "Managing the risk of extreme events (droughts and floods)" in 6th National Conference on Water Resources Management, University of Kurdistan-Iran; 04/2016

Award and scholarship

2018 Dissertation completion fellowship, awarded by center of doctoral studies, University of Vienna, prepared and submitted by E. Sharifi.

2016 Conference travel grant, awarded by Research Services and Career Development, University of Vienna, to attend the 6th Iranian National Conference on Water Resources Management - April 20-22, 2016, at the University of Kurdistan-Iran.

2016 Author of top paper in 6th Iranian National Conference on Water Resources Management, University of Kurdistan-Iran; 04/2016

Computer skill

Platform Linux, Windows

Programming MATLAB, Python, Linux Shell

Software ArcGIS, APRun,

General	Office, Latex, SPSS, Endnote, Citavi, Prezi

Language

English	Fluent
Persian	Native
German	Upper-Intermediate
Arabic	Basic

Membership

2015-Present	European Geosciences Union (EGU)
2010-Present	Iranian Society of Crop and Plant Breeding Sciences
2005-2012	Agriculture and Natural Resources Engineering Organization-Kermanshah, Iran
2009-2011	Canoe-Kayak National Team-Iran